Acta Pharmacologica Sinica (2011) 32: 861–872
 1671-4083/11 $32.00
www.nature.com/aps

Review

CaMKII in cerebral ischemia

Steven J COULTRAP[1], Rebekah S VEST[1], Nicole M ASHPOLE[2], Andy HUDMON[2, 3, *], K Ulrich BAYER[1, *]

[1]*Department of Pharmacology, University of Colorado Denver-School of Medicine, Aurora, CO 80045, USA;* [2]*Stark Neuroscience Research Institute,* [3]*Department of Biochemistry and Molecular Biology, Indiana University School of Medicine, Indianapolis, IN 46202, USA*

Ischemic insults on neurons trigger excessive, pathological glutamate release that causes Ca^{2+} overload resulting in neuronal cell death (excitotoxicity). The Ca^{2+}/calmodulin (CaM)-dependent protein kinase II (CaMKII) is a major mediator of physiological excitatory glutamate signals underlying neuronal plasticity and learning. Glutamate stimuli trigger autophosphorylation of CaMKII at T286, a process that makes the kinase "autonomous" (partially active independent from Ca^{2+} stimulation) and that is required for forms of synaptic plasticity. Recent studies suggested autonomous CaMKII activity also as potential drug target for post-insult neuroprotection, both after glutamate insults in neuronal cultures and after focal cerebral ischemia *in vivo*. However, CaMKII and other members of the CaM kinase family have been implicated in regulation of both neuronal death and survival. Here, we discuss past findings and possible mechanisms of CaM kinase functions in excitotoxicity and cerebral ischemia, with a focus on CaMKII and its regulation.

Keywords: brain ischemia; excitotoxicity; glutamate; CaMKII; CaM kinases; stroke

Acta Pharmacologica Sinica (2011) 32: 861–872; doi: 10.1038/aps.2011.68; published online 20 Jun 2011

Introduction

Global cerebral ischemia is caused by a general loss of oxygen supply to the brain (during drowning, suffocation, or cardiac arrest). While the increased availability of automated external defibrillators has dramatically increased the survival rate after cardiac arrest, survivors may suffer from neuronal damage caused by the oxygen deficit in the brain. Despite increased demand for a neuroprotective treatment of global cerebral ischemia, no effective therapy has been developed to date. Focal cerebral ischemia (stroke) also involves decreased oxygen supply to parts of the brain. However, focal cerebral ischemia is caused by regional lack of blood supply after clotting or hemorrhage of blood vessels in the brain. The focal core area of the stroke is generally considered to be beyond rescue, however, neurons in the surrounding penumbra (where secondary cell loss occurs) are potential targets for therapeutic intervention[1] (Figure 1). Currently, the only available FDA approved pharmacological treatment is haemolytic therapy with tissue plasminogen activator (tPA). However, tPA is contra-indicated in hemorrhagic stroke, and by the time most patients receive diagnostic evaluation, tPA is no longer effective (and may even do more harm than good)[2–4]. Thus, less than 2% of stroke patients actually receive tPA[5], leaving a significant void in therapies that are more universally applicable for stroke treatment. Two independent studies recently implicated CaMKII as a promising drug target for post-insult neuroprotection[6, 7]. Here, we discuss the CaM kinase family and its possible involvement in the regulation of neuronal cell death, with a focus on CaMKII and its regulation.

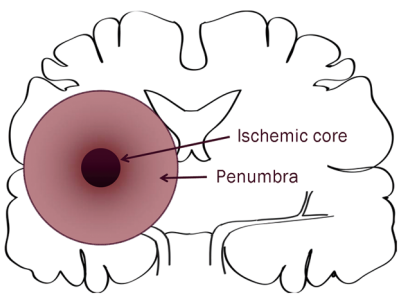

Figure 1. Ischemic core and penumbra after stroke. While neurons in the ischemic core are considered beyond rescue, neurons in the penumbra are potential targets for therapeutic intervention.

* To whom correspondence should be addressed.
E-mail ulli.bayer@ucdenver.edu (K Ulrich BAYER);
ahudmon@iupui.edu (Andy HUDMON)
Received 2011-03-03 Accepted 2011-04-22

Glutamate excitotoxicity causes neuronal cell death after cerebral ischemia

Glutamate is the major excitatory neurotransmitter in the mammalian brain. However, excessive glutamate also leads to neuronal cell death via "glutamate excitotoxicity", a process that involves Ca^{2+} overload[8] and that was first demonstrated in retinal neurons[9], and subsequently in the brain[10, 11]. Ischemic conditions trigger anoxic depolarization of neurons, which in turn triggers massive release of glutamate[1, 12, 13]. It is thought that the excitotoxic effect of such glutamate overstimulation causes much of the neuronal cell death seen following cerebral ischemia[13–16]. Additionally, excitotoxic glutamate signaling is thought to contribute to neuronal cell death after traumatic brain injury and in neurodegenerative diseases[16–18]. Excitotoxicity can cause neuronal death with apoptotic or necrotic appearance[19, 20], but both may involve similar signaling pathways despite a different morphological end state[14, 21, 22]. Overstimulation of most glutamate receptors can cause neuronal cell death, but the Ca^{2+} conducting NMDA-type glutamate receptors appear to be the most sensitive "death receptors"[23–26]: Even relatively brief (~5 min) application of glutamate or NMDA to cultured neurons can trigger signaling events that cause significant cell death within 24 h. Consequently, extensive efforts were made to develop NMDA-receptor inhibitors into stroke therapies, unfortunately without success[27, 28]. Alternative strategies include targeting signaling molecules downstream of the NMDA-receptor, such as CaMKII, which has been shown to mediate key effects of physiological NMDA-receptor stimulation in neuronal plasticity and learning and memory[29–31].

CaMKII and the CaM kinase family

CaM kinases (Figure 2) are a large family of Ser/Thr protein kinases that include kinases with broad substrate spectrum (*ie* multifunctional kinases such as CaMKI, CaMKII, and CaMKIV) and with high substrate selectivity [*ie* dedicated kinases such as myosin light chain kinases (MLCKs) and phosphorylase kinase (PhK)]. As the name implies, CaM kinases are generally activated by binding of Ca^{2+}/CaM to their regulatory region. However, several CaM kinases (including DAPK3 and AMPKs) lack a CaM-binding regulatory region, but are included in the CaM kinase family based on high homology of their core kinase domain. Regulation by Ca^{2+}/CaM does not automatically classify a kinase in the CaM kinase family. For instance, CaMKIII (now termed eEF2 kinase), which is also activated by Ca^{2+}/CaM, is not closely related to the other CaM kinases[32] and is instead grouped with the family of atypical protein kinases[33]. Like many other kinases (including PKA, PKB/Akt, and PKC), several CaM kinase family members require phosphorylation within the activation loop of their core kinase domain for full activity (including CaMKI T177, CaMKIV T196, and AMPKs T172). Interestingly, an upstream kinase that phosphorylates the activation loop of CaMKI, CaMKIV, and AMPK (as well as PKB/Akt, which is not a CaM kinase) is CaMKK, which is itself a Ca^{2+}/CaM-stimulated kinase[34]. However, other CaM kinases (including CaMKII and DAPKs) do not even have a phosphorylatable residue at the homologous activation loop position, even though their activity can be regulated by other phosphorylation events outside of their core kinase domains (such as T286 of CaMKII, which makes the kinase partially Ca^{2+}/CaM-independent[35–38], and S735 of DAPK1, which further enhances Ca^{2+}/CaM stimulated activity[39]).

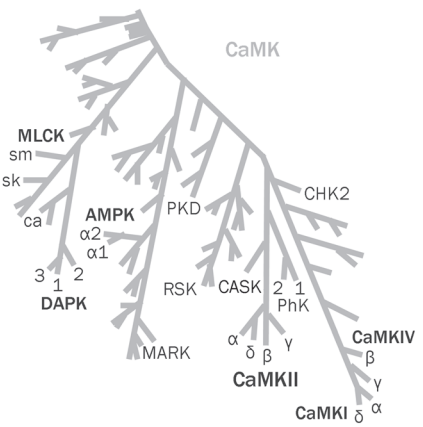

Figure 2. The CaM kinase family tree[33], with a limited number of example CaM kinases marked.

Functionally, DAPKs (death associated protein kinases) are associated with regulation of cell death[40], MLCKs (myosin light chain kinases) regulate smooth muscle contraction[41], and AMPKs (AMP activated kinases) are regulators of energy metabolism[42]. CaMKI, CaMKII, and CaMKIV have been implicated in various neuronal functions, including plasticity[30, 31, 43]. CaMKII comprises a family of closely related kinases, with four isoforms (α, β, γ, and δ) encoded by different genes, and alternative splicing gives rise to additional diversity[31]. At least one CaMKII isoform was found to be expressed in every cell type examined, with CaMKIIγ and CaMKIIδ being the most ubiquitous isoforms[44, 45]. CaMKIIα is almost exclusively expressed in brain, where it is also extremely abundant, making up more than 1% of total protein in some brain regions, such as the hippocampus[46]. Notably, the hippocampus, specifically its CA1 region, is also the brain area that is most sensitive to damage following global cerebral ischemia[47]. The hippocampus is important in memory formation, and the CaMKIIα knockout mice were the first knockout mice described to show impaired neuronal plasticity and learning[48, 49].

CaMKII structure and regulation

The relationship between CaMKII structure and regulation has been reviewed previously in detail[31]. However, there have since been several significant advances, especially regarding CaMKII structure[50–53] (Figure 3). CaMKII forms 12meric holoenzymes, with the C-terminal association domains forming a central hub and the N-terminal kinase domains radiating outwards like spokes or petals (Figure 3A). Between the core kinase domain and the association domain, the CaMKII

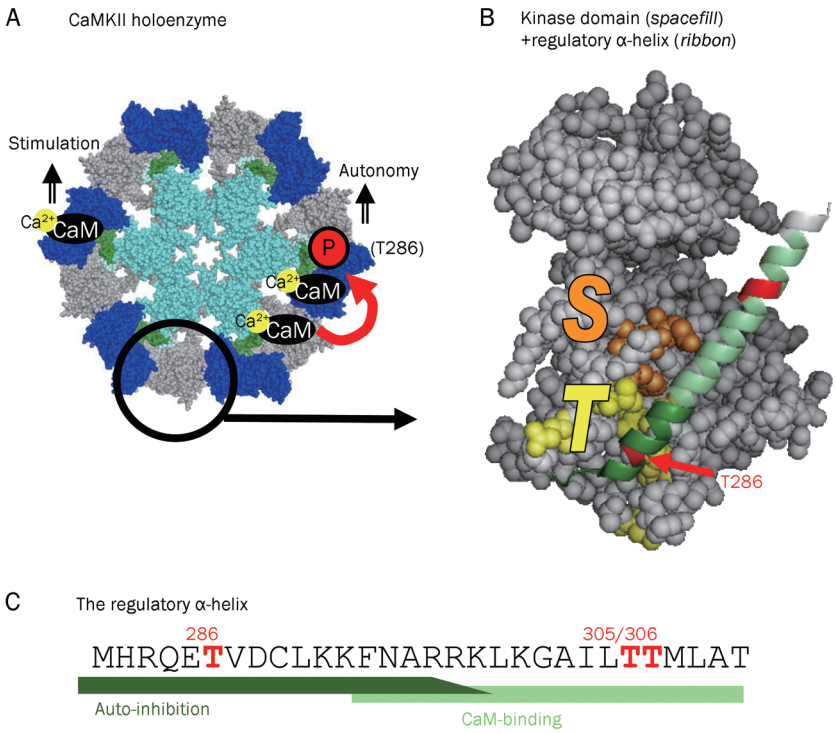

Figure 3. CaMKII structure[50, 51] and regulation. (A) CaMKII forms multimeric holoenzymes via C-terminal association domains (acqua). Each kinase domain (grey, dark blue) is stimulated separately by Ca^{2+}/CaM binding, but intersubunit autophosphorylation at T286 generates autonomous activity that persists even after dissociation of Ca^{2+}/CaM. (B) In the basal state, the regulatory α-helix (ribbon) interacts with the T-site (yellow) and prevents access to the substrate binding S-site (orange). Autophosphorylation sites (red) generate autonomous activity (T286) or prevent CaM binding (T305/306) and affect targeting. (C) The sequence of the regulatory α-helix. The regions contributing to CaM-binding and to auto-inhibition are marked.

subunits contain a Ca^{2+}/CaM-binding autoregulatory region followed by a variable region that is subject to extensive alternative splicing. The largest described splice variant is CaMKII βM (72 kDa)[54]; the dominant isoforms in brain are α (50 kDa) and β (60 kDa)[55, 56]. Holoenzymes can be homomeric or heteromeric (*ie* formed by subunits of the same or different isoforms)[54, 56–60], with a molecular weight of ~600–750 kDa and a diameter of ~20 nm[38, 50–52, 61, 62].

The α-helical autoregulatory region is responsible for holding CaMKII in an inactive state under basal conditions (Figure 3B). Its N-terminal part surrounding T286 interacts with the core kinase domain at a region termed the T286-binding site (T-site)[51, 63, 64]. When the autoregulatory region is bound to the T-site, access to the adjacent substrate binding S-site is blocked, thus preventing CaMKII activity (Figure 3B). Each kinase subunit within a holoenzyme is activated separately by direct binding of Ca^{2+}/CaM to the autoregulatory region ("stimulated activity"). This Ca^{2+}/CaM-binding displaces the autoregulatory region from the T-site, allowing the kinase to make other protein-protein interactions via the T-site (see below). Importantly, displacement of the autoregulatory region also allows access to the S-site, thereby activating the kinase. Additionally, releasing T286 from the T-site makes T286 accessible for auto-phosphorylation by neighboring subunits within the holoenzyme, provided these neighboring subunits are also activated with an exposed S-site[65, 66]. This auto-phosphorylation of T286 prevents complete re-association of the autoregulatory region with the T- and S-sites, leaving CaMKII partially active even after dissociation of Ca^{2+}/CaM ("autonomous activity")[35–37,67]. This autonomous activity has been described as a molecular memory mechanism and is indeed important for synaptic plasticity and learning[67, 68]. More recently, autonomous CaMKII activity has also been identified as a drug target for post-insult neuroprotection[6, 7].

An additional regulatory auto-phosphorylation at T305/306 can occur as an intra-subunit reaction and prevents subsequent Ca^{2+}/CaM binding[69–72] (Figure 3B). *Vice versa*, Ca^{2+}/CaM binding prevents this inhibitory auto-phosphorylation. Thus, efficient T305/306 auto-phosphorylation occurs only after generation of autonomous activity by T286 auto-phosphorylation and subsequent Ca^{2+}/CaM dissociation. Such a triple-phosphorylated CaMKII would be locked in a partially active state that cannot be further stimulated[67], but it would be completely inactivated only after selective T286 dephosphorylation.

Glutamate-induced translocation of CaMKII

Ca^{2+}-influx through NMDA-type glutamate receptors stimulates CaMKII activity and T286 auto-phosphorylation. Both are required for induction of long-term potentiation of synaptic strength[68, 73, 74], a form of synaptic plasticity underlying learning and memory[29, 30, 75]. Additionally, glutamate-induced Ca^{2+}-influx causes two forms of CaMKII translocation: (i) to post-synaptic sites[64, 76–78], and (ii) to extra-synaptic clusters[79–82]. Synaptic translocation occurs after physiological glutamate stimuli and is involved in synaptic plasticity[83, 84]. Several synaptic proteins have been described as binding partners for CaMKII, but the NMDA receptor subunit GluN2B (formerly known as NR2B) appears to be most important for CaMKII translocation to the synapse[64, 78, 85–89]. Extra-synaptic clustering has been described after pathological glutamate stimuli and ischemic conditions[79–82], and is likely mediated by

self-association of multiple CaMKII holoenzymes into large insoluble complexes[79, 90, 91], a process here termed aggregation. Both types of translocation require protein-interactions via the CaMKII T-site, specifically T-site binding to the GluN2B region around S1303[64, 85, 92] or the region around T286 of a CaMKII subunit within another holoenzyme[82, 90, 91]. Accordingly, both interactions require Ca^{2+}/CaM-binding, in order to make the T-site accessible. Both interactions are also enhanced by nucleotide. However, holoenzyme aggregation *in vitro* requires mimicking ischemic conditions, *ie* low ATP/ADP ratio and low pH. High ATP concentrations favor T286 auto-phosphorylation, which enhances CaMKII binding to GluN2B[64, 85], but inhibits CaMKII aggregation (as it inhibits interaction of T286 with the T-site)[91]. The molecular basis for requirement of a pH below 6.8 for CaMKII aggregation is unclear, but may involve protonation of His282, which is located at the hinge of the auto-regulatory α-helix (Figure 3B). CaMKII aggregation causes a reduction in the degree of activity that can be stimulated by Ca^{2+}/CaM[79], an effect also observed in brain after ischemia[93–95]. For this reason, it has been speculated that CaMKII aggregation may be a neuroprotective mechanism, as it would limit aberrant CaMKII activity during disregulated, pathological Ca^{2+} signaling[79]. However, the potential neuroprotective functions of CaMKII aggregation have yet to be determined.

Inhibitors of CaMKII

The traditional small molecule CaMKII inhibitors KN62 and KN93[96, 97] have proved to be very useful tools for studying CaMKII functions in cells, as they are membrane penetrating and their selectivity for CaMKII is relatively good[96–98]. However, the KN inhibitors cannot distinguish between CaMKII and CaMKIV[99]. Through an unusual affect on the scaffolding protein AKAP79/150[100], KN inhibitors can also inhibit PKC action at the synapse[101]. Maybe more importantly, KN inhibitors additionally affect voltage gated Ca^{2+} and K^+ channels[102, 103]. Another limitation is that both KN62 and KN93 are competitive with CaM and inhibit only stimulated but not autonomous CaMKII activity[6, 96, 97]. Peptide inhibitors derived from the CaMKII autoregulatory region, such as AC3-I or AIP[7, 104, 105], are generally thought to be more selective than the KN compounds. However, they can also inhibit other kinases, including PKC, MLCK, and PKD[106–108]. Additionally, some studies indicated a relatively low potency (IC_{50} of ~3 μmol/L)[109, 110].

More recently, an alternative was provided by CN21, a potent and selective CaMKII inhibitor[111]. CN21 is a 21mer peptide derived from the natural CaMKII inhibitory protein CaM-KIIN[112]. Peptides and even proteins can be made cell penetrating by fusion with sequence motifs such as ant/penetratin or tat[113–115]. In initial attempts to make CN peptides cell penetrating, ant fusion was used[116, 117]. However, it was subsequently shown that the ant/penetratin sequence directly binds CaM, an effect further enhanced by fusion with CN21[74]. Thus, while fusion of CN to ant added an additional CaMKII-inhibitory mechanism, selectivity for CaMKII was compromised. However, alternative fusion of CN21 to tat still allowed cell-penetration without the caveat of binding CaM[74]. The resulting tatCN21 is a potent (IC_{50} of ~50 nmol/L), selective, and cell penetrating peptide inhibitor of both stimulated and autonomous CaMKII activity[6, 74, 111]. Consistent with previous reports that tat fusion peptides can cross the blood brain barrier[26, 118], tatCN21 inhibited CaMKII functions in brain even after systemic application[6, 74].

CaMKII autonomy as a drug target for post-insult neuroprotection

Inhibiting stimulated and autonomous CaMKII activity with tatCN21 attenuated neuronal cell death induced by glutamate insult in primary cultures as well as in a mouse model of stroke (middle cerebral arterial occlusion; MCAO), even when administered significantly after the insult[6]. The longest post-insult time periods tested in this study were 6 h in hippocampal cultures, 1 h in cortical cultures, and 1 h *in vivo*[6]. A recent study independently confirmed post-insult neuroprotection by CaMKII inhibition, using both tatCN21 and tatAIP[7]. This study found significant neuroprotection in cortical cultures also when tatCN21 was administered 2 h after the insult[7]. By contrast, the traditional CaMKII inhibitor KN93 was neuroprotective only when administered during but not after the insult in both studies[6, 7]. During an insult, tatCN21, tatAIP, and KN93 can inhibit CaMKII activation and/or generation of autonomous activity. However, after the insult, tatCN21 and tatAIP but not KN93 can inhibit autonomous CaMKII activity that has already been generated. Thus, these findings indicated that autonomous CaMKII activity is the relevant drug target for post-insult neuroprotection by tatCN21. Indeed, overexpression of CaMKII wild-type or the constitutively autonomous T286D mutant (which mimics T286 phosphorylation) increased glutamate-induced neuronal death significantly more than overexpression of the autonomy-incompetent T286A mutant[6]. Consistent with these recent results[6, 7], neuroprotection by CaMKII inhibition had been described previously, although only for inhibition during or prior to excitotoxic insults[119–123]. Protection was seen in cortical cultures[6, 7, 119, 121], hippocampal cultures[6, 123] and retinal cells[120, 122]. However, other studies indicated an opposite effect, *ie* that abolishing CaMKII activity can promote neuronal cell death[124–128]. Some of these results may be explained by different death-inducing stimuli and different culture systems, as cerebellar granule cells and spiral ganglion cells depend on depolarization-induced Ca^{2+} signals for survival[126–128]. Additionally, different results using the inhibitor KN93 may depend on the balance between death- and survival-promoting signals mediated by CaMKII and CaMKIV, respectively[125]. Notably, however, genetic knock-out of CaMKIIα resulted in increased infarct size in a mouse model of stroke[124], the opposite effect from the observation after acute CaMKII inhibition with tatCN21[6]. This difference could be explained by developmental effects caused by the absence of CaMKIIα. Indeed, the CaMKIIα knock-out mice are epileptic[129], and hyper-excitability may contribute to higher susceptibility to ischemic insults. Additionally, inhibition of

CaMKII and complete removal of CaMKIIα protein may have profoundly different effects on glutamate-induced neuronal death. Thus, it will be interesting to compare CaMKII knock down by RNAi with CaMKII inhibition in neuronal cultures and to compare CaMKIIα knock-out mice with existing knock-in mice that carry the inactive CaMKIIα K42R mutation[130]. However, a recent study indicated that long-term (8–24 h) inhibition of CaMKII activity (without loss of CaMKII protein) is sufficient to increase vulnerability to subsequent excitotoxic insults[7], even though acute CaMKII inhibition during or after the insults reduced neuronal cell death (Table 1)[6, 7].

Table 1. Post-insult neuroprotection by CaMKII inhibitors[6, 7]. Tested were glutamate insults in hippocampal and/or cortical cultures, and a MCAO stroke model in mouse. (Stim, stimulated; Aut, autonomous).

Inhibitor	CaMKII activity blocked		Neuroprotection when applied		
	Stim	Aut	During insult	After insult	After stroke
KN93	x	–	x	–	?
tatCN21	x	x	x	x	x
tatAIP	x	x	x	x	?

Other CaM kinases in neuronal death and survival

CaMKII is not the only CaM kinase family member implicated in the regulation of neuronal survival and cell death. For example, CaMKIV activity has been described to be neuroprotective in multiple systems, likely by its phosphorylation and activation of the transcription factor CREB[127, 131–133]. CaMKI may have a similar effect, as it can activate Mek/Erk, which, in turn, also activates CREB[134]. CaMKK activity is also neuroprotective, as its inhibition by STO-609[135] increases neuronal cell death[6]. CaMKK is an upstream activator of at least two survival kinases, CaMKIV (see above) and Akt/PKB (which is not a member of the CaM kinase family)[136]. However, CaMKK is also an upstream activator of AMPK, a non-CaM-binding CaM kinase family member that has been implicated in promoting stroke-related neuronal death[137, 138]. Interestingly, acute treatment with the AMPK activator metformin during stroke insults increases neuronal death, while previous treatment with metformin before the insult reduces cell death[139]. This is similar to the phenomenon of ischemic preconditioning, in which previous mild insults can partially protect from the effect of subsequent stronger insults[140–143], indicating that AMPK may be part of a mechanism for this ischemic preconditioning. Thus, AMPK is also a possible target for stroke treatment, however, the effect of therapeutically relevant post-insult AMPK inhibition has not yet been tested[144].

Death-associated protein kinases (DAPKs) are another branch of the CaM kinases family associated with the regulation of cell death and survival[40]. DAPK1 has specifically been implicated in mediating excitotoxicity and stroke related death of neurons[145]. Interestingly, this required an interaction between DAPK1 and the NMDA-receptor subunit GluN2B[145] at the same site that also interacts with CaMKII[64, 92]. This raises the possibility that some of the neuroprotective treatments designed to target DAPK1 or CaMKII may act in part through effects on the other kinase; in fact, targeting both kinases with the same compound may be desirable for maximal therapeutic effect. However, molecular manipulations indicated that targeting each kinase separately is also neuroprotective independent from effects on the other kinase[6, 145]. Interestingly, manipulations that dissociate the scaffolding protein PSD95 from GluN2B also protect neurons from excitotoxic and stroke induced death[26, 146]. It has been proposed that this neuroprotection is due to the resulting dissociation of neuronal nitric oxide synthase (nNOS) from the NMDA-receptor[26, 146]. It will be interesting to test if this manipulation additionally indirectly affects GluN2B interaction with CaMKII and/or DAPK1.

What are the downstream targets for CaMKII after excitotoxic insults?

The mechanisms by which inhibition of autonomous CaMKII activity may mediate post-insult neuroprotection are currently unclear. Possible pathways by which CaMKII may participate in the regulation of neuronal death and survival are described below and summarized in Figure 4. Potentially death promoting effects of CaMKII activity include increase of AMPA-receptor single channel conductance by phosphorylating its GluR1 subunit at S831[147, 148]. This effect is especially pronounced for GluR1-homomeric AMPA-receptors[149], which are (in contrast to GluR2 containing channels) Ca^{2+}-conducting[150, 151], and could thus further promote death-inducing Ca^{2+} overload. Indeed, such Ca^{2+}-conducting AMPA-receptors have been implicated in ischemic injury[152]. CaMKII could also further increase the Ca^{2+} overload by facilitating or potentiating L-type voltage dependent Ca^{2+} channels (VDCCs) via their α or β subunits[153, 154]. Additionally, CaMKII can directly interact with connexin hemichannels[155], which are important in neuronal homeostasis and for neuron-glia communication and have been implicated in glutamate-induced cell death[156–158]. CaMKII activity may also contribute to neuronal cell death through phosphorylation of acid-sensing ion channels, which enhances the ischemia-induced activation of the ion channel[123]. Recently, CaMKII activity was also shown to be required for ischemia-induced shuttling of cytoplasmic polyadenylation element binding 4 (CPEB4) into the nucleus[159]. CPEBs regulate cytoplasmic polyadenylation and translation in neurons[160, 161], and some cross-talk between CPEB1 and CaMKII signaling has been described[162, 163]. CPEB4 knock down induces neuronal death, which can be rescued by re-expression of CPEB4 wild type, but not to the same extent by its nuclear export-incompetent mutant[159]. Thus, nuclear retention of CPEB4 by CaMKII activity may contribute to ischemia-induced neuronal death. Another protein that induces neuronal death upon nuclear shuttling is apoptosis inducing

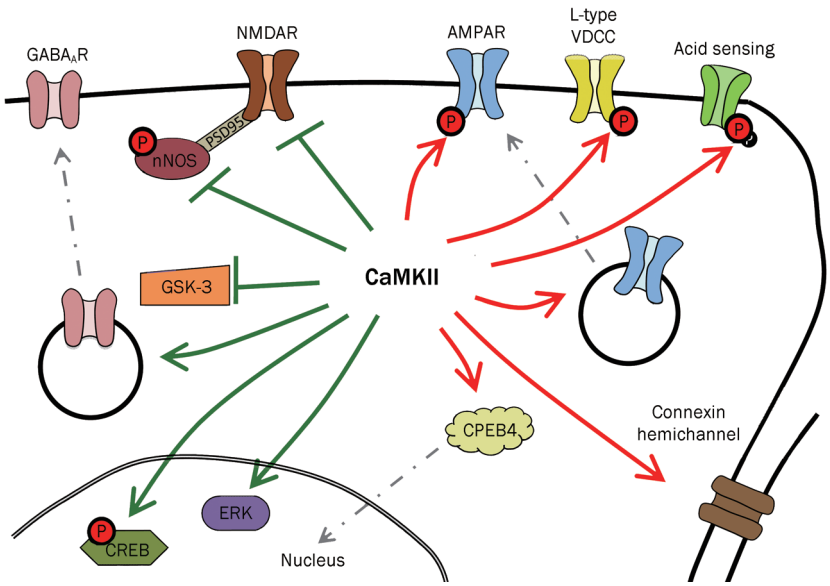

Figure 4. CaMKII downstream targets that may be involved in regulation of neuronal viability. CaMKII signaling may promote excitotoxic cell death (red) or neuronal survival (green). Activation (arrow) or inhibition (bar) of the downstream targets is indicated. Some but not all of these downstream effects are mediated by direct phosphorylation of the target.

factor (AIF)[164]. However, involvement of CaMKII in nuclear shuttling of AIF has not yet been tested.

On the other hand, several downstream effects of CaMKII activity could instead promote neuronal survival. Maybe most prominently, CaMKII can phosphorylate and inhibit nNOS[165–168], thereby reducing production of nitric oxide, which is neuro-toxic[14, 169–172]. CaMKII can also regulate several ion channels in a way that may afford neuroprotection from excitotoxic insults: It promotes desensitization NMDA-receptors[173], and it enhances surface expression of the inhibitory $GABA_A$-receptors[174, 175]. Additionally, CaMKII can activate pro-survival proteins such as Erk[117, 176] and CREB[177], inhibit death-promoting proteins such GSK-3[178] and Bad[127]. CaMKII can also promote neuronal survival by inhibiting HDAC5[126], a CaMKII substrate that inhibits the pro-survival transcription factor MEF[179]. These possible mechanisms may explain why the effect of CaMKII inhibition on cell survival can depend on the cell type and/or the death-inducing stimulus. Maybe more importantly, it may also explain why prolonged reduction of CaMKII activity increases vulnerability to subsequent excitotoxic insults[7, 124]. However, there is ample evidence that acute CaMKII inhibition protects hippocampal, cortical, and retinal neurons from glutamate excitotoxicity[6, 7, 119–123], consistent with the neuroprotection seen in a mouse model of stroke[6].

CaMKII regulation of apoptotic cell death: lessons from non-neuronal systems?

Apoptosis is a common mechanism of regulated cell death that involves caspase activation, nuclear condensation, and DNA fragmentation[180–183]. Ca^{2+} signaling and CaMKII have been linked to the regulation of apoptosis also in non-neuronal systems. However, as for the neuronal CaMKII targets discussed above, some of these links to apoptosis can promote cell death while others promote survival. CaMKII has been shown to be involved in mediating apoptosis induced by TNFα and UV irradiation[184] microcystein (phosphatase inhibitor)[185, 186], GW7845 (PPARγ agonist)[187], ER stress[188], TRAIL[189], and -in cardiac myocytes- by isoproterenol (β adrenergic agonist)[190, 191], ouabain (Na^+/K^+-ATPase inhibitor)[192], oxidative stress (induced by H_2O_2 or angiotensin II)[193–195], and cardiac ischemia[196–198]. In these cases, CaMKII inhibition attenuated apoptotic death. However, CaMKII inhibition has also been described to enhance apoptosis, indicating that CaMKII can also suppress apoptosis in other systems[199–204]. Anti-apoptotic CaMKII mechanisms included inhibition of caspase 2[199], enhancing expression of Bcl-xL[203], and promoting Akt-mediated inhibition of Bad[204]. Interestingly, CaMKII-mediated activation of Akt has been linked to both pro-[189] and anti-apoptotic[200, 201, 204] functions.

In the heart, CaMKII contributes to cell death in response to a variety of insults, and CaMKII inhibition consistently promoted cell survival[205] (see above). However, even in the heart, the situation is more complicated: While cytoplasmic CaMKII isoforms were consistently found to promote cell death, nuclear isoforms (*ie* CaMKII δ_B)[206] may instead promote survival[194, 207].

Clearly, the mechanisms by which CaMKII can regulate cell viability are complex and in need of further elucidation. However, the dual role for CaMKII in mediating both cell survival and death may not be that surprising after all, given that its principal activator, Ca^{2+}, is already well established to mediate both[208, 209]. Even Ca^{2+} signaling mediated by NMDA receptors can promote not only death but also survival[210, 211]. Generally, CaMKII appears likely to have pro-survival function in systems and situations in which Ca^{2+} is required for maintaining cell viability (such as activity-mediated neuronal survival). By contrast, in situations where Ca^{2+} acts instead as a trigger of death signaling, CaMKII is likely to be involved as a major mediator of cell death (such as in cerebral ischemia and exitotoxicity).

Concluding remarks and therapeutic potential

Recent results implicated that autonomous activity of CaMKII, induced by T286 auto-phosphorylation, provides a promising drug target for post-insult neuroprotection after cerebral ischemia and possibly other conditions involving glutamate excitotoxicity[6,7]. In the future, therapy development may include identification of selective small-molecule inhibitors of autonomous CaMKII. However, the peptide inhibitor tatCN21 itself also holds promise, as it was effective even after systemic delivery in an animal model[6, 74]. The toxicology for tatCN21 is still lacking, but no immediately obvious toxic effects were observed in mice. TatCN21 did interfere with learning in mice, which could be a potential contraindication for chronic treatment in humans[74]. However, for acute treatment after stroke, a temporary learning impairment would be more than acceptable, especially since tatCN21 did not interfere with memory storage or retrieval[74], and is thus unlikely to induce retrograde amnesia. Potency of tatCN21 is very reasonable, with an IC_{50} of ~50 nmol/L[74], and further improvements of potency may be possible. However, further studies are needed in order to elucidate the downstream mechanisms linking CaMKII to the neuronal cell death that is induced by ischemic conditions. Additionally, the window of therapeutic opportunity (at least 1 h in a mouse model of stroke[6]) needs to be evaluated more closely after different types of ischemic insults *in vivo*. After glutamate insults in culture, hippocampal neurons were significantly protected by tatCN21 application even 6 h after the insult[6], while protection of cortical neurons was only seen when tatCN21 was applied less than 3 h after the insult[7]. This difference may be caused by the type of glutamate insult (400 μmol/L for 5 min[6], versus 100 μmol/L for 60 min[7]). However, if the difference is instead inherent to the neuronal cell type, tatCN21 may have an even longer window of therapeutic opportunity after global cerebral ischemia, which particularly affects the hippocampus[47], compared to focal cerebral ischemia (stroke). Additionally, the therapeutic potential in other acute conditions involving glutamate excitotoxicity, such as traumatic brain injury, should be evaluated.

Financial disclosure

The University of Colorado is currently seeking patent protection for tatCN21, its derivatives, and its uses (including the ones outlined here).

Acknowledgements

The structural model of the CaMKII holoenzyme was kindly provided by Drs Luke CHAO and John KURIYAN (University of California, Berkeley). Support was provided by NIH training grants T32GM007635 and F31NS061584 (RSV), Ralph W and Grace M Showalter (AH), Indiana State Department of Health, Spinal Cord Brain Injury research grant ISDH/A70-0-0-079212 (AH), and NIH R01NS052644 (KUB).

References

1 Liu S, Levine SR, Winn HR. Targeting ischemic penumbra: part I – from pathophysiology to therapeutic strategy. J Exp Stroke Transl Med 2010; 3: 47–55.
2 Weinberger JM. Evolving therapeutic approaches to treating acute ischemic stroke. J Neurol Sci 2006; 249: 101–9.
3 Kaur J, Zhao Z, Klein GM, Lo EH, Buchan AM. The neurotoxicity of tissue plasminogen activator? J Cereb Blood Flow Metab 2004; 24: 945–63.
4 Wang X, Tsuji K, Lee SR, Ning M, Furie KL, Buchan AM, *et al*. Mechanisms of hemorrhagic transformation after tissue plasminogen activator reperfusion therapy for ischemic stroke. Stroke 2004; 35: 2726–30.
5 Kleindorfer D, Lindsell CJ, Brass L, Koroshetz W, Broderick JP. National US estimates of recombinant tissue plasminogen activator use: ICD-9 codes substantially underestimate. Stroke 2008; 39: 924–8.
6 Vest RS, O'Leary H, Coultrap SJ, Kindy MS, Bayer KU. Effective post-insult neuroprotection by a novel Ca^{2+}/calmodulin-dependent protein kinase II (CaMKII) inhibitor. J Biol Chem 2010; 285: 20675–82.
7 Ashpole NM, Hudmon A. Excitotoxic neuroprotection and vulnerability with CaMKII inhibition. Mol Cell Neurosci 2011; 46: 720–30.
8 Choi DW. Ionic dependence of glutamate neurotoxicity. J Neurosci 1987; 7: 369–79.
9 Lucas DR, Newhouse JP. The toxic effect of sodium L-glutamate on the inner layers of the retina. AMA Arch Ophthalmol 1957; 58: 193–201.
10 Olney JW. Brain lesions, obesity, and other disturbances in mice treated with monosodium glutamate. Science 1969; 164: 719–21.
11 Olney JW, Sharpe LG. Brain lesions in an infant rhesus monkey treated with monsodium glutamate. Science 1969; 166: 386–8.
12 Hubschmann OR, Kornhauser D. Cortical cellular response in acute subarachnoid hemorrhage. J Neurosurgery 1980; 52: 456–62.
13 Doyle KP, Simon RP, Stenzel-Poore MP. Mechanisms of ischemic brain damage. Neuropharmacology 2008; 55: 310–8.
14 Hara MR, Snyder SH. Cell signaling and neuronal death. Annu Rev Pharmacol Toxicol 2007; 47: 117–41.
15 Aarts MM, Tymianski M. Molecular mechanisms underlying specificity of excitotoxic signaling in neurons. Curr Mol Med 2004; 4: 137–47.
16 Bramlett HM, Dietrich WD. Pathophysiology of cerebral ischemia and brain trauma: similarities and differences. J Cereb Blood Flow Metab 2004; 24: 133–50.
17 Greve MW, Zink BJ. Pathophysiology of traumatic brain injury. Mount Sinai Journal of Medicine: J Translation Personalized Med 2009; 76: 97–104.
18 Mattson MP. Excitotoxic and excitoprotective mechanisms: abundant targets for the prevention and treatment of neurodegenerative disorders. Neuromolecular Med 2003; 3: 65–94.
19 Ankarcrona M, Dypbukt JM, Bonfoco E, Zhivotovsky B, Orrenius S, Lipton SA. Glutamate-induced neuronal death: a succession of necrosis or apoptosis depending on mitochondrial function. Neuron 1995; 15: 961–73.
20 McDonald JW, Behrens MI, Chung C, Bhattacharyya T, Choi DW. Susceptibility to apoptosis is enhanced in immature cortical neurons. Brain Res 1997; 759: 228–232.
21 Yuan J, Lipinski M, Degterev A. Diversity in the mechanisms of neuronal cell death. Neuron 2003; 40: 401–13.
22 Broughton BRS, Reutens DC, Sobey CG. Apoptotic mechanisms after cerebral ischemia. Stroke 2009; 40: e331–9.
23 Choi DW, Koh JY, Peters S. Pharmacology of glutamate neurotoxicity in cortical cell culture: attenuation by NMDA antagonists. J Neurosci 1988; 8: 185–96.

24 Frandsen A, Drejer J, Schousboe A. Direct evidence that excitotoxicity in cultured neurons is mediated via *N*-methyl-*D*-aspartate (NMDA) as well as non-NMDA receptors. J Neurochem 1989; 53: 297–9.
25 Noh KM, Yokota H, Mashiko T, Castillo PE, Zukin RS, Bennett MV. Blockade of calcium-permeable AMPA receptors protects hippocampal neurons against global ischemia-induced death. Proc Natl Acad Sci U S A 2005; 102: 12230–5.
26 Aarts M, Liu Y, Liu L, Besshoh S, Arundine M, Gurd JW, *et al*. Treatment of ischemic brain damage by perturbing NMDA receptor-PSD-95 protein interactions. Science 2002; 298: 846–50.
27 Ginsberg MD. Neuroprotection for ischemic stroke: past, present and future. Neuropharmacology 2008; 55: 363–89.
28 Villmann C, Becker CM. On the hypes and falls in neuroprotection: targeting the NMDA receptor. Neuroscientist 2007; 13: 594–615.
29 Malenka RC, Nicoll RA. Long-term potentiation — a decade of progress? Science 1999; 285: 1870–4.
30 Lisman J, Schulman H, Cline H. The molecular basis of CaMKII function in synaptic and behavioural memory. Nat Rev Neurosci 2002; 3: 175–90.
31 Hudmon A, Schulman H. Neuronal Ca^{2+}/calmodulin-dependent protein kinase II: the role of structure and autoregulation in cellular function. Annu Rev Biochem 2002; 71: 473–510.
32 Ryazanov AG, Ward MD, Mendola CE, Pavur KS, Dorovkov MV, Wiedmann M, *et al*. Identification of a new class of protein kinases represented by eukaryotic elongation factor-2 kinase. Proc Natl Acad Sci U S A 1997; 94: 4884–9.
33 Manning G, Whyte DB, Martinez R, Hunter T, Sudarsanam S. The protein kinase complement of the human genome. Science 2002; 298: 1912–34.
34 Haribabu B, Hook SS, Selbert MA, Goldstein EG, Tomhave ED, Edelman AM, *et al*. Human calcium-calmodulin dependent protein kinase I: cDNA cloning, domain structure and activation by phosphorylation at threonine-177 by calcium-calmodulin dependent protein kinase I kinase. EMBO J 1995; 14: 3679–86.
35 Miller SG, Kennedy MB. Regulation of brain type II Ca^{2+}/calmodulin-dependent protein kinase by autophosphorylation: a Ca^{2+}-triggered molecular switch. Cell 1986; 44: 861–70.
36 Lou LL, Lloyd SJ, Schulman H. Activation of the multifunctional Ca^{2+}/calmodulin-dependent protein kinase by autophosphorylation: ATP modulates production of an autonomous enzyme. Proc Natl Acad Sci U S A 1986; 83: 9497–501.
37 Schworer CM, Colbran RJ, Soderling TR. Reversible generation of a Ca^{2+}-independent form of Ca^{2+}(calmodulin)-dependent protein kinase II by an autophosphorylation mechanism. J Biol Chem 1986; 261: 8581–4.
38 Kolodziej SJ, Hudmon A, Waxham MN, Stoops JK. Three-dimensional reconstructions of calcium/calmodulin-dependent (CaM) kinase II and truncated CaM kinase II reveal a unique organization for its structural core and functional domains. J Biol Chem 2000; 275: 14354–9.
39 Chen CH, Wang WJ, Kuo JC, Tsai HC, Lin JR, Chang ZF. Bidirectional signals transduced by DAPK-ERK interaction promote the apoptotic effect of DAPK. EMBO J 2005; 24: 294–304.
40 Bialik S, Kimchi A. The death-associated protein kinases: structure, function, and beyond. Annu Rev Biochem 2006; 75: 189–210.
41 Stull JT, Lin PJ, Krueger JK, Trewhella J, Zhi G. Myosin light chain kinase: functional domains and structural motifs. Acta Physiol Scand 1998; 164: 471–82.
42 Oakhill JS, Scott JW, Kemp BE. Structure and function of AMP-activated protein kinase. Acta Physiol 2009; 196: 3–14.
43 Wayman GA, Lee YS, Tokumitsu H, Silva A, Soderling TR. Calmodulin-kinases: modulators of neuronal development and plasticity. Neuron 2008; 59: 914–31.
44 Tobimatsu T, Fujisawa H. Tissue-specific expression of four types of rat calmodulin-dependent protein kinase II mRNAs. J Biol Chem 1989; 264: 17907–12.
45 Bayer KU, Lohler J, Schulman H, Harbers K. Developmental expression of the CaM kinase II isoforms: ubiquitous gamma- and delta-CaM kinase II are the early isoforms and most abundant in the developing nervous system. Brain Res Mol Brain Res 1999; 70: 147–54.
46 Erondu NE, Kennedy MB. Regional distribution of type II Ca^{2+}/calmodulin-dependent protein kinase in rat brain. J Neurosci 1985; 5: 3270–7.
47 Hatakeyama T, Matsumoto M, Brengman J, Yanagihara T. Immunohistochemical investigation of ischemic and postischemic damage after bilateral carotid occlusion in gerbils. Stroke 1988; 19: 1526–34.
48 Silva AJ, Stevens CF, Tonegawa S, Wang Y. Deficient hippocampal long-term potentiation in alpha-calcium-calmodulin kinase II mutant mice. Science 1992; 257: 201–6.
49 Silva AJ, Paylor R, Wehner JM, Tonegawa S. Impaired spatial learning in alpha-calcium-calmodulin kinase II mutant mice. Science 1992; 257: 206–11.
50 Hoelz A, Nairn AC, Kuriyan J. Crystal structure of a tetradecameric assembly of the association domain of Ca^{2+}/calmodulin-dependent kinase II. Mol Cell 2003; 11: 1241–51.
51 Rosenberg OS, Deindl S, Sung RJ, Nairn AC, Kuriyan J. Structure of the autoinhibited kinase domain of CaMKII and SAXS analysis of the holoenzyme. Cell 2005; 123: 849–60.
52 Rosenberg OS, Deindl S, Comolli LR, Hoelz A, Downing KH, Nairn AC, *et al*. Oligomerization states of the association domain and the holoenzyme of Ca/CaM kinase II. FEBS J 2006; 273: 682–94.
53 Rellos P, Pike AC, Niesen FH, Salah E, Lee WH, von Delft F, *et al*. Structure of the CaMKIIdelta/calmodulin complex reveals the molecular mechanism of CaMKII kinase activation. PLoS Biol 2010; 8: e1000426.
54 Bayer KU, Harbers K, Schulman H. alphaKAP is an anchoring protein for a novel CaM kinase II isoform in skeletal muscle. EMBO J 1998; 17: 5598–605.
55 Schulman H, Greengard P. Stimulation of brain membrane protein phosphorylation by calcium and an endogenous heat-stable protein. Nature 1978; 271: 478–9.
56 Bennett MK, Erondu NE, Kennedy MB. Purification and characterization of a calmodulin-dependent protein kinase that is highly concentrated in brain. J Biol Chem 1983; 258: 12735–44.
57 Yamauchi T, Ohsako S, Deguchi T. Expression and characterization of calmodulin-dependent protein kinase II from cloned cDNAs in Chinese hamster ovary cells. J Biol Chem 1989; 264: 19108–16.
58 Kolb SJ, Hudmon A, Ginsberg TR, Waxham MN. Identification of domains essential for the assembly of calcium/calmodulin-dependent protein kinase II holoenzymes. J Biol Chem 1998; 273: 31555–64.
59 Brocke L, Chiang LW, Wagner PD, Schulman H. Functional implications of the subunit composition of neuronal CaM kinase II. J Biol Chem 1999; 274: 22713–22.
60 Lantsman K, Tombes RM. CaMK-II oligomerization potential determined using CFP/YFP FRET. Biochim Biophys Acta 2005; 1746: 45–54.
61 Kanaseki T, Ikeuchi Y, Sugiura H, Yamauchi T. Structural features of Ca^{2+}/calmodulin-dependent protein kinase II revealed by electron microscopy. J Cell Biol 1991; 115: 1049–60.
62 Morris EP, Török K. Oligomeric structure of [alpha]-calmodulin-dependent protein kinase II. J Mol Biol 2001; 308: 1–8.
63 Yang E, Schulman H. Structural examination of autoregulation of multifunctional calcium/calmodulin-dependent protein kinase II. J

Biol Chem 1999; 274: 26199–208.
64 Bayer KU, De Koninck P, Leonard AS, Hell JW, Schulman H. Interaction with the NMDA receptor locks CaMKII in an active conformation. Nature 2001; 411: 801–5.
65 Hanson PI, Meyer T, Stryer L, Schulman H. Dual role of calmodulin in autophosphorylation of multifunctional CaM kinase may underlie decoding of calcium signals. Neuron 1994; 12: 943–56.
66 Rich RC, Schulman H. Substrate-directed function of calmodulin in autophosphorylation of Ca^{2+}/calmodulin-dependent protein kinase II. J Biol Chem 1998; 273: 28424–9.
67 Coultrap SJ, Buard I, Kulbe JR, Dell'Acqua ML, Bayer KU. CaMKII autonomy is substrate-dependent and further stimulated by Ca^{2+}/calmodulin. J Biol Chem 2010; 285: 17930–7.
68 Giese KP, Fedorov NB, Filipkowski RK, Silva AJ. Autophosphorylation at Thr286 of the alpha calcium-calmodulin kinase II in LTP and learning. Science 1998; 279: 870–3.
69 Colbran RJ, Soderling TR. Calcium/calmodulin-independent autophosphorylation sites of calcium/calmodulin-dependent protein kinase II. Studies on the effect of phosphorylation of threonine 305/306 and serine 314 on calmodulin binding using synthetic peptides. J Biol Chem 1990; 265: 11213–9.
70 Hanson PI, Schulman H. Inhibitory autophosphorylation of multifunctional Ca^{2+}/calmodulin-dependent protein kinase analyzed by site-directed mutagenesis. J Biol Chem 1992; 267: 17216–24.
71 Colbran RJ. Inactivation of Ca^{2+}/calmodulin-dependent protein kinase II by basal autophosphorylation. J Biol Chem 1993; 268: 7163–70.
72 Lu CS, Hodge JJ, Mehren J, Sun XX, Griffith LC. Regulation of the Ca^{2+}/CaM-responsive pool of CaMKII by scaffold-dependent autophosphorylation. Neuron 2003; 40: 1185–97.
73 Malinow R, Schulman H, Tsien RW. Inhibition of postsynaptic PKC or CaMKII blocks induction but not expression of LTP. Science 1989; 245: 862–6.
74 Buard I, Coultrap SJ, Freund RK, Lee YS, Dell'Acqua ML, Silva AJ, *et al*. CaMKII "autonomy" is required for initiating but not for maintaining neuronal long-term information storage. J Neurosci 2010; 30: 8214–20.
75 Lee YS, Silva AJ. The molecular and cellular biology of enhanced cognition. Nat Rev Neurosci 2009; 10: 126–40.
76 Shen K, Meyer T. Dynamic control of CaMKII translocation and localization in hippocampal neurons by NMDA receptor stimulation. Science 1999; 284: 162–6.
77 Otmakhov N, Tao-Cheng JH, Carpenter S, Asrican B, Dosemeci A, Reese TS, *et al*. Persistent accumulation of calcium/calmodulin-dependent protein kinase II in dendritic spines after induction of NMDA receptor-dependent chemical long-term potentiation. J Neurosci 2004; 24: 9324–31.
78 Bayer KU, LeBel E, McDonald GL, O'Leary H, Schulman H, De Koninck H, *et al*. Transition from reversible to persistent binding of CaMKII to postsynaptic sites and NR2B. J Neurosci 2006; 26: 1164–74.
79 Hudmon A, Aronowski J, Kolb SJ, Waxham MN. Inactivation and self-association of Ca^{2+}/calmodulin-dependent protein kinase II during autophosphorylation. J Biol Chem 1996; 271: 8800–8.
80 Dosemeci A, Reese TS, Petersen J, Tao-Cheng JH. A novel particulate form of Ca^{2+}/CaMKII-dependent protein kinase II in neurons. J Neurosci 2000; 20: 3076–84.
81 Tao-Cheng JH, Vinade L, Smith C, Winters CA, Ward R, Brightman MW, *et al*. Sustained elevation of calcium induces Ca^{2+}/calmodulin-dependent protein kinase II clusters in hippocampal neurons. Neuroscience 2001; 106: 69–78.
82 Hudmon A, Lebel E, Roy H, Sik A, Schulman H, Waxham MN, *et al*. A mechanism for Ca^{2+}/calmodulin-dependent protein kinase II clustering at synaptic and nonsynaptic sites based on self-association. J Neurosci 2005; 25: 6971–83.
83 Barria A, Malinow R. NMDA receptor subunit composition controls synaptic plasticity by regulating binding to CaMKII. Neuron 2005; 48: 289–301.
84 Zhou Y, Takahashi E, Li W, Halt A, Wiltgen B, Ehninger D, *et al*. Interactions between the NR2B receptor and CaMKII modulate synaptic plasticity and spatial learning. J Neurosci 2007; 27: 13843–53.
85 Strack S, Colbran RJ. Autophosphorylation-dependent targeting of calcium/calmodulin-dependent protein kinase II by the NR2B subunit of the *N*-methyl-*D*-aspartate receptor. J Biol Chem 1998; 273: 20689–92.
86 Leonard AS, Bayer KU, Merrill MA, Lim IA, Shea MA, Schulman H, *et al*. Regulation of calcium/calmodulin-dependent protein kinase II docking to *N*-methyl-*D*-aspartate receptors by calcium/calmodulin and alpha-actinin. J Biol Chem 2002; 277: 48441–8.
87 Bayer KU, Schulman H. Regulation of signal transduction by protein targeting: the case for CaMKII. Biochem Biophys Res Commun 2001; 289: 917–23.
88 Colbran RJ, Brown AM. Calcium/calmodulin-dependent protein kinase II and synaptic plasticity. Curr Opin Neurobiol 2004; 14: 318–27.
89 Merrill MA, Chen Y, Strack S, Hell JW. Activity-driven postsynaptic translocation of CaMKII. Trends Pharmacol Sci 2005; 26: 645–53.
90 Hudmon A, Kim SA, Kolb SJ, Stoops JK, Waxham MN. Light scattering and transmission electron microscopy studies reveal a mechanism for calcium/calmodulin-dependent protein kinase II self-association. J Neurochem 2001; 76: 1364–75.
91 Vest RS, O'Leary H, Bayer KU. Differential regulation by ATP versus ADP further links CaMKII aggregation to ischemic conditions. FEBS Lett 2009; 583: 3577–81.
92 Strack S, McNeill RB, Colbran RJ. Mechanism and regulation of calcium/calmodulin-dependent protein kinase II targeting to the NR2B subunit of the *N*-methyl-*D*-aspartate receptor. J Biol Chem 2000; 275: 23798–806.
93 Aronowski J, Grotta JC, Waxham MN. Ischemia-induced translocation of Ca^{2+}/calmodulin-dependent protein kinase II: potential role in neuronal damage. J Neurochem 1992; 58: 1743–53.
94 Westgate SA, Brown J, Aronowski J, Waxham MN. Activity of Ca^{2+}/calmodulin-dependent protein kinase II following ischemia: a comparison between CA1 and dentate gyrus in a hippocampal slice model. J Neurochem 1994; 63: 2217–24.
95 Churn S, Limbrick D, Sombati S, DeLorenzo R. Excitotoxic activation of the NMDA receptor results in inhibition of calcium/calmodulin kinase II activity in cultured hippocampal neurons. J Neurosci 1995; 15: 3200–14.
96 Tokumitsu H, Chijiwa T, Hagiwara M, Mizutani A, Terasawa M, Hidaka H. KN-62,1-[N,O-bis(5-isoquinolinesulfonyl)-*N*-methyl-*L*-tyrosyl]-4-phenylpiperazi ne, a specific inhibitor of Ca^{2+}/calmodulin-dependent protein kinase II. J Biol Chem 1990; 265: 4315–20.
97 Sumi M, Kiuchi K, Ishikawa T, Ishii A, Hagiwara M, Nagatsu T, *et al*. The newly synthesized selective Ca^{2+}/calmodulin dependent protein kinase II inhibitor KN-93 reduces dopamine contents in PC12h cells. Biochem Biophys Res Commun 1991; 181: 968–75.
98 Davies SP, Reddy H, Caivano M, Cohen P. Specificity and mechanism of action of some commonly used protein kinase inhibitors. Biochem J 2000; 351: 95–105.
99 Enslen H, Sun P, Brickey D, Soderling SH, Klamo E, Soderling TR. Characterization of Ca^{2+}/calmodulin-dependent protein kinase IV. Role in transcriptional regulation. J Biol Chem 1994; 269: 15520–7.
100 Dell'Acqua ML, Scott JD. Protein kinase A anchoring. J Biol Chem 1997; 272: 12881–4.
101 Brooks IM, Tavalin SJ. CaMKII inhibitors disrupt AKAP79-dependent PKC signaling to GluA1 AMPA receptors. J Biol Chem 2011; 286:

6697–706.
102 Li G, Hidaka H, Wollheim CB. Inhibition of voltage-gated Ca^{2+} channels and insulin secretion in HIT cells by the Ca^{2+}/calmodulin-dependent protein kinase II inhibitor KN-62: comparison with antagonists of calmodulin and L-type Ca^{2+} channels. Mol Pharmacol 1992; 42: 489–8.
103 Ledoux J, Chartier D, Leblanc N. Inhibitors of calmodulin-dependent protein kinase are nonspecific blockers of voltage-dependent K^+ channels in vascular myocytes. J Pharmacol Exp Ther 1999; 290: 1165–74.
104 Ishida A, Kameshita I, Okuno S, Kitani T, Fujisawa H. A novel highly specific and potent inhibitor of calmodulin-dependent protein kinase II. Biochem Biophys Res Commun 1995; 212: 806–12.
105 Patel R, Holt M, Philipova R, Moss S, Schulman H, Hidaka H, *et al*. Calcium/calmodulin-dependent phosphorylation and activation of human Cdc25-C at the G_2/M phase transition in HeLa cells. J Biol Chem 1999; 274: 7958–68.
106 Hvalby O, Hemmings HC Jr, Paulsen O, Czernik AJ, Nairn AC, Godfraind JM, *et al*. Specificity of protein kinase inhibitor peptides and induction of long-term potentiation. Proc Natl Acad Sci U S A 1994; 91: 4761–5.
107 Smith MK, Colbran RJ, Soderling TR. Specificities of autoinhibitory domain peptides for four protein kinases. Implications for intact cell studies of protein kinase function. J Biol Chem 1990; 265: 1837–40.
108 Backs J, Backs T, Neef S, Kreusser MM, Lehmann LH, Patrick DM, *et al*. The delta isoform of CaM kinase II is required for pathological cardiac hypertrophy and remodeling after pressure overload. Proc Natl Acad Sci U S A 2009; 106: 2342–7.
109 Patel R, Holt M, Philipova R, Moss S, Schulman H, Hidaka H, *et al*. Calcium/calmodulin-dependent phosphorylation and activation of human Cdc25-C at the G_2/M phase transition in HeLa cells. J Biol Chem 1999; 274: 7958–68.
110 Chen HX, Otmakhov N, Strack S, Colbran RJ, Lisman JE. Is persistent activity of calcium/calmodulin-dependent kinase required for the maintenance of LTP? J Neurophysiol 2001; 85: 1368–76.
111 Vest RS, Davies KD, O'Leary H, Port JD, Bayer KU. Dual mechanism of a natural CaMKII inhibitor. Mol Biol Cell 2007; 18: 5024–33.
112 Chang BH, Mukherji S, Soderling TR. Characterization of a calmodulin kinase II inhibitor protein in brain. Proc Natl Acad Sci U S A 1998; 95: 10890–5.
113 Schwartz JJ, Zhang S. Peptide-mediated cellular delivery. Curr Opin Mol Ther 2000; 2: 162–7.
114 Green I, Christison R, Voyce CJ, Bundell KR, Lindsay MA. Protein transduction domains: are they delivering? Trends Pharmacol Sci 2003; 24: 213–5.
115 Joliot A, Prochiantz A. Transduction peptides: from technology to physiology. Nat Cell Biol 2004; 6: 189–96.
116 Fink CC, Bayer KU, Myers JW, Ferrell JE Jr, Schulman H, Meyer T. Selective regulation of neurite extension and synapse formation by the beta but not the alpha isoform of CaMKII. Neuron 2003; 39: 283–97.
117 Illario M, Cavallo AL, Bayer KU, Di Matola T, Fenzi G, Rossi G, *et al*. Calcium/calmodulin-dependent protein kinase II binds to Raf-1 and modulates integrin-stimulated ERK activation. J Biol Chem 2003; 278: 45101–8.
118 Schwarze SR, Ho A, Vocero-Akbani A, Dowdy SF. *In vivo* protein transduction: delivery of a biologically active protein into the mouse. Science 1999; 285: 1569–72.
119 Hajimohammadreza I, Probert AW, Coughenour LL, Borosky SA, Marcoux FW, Boxer PA, *et al*. A specific inhibitor of calcium/calmodulin-dependent protein kinase-II provides neuroprotection against NMDA- and hypoxia/hypoglycemia-induced cell death. J Neurosci 1995; 15: 4093–101.
120 Laabich A, Cooper NG. Neuroprotective effect of AIP on *N*-methyl-*D*-aspartate-induced cell death in retinal neurons. Brain Res Mol Brain Res 2000; 85: 32–40.
121 Takano H, Fukushi H, Morishima Y, Shirasaki Y. Calmodulin and calmodulin-dependent kinase II mediate neuronal cell death induced by depolarization. Brain Res 2003; 962: 41–7.
122 Fan W, Agarwal N, Cooper NG. The role of CaMKII in BDNF-mediated neuroprotection of retinal ganglion cells (RGC-5). Brain Res 2006; 1067: 48–57.
123 Gao J, Duan B, Wang DG, Deng XH, Zhang GY, Xu L, *et al*. Coupling between NMDA receptor and acid-sensing ion channel contributes to ischemic neuronal death. Neuron 2005; 48: 635–46.
124 Waxham MN, Grotta JC, Silva AJ, Strong R, Aronowski J. Ischemia-induced neuronal damage: a role for calcium/calmodulin-dependent protein kinase II. J Cereb Blood Flow Metab 1996; 16: 1–6.
125 Mabuchi T, Kitagawa K, Kuwabara K, Takasawa K, Ohtsuki T, Xia Z, *et al*. Phosphorylation of cAMP response element-binding protein in hippocampal neurons as a protective response after exposure to glutamate *in vitro* and ischemia *in vivo*. J Neurosci 2001; 21: 9204–13.
126 Linseman DA, Bartley CM, Le SS, Laessig TA, Bouchard RJ, Meintzer MK, *et al*. Inactivation of the myocyte enhancer factor-2 repressor histone deacetylase-5 by endogenous Ca^{2+}/calmodulin-dependent kinase II promotes depolarization-mediated cerebellar granule neuron survival. J Biol Chem 2003; 278: 41472–81.
127 Bok J, Wang Q, Huang J, Green SH. CaMKII and CaMKIV mediate distinct prosurvival signaling pathways in response to depolarization in neurons. Mol Cell Neurosci 2007; 36: 13–26.
128 Hansen MR, Bok J, Devaiah AK, Zha XM, Green SH. Ca^{2+}/calmodulin-dependent protein kinases II and IV both promote survival but differ in their effects on axon growth in spiral ganglion neurons. J Neurosci Res 2003; 72: 169–84.
129 Butler LS, Silva AJ, Abeliovich A, Watanabe Y, Tonegawa S, McNamara JO. Limbic epilepsy in transgenic mice carrying a Ca^{2+}/calmodulin-dependent kinase II alpha-subunit mutation. Proc Natl Acad Sci U S A 1995; 92: 6852–5.
130 Yamagata Y, Kobayashi S, Umeda T, Inoue A, Sakagami H, Fukaya M, *et al*. Kinase-dead knock-in mouse reveals an essential role of kinase activity of Ca^{2+}/calmodulin-dependent protein kinase II{alpha} in dendritic spine enlargement, long-term potentiation, and learning. J Neurosci 2009; 29: 7607–18.
131 Finkbeiner S, Tavazoie SF, Maloratsky A, Jacobs KM, Harris KM, Greenberg ME. CREB: a major mediator of neuronal neurotrophin responses. Neuron 1997; 19: 1031–47.
132 See V, Boutillier AL, Bito H, Loeffler JP. Calcium/calmodulin-dependent protein kinase type IV (CaMKIV) inhibits apoptosis induced by potassium deprivation in cerebellar granule neurons. FASEB J 2001; 15: 134–44.
133 Wu GY, Deisseroth K, Tsien RW. Activity-dependent CREB phosphorylation: convergence of a fast, sensitive calmodulin kinase pathway and a slow, less sensitive mitogen-activated protein kinase pathway. Proc Natl Acad Sci U S A 2001; 98: 2808–13.
134 Wayman GA, Impey S, Marks D, Saneyoshi T, Grant WF, Derkach V, *et al*. Activity-dependent dendritic arborization mediated by CaM-kinase I activation and enhanced CREB-dependent transcription of Wnt-2. Neuron 2006; 50: 897–909.
135 Tokumitsu H, Inuzuka H, Ishikawa Y, Ikeda M, Saji I, Kobayashi R. STO-609, a specific inhibitor of the Ca^{2+}/calmodulin-dependent protein kinase kinase. J Biol Chem 2002; 277: 15813–8.
136 Yano S, Tokumitsu H, Soderling TR. Calcium promotes cell survival through CaM-K kinase activation of the protein-kinase-B pathway. Nature 1998; 396: 584–7.

137 Hurley RL, Anderson KA, Franzone JM, Kemp BE, Means AR, Witters LA. The Ca^{2+}/calmodulin-dependent protein kinase kinases are AMP-activated protein kinase kinases. J Biol Chem 2005; 280: 29060–6.
138 Li J, McCullough LD. Effects of AMP-activated protein kinase in cerebral ischemia. J Cereb Blood Flow Metab 2010; 30: 480–92.
139 Li J, Benashski SE, Venna VR, McCullough LD. Effects of metformin in experimental stroke. Stroke 2010; 41: 2645–52.
140 Schurr A, Reid KH, Tseng MT, West C, Rigor BM. Adaptation of adult brain tissue to anoxia and hypoxia *in vitro*. Brain Res 1986; 374: 244–8.
141 Kitagawa K, Matsumoto M, Tagaya M, Hata R, Ueda H, Niinobe M, *et al*. Ischemic tolerance' phenomenon found in the brain. Brain Res 1990; 528: 21–4.
142 Liu Y, Kato H, Nakata N, Kogure K. Protection of rat hippocampus against ischemic neuronal damage by pretreatment with sublethal ischemia. Brain Research 1992; 586: 121–4.
143 Kirino T. Ischemic tolerance. J Cereb Blood Flow Metab 2002; 22: 1283–96.
144 McCullough LD, Zeng Z, Li H, Landree LE, McFadden J, Ronnett GV. Pharmacological inhibition of AMP-activated protein kinase provides neuroprotection in stroke. J Biol Chem 2005; 280: 20493–502.
145 Tu W, Xu X, Peng L, Zhong X, Zhang W, Soundarapandian MM, *et al*. DAPK1 interaction with NMDA receptor NR2B subunits mediates brain damage in stroke. Cell 2010; 140: 222–34.
146 Zhou L, Li F, Xu HB, Luo CX, Wu HY, Zhu MM, *et al*. Treatment of cerebral ischemia by disrupting ischemia-induced interaction of nNOS with PSD-95. Nat Med 2010; 16: 1439–43.
147 Derkach V, Barria A, Soderling TR. Ca^{2+}/calmodulin-kinase II enhances channel conductance of alpha-amino-3-hydroxy-5-methyl-4-isoxazolepropionate type glutamate receptors. Proc Natl Acad Sci U S A 1999; 96: 3269–74.
148 Barria A, Muller D, Derkach V, Griffith LC, Soderling TR. Regulatory phosphorylation of AMPA-type glutamate receptors by CaM-KII during long-term potentiation. Science 1997; 276: 2042–5.
149 Oh MC, Derkach VA. Dominant role of the GluR2 subunit in regulation of AMPA receptors by CaMKII. Nat Neurosci 2005; 8: 853–4.
150 Hollmann M, Hartley M, Heinemann S. Ca^{2+} permeability of KA-AMPA-gated glutamate receptor channels depends on subunit composition. Science 1991; 252: 851–3.
151 Verdoorn T, Burnashev N, Monyer H, Seeburg P, Sakmann, B. Structural determinants of ion flow through recombinant glutamate receptor channels. Science 1991; 252: 1715–8.
152 Liu SJ, Zukin RS. Ca^{2+}-permeable AMPA receptors in synaptic plasticity and neuronal death. Trends Neurosci 2007; 30: 126–34.
153 Hudmon A, Schulman H, Kim J, Maltez JM, Tsien RW, Pitt GS. CaMKII tethers to L-type Ca^{2+} channels, establishing a local and dedicated integrator of Ca^{2+} signals for facilitation. J Cell Biol 2005; 171: 537–47.
154 Grueter CE, Abiria SA, Dzhura I, Wu Y, Ham AJ, Mohler PJ, *et al*. L-type Ca^{2+} channel facilitation mediated by phosphorylation of the beta subunit by CaMKII. Mol Cell 2006; 23: 641–50.
155 Alev C, Urschel S, Sonntag S, Zoidl G, Fort AG, Hoher T, *et al*. The neuronal connexin36 interacts with and is phosphorylated by CaMKII in a way similar to CaMKII interaction with glutamate receptors. Proc Natl Acad Sci U S A 2008; 105: 20964–9.
156 Oguro K, Jover T, Tanaka H, Lin Y, Kojima T, Oguro N, *et al*. Global ischemia-induced increases in the gap junctional proteins connexin 32 (Cx32) and Cx36 in hippocampus and enhanced vulnerability of Cx32 knock-out mice. J Neurosci 2001; 21: 7534–42.
157 Bargiotas P, Monyer H, Schwaninger, M. Hemichannels in cerebral ischemia. Curr Mol Med 2009; 9: 186–94.
158 Contreras JE, Sanchez HA, Veliz LP, Bukauskas FF, Bennett MV, Saez JC. Role of connexin-based gap junction channels and hemichannels in ischemia-induced cell death in nervous tissue. Brain Res Brain Res Rev 2004; 47: 290–303.
159 Kan MC, Oruganty-Das A, Cooper-Morgan A, Jin G, Swanger SA, Bassell GJ, *et al*. CPEB4 is a cell survival protein retained in the nucleus upon ischemia or endoplasmic reticulum calcium depletion. Mol Cell Biol 2010; 30: 5658–71.
160 Wells DG. RNA-binding proteins: a lesson in repression. J Neurosci 2006; 26: 7135–8.
161 Richter JD. CPEB: a life in translation. Trends Biochem Sci 2007; 32: 279–85.
162 Wu L, Wells D, Tay J, Mendis D, Abbott MA, Barnitt A, *et al*. CPEB-mediated cytoplasmic polyadenylation and the regulation of experience-dependent translation of [alpha]-camkii mrna at synapses. Neuron 1998; 21: 1129–39.
163 Kundel M, Jones KJ, Shin CY, Wells DG. Cytoplasmic polyadenylation element-binding protein regulates neurotrophin-3-dependent {beta}-catenin mrna translation in developing hippocampal neurons. J Neurosci 2009; 29: 13630–9.
164 Li X, Klaus JA, Zhang J, Xu Z, Kibler KK, Andrabi SA, *et al*. Contributions of poly(ADP-ribose) polymerase-1 and -2 to nuclear translocation of apoptosis-inducing factor and injury from focal cerebral ischemia. J Neurochem 2010; 113: 1012–22.
165 Komeima K, Hayashi Y, Naito Y, Watanabe Y. Inhibition of neuronal nitric-oxide synthase by calcium/calmodulin-dependent protein kinase II through Ser847 phosphorylation in NG108-15 neuronal cells. J Biol Chem 2000; 275: 28139–43.
166 Osuka K, Watanabe Y, Usuda N, Nakazawa A, Fukunaga K, Miyamoto E, *et al*. Phosphorylation of neuronal nitric oxide synthase at Ser847 by CaM-KII in the hippocampus of rat brain after transient forebrain ischemia. J Cereb Blood Flow Metab 2002; 22: 1098–106.
167 Rameau GA, Chiu LY, Ziff EB. Bidirectional regulation of neuronal nitric-oxide synthase phosphorylation at Serine 847 by the *N*-methyl-*D*-aspartate receptor . J Biol Chem 2004; 279: 14307–14.
168 Rameau GA, Tukey DS, Garcin-Hosfield ED, Titcombe RF, Misra C, Khatri L, *et al*. Biphasic coupling of neuronal nitric oxide synthase phosphorylation to the NMDA receptor regulates AMPA receptor trafficking and neuronal cell death. J Neurosci 2007; 27: 3445–55.
169 Dawson V, Kizushi V, Huang P, Snyder S, Dawson T. Resistance to neurotoxicity in cortical cultures from neuronal nitric oxide synthase-deficient mice. J Neurosci 1996; 16: 2479–87.
170 Eliasson MJL, Huang Z, Ferrante RJ, Sasamata M, Molliver ME, Snyder SH, *et al*. Neuronal nitric oxide synthase activation and peroxynitrite formation in ischemic stroke linked to neural damage. J Neurosci 1999; 19: 5910–8.
171 Oka M, Hirouchi M, Itoh Y, Ukai Y. Involvement of peroxynitrite and hydroxyradical generated from nitric oxide in hypoxia/reoxygenation injury in rat cerebrocortical slices. Neuropharmacology 2000; 39: 1319–30.
172 Zhou L, Zhu DY. Neuronal nitric oxide synthase: structure, subcellular localization, regulation, and clinical implications. Nitric Oxide 2009; 20: 223–30.
173 Sessoms-Sikes S, Honse Y, Lovinger DM, Colbran RJ. CaMKIIalpha enhances the desensitization of NR2B-containing NMDA receptors by an autophosphorylation-dependent mechanism. Mol Cell Neurosci 2005; 29: 139–47.
174 Marsden KC, Beattie JB, Friedenthal J, Carroll RC. NMDA receptor activation potentiates inhibitory transmission through GABA receptor-associated protein-dependent exocytosis of GABAA receptors. J Neurosci 2007; 27: 14326–37.
175 Marsden KC, Shemesh A, Bayer KU, Carroll RC. Selective translocation of Ca^{2+}/calmodulin protein kinase IIalpha (CaMKIIalpha) to inhibitory synapses. Proc Natl Acad Sci U S A 2010; 107: 20559–64.
176 Nguyen A, Chen P, Cai H. Role of CaMKII in hydrogen peroxide

activation of ERK1/2, p38 MAPK, HSP27 and actin reorganization in endothelial cells. FEBS Lett 2004; 572: 307–13.

177 Wheeler DG, Barrett CF, Groth RD, Safa P, Tsien RW. CaMKII locally encodes L-type channel activity to signal to nuclear CREB in excitation-transcription coupling. J Cell Biol 2008; 183: 849–63.

178 Song B, Lai B, Zheng Z, Zhang Y, Luo J, Wang C, *et al*. Inhibitory phosphorylation of GSK-3 by CaMKII couples depolarization to neuronal survival. J Biol Chem 2010; 285: 41122–34.

179 Mao Z, Bonni A, Xia F, Nadal-Vicens M, Greenberg ME. Neuronal activity-dependent cell survival mediated by transcription factor MEF2. Science 1999; 286: 785–90.

180 Rudin CM, Thompson CB. Apoptosis and disease: regulation and clinical relevance of programmed cell death. Annu Rev Med 1997; 48: 267–81.

181 Strasser A, O'Connor L, Dixit VM. Apoptosis signaling. Annu Rev Biochem 2000; 69: 217–45.

182 Hengartner MO. The biochemistry of apoptosis. Nature 2000; 407: 770–6.

183 Heidenreich KA. Molecular mechanisms of neuronal cell death. Ann NY Acad Sci 2003; 991: 237–250.

184 Wright S, Schellenberger U, Ji L, Wang H, Larrick J. Calmodulin-dependent protein kinase II mediates signal transduction in apoptosis. FASEB J 1997; 11: 843–9.

185 Fladmark KE, Brustugun OT, Mellgren G, Krakstad C, Boe R, Vintermyr OK, *et al*. Ca^{2+}/calmodulin-dependent protein kinase ii is required for microcystin-induced apoptosis. J Biol Chem 2002; 277: 2804–11.

186 Krakstad C, Herfindal L, Gjertsen BT, Boe R, Vintermyr OK, Fladmark KE, *et al*. CaM-kinaseII-dependent commitment to microcystin-induced apoptosis is coupled to cell budding, but not to shrinkage or chromatin hypercondensation. Cell Death Differ 2005; 13: 1191–202.

187 Bissonnette SL, Haas A, Mann KK, Schlezinger JJ. The role of CaMKII in calcium-activated death pathways in bone marrow B cells. Toxicol Sci 2010; 118: 108–18.

188 Timmins JM, Ozcan L, Seimon TA, Li G, Malagelada C, Backs J, *et al*. Calcium/calmodulin-dependent protein kinase II links ER stress with Fas and mitochondrial apoptosis pathways. J Clin Invest 2009; 119: 2925–41.

189 Fujikawa K, Kawakami A, Tanaka F, Iwamoto N, Tamai M, Eguchi K. Calcium/calmodulin-dependent protein kinase II (CaMKII) regulates tumour necrosis factor-related apoptosis inducing ligand (TRAIL)-mediated apoptosis of fibroblast-like synovial cells (FLS) by phosphorylation of Akt. Clin Exp Rheumatol 2009; 27: 952–7.

190 Zhu WZ, Wang SQ, Chakir K, Yang D, Zhang T, Brown JH, *et al*. Linkage of beta1-adrenergic stimulation to apoptotic heart cell death through protein kinase A-independent activation of Ca^{2+}/calmodulin kinase II. J Clin Invest 2003; 111: 617–25.

191 Yang Y, Zhu WZ, Joiner MI, Zhang R, Oddis CV, Hou Y, *et al*. Calmodulin kinase II inhibition protects against myocardial cell apoptosis *in vivo*. Am J Physiol-Heart Circ Physiol 2006; 291: H3065–75.

192 Sapia L, Palomeque J, Mattiazzi A, Petroff MV. Na^+/K^+-ATPase inhibition by ouabain induces CaMKII-dependent apoptosis in adult rat cardiac myocytes. J Mol Cell Cardiol 2010; 49: 459–68.

193 Palomeque J, Rueda OV, Sapia L, Valverde CA, Salas M, Petroff MV, *et al*. Angiotensin II-induced oxidative stress resets the ca^{2+} dependence of Ca^{2+}-calmodulin protein kinase ii and promotes a death pathway conserved across different species. Circ Res 2009; 105: 1204–12.

194 Peng W, Zhang Y, Zheng M, Cheng H, Zhu W, Cao CM, *et al*. Cardioprotection by CaMKII-{delta}B is mediated by phosphorylation of heat shock factor 1 and subsequent expression of inducible heat shock protein 70. Circ Res 2010; 106: 102–10.

195 Erickson JR, Joiner ML, Guan X, Kutschke W, Yang J, Oddis CV, *et al*. A dynamic pathway for calcium-independent activation of CaMKII by methionine oxidation. Cell 2008; 133: 462–74.

196 Vila-Petroff M, Salas MA, Said M, Valverde CA, Sapia L, Portiansky E, *et al*. CaMKII inhibition protects against necrosis and apoptosis in irreversible ischemia-reperfusion injury. Cardiovas Res 2007; 73: 689–98.

197 Salas MA, Valverde CA, Sánchez G, Said M, Rodriguez JS, Portiansky EL, *et al*. The signalling pathway of CaMKII-mediated apoptosis and necrosis in the ischemia/reperfusion injury. J Mol Cell Cardiol 2010; 48: 1298–306.

198 Mishra S, Ling H, Grimm M, Zhang T, Bers DM, Brown JH. Cardiac hypertrophy and heart failure development through Gq and Cam kinase II signaling. J Cardiovasc Pharmacol 2010; 56: 598–603.

199 Nutt LK, Margolis SS, Jensen M, Herman CE, Dunphy WG, Rathmell JC, *et al*. Metabolic regulation of oocyte cell death through the CaMKII-mediated phosphorylation of caspase-2. Cell 2005; 123: 89–103.

200 Rokhlin OW, Taghiyev AF, Bayer KU, Bumcrot D, Koteliansk VE, Glover RA, *et al*. Calcium/calmodulin-dependent kinase II plays an important role in prostate cancer cell survival. Cancer Biol Ther 2007; 6: 732–42.

201 Ma S, Yang Y, Wang C, Hui N, Gu L, Zhong H, *et al*. Endogenous human CaMKII inhibitory protein suppresses tumor growth by inducing cell cycle arrest and apoptosis through down-regulation of the phosphatidylinositide 3-kinase/Akt/HDM2 pathway. J Biol Chem 2009; 284: 24773–82.

202 Yang CS, Thomenius MJ, Gan EC, Tang W, Freel CD, Merritt TJS, *et al*. Metabolic regulation of *Drosophila* apoptosis through inhibitory phosphorylation of Dronc. EMBO J 2010; 29: 3196–207.

203 Kajihara R, Fukushige S, Shioda N, Tanabe K, Fukunaga K, Inui S. CaMKII phosphorylates serine 10 of p27 and confers apoptosis resistance to HeLa cells. Biochem Biophys Res Commun 2010; 401: 350–5.

204 Tano JY, Vazquez G. Requirement for non-regulated, constitutive calcium influx in macrophage survival signaling. Biochem Biophys Res Commun 2011; 407: 432–7.

205 Anderson ME, Brown JH, Bers DM. CaMKII in myocardial hypertrophy and heart failure. J Mol Cell Cardiol 2011. doi: 10.1016/j.yjmcc.2011.01.012.

206 Srinivasan M, Edman CF, Schulman H. Alternative splicing introduces a nuclear localization signal that targets multifunctional CaM kinase to the nucleus. J Cell Biol 1994; 126: 839–52.

207 Little GH, Saw A, Bai Y, Dow J, Marjoram P, Simkhovich B, *et al*. Critical role of nuclear calcium/calmodulin-dependent protein kinase iideltab in cardiomyocyte survival in cardiomyopathy. J Biol Chem 2009; 284: 24857–68.

208 Ghosh A, Greenberg M. Calcium signaling in neurons: molecular mechanisms and cellular consequences. Science 1995; 268: 239–47.

209 Arundine M, Tymianski M. Molecular mechanisms of calcium-dependent neurodegeneration in excitotoxicity. Cell Calcium 2003; 34: 325–37.

210 Hardingham GE, Fukunaga Y, Bading H. Extrasynaptic NMDARs oppose synaptic NMDARs by triggering CREB shut-off and cell death pathways. Nat Neurosci 2002; 5: 405–14.

211 Zhang SJ, Buchthal B, Lau D, Hayer S, Dick O, Schwaninger M, *et al*. A Signaling cascade of nuclear calcium-CREB-ATF3 activated by synaptic NMDA receptors defines a gene repression module that protects against extrasynaptic NMDA receptor-induced neuronal cell death and ischemic brain damage. J Neurosci 2011; 31: 4978–90.

Acta Pharmacologica Sinica (2011) 32: 873–878
 1671-4083/11 $32.00
www.nature.com/aps

Original Article

Association of serum omentin-1 levels with coronary artery disease

Xia ZHONG[1, #], Hai-yang ZHANG[1, #], Hui TAN[1], Yi ZHOU[1], Fu-li LIU[1], Fu-qin CHEN[2, *], De-ya SHANG[1, *]

[1]*Department of Emergency, Provincial Hospital Affiliated to Shandong University, Ji-nan 250021, China;* [2]*Department of Endocrinology, Qilu Hospital, Shandong University, Ji-nan 250012, China*

Aim: Omentin-1, a novel adipokine expressed in visceral adipose tissue, is negatively correlated with insulin resistance and obesity. Decreased omentin-1 expression has been found in many chronic inflammatory diseases. However, the role of omentin-1 in coronary artery disease (CAD) has not been elucidated. The aim of the present study was to determine whether serum concentration of omentin-1 was independently associated with CAD.
Methods: One hundred and fifty five patients with CAD were divided into two groups: acute coronary syndrome (ACS) and stable angina pectoris (SAP). A total of 52 healthy participants served as controls. Serum concentrations of omentin-1 and interleukin-6 (IL-6) were measured using ELISA. The association of omentin-1 with CAD and cardiovascular disease risk factors was evaluated.
Results: Serum omentin-1 levels were lower in patients with ACS or SAP compared with controls (ACS, 113.08±61.43 ng/mL; SAP, 155.41±66.89 ng/mL; control, 254.00±72.9 ng/mL; $P<0.01$). Patients with ACS also had lower serum concentrations of omentin-1 compared with patients with SAP ($P<0.01$). Serum concentration of omentin-1 was negatively correlated with body mass index ($r=-0.17$, $P<0.05$) and serum IL-6 concentration ($r=-0.19$, $P<0.05$). Furthermore, multiple logistic regression analysis showed that serum omentin-1 concentrations were independently correlated with CAD.
Conclusion: The findings suggest that serum concentrations of omentin-1 are related to CAD.

Keywords: coronary artery disease; acute coronary syndrome; adipokines; omentin-1; interleukin-6

Acta Pharmacologica Sinica (2011) 32: 873–878; doi: 10.1038/aps.2011.26; published online 23 May 2011

Introduction

Adipose tissue secretes many adipokines including adiponectin, chemerin, leptin, resistin, retinol binding protein 4, tumor necrosis factor-α (TNF-α), and interleukin-6 (IL-6)[1]. These adipokines play important roles in carbohydrate and lipid metabolism, homeostasis, insulin resistance, diabetes, atherosclerosis, vascular endothelial dysfunction, inflammation, and cardiovascular function[2–6].

Omentin, a recently identified fat deposition-specific adipokine codified by two genes (1 and 2), is highly and selectively expressed in visceral omental adipose tissue[7]. While its biological activity is not well understood, omentin-1 has been shown to be the major circulating isoform in human plasma with reportedly lower levels in overweight or obese subjects and those with impaired glucose regulation (IGR) or type 2 diabetes mellitus (T2DM)[8–10]. Recent studies have shown that omentin-1 levels are negatively correlated with body mass index (BMI), leptin, waist circumference, fasting insulin, and homeostasis model assessment (HOMA) index, and omentin-1 levels are positively associated with adiponectin and high density lipoprotein cholesterol (HDL-C)[8, 11]. Several reports indicated that omentin-1 was implicated in many chronic inflammatory diseases[12, 13]. In addition, Yamawaki *et al* demonstrated a vasodilating effect of omentin on isolated blood vessels, suggesting omentin involvement in endothelial function[14].

There have been several reports showing that other adipokines, such as adiponectin[15–17], resistin[17–20], leptin[19], visfatin[21–23], TNF-α[24], and IL-6[25], are related to inflammation and coronary artery disease (CAD). We hypothesized that omentin-1 might be implicated in CAD due to a possible association with inflammation and endothelial function. To test the hypothesis, we measured serum omentin-1 levels in patients with CAD and evaluated possible correlations with other cardiovascular risk factors such as age, sex, smoking, CAD family history, lipid levels, fasting glucose (FG), and blood pressure.

# These authors contributed equally to this work.
* To whom correspondence should be addressed.
E-mail sdslyysdy@126.com (De-ya SHANG);
chenfuqin@medmail.com.cn (Fu-qin CHEN)
Received 2010-12-10 Accepted 2011-03-07

We investigated whether serum omentin-1 levels were independently related to the incidence of CAD.

Materials and methods

Subjects

The protocol was authorized by the Ethical Committee of Shandong Provincial Hospital. Prior written informed consent was obtained from all participants. The study group consisted of 155 patients undergoing coronary angiography primarily for chest pain or dyspnea on exertion in Shandong Provincial Hospital between June 2009 and September 2010. Patients with valvular heart disease, coronary artery bypass graft surgery, malignant disease, infectious disease, inflammatory disease such as collagen disease, neoplasm, hematological disorders, advanced renal disease (defined as either creatinine>220 μmol/L or glomerular filtration rate<60 mL/min per 1.73 m^2 according to the Kidney Disease Outcomes Quality Initiative Clinical Practice Guidelines)[26], and liver disease (aspartate transaminase and alanine transaminase>2 times the upper limit of normal) were excluded. Patients with CAD were divided into two groups: 1) acute coronary syndrome (ACS), including acute myocardial infarction (AMI) or unstable angina pectoris (UAP); and 2) stable angina pectoris (SAP).

There were 61 patients diagnosed with AMI based on clinical symptoms; electrocardiogram evidence (ST elevation in two or more leads); coronary angiography findings (occlusion of a main coronary artery branch) with thrombolysis in myocardial infarction (TIMI) grade flow of 0, 1, or 2; and significantly increased serum creatine kinase (CK)-MB and troponin-I levels (more than twice the upper limit of normal). All AMI patients were catheterized within 12 h of onset of chest pain. Sixty-six patients were diagnosed with UAP using the following criteria: new onset chest pain or unexplained changes in the pattern of stable angina (such as increased frequency, intensity or duration or decreased response to nitrates); angiographic evidence (documented stenosis of >50% in one or more principal coronary arteries); and no increase in serum CK-MB and troponin-I concentrations in the previous 2 months. Twenty-eight patients were diagnosed with SAP based on symptoms, specifically typical precordial chest pain during exercise and no episodes of angina at rest and documented stenosis of >50% in one or more principal coronary arteries upon coronary angiography.

The reference (control) group consisted of 52 healthy participants matched by age and BMI. Among the reference group, 36 participants underwent coronary angiography; of those, 16 participants were examined by coronary CT angiography. None of the controls was diagnosed with CAD.

Measurement of serum concentrations of omentin-1 and other parameters

Each blood sample was obtained between 7 and 8 h after an overnight fast and was collected in chilled polypropylene tubes. Serum was separated by centrifugation at 750×*g* for 15 min and stored at -80 °C until being assayed.

Routine lab tests including FG, low density lipoprotein cholesterol (LDL-C), HDL-C, total cholesterol (TC), triglycerides (TG), uric acid, and creatinine were assayed by an automatic analyzer (Olympus, Irish Branch) in the hospital clinical laboratories. Serum omentin-1 and IL-6 concentrations were measured using Human Enzyme-linked immunosorbent assay (ELISA) kits (Cusabio Biotech Corporation, USA). Serum samples were diluted and assayed according to manufacturer instructions.

Statistical analysis

Continuous variables with normal distributions were expressed as mean±SD. Differences in the mean values between groups were compared by One-Way Analysis of Variance (ANOVA). Continuous variables with skewed distributions were summarized as median and quartile ranges and compared using the Kruskal-Wallis test. The χ^2 test was used to test categorical variables. Correlations between serum concentrations of omentin-1 and other parameters were studied by Pearson correlation analysis. We first used simple logistic regression and then multivariate analysis to analyze correlations between CAD and all other parameters. SPSS 12.0 software was used for statistical analysis. $P<0.05$ was considered statistically significant.

Results

Study group characteristics

The clinical characteristics and laboratory data of the study groups are shown in Table 1. There were no differences in age, BMI, sex, smoking, family history of CAD, TG, uric acid, and creatinine between patients and controls. Compared to the control group, those in the ACS or SAP groups had higher systolic blood pressure (SBP), serum concentrations of FG, LDL-C, TC, and IL-6 and lower serum omentin-1 and HDL-C levels. Compared with patients with SAP, patients with ACS also had lower serum concentrations of omentin-1 and SBP and higher serum IL-6 concentrations.

Correlation between serum concentrations of omentin-1 and other parameters

As Figure 1 showed, there was a negative correlation between serum concentrations of omentin-1 and BMI (r=-0.17, $P<0.05$) in patients with CAD. Notably, as presented in Figure 2, serum omentin-1 levels were also negatively associated with serum IL-6 levels (r=-0.19, $P<0.05$). However, we did not find any association between serum omentin-1 levels and other variables such as lipid parameters, blood pressure, age, smoking, sex, and family history of CAD.

Omentin-1 and CAD

Initially, a simple logistic regression analysis was performed. As shown in Table 2, the incidence of CAD was correlated with SBP, DBP, serum concentrations of TC, LDL-C, HDL-C, FG, omentin-1, and IL-6 ($P<0.05$). In multiple stepwise logistic regression analysis, serum concentrations of TC, omentin-1 and IL-6 were independently associated with the development

Table 1. Clinical characteristics and aborotary data of the study group. [b]*P*<0.05, [c]*P*<0.01 *vs* control; [e]*P*<0.05, [f]*P*<0.01 for ACS *vs* SAP.

Variable	ACS (*n*=127)	SAP (*n*=28)	Control (*n*=52)	*P* value
Age (year)	61.85±12.05(1)	60.61±15.02(1)	59.81±9.88(1)	0.5663
Men (%)	90 (70.87)(2)	15 (53.57)(2)	38 (73.08)(2)	0.1548
BMI (kg/m^2)	25.52±3.35(1)	24.71±3.74(1)	25.73±3.14(1)	0.4171
Smoking (%)	54 (42.52)(2)	9 (32.14)(2)	14 (26.92)(2)	0.1227
Family history (%)	25 (19.69)(2)	7 (25.00)(2)	9 (17.31)(2)	0.7114
SBP (mmHg)	135.00 (33.00)(3)ce	145.36±24.52(1)c	119.35±13.83(1)	<0.0001
DBP (mmHg)	78.00 (19.00)(3)b	80.82±15.51(1)	73.85±10.39(1)	0.0915
FG (mmol/L)	5.74 (2.22)(3)c	6.37±1.53(1)c	5.05±1.03(1)	<0.0001
TC (mmol/L)	4.78 (1.63)(3)c	4.91±0.95(1)c	3.94±1.07(1)	<0.0001
LDL -C (mmol/L)	2.91 (1.19)(3)c	2.80±0.72(1)c	2.29±0.80(1)	<0.0001
HDL-C (mmol/L)	1.24 (0.36)(3)c	1.27 (0.45)(3)c	1.67 (0.46)(3)	<0.0001
TG (mmol/L)	1.33 (1.19)(3)	1.30 (1.00)(3)	1.66 (1.03)(3)	0.1317
Uric acid (μmol/L)	321.00 (118.00(3)	318.64±98.14(1)	328.94±86.81(1)	0.6953
Creatinine (μmol/L)	85.30 (29.40)(3)	89.65 (34.60)(3)	93.54±12.33(1)	0.1019
Omentin-1 (ng/mL)	113.08±61.43(1)cf	155.41±66.89(1)c	254.00 (72.98)(3)	<0.0001
IL-6 (pg/mL)	108.11±69.77(1)cf	55.98 (35.77)(3)c	16.12±7.62(1)	<0.0001

(1) mean±SD ; (2) *n* (%); (3) median (quartile range).

ACS, acute coronary syndrome; SAP, stable angina pectoris; BMI, body mass index; SBP, systolic blood pressure; DBP, diastolic blood pressure; FG, fasting glucose; TC, total cholesterol; LDL-C, low density lipoprotein cholesterol; HDL-C, high density lipoprotein cholesterol; TG, triglycerides; IL-6, interleukin-6.

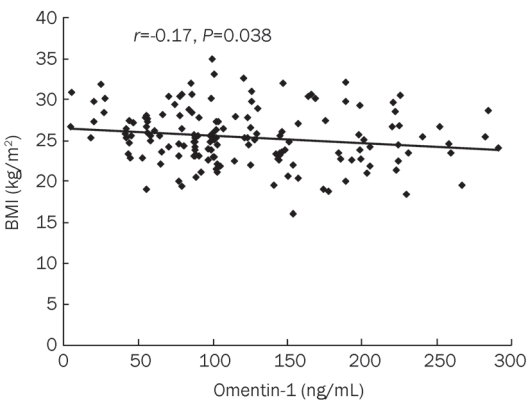

Figure 1. Correlation of serum concentrations of omentin-1 with body mass index (BMI). There was a negative correlation between serum omentin-1 levels and BMI in patients with coronary artery disease.

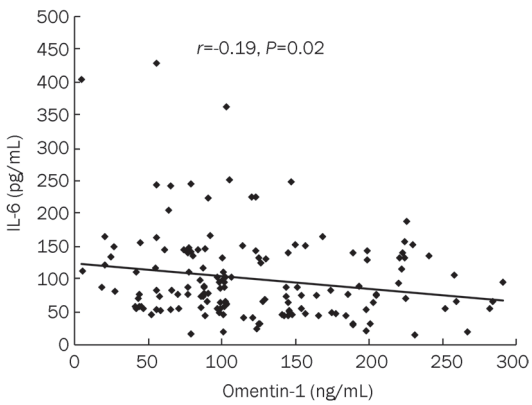

Figure 2. Correlation of serum concentrations of omentin-1 with interleukin-6 (IL-6). Serum concentrations of omentin-1 correlated negatively with serum IL-6 levels in patients with coronary artery disease.

of CAD (*P*<0.05, Table 3).

Discussion

Our present study showed that serum omentin-1 levels were lower in patients with CAD than in control participants. Patients with ACS also had lower serum concentrations of omentin-1 and higher serum concentrations of IL-6 compared with patients with SAP. In addition, serum omentin-1 levels were negatively correlated with BMI and IL-6 in patients. More importantly, we found that serum omentin-1 levels were independently associated with CAD prevalence.

Association of serum concentrations of omentin-1 with CAD

In the present study, mechanisms of the association of omentin-1 with CAD have not been elucidated; however, one could consider several possibilities. First, omentin induces endothelium-dependent relaxation via endothelium-derived NO through phosphorylation of eNOS in rat isolated aorta[14]. CAD may also be associated with impaired endothelium-dependent coronary dilatation[27]. Therefore, omentin may participate in CAD development at least in part through regulation of coronary contractility. Second, omentin has been shown to increase insulin sensitivity[28]. Rodrigues *et al*[29]

Table 2. Simple logistic regression analysis with CAD.

Variable	β	Standard error	Wald χ^2	*P* value	OR	95% CI
Age	0.0128	0.0135	0.8985	0.3432	1.013	0.986–1.040
Sex	0.2566	0.3567	0.5173	0.4720	1.292	0.642–2.601
BMI	-0.0319	0.0479	0.4436	0.5054	0.969	0.882–1.064
Smoking	-0.6199	0.3528	3.0866	0.0789	0.538	0.269–1.074
Family history	0.2175	0.4168	0.2723	0.6018	1.243	0.549–2.814
SBP[c]	0.0419	0.0096	19.1519	<0.0001	1.043	1.023–1.063
DBP[b]	0.0317	0.0131	5.8495	0.0156	1.032	1.006–1.059
FG[c]	0.9294	0.2077	20.0243	<0.0001	2.533	1.686–3.806
TC[c]	0.8003	0.1780	20.2149	<0.0001	2.226	1.571–3.156
LDL-C[c]	0.9918	0.2350	17.8124	<0.0001	2.696	1.701–4.274
HDL-C[c]	-3.6301	0.6545	30.7629	<0.0001	0.027	0.007–0.096
TG	-0.0172	0.0841	0.0418	0.8380	0.983	0.834–1.159
Uric acid	0.0007	0.0015	0.2319	0.6301	1.001	0.998–1.004
Creatinine	0.0017	0.0044	0.1514	0.6972	1.002	0.993–1.010
Omentin-1[c]	-0.0330	0.0051	41.7697	<0.0001	0.968	0.958–0.977
IL-6[c]	0.2088	0.0437	22.8128	<0.0001	1.232	1.131–1.342

[b]*P*<0.05, [c]*P*<0.01 with logistic regression analysis.

CAD, coronary artery disease; OR, odds ratio; CI, confidence interval; BMI, body mass index; SBP, systolic blood pressure; DBP, diastolic blood pressure; FG, fasting glucose; TC, total cholesterol; LDL-C, low density lipoprotein cholesterol; HDL-C, high density lipoprotein cholesterol; TG, triglycerides; IL-6, interleukin-6.

Table 3. Multivariable logistic regression analysis with CAD.

Variable	β	Standard error	Wald χ^2	*P* value	OR	95% CI
TC[b]	1.3313	0.5219	6.5082	0.0107	3.786	1.361–10.529
Omentin-1[b]	-0.0371	0.0154	5.8039	0.0160	0.964	0.935–0.993
IL-6[b]	0.2427	0.0976	6.1857	0.0129	1.275	1.053–1.543

[b]*P*<0.05 with logistic regression analysis.

CAD, coronary artery disease; OR, odds ratio; CI, confidence interval; TC, total cholesterol; IL-6, interleukin-6.

recently named insulin resistance as one of the most important risk factors for subclinical atherosclerosis and reported an association with coronary artery calcification in patients with type 1 diabetes mellitus (T1DM). In one study, decreased insulin sensitivity was associated with increased incidence of myocardial infarction and death, even after adjusting cardiovascular risk for smoking and low physical activity. Bertoluci *et al* also indicated that increased HOMA of insulin resistance was positively associated with angiographic coronary artery disease[30]. As a result, decreased omentin-1 levels may contribute to development of CAD by modulating insulin action. Third, consistent with other reports, our present data showed that decreased omentin expression is implicated in a variety of chronic inflammatory diseases. It was reported that plasma omentin-1 was decreased in T1DM subjects[31]. Expression of the omentin gene was detected in omental adipose tissue of patients with Crohn's disease, suggesting that it may play an important role in chronic inflammatory diseases[12]. Senolt *et al*[13] also demonstrated significantly lower omentin levels in the synovial fluid of patients with rheumatoid arthritis than in patients with osteoarthritis. In addition, synovial fluid levels of omentin were significantly correlated with serum levels of anticitrullinated peptide antibodies and IgM-rheumatoid factor. Based on these reports, omentin-1 might be involved in the development of CAD via dysfunction of endothelium-dependent coronary dilatation, insulin activity and inflammation.

Correlation between serum concentrations of omentin-1 and other factors

We reported that omentin-1 was related to IL-6 in patients with CAD. A large number of reports have shown that IL-6 is pathogenetically involved in CAD. Pan *et al*[9] also reported a negative correlation between the level of serum omentin-1 and IL-6 in patients with newly diagnosed and untreated type 2 diabetes. Several groups have reported that IL-6 regulates the production of other adipokines, including leptin, adiponectin, and visfatin[32–34]. IL-6 and omentin are primarily produced by stromal vascular fraction cells of adipose tissue with paracrine or endocrine effects directly on other cells locally and sys-

temically. Whether IL-6 profoundly influences the release of omentin from visceral tissue should be elucidated.

In our study, serum omentin-1 levels were negatively correlated with BMI in patients with CAD. Several reports have shown an association of omentin-1 with BMI[8, 9]. Another report also indicated that baseline circulating omentin-1 concentrations were negatively correlated with BMI, increasing significantly after weight loss[11]. These data suggest that obesity negatively regulates omentin expression. Further investigation is needed to determine the mechanism and pathogenesis.

We found no correlation between serum omentin-1 levels and lipid parameters. One report showed that plasma omentin-1 correlates positively with HDL[8], whereas other reports have shown no correlation[9, 11]. The majority of patients in our study had already received statin therapy; thus, the relationship between serum concentrations of omentin-1 and lipid variables may best be observed in newly diagnosed and untreated patients with CAD.

Serum omentin-1 levels negatively correlated with BMI and IL-6; however, the correlation coefficients are weak, likely because relatively small numbers of participants were investigated. Future research should observe a large sample of patients with CAD. Second, only patients with typical symptoms suggestive of angina were included in our study; we did not include CAD patients with no chest discomfort.

Conclusion

Serum omentin-1 concentrations may be associated with CAD. These findings may have important implications for the pathophysiology and therapy of CAD.

Acknowledgements

The authors express sincere thanks to Hua GAO and Xiu-bin CUI in the Clinical Laboratories of Shandong Provincial Hospital for their technical support.

Author contribution

Xia ZHONG, Fu-qin CHEN, and De-ya SHANG designed the research; Xia ZHONG and Hai-yang ZHANG performed the research; Hui TAN and Fu-li LIU contributed new analytical tools and reagents; Hui TAN, Fu-li LIU, and Xia ZHONG analyzed the data; Xia ZHONG, Hai-yang ZHANG, and Yi ZHOU wrote the manuscript.

References

1 Gelsinger C, Tschoner A, Kaser S, Ebenbichler CF. Adipokine update — new molecules, new functions. Wien Med Wochenschr 2010; 160: 377–90.
2 Ekmekçi H, Ekmekçi OB, Erdine S, Sönmez H, Ataev Y, Oztürk Z, *et al*. Effects of serum homocysteine and adiponectin levels on platelet aggregation in untreated patients with essential hypertension. J Thromb Thrombolysis 2009; 28: 418–24.
3 Schutte AE, Huisman HW, Schutte R, van Rooyen JM, Malan L, Fourie CM, *et al*. Adipokines and cardiometabolic function: How are they interlinked? Regul Pept 2010; 164: 133–8.
4 Zhang H, Cui J, Zhang C. Emerging role of adipokines as mediators in atherosclerosis. World J Cardiol 2010; 2: 370-6.
5 Hivert MF, Sullivan LM, Fox CS, Nathan DM, D'Agostino RB, Wilson WF, *et al*. Associations of adiponectin,resistin, and tumor necrosis factor-a with insulin resistance. J Clin Endocrinol Metab 2008; 93: 3165–72.
6 Abe Y, Ono K, Kawamura T, Wada H, Kita T, Shimatsu A, *et al*. Leptin induces elongation of cardiac myocytes and causes eccentric left ventricular dilatation with compensation. Am J Physiol Heart Circ Physiol 2007; 292: H2387–96.
7 Yang R, Xu A, Pray J, Hu H, Jadhao S, Hansen B, *et al*. Cloning of omentin, a new adipocytokine from omental fat tissue in humans. Diabetes 2003; 52: A1.
8 Souza Batista CM, Yang RZ, Lee MJ, Glynn NM, Yu DZ, Pray J, *et al*. Omentin plasma levels and gene expression are decreased in obesity. Diabetes 2007; 56: 1655–61.
9 Pan HY, Guo L, Li Q. Changes of serum omentin-1 levels in normal subjects and in patients with impaired glucose regulation and with newly diagnosed and untreated type 2 diabetes. Diabetes Res Clin Pract 2010; 88: 29–33.
10 Saremi A, Asghari M, Ghorbani A. Effects of aerobic training on serum omentin-1 and cardiometabolic risk factors in overweight and obese men. J Sports Sci 2010; 28: 993–8.
11 Moreno-Navarrete JM, Catalán V, Ortega F, Gómez-Ambrosi J, Ricart W, Frühbeck G, *et al*. Circulating omentin concentration increases after weight loss. Nutr Metab (Lond) 2010; 7: 27.
12 Schäffler A, Zeitoun M, Wobser H, Buechler C, Aslanidis C, Herfarth H. Frequency and significance of the novel single nucleotide missense polymorphism Val109Asp in the human gene encoding omentin in Caucasian patients with type 2 diabetes mellitus or chronic inflammatory bowel diseases. Cardiovasc Diabetol 2007; 6: 3.
13 Senolt L, Polanská M, Filková M, Cerezo LA, Pavelka K, Gay S, *et al*. Vaspin and omentin: new adipokines differentially regulated at the site of inflammation in rheumatoid arthritis. Ann Rheum Dis 2010; 69: 1410–1.
14 Yamawaki H, Tsubaki N, Mukohda M, Okada M, Hara Y. Omentin, a novel adipokine, induces vasodilation in rat isolated blood vessels. Biochem Biophys Res Commun 2010; 393: 668–72.
15 Saely CH, Risch L, Hoefle G, Rein P, Muendlein A, Marte T, *et al*. Low serum adiponectin is independently associated with both the metabolic syndrome and angiographically determined coronary atherosclerosis. Clin Chim Acta 2007; 383: 97–102.
16 Liang KW, Sheu WH, Lee WL, Liu TJ, Ting CT, Hsieh YC, *et al*. Decreased circulating protective adiponectin level is associated with angiographic coronary disease progression in patients with angina pectoris. Int J Cardiol 2008; 129: 76–80.
17 Yaturu S, Daberry RP, Rains J, Jain S. Resistin and adiponectin levels in subjects with coronary artery disease and type 2 diabetes. Cytokine 2006; 34: 219–23.
18 On YK, Park HK, Hyon MS, Jeon ES. Serum resistin as a biological marker for coronary artery disease and restenosis in type 2 diabetic patients. Circ J 2007; 71: 868–73.
19 Lago F, Dieguez C, Gómez-Reino J, Gualillo O. Adipokines as emerging mediators of immune response and inflammation. Nat Clin Pract Rheumatol 2007; 3: 716–24.
20 Tang NP, Wang LS, Yang L, Zhou B, Gu HJ, Sun QM, *et al*. A polymorphism in the resistin gene promoter is related to increased C-reactive protein levels in patients with coronary artery disease. Clin Chem Lab Med 2007; 45: 1471–5.
21 Liu SW, Qiao SB, Yuan JS, Liu DQ. Association of plasma visfatin levels with inflammation, atherosclerosis and acute coronary syndromes (ACS) in humans. Clin Endocrinol (Oxf) 2009; 71: 202–7.

22 Sonoli SS, Shivprasad S, Prasad CV, Patil AB, Desai PB, Somannavar MS. Visfatin — a review. Eur Rev Med Pharmacol Sci 2011; 15: 9–14.
23 Tilg H, Moschen AR. Adipocytokines: mediators linking adipose tissue, infl ammation and immunity. Nat Rev Immunol 2006; 6: 772–83.
24 Safranow K, Dziedziejko V, Rzeuski R, Czyzycka E, Wojtarowicz A, Bińczak-Kuleta A, *et al*. Plasma concentrations of TNF-alpha and its soluble receptors sTNFR1 and sTNFR2 in patients with coronary artery disease. Tissue Antigens 2009; 74: 386–92.
25 Kuo LT, Yang NI, Cherng WJ, Verma S, Hung MJ, Wang SY, *et al*. Serum interleukin-6 levels, not genotype, correlate with coronary plaque complexity. Int Heart J 2008; 49: 391–402.
26 Levey AS, Coresh J, Balk E, Kausz AT, Levin A, Steffes MW, *et al*. National Kidney Foundation practice guidelines for chronic kidney disease: evaluation, classification, and stratification. Ann Intern Med 2003; 139: 137–47.
27 Thanyasiri P, Celermajer DS, Adams MR. Endothelial dysfunction occurs in peripheral circulation patients with acute and stable coronary artery disease. Am J Physiol Heart Circ Physiol 2005; 289: H513–7.
28 Yang RZ, Lee MJ, Hu H, Pray J, Wu HB, Hansen BC, *et al*. Identification of omentin as a novel depot-specific adipokine in human adipose tissue: possible role in modulating insulin action. Am J Physiol Endocrinol Metab 2006; 290: E1253–61.
29 Rodrigues TC, Biavatti K, Almeida FK, Gross JL. Coronary artery calcification is associated with insulin resistance index in patients with type 1 diabetes. Braz J Med Biol Res 2010 43: 1084–7.
30 Bertoluci MC, Quadros AS, Sarmento-Leite R, Schaan BD. Insulin resistance and triglyceride/HDLc index are associated with coronary artery disease. Diabetol Metab Syndr 2010; 2: 11.
31 Tan BK, Pua S, Syed F, Lewandowski KC, O'Hare JP, Randeva HS. Decreased plasma omentin-1 levels in Type 1 diabetes mellitus. Diabet Med 2008; 25: 1254–5.
32 Kralisch S, Klein J, Lossner U, Bluher M, Paschke R, Stumvoll M, *et al*. Interleukin-6 is a negative regulator of visfatin gene expression in 3T3-L1 adipocytes. Am J Physiol Endocrinol Metab 2005; 289: E586–90.
33 Simons PJ, van den Pangaart PS, Aerts JM, Boon L. Proinflammatory delipidizing cytokines reduce adiponectin secretion from human adipocytes without affecting adiponectin oligomerization. J Endocrinol 2007; 192: 289–99.
34 Fasshauer M, Kralisch S, Klier M, Lossner U, Bluher M, Klein J, *et al*. Adiponectin gene expression and secretion is inhibited by interleukin-6 in 3T3-L1 adipocytes. Biochem Biophys Res Commun 2003; 301: 1045–50.

Acta Pharmacologica Sinica (2011) 32: 879–887

www.nature.com/aps

Original Article

Metformin attenuates pressure overload-induced cardiac hypertrophy via AMPK activation

Yong-nan FU#, Han XIAO#, Xiao-wei MA, Sheng-yang JIANG, Ming XU, You-yi ZHANG*

Institute of Vascular Medicine, Peking University Third Hospital and Key Laboratory of Molecular Cardiovascular Sciences, Ministry of Education, Beijing 100191, China

Aim: To identify the role of metformin in cardiac hypertrophy and investigate the possible mechanism underlying this effect.
Methods: Wild type and AMPKα2 knockout (AMPKα2$^{-/-}$) littermates were subjected to left ventricular pressure overload caused by transverse aortic constriction. After administration of metformin (200 mg·kg^{-1}·d^{-1}) for 6 weeks, the degree of cardiac hypertrophy was evaluated using echocardiography and anatomic and histological methods. The antihypertrophic mechanism of metformin was analyzed using Western blotting.
Results: Metformin significantly attenuated cardiac hypertrophy induced by pressure overload in wild type mice, but the antihypertrophic actions of metformin were ablated in AMPKα2$^{-/-}$ mice. Furthermore, metformin suppressed the phosphorylation of Akt/protein kinase B (AKT) and mammalian target of rapamycin (mTOR) in response to pressure overload in wild type mice, but not in AMPKα2$^{-/-}$ mice.
Conclusion: Long-term administration of metformin may attenuate cardiac hypertrophy induced by pressure overload in nondiabetic mice, and this attenuation is highly dependent on AMPK activation. These findings may provide a potential therapy for patients at risk of developing pathological cardiac hypertrophy.

Keywords: metformin; cardiac hypertrophy; AMP-activated protein kinase; protein synthesis; transverse aortic constriction; Akt/protein kinase B; mammalian target of rapamycin

Acta Pharmacologica Sinica (2011) 32: 879–887; doi: 10.1038/aps.2010.229; published online 9 May 2011

Introduction

Metformin is one of the most commonly prescribed antihyperglycemic drugs for the treatment of type 2 diabetes that does not cause hypoglycemia. Apart from its antihyperglycemic effect, metformin has been believed to have other potential effects, as indicated in two large-scale clinical trials[1, 2]. Those trials suggested that metformin could significantly decrease the risk of diabetes-related cardiovascular end points and all cause deaths compared with conventional therapies when lowering blood glucose to similar levels. However, the exact mechanism associated with the cardioprotective role of metformin is still elusive.

AMPK is a serine-threonine kinase that acts as an energy sensor in various cell types[3]. It also plays an important role in cardioprotective effects[4, 5]. Zhou *et al*[6] demonstrated that metformin could activate AMPK. Recent studies have suggested that metformin could inhibit cardiomyocyte apoptosis and improve cardiac function through AMPK activation[7, 8]. Pathological left ventricular hypertrophy is a crucial pathological condition that triggers several serious cardiac events, including arrhythmias, heart failure, and sudden death[9, 10]. However, whether metformin has an inhibitory effect on cardiac hypertrophy has not been elucidated. Thus, we hypothesized that metformin might have a direct antihypertrophic effect via AMPK activation.

In this study, we aim to determine whether metformin inhibits cardiac hypertrophy induced by pressure overload and how metformin exerts its antihypertrophic effect.

Materials and methods

Animals

The research protocol was designed in compliance with the Guide for the Care and Use of Laboratory Animals by the National Institutes of Health of the United States of America (NIH Publication No 85–23, revised 1996). All experimental protocols were approved by the Institutional Committee for Animal Care and Use of Peking University. Heterozygous

# These authors contributed equally to this work.
* To whom correspondence should be addressed.
E-mail zhangyy@bjmu.edu.cn
Received 2010-09-29 Accepted 2010-12-22

AMPKα2 knockout C57BL/6 mice were kindly donated by Professor Benoit VIOLLET (Institute National de la Santé et de la Recherche Médicale U567, Paris, France) and bred in an specific pathogen free (SPF) environment with a 12 h/12 h light-dark cycle and received standard rodent food. Male AMPKα2$^{-/-}$ mice and wild-type (WT) littermates (10 weeks old) were bred from the heterozygotes.

TAC and drug treatment

Transverse aortic constriction (TAC) was carried out as previously described[11]. Briefly, the mice were anesthetized with tribromoethanol (200 mg/kg, ip; Sigma-Aldrich, Milwaukee, WI, USA) and ventilated with a pressure-controlled ventilator (Kent Scientific, CT, USA). A longitudinal cut was made in the proximal portion of the sternum. A 7–0 silk suture was placed around the aorta between the right innominate artery and the left common carotid artery. The suture was tied around a 26-gauge needle and the aorta. After ligation, the needle was promptly removed. The sham procedure was identical, except the aorta was not ligated. Three days after aortic constriction, the mice were injected with metformin (200 mg·kg^{-1}·d^{-1}, sc, Sigma-Aldrich, St Louis, MO, USA) or saline (as a control) every day for 6 weeks.

Echocardiography and evaluation of left ventricular (LV) hemodynamics

After anesthetizing the mice with 1.5% isoflurane (Baxter Healthcare Corporation, New Providence, NJ, USA), we obtained echocardiographic images with a VisualSonics high-resolution Vevo 770 system (VisualSonics, Toronto, ON, Canada). For measurement of the aortic and LV pressure, a 1.4-F micromanometer conductance catheter (SPR-835; Millar Instruments, Houston, TX, USA) was introduced through the right common carotid artery into the ascending aorta and then advanced into the LV as previously described[12].

Histological analysis

The mice were anesthetized with tribromoethanol, and the hearts were harvested, retrograde-perfused with phosphate-buffered saline (PBS), fixed with 4% paraformaldehyde overnight, and then embedded in paraffin. Serial 6-μm-thick LV cross sections were stained with hematoxylin and eosin (HE). Morphometric evaluation of the tissue was performed in a blinded fashion using the Leica Q550 IW imaging workstation (Leica Microsystems Imaging Solutions Ltd, Cambridge, UK). The mean myocyte cross-sectional area was calculated by measuring 100 cells in the HE-stained sections.

Quantitative real-time PCR

Total RNA was isolated from the heart tissue with Trizol Reagent (Invitrogen, Carlsbad, CA, USA). Relative quantitation by real-time PCR involved SYBR Green detection of PCR products in real time with the ABI PRISM 7700 Sequence Detection System (Applied Biosystems). The PCR used the following primers: atrial natriuretic factor (ANF), 5′-GCCCTGAGTGAGCAGACTG-3′ (forward) and 5′-CGGAAGCTGTTGCAGCCTA-3′ (reverse); β-myosin heavy chain (β-MHC), 5′-ACCTAC CAGACAGAGGAAGA-3′ (forward) and 5′-TTGCAAAGAGTCCAGGTCTGAG-3′ (reverse); and GAPDH, 5′-TCCTGGTATGACAATGAATACGGC-3′ (forward) and 5′-TCTTGCTCAGTGTCCTTGCTGG-3′ (reverse). The GAPDH RNA was amplified as a reference standard. The reactions were conducted in triplicate by heating the reactant to 95 °C for 5 min, followed by 40 cycles of 94 °C for 30 s, 58 °C for 30 s and 72 °C for 30 s.

Western blot analysis

The heart extracts were subjected to sodium dodecyl sulfate polyacrylamide gel electrophoresis (SDS-PAGE) and blotted on nitrocellulose membranes. The membranes were incubated with antibodies against phosphorylated AMPK, acetyl CoA carboxylase (ACC), eukaryotic elongation factor-2 (eEF2), mammalian target of rapamycin (mTOR) and Akt/protein kinase B (AKT) and then against the respective total level of each protein (antibodies from Cell Signaling Technology Incorporated, Danvers, MA, USA). The protein bands were visualized with Supersignal West Dura Extended Duration Substrate (Thermo Fisher Scientific, Rockford, IL, USA). The blots were subsequently reprobed with the antibody eIF5 (Santa Cruz Biotechnology, Santa Cruz, CA, USA) to confirm equal loading.

Statistical analysis

The data are expressed as the means±SEM. Intergroup comparisons were performed using Prism 4 (GraphPad Software Incorporate, La Jolla, CA, USA) with Student's paired two-tailed *t*-test or two-way ANOVA. For the ANOVA, if a significant variance was found, the Tukey or Bonferroni test was used as the *post hoc* analysis. $P<0.05$ was considered statistically significant.

Results

Metformin attenuates cardiac hypertrophy induced by TAC in WT mice

To determine whether metformin plays a part in cardiac hypertrophy induced by TAC, we treated TAC-operated mice with metformin (200 mg·kg^{-1}·d^{-1}) or saline for 6 weeks after surgery. Echocardiographic data showed no significant difference in the WT mice before sham or TAC operation (data not shown). The mice that received TAC developed cardiac hypertrophy with normal cardiac systolic function 6 weeks after the operation (Figure 1, Table 1). Sustained treatment with metformin decreased the LV posterior wall dimension in diastole (LVPWd) compared with saline-treated hearts (Figure 1A, 1B). The heart weight/tibial length (HW/TL) of the TAC+saline group increased by 26% compared with the sham+saline group ($P<0.01$; Figure 1C). In contrast, the HW/TL of TAC+metformin group increased by only 11.7% compared with the sham+saline group. It could therefore be calculated that metformin suppressed the TAC-induced increase in HW/TL by 55% ($P<0.05$; Figure 1C). The cardiomyocyte cross-sectional area also decreased in the metformin-treated

Table 1. Anatomic and functional data for WT mice and AMPKα2$^{-/-}$ littermates 6 weeks after sham or TAC operation. Values are means±SEM; in WT groups, $^{c}P<0.01$ *vs* sham+saline; $^{e}P<0.05$ *vs* TAC+saline; in AMPKα2$^{-/-}$ groups, $^{h}P<0.05$ and $^{i}P<0.01$ *vs* sham+saline; $^{j}P>0.05$ *vs* TAC+saline.

	WT				AMPKα2$^{-/-}$			
	Sham		TAC		Sham		TAC	
	Saline	Metformin	Saline	Metformin	Saline	Metformin	Saline	Metformin
Anatomic data								
n	9	7	9	9	8	6	9	8
Body weight (g)	25.9±0.96	25.3±1.02	27.0±1.03	25.0±0.75	26.1±0.82	27±0.99	27.6±0.78	26.7±0.80
Heart weight (mg)	114.1±3.7	109.4±4.4	150.0±7.2^{c}	126.4±4.9^{e}	117.5±3.4	112.8±4.7	152.5±5.7^{i}	158.2±6.3^{j}
HW/BW (mg/g)	4.42±0.07	4.31±0.09	5.59±0.18^{c}	5.04±0.13^{e}	4.47±0.14	4.18±0.05	5.62±0.17^{i}	5.9±0.25^{j}
Echocardiographic data								
n	9	7	9	9	8	6	9	8
HR (bpm)	408±8	440±12	421±15	431±19	425±11	411±10	447±17	428±10
LVIDd (mm)	4.02±0.10	3.93±0.13	4.14±0.11	3.79±0.10	3.92±0.09	3.91±0.12	4.04±0.11	4.16±0.08
LVIDs (mm)	2.79±0.13	2.62±0.17	3.02±0.15	2.60±0.11	2.61±0.12	2.66±0.13	2.91±0.14	3.01±0.14
LVAWd (mm)	0.82±0.03	0.76±0.02	1.02±0.03^{c}	0.89±0.02^{e}	0.83±0.03	0.80±0.02	1.07±0.05^{i}	1.08±0.05^{j}
FS%	31.0±1.76	33.5±2.33	31.7±1.08	32.9±1.29	32.8±1.55	32.1±1.95	29.8±1.54	30.7±1.22
Hemodynamic data								
n	8	7	8	9	8	6	9	8
HR (bpm)	479±15	475±26	491±29	474±20	493±18	479±19	494.2±21	471.6±16
Systolic BP (mmHg)	81.2±5.4	82.8±2.4	127.5±7.0^{c}	124.2±9.2	89.5±2.5	91.4±4.1	131.7±8.3^{i}	133.1±7.1
Diastolic BP (mmHg)	55.0±4.5	57.7±3.5	67.9±6.9	61.3±5.5	57.4±3.1	62.5±5.8	70.9±4.9	66.3±4.6
LVSP (mmHg)	81.8±4.1	83.6±3.4	132.8±6.7^{c}	130.8±8.1	91.4±3.0	92.3±5.2	132.5±8.8^{i}	135.7±5.5
LVEDP (mmHg)	1.2±0.8	1.9±1.3	8.7±1.0^{c}	5.2±1.5^{e}	2.0±1.0	2.5±0.8	9.9±1.6^{h}	7.8±1.4
+d*p*/d*t* (mmHg/s)	8414±514	7318±435	8259±679	7548±790	8619±543	8618±651	8577±755	7892±328
−d*p*/d*t* (mmHg/s)	-7973±364	-7124±286	-8498±673	-8657±471	-8582±303	-7928±306	-8720±768	-7190±753

TAC, thoracic aortic constriction; *n*, number of mice; HW, heart weight; BW, body weight; HR, heart rate; LVIDd, left ventricular (LV) internal diameter in diastole; LVIDs, LV internal diameter in systole; LVAWd, LV anterior wall diameter in diastole; FS, fractional shortening; LVSP, LV peak systolic pressure; LVEDP, LV end-diastolic pressure; +d*p*/d*t* and -d*p*/d*t*, the rise and decline of the first derivative of pressure, respectively.

group compared with the saline-treated group ($P<0.01$; Figure 1D, 1E). Echocardiographic and hemodynamic data showed that sustained treatment with metformin did not affect the cardiac systolic function, but mitigated the diastolic function impairment induced by TAC ($P<0.05$; Table 1). The treatment with metformin did not affect the systolic blood pressure (SBP) or the LV peak systolic pressure (LVSP) (Table 1). Additionally, metformin treatment inhibited the TAC-induced increase in mRNA levels of ANF and β-MHC (Figure 1F, 1G). Taken together, these results indicate that metformin attenuated the development of TAC-induced cardiac hypertrophy independent of hemodynamics. Moreover, there was no significant difference in anatomic and functional data (Table 1) between the sham+saline group and the sham+metformin group; therefore, metformin did not affect normal cardiac structure or function.

Metformin does not attenuate cardiac hypertrophy induced by TAC in AMPKα2$^{-/-}$ mice

To investigate whether AMPK was critical for the inhibitory effect of metformin on cardiac hypertrophy, we subjected AMPKα2$^{-/-}$ littermates to pressure overload caused by TAC. Similar to what was observed in WT mice, TAC induced cardiac hypertrophy without deteriorating cardiac systolic function. However, sustained treatment with metformin did not decrease the LVPWd compared with saline-treated hearts (Figure 2A, 2B). The HW/TL did not decrease in the TAC+metformin group compared with the TAC+saline group (Figure 2C, Table 1). The cardiomyocyte cross-sectional area was similar in the TAC+metformin group and the TAC+saline group (Figure 2D, 2E). Echocardiographic and hemodynamic data showed that sustained metformin treatment did not affect cardiac systolic function (Table 1). Contrary to the findings in WT mice, metformin did not improve diastolic function that was impaired by TAC ($P>0.05$, Table 1). Moreover, metformin treatment in the AMPKα2$^{-/-}$ littermates did not inhibit the TAC-induced increase in mRNA levels of ANF and β-MHC (Figure 2F, 2G). It can therefore be concluded that the inhibitory effect of metformin on cardiac hypertrophy is dependent on AMPK.

We also measured the postoperative level of fasting blood glucose every week for 6 weeks in each group. There was no significant difference in the fasting blood glucose between saline- and metformin-treated mice (data not shown). These results suggest that metformin did not affect the level of fasting blood glucose in nondiabetic mice.

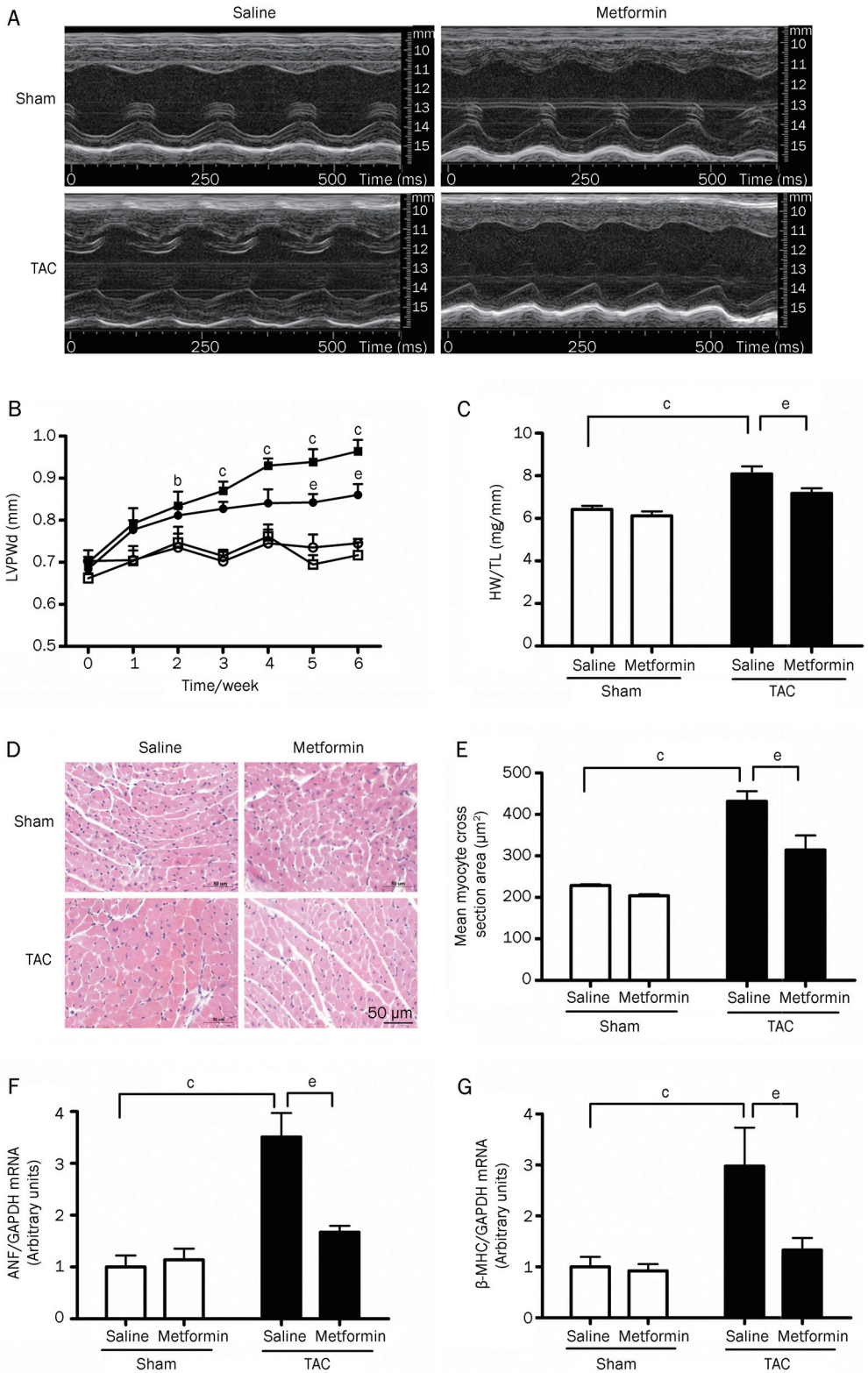

Figure 1. Metformin attenuates cardiac hypertrophy induced by TAC in WT mice. (A) Representative M-mode echocardiograms of the parasternal short-axis view at the level of the midpapillary muscle obtained in each group 6 weeks after sham or TAC operation. (B) Left ventricular posterior wall diameter in diastole (LVPWd) before the surgery and every week for 6 weeks after the surgery (□, sham+saline, ○, sham+metformin, ■, TAC+saline, and ●, TAC+metformin; n=7–9). (C) The HW/TL was calculated 6 weeks after the sham or TAC operation (n=7–9). (D) HE staining of heart cross-sections (×400), bar=50 μm (E) Assessment of the myocyte cross-sectional cell area from left ventricular histological sections (n=6, each with a minimum of 100 cells counted). Quantitative real-time PCR analyses of ANF (F) and β-MHC (G) mRNA levels (n=4). The data are presented as means±SEM. ^{b}P<0.05, ^{c}P<0.01 *vs* sham+saline; ^{e}P<0.05 *vs* TAC+saline.

Effect of metformin on AMPK phosphorylation and protein synthesis.

To examine the role of AMPK in the antihypertrophic action of metformin, we assessed the extent of phosphorylated AMPK in WT mouse hearts. There was a significant increase in the phosphorylation of AMPK at threonine residue 172 in the metformin-treated group compared with the saline-treated group (P<0.05; Figure 3). Metformin treatment also increased the amount of phosphorylated acetyl coenzyme A (CoA) carboxylase (p-ACC), which serves as an indicator of AMPK activity.

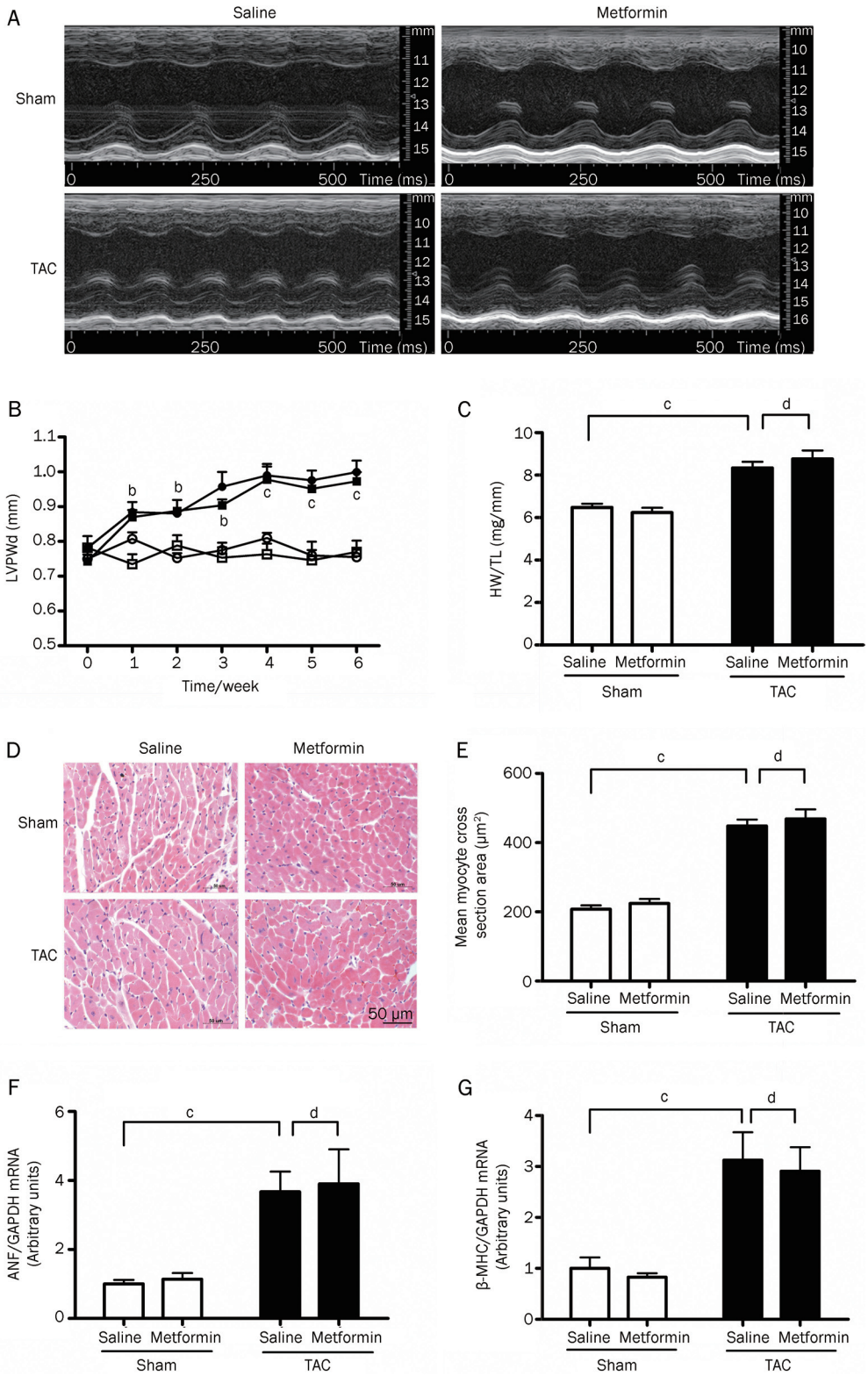

Figure 2. Metformin could not attenuate cardiac hypertrophy induced by TAC in AMPKα2$^{-/-}$ mice. (A) Representative M-mode echocardiograms of the parasternal short-axis view at the level of the midpapillary muscle obtained in AMPKα2$^{-/-}$ mice 6 weeks after the sham or TAC operation. (B) Left ventricular posterior wall diameter in diastole (LVPWd) before surgery and every week for 6 weeks after the surgery (□, sham+saline, ○, sham+metformin, ■, TAC+saline, and ●, TAC+metformin; *n*=6–9). (C) HW/TL was calculated 6 weeks after the sham or TAC operation (*n*=6–9). (D) HE staining of heart cross-sections (×400), bar =50 μm. (E) Assessment of myocyte cross-sectional cell area from left ventricular histological sections (*n*=6, each with a minimum of 100 cells counted). Quantitative real-time PCR analyses of ANF (F) and β-MHC (G) mRNA levels (*n*=4). The data are presented as means±SEM. $^{b}P<0.05$, $^{c}P<0.01$ *vs* sham+saline; $^{d}P>0.05$ *vs* TAC+saline.

Total myocardial AMPKα and phosphorylated AMPKα were significantly decreased in AMPKα2$^{-/-}$ mice, both under control conditions and after TAC, compared with the WT mice (Figure 4). After TAC for 6 weeks, the increase in total AMPKα protein indicated a compensatory increase in AMPKα1 in AMPKα2$^{-/-}$ mice, yet it was unable to compensate for the AMPKα2 deficiency, as demonstrated by significantly lower levels of p-ACC (Figure 4).

LVH is characterized by an increased myocardial cell size in which protein synthesis is a necessary mediator. mTOR,

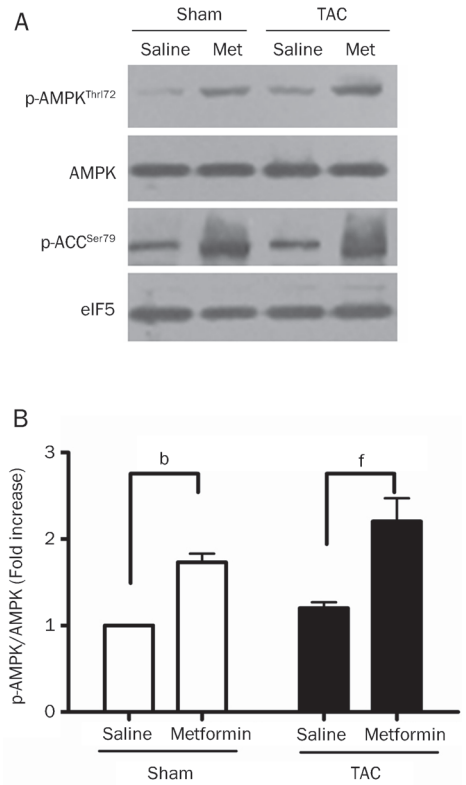

Figure 3. The effect of metformin on the phosphorylation of AMPK and ACC in WT mice 6 weeks after the sham or TAC operation. (A) Western blot of heart extracts for phosphorylated AMPK, phosphorylated ACC, total AMPK, and eIF5. (B) The ratio of phosphorylated AMPK to total AMPK is shown as means±SEM of 6 animals per group. $^{b}P<0.05$ *vs* sham+saline; $^{f}P<0.01$ *vs* TAC+saline.

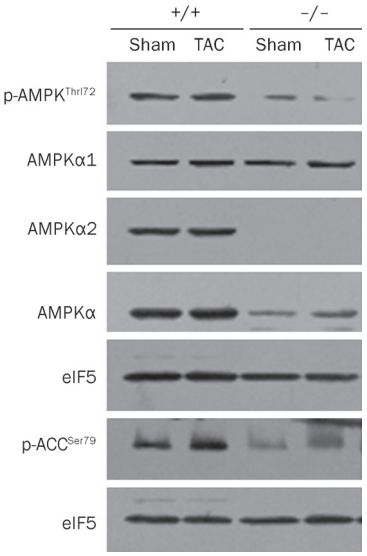

Figure 4. The myocardial AMPKα activity was decreased in AMPKα2$^{-/-}$ mice. Western blot analysis of myocardial phosphorylated AMPKα (total AMPKα1, AMPKα2, and AMPKα), phosphorylated ACC and eIF5 in WT and AMPKα2$^{-/-}$ mice 6 weeks after the sham or TAC operation.

AKT, and eEF2 all play essential roles in the process of protein synthesis and cell growth. Western blot analysis showed a significant increase in phosphorylated mTOR and AKT in the TAC+saline group, but this increase was significantly inhibited in the TAC+metformin group ($P<0.05$; Figure 5A, 5B). However, the phosphorylation level of eEF2 did not show a significant change in any of the groups (Figure 5).

Next we tested the phosphorylation level of these proteins in AMPKα2$^{-/-}$ mice hearts. Similar to the effect in WT mice, TAC induced a significant increase in phosphorylated mTOR and AKT ($P<0.05$; Figure 5A, 5C). Interestingly, metformin did not inhibit the TAC-induced increase of phosphorylated mTOR and AKT in AMPKα2$^{-/-}$ mice (Figure 5A, 5C), suggesting that the inhibitory effect of metformin on protein synthesis may rely on AMPK.

Discussion

This study demonstrated that long-term (6 weeks) administration of metformin, a widely used antidiabetic agent, attenuated pressure-overload-induced cardiac hypertrophy in nondiabetic mice, and the mechanism of this antihypertrophic action was dependent on AMPK activation.

Chan *et al*[13] have shown that metformin inhibits cardiomyocyte hypertrophy induced by phenylephrine. However, it is still unclear whether metformin has an inhibitory effect on cardiac hypertrophy *in vivo* and what dose is necessary for this inhibitory effect, if it exists. In this study, we used a cardiac hypertrophy mouse model in which cardiac hypertrophy without systolic dysfunction was induced by treatment with TAC for 6 weeks. Metformin treatment (200 mg·kg^{-1}·d^{-1}) was found to significantly alleviate the cardiac hypertrophy induced by TAC. In the preliminary examination, we also tested metformin at a dosage of 50 mg·kg^{-1}·d^{-1} in the wild type mice and found that this dosage of metformin had no significant effect on cardiac hypertrophy (date not shown). Although the dose of metformin we used in this study is higher than that used in diabetes patients (10–40 mg/kg), previous reports investigating the anti-diabetic and anti-tumor effects of metformin in the mouse model used a much higher amount of metformin (250–350 mg/kg) due to the difference in drug sensitivity between rodents and humans[14–16]. The dosage of 200 mg·kg^{-1}·d^{-1} that we used in this study was effective on hypertrophy and had no side effect of hypoglycemia. Thus, we believe that the dose of 200 mg·kg^{-1}·d^{-1} is appropriate.

To demonstrate that metformin has a direct inhibitory effect on cardiac hypertrophy rather than a secondary effect due to lowering pressure overload, we measured the aortic and LV pressure in each group. TAC mice had a marked increase in the SBP and LVSP ($P<0.001$; Table 1) compared with sham-operated mice. There was no significant difference in the SBP or LVSP (Table 1) between the TAC+saline and the TAC+metformin group. Our study indicated that metformin did not affect pressure overload, and it had a direct inhibitory effect on cardiac hypertrophy. Similarly, a clinical trial also suggested that metformin had only a clinically insignificant

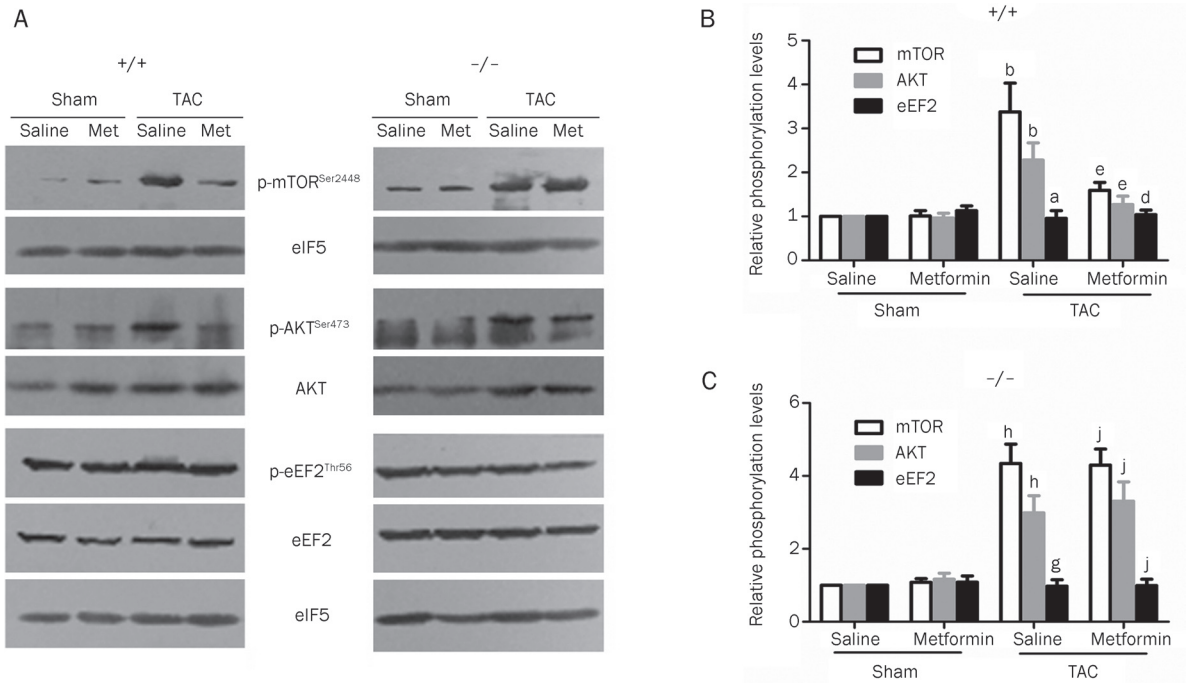

Figure 5. The inhibitory effect of metformin on the protein synthesis pathway is dependent on AMPK activation. (A) Western blot of heart extracts for phosphorylated mTOR, phosphorylated AKT, phosphorylated eEF2, total AKT, total eEF2, and eIF5. Quantitative densitometry for mTOR, AKT, and eEF2 phosphorylation in the WT groups (B) and AMPKα2$^{-/-}$groups (C). The data are presented as means±SEM of 6 animals per group. In the WT groups, $^{a}P>0.05$, $^{b}P<0.05$ vs sham+saline group; $^{d}P>0.05$, $^{e}P<0.05$ *vs* TAC+saline group; in AMPKα2$^{-/-}$ groups, $^{g}P>0.05$, $^{h}P<0.05$ *vs* sham+saline group; $^{j}P>0.05$ *vs* TAC+saline group.

effect on blood pressure in non-diabetic hypertensives[17].

We previously reported that metformin inhibited cardiac fibrosis in the TAC-mouse model and demonstrated that it inhibited collagen synthesis, likely via inhibition of the TGF-β_1-Smad3 signaling pathway[18]. Some studies have suggested an important role for TGF-β_1 in regulating cardiac hypertrophy. Transgenic mice overexpressing TGF-β_1 have been shown to develop cardiac hypertrophy[19]. Conversely, wild-type mice, but not TGF-β_1-deficient mice, treated chronically with angiotensin II manifested cardiac hypertrophy[20]. However, the effect of TGF-β_1 signaling on TAC-induced cardiac hypertrophy is still not fully understood. Some studies have shown that a change in the TGF-β signaling pathway did not affect TAC-induced cardiac hypertrophy. Kuwahara *et al*[21] found that an anti-TGF-β neutralizing antibody inhibited myocardial fibrosis, but not myocyte hypertrophy. Another study also found that candesartan (an ACE inhibitor) suppressed the induction of TGF-β and fibroblast proliferation in pressure-overloaded hearts, but did not affect myocyte hypertrophy[22]. In this study, we focused on AMPK signaling cascades, and we did not investigate whether the TGF-β_1-Smad3 signaling pathway was involved in the metformin mediated antihypertrophic effect.

The inhibitory effect of metformin on cardiac hypertrophy via AMPK activation

Many studies have recently suggested that the cardioprotective mechanism of metformin is mediated by AMPK. Metformin protects the heart against ischemia-reperfusion injury through AMPK activation[7]. Sasaki *et al*[8] demonstrated that metformin inhibited cardiomyocyte apoptosis induced by H_2O_2 and prevented the progression of heart failure in dogs with the activation of AMPK. Tian *et al*[23] reported that the activity of AMPK was increased in rat hearts 12 weeks after TAC operation. Zhang *et al*[24] found that AMPKα2 deficiency exacerbated pressure-overload-induced left ventricular hypertrophy and dysfunction in mice. Those findings indicate that AMPKα2 exerts a cardiac protective effect against ventricular hypertrophy and dysfunction triggered by pressure overload. In this study, we found that long-term metformin treatment significantly increased the phosphorylation of AMPK and attenuated cardiac hypertrophy induced by TAC. Interestingly, the antihypertrophic actions of metformin were ablated in AMPKα2$^{-/-}$ mice. These results suggest that the chronic activation of AMPK during the development of cardiac hypertrophy is a critical mechanism that mediates the beneficial actions of metformin.

Although our data demonstrated that AMPKα2 had a cardiac antihypertrophic effect in TAC-operated mice, we did not find a significant increase in the phosphorylation of AMPK in the TAC+saline group compared with the sham+saline group. Previous reports disagree on this issue. Stuck *et al*[25] reported that the phosphorylation of AMPK decreased 30 min after TAC operation, while in the study by Lei *et al*[26],

the phosphorylation of AMPK decreased the second week after TAC, followed by a minor increase by the sixth week. In addition, we did not find that a selective deletion of AMPKα2 exacerbated the development of TAC-induced cardiac hypertrophy and LV dysfunction. These results were inconsistent with those of Zhang *et al*[24]. The reason underlying this discrepancy is not clear; one possible explanation is the degree of aortic constriction by the TAC operation. The wild type mice developed heart failure during the third week after TAC in the work of Zhang *et al*[24]. However, in the present study, both AMPKα2$^{-/-}$ and WT mice had normal cardiac systolic function after TAC for 6 weeks. Thus, the degree of aortic constriction in the TAC models in the work of Zhang *et al*[24] was greater than that of ours.

AMPK is an endogenous protective protein. AMPK may have no or a minor effect on cardioprotection when the heart is subjected to a mild stimulus. This concept was confirmed by transgenic mouse models in which the AMPK gene was deleted[27] or the dominant mutation gene of AMPK was overexpressed[28]. These transgenic mice live without abnormalities. AMPK is activated and plays a role in the cardiac protective response to high-intensity stimulation, as demonstrated by many studies[5, 29, 30]. Thus, we suppose that the induction of AMPK-related cardiac protective activity is significantly related to the stimulus intensity.

Metformin inhibited signaling pathways that regulate protein synthesis through AMPK activation

Cardiac hypertrophy involves an increase in protein synthesis. To investigate the mechanism for the antihypertrophic effect of metformin, we measured the action of metformin on the signaling pathways that regulate protein synthesis. It was reported that AKT/PKB, an important signaling pathway in regulating protein synthesis, regulates the physiological growth of the heart. Akt1-null mice had a 20% reduction in body size, with a concomitant reduction in heart size. These mice were shown to be defective in exercise-induced cardiac hypertrophy[31]. Sasaki *et al*[8] recently reported that metformin and 5-aminoimidazole 4-carboxamide ribonucleotide (AICAR) inhibited the increase in AKT that was induced by pacing. In the present study, we found that TAC induced a significant increase in the phosphorylation of AKT, which was inhibited by metformin in an AMPK-dependent manner. Although it was also reported that Akt1-null mice developed an exacerbated cardiac dysfunction in response to TAC[31], the decreased phosphorylation of AKT may be involved in the attenuation of hypertrophy.

mTOR can regulate protein synthesis through two pathways. It can activate p70/85 S6 kinase-1 (S6K1) and p54/56 S6K2, which increase ribosomal biosynthesis and protein translation. It also triggers the release of 4E-binding protein-1 from eIF4E; eIF4E can then bind to other initiation factors such as eIF4G, leading to the initiation of translation[32]. mTOR has been proposed to regulate pathological hypertrophy of the heart. The inhibition of mTOR by rapamycin was found to attenuate pathological cardiac hypertrophy and reverse myocardial dysfunction[33]. Dowling *et al*[34] recently reported that metformin inhibited mTOR in a TSC2 and LKB1 dependent manner, which in turn decreased protein synthesis and inhibited cancer cell growth. Another study also demonstrated that metformin inhibited the increase in the phosphorylation of p70s6 kinase induced by phenylephrine *in vitro*[13]. Similarly, we found that the phosphorylation level of mTOR was significantly increased in the TAC group, but almost reversed to a normal state by 6 weeks of metformin treatment. This effect of metformin was not observed in AMPKα2$^{-/-}$ mice, suggesting that the metformin-induced mTOR inhibition was AMPK-dependent. It has also been reported that mTOR could be activated by AKT[35]. Although both AKT and mTOR phosphorylation were increased in TAC-operated mice in our study, whether mTOR was activated by AKT in the TAC model needs further study to be validated.

AMPK activation can lead to an increase in eEF2 phosphorylation, which inhibits the translocation step during elongation. Chan *et al*[13] found that metformin and AICAR inhibited the decrease of eEF2 phosphorylation. However, we did not find a significant decrease in eEF2 phosphorylation in TAC-operated mice hearts, and the level of eEF2 phosphorylation was similar in saline- and metformin-treated groups. These data are in agreement with the findings of Zhang *et al*[24]. Therefore, eEF2 may not be involved in TAC-induced cardiac hypertrophy in mice.

Conclusion

Our findings in the present study demonstrate that long-term administration of metformin attenuates cardiac hypertrophy induced by pressure overload in nondiabetic mice. The antihypertrophic effect of metformin may be dependent on AMPK activation. Long-term metformin treatment could therefore be a potential therapy for patients at risk of developing pathological cardiac hypertrophy.

Acknowledgements

Professor Benoit VIOLLET (Institute National de la Santé et de la Recherche Médicale U567, Paris, France) kindly provided the AMPKα2-knockout line. This work was supported by the National Natural Science Foundation of China (No 81030001, 30821001) and the Projects of International Cooperation and Exchanges NSFC (No 30910103902).

Author contribution

You-yi ZHANG and Han XIAO conceived and designed the experiments. Yong-nan FU, Han XIAO, Xiao-wei MA, and Sheng-yang JIANG performed the experiments. Yong-nan FU and Han XIAO analyzed the data. Yong-nan FU, You-yi ZHANG, Han XIAO, and Ming XU wrote the paper.

References

1 Effect of intensive blood-glucose control with metformin on complications in overweight patients with type 2 diabetes (UKPDS 34). UK Prospective Diabetes Study (UKPDS) Group. Lancet 1998; 352: 854–65.

2 Holman RR, Paul SK, Bethel MA, Matthews DR, Neil HA. 10-year follow-up of intensive glucose control in type 2 diabetes. N Engl J Med 2008; 359: 1577–89.
3 Hardie DG, Hawley SA, Scott JW. AMP-activated protein kinase-development of the energy sensor concept. J Physiol 2006; 574: 7–15.
4 Li YJ, Wang PH, Chen C, Zou MH, Wang DW. Improvement of mechanical heart function by trimetazidine in *db/db* mice. Acta Pharmacol Sin 2010; 31: 560–9.
5 Arad M, Seidman CE, Seidman JG. AMP-activated protein kinase in the heart: role during health and disease. Circ Res 2007; 100: 474–88.
6 Zhou G, Myers R, Li Y, Chen Y, Shen X, Fenyk-Melody J, *et al*. Role of AMP-activated protein kinase in mechanism of metformin action. J Clin Invest 2001; 108: 1167–74.
7 Gundewar S, Calvert JW, Jha S, Toedt-Pingel I, Ji SY, Nunez D, *et al*. Activation of AMP-activated protein kinase by metformin improves left ventricular function and survival in heart failure. Circ Res 2009; 104: 403–11.
8 Sasaki H, Asanuma H, Fujita M, Takahama H, Wakeno M, Ito S, *et al*. Metformin prevents progression of heart failure in dogs: role of AMP-activated protein kinase. Circulation 2009; 119: 2568–77.
9 Lorell BH. Transition from hypertrophy to failure. Circulation 1997; 96: 3824–7.
10 Frey N, Olson EN. Cardiac hypertrophy: the good, the bad, and the ugly. Annu Rev Physiol 2003; 65: 45–79.
11 Tarnavski O, McMullen JR, Schinke M, Nie Q, Kong S, Izumo S. Mouse cardiac surgery: comprehensive techniques for the generation of mouse models of human diseases and their application for genomic studies. Physiol Genomics 2004; 16: 349–60.
12 Wang J, Xu N, Feng X, Hou N, Zhang J, Cheng X, *et al*. Targeted disruption of Smad4 in cardiomyocytes results in cardiac hypertrophy and heart failure. Circ Res 2005; 97: 821–8.
13 Chan AY, Soltys CL, Young ME, Proud CG, Dyck JR. Activation of AMP-activated protein kinase inhibits protein synthesis associated with hypertrophy in the cardiac myocyte. J Biol Chem 2004; 279: 32771–9.
14 Buzzai M, Jones RG, Amaravadi RK, Lum JJ, DeBerardinis RJ, Zhao F, *et al*. Systemic treatment with the antidiabetic drug metformin selectively impairs p53-deficient tumor cell growth. Cancer Res 2007; 67: 6745–52.
15 Zou MH, Kirkpatrick SS, Davis BJ, Nelson JS, Wiles WG 4th, Schlattner U, *et al*. Activation of the AMP-activated protein kinase by the anti-diabetic drug metformin *in vivo*. Role of mitochondrial reactive nitrogen species. J Biol Chem 2004; 279: 43940–51.
16 Bergheim I, Guo L, Davis MA, Lambert JC, Beier JI, Duveau I, *et al*. Metformin prevents alcohol-induced liver injury in the mouse: critical role of plasminogen activator inhibitor-1. Gastroenterology 2006; 130: 2099–112.
17 Snorgaard O, Kober L, Carlsen J. The effect of metformin on blood pressure and metabolism in nondiabetic hypertensive patients. J Intern Med 1997; 242: 407–12.
18 Xiao H, Ma X, Feng W, Fu Y, Lu Z, Xu M, *et al*. Metformin attenuates cardiac fibrosis by inhibiting the TGFβ1-Smad3 signalling pathway. Cardiovasc Res 2010; 87: 504–13.
19 Rosenkranz S, Flesch M, Amann K, Haeuseler C, Kilter H, Seeland U, *et al*. Alterations of β-adrenergic signaling and cardiac hypertrophy in transgenic mice overexpressing TGF-β_1. Am J Physiol Heart Circ Physiol 2002; 283: H1253–62.
20 Schultz JJ, Witt SA, Glascock BJ, Nieman ML, Reiser PJ, Nix SL, *et al*. TGF-β_1 mediates the hypertrophic cardiomyocyte growth induced by angiotensin II. J Clin Invest 2002; 109: 787–96.
21 Kuwahara F, Kai H, Tokuda K, Kai M, Takeshita A, Egashira K, *et al*. Transforming growth factor-β function blocking prevents myocardial fibrosis and diastolic dysfunction in pressure-overloaded rats. Circulation 2002; 106: 130–5.
22 Tokuda K, Kai H, Kuwahara F, Yasukawa H, Tahara N, Kudo H, *et al*. Pressure-independent effects of angiotensin II on hypertensive myocardial fibrosis. Hypertension 2004; 43: 499–503.
23 Tian R, Musi N, D'Agostino J, Hirshman MF, Goodyear LJ. Increased adenosine monophosphate-activated protein kinase activity in rat hearts with pressure-overload hypertrophy. Circulation 2001; 104: 1664–9.
24 Zhang P, Hu X, Xu X, Fassett J, Zhu G, Viollet B, *et al*. AMP activated protein kinase-α2 deficiency exacerbates pressure-overload-induced left ventricular hypertrophy and dysfunction in mice. Hypertension 2008; 52: 918–24.
25 Stuck BJ, Lenski M, Bohm M, Laufs U. Metabolic switch and hypertrophy of cardiomyocytes following treatment with angiotensin II are prevented by AMP-activated protein kinase. J Biol Chem 2008; 283: 32562–9.
26 Lei B, Chess DJ, Keung W, O'Shea KM, Lopaschuk GD, Stanley WC. Transient activation of p38 MAP kinase and up-regulation of Pim-1 kinase in cardiac hypertrophy despite no activation of AMPK. J Mol Cell Cardiol 2008; 45: 404–10.
27 Zarrinpashneh E, Beauloye C, Ginion A, Pouleur AC, Havaux X, Hue L, *et al*. AMPKα2 counteracts the development of cardiac hypertrophy induced by isoproterenol. Biochem Biophys Res Commun 2008; 376: 677–81.
28 Xing Y, Musi N, Fujii N, Zou L, Luptak I, Hirshman MF, *et al*. Glucose metabolism and energy homeostasis in mouse hearts overexpressing dominant negative α2 subunit of AMP-activated protein kinase. J Biol Chem 2003; 278: 28372–7.
29 Russell RR 3rd, Li J, Coven DL, Pypaert M, Zechner C, Palmeri M, *et al*. AMP-activated protein kinase mediates ischemic glucose uptake and prevents postischemic cardiac dysfunction, apoptosis, and injury. J Clin Invest 2004; 114: 495–503.
30 Yang J, Holman GD. Insulin and contraction stimulate exocytosis, but increased AMP-activated protein kinase activity resulting from oxidative metabolism stress slows endocytosis of GLUT4 in cardiomyocytes. J Biol Chem 2005; 280: 4070–8.
31 DeBosch B, Treskov I, Lupu TS, Weinheimer C, Kovacs A, Courtois M, *et al*. Akt1 is required for physiological cardiac growth. Circulation 2006; 113: 2097–104.
32 Heineke J, Molkentin JD. Regulation of cardiac hypertrophy by intracellular signalling pathways. Nat Rev Mol Cell Biol 2006; 7: 589–600.
33 McMullen JR, Sherwood MC, Tarnavski O, Zhang L, Dorfman AL, Shioi T, *et al*. Inhibition of mTOR signaling with rapamycin regresses established cardiac hypertrophy induced by pressure overload. Circulation 2004; 109: 3050–5.
34 Dowling RJ, Zakikhani M, Fantus IG, Pollak M, Sonenberg N. Metformin inhibits mammalian target of rapamycin-dependent translation initiation in breast cancer cells. Cancer Res 2007; 67: 10804–12.
35 Cantley LC. The phosphoinositide 3-kinase pathway. Science 2002; 296: 1655–7.

Acta Pharmacologica Sinica (2011) 32: 888–894
 1671-4083/11 $32.00
www.nature.com/aps

Original Article

Proteomic alterations in mouse kidney induced by andrographolide sodium bisulfite

Hong LU[1, #, *], Xin-yue ZHANG[2, #], Yan-quan ZHOU[1, 3], Xin WEN[4], Li-ying ZHU[3, *]

[1]School of Pharmacology, Zhejiang Chinese Medical University, Hangzhou 310053, China; [2]Institute of Materia Medica, Zhejiang Academy of Medical Sciences, Hangzhou 310013, China; [3]State Key Laboratory Breeding Base for Zhejiang Sustainable Pest and Disease Control, Institute of Plant Protection and Microbiology, Zhejiang Academy of Agricultural Sciences, Hangzhou 310021, China; [4]Center for Craniofacial Molecular Biology, School of Dentistry, University of Southern California, Los Angeles, CA 90033, USA

Aim: To identify the key proteins involved in the nephrotoxicity induced by andrographolide sodium bisulfite (ASB).
Methods: Male ICR mice were intravenously administrated with ASB (1000 or 150 mg·kg^{-1}·d^{-1}) for 7 d. The level of malondialdehyde (MDA) and the specific activity of superoxide dismutase (SOD) in kidneys were measured. The renal homogenates were separated by two-dimensional electrophoresis, and the differential protein spots were identified using a matrix-assisted laser desorption/ionization (MALDI) time-of-flight (TOF)/TOF mass spectrometry.
Results: The high dose (1000 mg/kg) of ASB significantly increased the MDA content, but decreased the SOD activity as compared to the control mice. The proteomic analysis revealed that 6 proteins were differentially expressed in the high-dose group. Two stress-responsive proteins, *ie* heat shock cognate 71 kDa protein (HSC70) and peroxiredoxin-6 (PRDX6), were regulated at the expression level. The remaining 4 proteins involving in cellular energy metabolism, including isoforms of methylmalonyl-coenzyme A mutase (MUT), nucleoside diphosphate-linked moiety X motif 19 (Nudix motif19), mitochondrial NADH dehydrogenase 1 alpha subcomplex subunit 10 (NDUFA10) and nucleoside diphosphate kinase B (NDK B), were modified at the post-translational levels.
Conclusion: Our findings suggest that the mitochondrion is the primary target of ASB and that ASB-induced nephrotoxicity results from oxidative stress mediated by superoxide produced by complex I.

Keywords: andrographolide sodium bisulfite; Lianbizhi injection; nephrotoxicity; proteomics; reactive oxygen species; peroxiredoxin-6

Acta Pharmacologica Sinica (2011) 32: 888–894; doi: 10.1038/aps.2011.39; published online 20 Jun 2011

Introduction

Andrographis paniculata (Burm f) Nees (Acanthaceae) (*A paniculata*, Chuanxinlian) is a widely used Chinese medicinal herb that is believed to be effective for relieving fever, inflammation and pain according to traditional Chinese medicine. Compared with other Chinese medicinal herbs, *A paniculata* has been well studied. The major bioactive compounds are diterpenoids, flavonoids and polyphenols[1, 2]. *A paniculata* has a variety of health benefits, including anti-inflammation, anti–cancer and immunity enhancement. Andrographolide ($C_{20}H_{30}O_5$), the major diterpenoid of *A paniculata*, has multiple pharmacological properties and is a potential chemotherapeutic agent[3].

# These authors contributed equally to this work.
* To whom correspondence should be addressed.
E-mail zhuliying@hotmail.co.jp (Li-ying ZHU);
luhong03@hotmail.com (Hong LU)
Received 2010-12-07 Accepted 2011-04-01

Andrographolide sodium bisulfite (ASB, $C_{20}H_{29}O_7SNa$, 436.23) is a water-soluble sulfonate of andrographolide that is synthesized by an addition reaction with sodium bisulfite. Lianbizhi (LBZ) injection, which contains ASB as its sole component, has been used clinically in mainland China to treat infectious diseases such as bacillary dysentery, mumps, laryngitis, tonsillitis and upper respiratory tract infections[4]. However, reports of adverse drug reactions (ADRs) have increased in the past decade, leading to the issue of a drug use warning from the State Food and Drug Administration of China[5]. The clinical ADRs to LBZ injection are diverse, the most serious of which is acute renal failure[4, 6–8]. There are various explanations for the cause of ADRs to LBZ, such as allergic reactions[6], cross-reactions with aminoglycosides in combination therapy[4] and nephrotoxicity[7], but extensive studies of the toxicology of LBZ injection are still scarce.

Injection agents for Chinese medicinal herbs generally include bioactive ingredients and additives. Bioactive ingre-

dients are usually synthesized, semi-synthesized or extracted from herbs; additives are added to increase the hydrophilicity of the active ingredient. The toxicities of the injection agents could therefore be due to the toxicities of the bioactive ingredients, additives, and/or impurities resulting from the manufacturing process. The potential nephrotoxicity of LBZ injections has been suggested by several recent toxicological studies. Renal damage triggered by a single intravenous injection of two kinds of LBZ with different purities has been reported[9]. We previously used purified ASB (>99% pure), the raw material for LBZ injection, to investigate its toxicity in kidneys[10]. Administration of ASB at a high dose (1000 mg/kg) for 7 d resulted in renal dysfunction and an increase in both the serum creatinine and blood urea nitrogen levels. In addition, microscopic examination revealed the presence of tubular interstitial injury and cloudy swelling in the proximal tubule in the high-dose group. However, the mechanism of renal toxicity of ASB remains unclear.

A global proteomics approach typically links separation and identification technologies to create a protein profile or differential protein display. Proteomic techniques have been used in kidney toxicity studies of chemicals such as the antibiotic gentamicin and the chemotherapeutic agent cisplatin and have provided insight into the mechanisms governing key proteins in critical biological pathways that create adverse drug effects[11].

In the present study, a differential proteomic analysis of the mouse kidney was performed to identify the key proteins involved in kidney dysfunction induced by ASB administration and to investigate the mechanism of ADRs to LBZ. A two-dimensional (2-D) electrophoresis proteomic approach revealed that six proteins were significantly differentially expressed in the murine kidney upon exposure to ASB.

Materials and methods

Animals and treatment

Male ICR mice weighing 18–22 g were purchased from the Zhejiang Experimental Animal Center. All animals were housed with a 12-h light/12-h dark cycle at 22 °C and 55%±5% relative humidity. Food (Zhejiang Experimental Animal Center, China) and tap water were provided *ad libitum*. All experiments were carried out according to the guidelines of China for the care and use of laboratory animals. Each of the mice was randomly assigned to one of three experimental groups (each n=10): high-dose ASB (1000 mg/kg), low-dose ASB (150 mg/kg) and a control group. The ASB groups were induced with daily intravenous (iv) injections of 20 mL/kg body weight of ASB (99%, Zhejiang Jiuxu Pharmaceutical Co, Ltd, China) in a 0.9% sodium chloride injection solution (Huadong Pharmaceutical Co, Ltd, Hangzhou, China) for 7 d. The control group received an equal volume of 0.9% sodium chloride injection solution. Mice were sacrificed 1 h after the last injection, and the kidneys were surgically removed for further analysis.

Measurement of malondialdehyde content and superoxide dismutase activity

One removed kidney from each animal was homogenized with saline 1:10 (*w/v*) and centrifuged at 3000×*g* for 10 min. The supernatant was used to measure the content of malondialdehyde (MDA), one of the end products of lipid peroxidation and an indicator of reactive oxygen species (ROS) production, and the specific activity of superoxide dismutase (SOD), using commercially available kits (Nanjing Jiancheng Bioengineering Institute, Nanjing, China) in accordance with the manufacturer's protocols. The data were statistically analyzed using Student's *t*-test to compare the means of two different groups.

Protein extraction for proteomic analysis

Renal proteins were extracted as previously described[12]. After removing the renal capsule, the kidney was excised into several thin slices and washed in ice-cold PBS to remove the contaminating blood. The tissue was frozen in liquid N_2, ground to powder, and resuspended in lysis buffer containing 7 mol/L urea, 2 mol/L thiourea, 4% (*w/v*) CHAPS, 2% (*v/v*) ampholyte (pH 3–10), 120 mmol/L DTT, 40 mmol/L Tris-base and protease inhibitor cocktail (50 μL for 1 mL lysis buffer, Sigma), followed by a 30-min incubation at RT. After centrifugation (10 000×*g* for 5 min at 4 °C), the supernatant was stored at -80 °C as a 500-μL aliquot, and the protein concentration was determined using the Bradford method with a Bio-Rad Protein Assay Kit (Bio-Rad Laboratories, Hercules, CA, USA).

2-D electrophoresis and staining

Immobiline™ DryStrips, pH 3–10 NL (non-linear), 13 cm long (Amersham Biosciences, Uppsala, Sweden) were rehydrated overnight with rehydration buffer (250 μL per strip) containing 7 mol/L urea, 2 mol/L thiourea, 2% (*w/v*) CHAPS, 0.5% (*v/v*) ampholytes (pH 3–10), 40 mmol/L DTT, 40 mmol/L Tris-base, and 0.002% (*w/v*) bromophenol blue. The first-dimension separation, isoelectric focusing (IEF), was performed in an Ettan IPGphor III IEF System (Amersham Biosciences, Uppsala, Sweden) at 20 °C using the stepwise mode to reach 23 100 V·h with cup loading. For each sample, 400 μg total protein was premixed with the rehydration buffer, followed by a short spin-down before loading a sample cup with 100 μL. After IEF, the proteins on the strip were equilibrated for 15 min in buffer containing 6 mol/L urea, 130 mmol/L DTT, 30% (*v/v*) glycerol, 75 mmol/L Tris-base, 2% (*w/v*) SDS, and 0.002% (*w/v*) bromophenol blue, and then in buffer containing 6 mol/L urea, 135 mmol/L iodoacetamide, 30% (*v/v*) glycerol, 75 mmol/L Tris-base, 2% (*w/v*) SDS, and 0.002% (*w/v*) bromophenol blue for 15 min. The IPG strip was then transferred onto a 12.5% acrylamide slab gel for the second-dimension separation, which was performed in an Ettan DALTsix Electrophoresis Unit (Amersham Biosciences, Uppsala, Sweden) with a current of 12 mA/gel for 4 h at 25 °C. The separated protein spots were visualized with CBB G-250 stain using the Colloidal Coomassie staining protocol in the GE Healthcare handbook (80-6429-60).

Spot analysis, matching and statistical analysis

Image Master 2D Platinum 7.0 (Amersham Biosciences) software was used to match and analyze protein spots on 2-D gels and for the statistical analysis. The parameters used for spot detection were (i) mini-mal area=5 pixels; (ii) smooth factor=3.0; and (iii) saliency=2000.

Protein identification

The protein spots of interest were analyzed by matrix-assisted laser desorption/ionization (MALDI) time-of-flight (TOF)/TOF mass spectrometry (MS) by a commercial company (Beijing Proteome Research Center, Beijing, China). The proteins were subsequently identified with the MASCOT search algorithm (http://www.matrixscience.com) using a combination of peptide mass fingerprint profiles and MS/MS sequencing data. The UniProt Knowledgebase and NCBI databases were used.

Results

Index of renal oxidation

Oxidative stress is a pathway for renal injury[13]. To investigate whether the renal damage induced by ASB is caused by ROS, the levels of SOD and MDA in the renal tissue were analyzed (Figure 1, 2). Upon ASB treatment, SOD activity decreased, whereas the MDA content increased. The downregulation of SOD activity and the upregulation of MDA were both dose-dependent. However, only the group treated with the high dose of ASB was significantly different from the control group, suggesting that the toxicity is only trigged by a high concentration of ASB, consistent with our previous results[10].

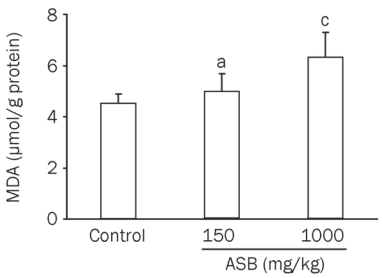

Figure 1. Concentration changes in MDA in the kidneys of mice exposed to ASB. The homogenates of kidneys from mice treated with or without ASB iv administration for 7 d were used to measure MDA content. n=10. Mean±SD. ^{a}P>0.05, ^{c}P<0.01 *vs* control, *t*-test.

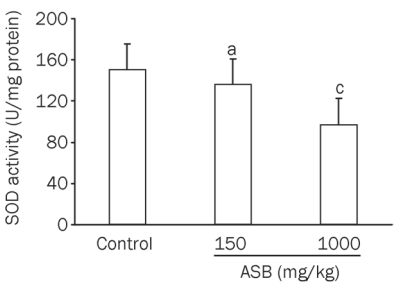

Figure 2. Specific activity changes in SOD in the kidneys of mice exposed to ASB. The homogenates of kidneys from mice treated with or without ASB iv administration for 7 d were used to measure the SOD specific activity. n=10. Mean±SD. ^{a}P>0.05, ^{c}P<0.01 *vs* control, *t*-test.

Differentially expressed renal proteins

Because only the high dose of ASB caused significant changes in renal function and redox status, this study focused on the proteomic analysis of the kidney after treatment with a high dose of ASB. Approximately 500 protein spots were visualized in each 2-D gel. Representative 2-D gels of both the high-dose group and the control group are illustrated in Figure 3, in which the proteins that were differentially expressed in the ASB group are numbered. In total, seven differentially expressed protein spots in the 2-D gel were identified by MALDI TOF/TOF MS (Table 1). Because two protein spots (spots 6 and 7) were identified as the same protein, nucleoside diphosphate kinase B (NDK B), six proteins were actually regulated by ASB administration. The individual changes in the seven spots were magnified (Figure 4). Of the seven protein spots, three were upregulated, including methylmalonyl-Coenzyme A mutase (MUT, spot 1), peroxiredoxin-6 (PRDX6, spot 5) and NDK B (spot 6). The other three spots, heat shock cognate 71 kDa protein (HSC70, spot 2), mitochondrial NADH dehydrogenase 1 alpha subcomplex subunit 10 (NDUFA10, spot 3) and NDK B (spot 7) were downregulated. The remaining spot (spot 4), which was identified as nucleoside diphosphate-linked moiety X motif 19 (Nudix motif19), displayed an acidic shift with a slight molecular weight increase in the ASB group, suggesting an ASB-induced post-translational modifi-

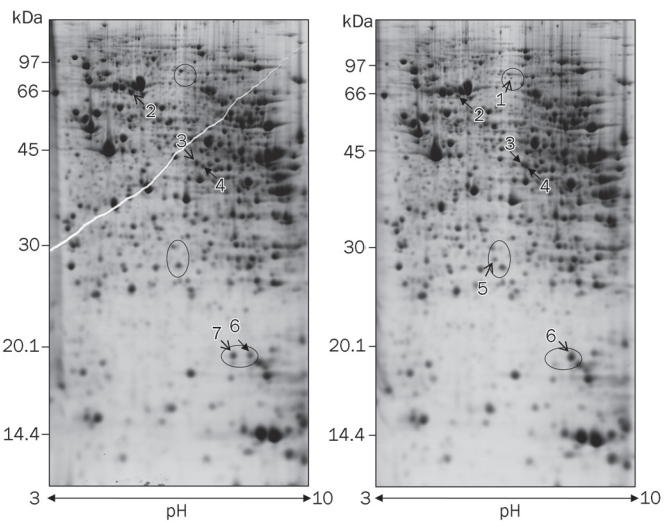

Figure 3. Representative 2-D gel images of kidney proteins isolated from mice with (right) or without (left) ASB treatment. For each sample, 400 μg of total protein extracted from the mouse kidney was loaded onto a 13-cm IPG strip for isoelectric focusing and separated by SDS-PAGE (12.5%) with CBB staining. The differentially expressed spots detected by Image Master 2D Platinum 7.0 are numbered and summarized in Table 1. Open arrows indicate spots with greater abundance between the corresponding gels.

Table 1. Differentially expressed proteins in the kidney of mouse treated with ASB identified by TOF/TOF MS.

Spot	Protein	Gene	Accession (UnifrotKB)	Functional classification	M_W* (kDa)	pI theoretical	pI estimated	Mascot score	Sequence coverage	ASB effect	Fold change
1	Methylmalonyl-Coenzyme A mutase (MUT)	*Mut*	Q3UJU1	Amino acid degradation; propanoate metabolism	82791.6	6.45	5.95	158	25%	↑	4.9
5	Peroxiredoxin-6 (PRDX6)	*Prdx6*	008709	Response to ROS	24871	5.7	5.7	351	40%	↑	4.6
6	Nucleoside diphosphate kinase B (NDK B)	*Nme2*	Q01768	Nucleotide metabolism	17351.9	6.97	7.48	184	59%	↑	1.9
2	Heat shock cognate 71 kDa protein (HSC70)	*Hspa8*, *Hsc70*	P63017	Stress response	68736.2	5.37	5.4	225	21%	↓	2.3
3	NADH dehydrogenase [ubiquinone] 1 alpha subcomplex subuint 10, mitochondrial (NDUFA10)	*Ndufa10*	Q99LC3	Oxidative phosphorylation	40577.7	7.63	6.1	72	23%	↓	1.3
7	Nucleoside diphosphate kinase B (NDK B)	*Nme2*	Q01768	Nucleotide metabolism	17351.9	6.97	6.97	252	46%	↓	6.2
4	Nucleoside diphosphate-linked moiety X motif 19, mitochondrial (Nudix motif19, RP2p)	*Nudt19*, *D7Rp2e*	P11930	Fatty acid oxidation	40294.4	6.22	6.18	261	16%	shift	–

* Molecular weights estimated from the experiment data in this study are all similar to the theoretic one.

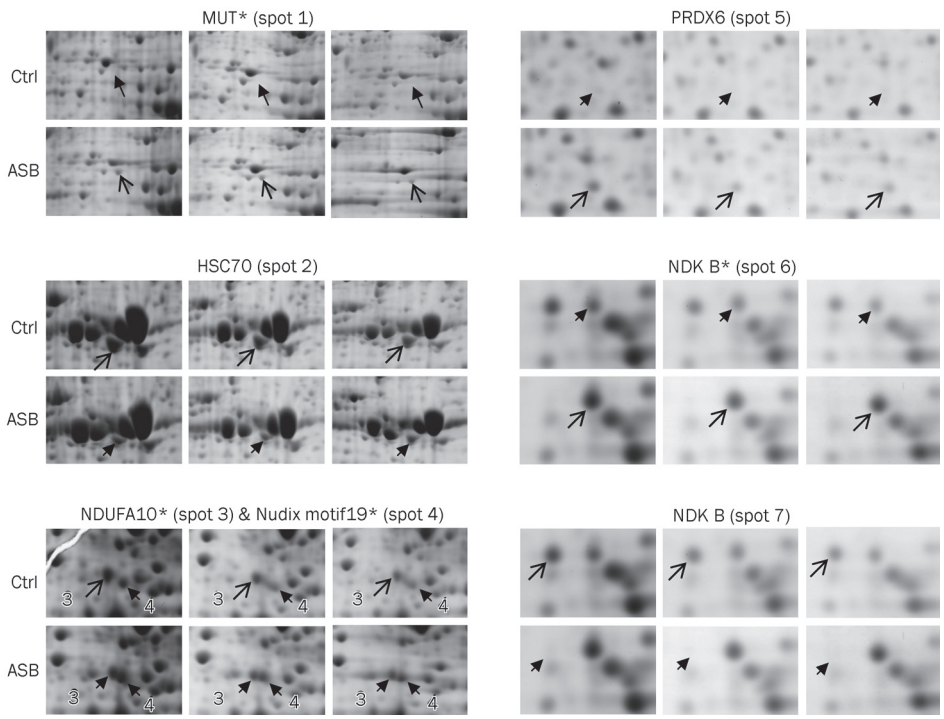

Figure 4. Magnified images of the altered proteins in the mouse kidney induced by ASB treatment. The spots numbered in Figure 3 are shown in the corresponding regions of the individual gels (n=3). The spots with pI values that differ from the theoretical values are marked with asterisks. Open arrows indicate spots with greater abundance between the corresponding gels.

cation (PTM). The increase in MUT (spot 1) was also due to an ASB-induced PTM because it showed an acidic shift relative to its theoretical pI and was found only in ASB group gels. In contrast, both NDUFA10 (spot 3) and NDK B (spot 6) exhibited different pIs from their theoretical values, even in the control group (Table 1), suggesting an acidic isoform of NDUFA10 and a basic isoform of NDK B, respectively. Because they were present in both the ASB group and the control group, NDUFA10 (spot 3) and NDK B (spot 6) were considered to be the respective isoforms under physiological conditions. Interestingly, the two spots of NDK B were regulated oppositely: the basic isoform (spot 6) was upregulated, whereas the spot exhibiting the theoretical pI (spot 7) was downregulated, suggesting that ASB treatment shifted NDK B to its basic isoform.

Discussion

In the present study, we used differential proteomic analysis to identify the proteins regulated by ASB in the mouse kidney. Seven spots, which were identified as six proteins, were differentially expressed and/or post-translationally modified after ASB treatment and identified by MALDI TOF/TOF MS (Table 1). This is report to demonstrate an alteration in kidney protein expression following ASB-induced renal injury.

Protein involved in cellular energetics

Nudix motif19 is a member of the Nudix hydrolase superfamily and was recently identified as a CoA diphosphatase involved in fatty acid β-oxidation[14]. Nudix motif19 is highly expressed in the mouse kidney at both the protein[15] and mRNA levels[16], suggesting it has an important role in the kidney. The slight PTM of Nudix motif19 induced by ASB reflects a disturbance in fatty acid catabolism, which could lead to catabolite accumulation and result in the inhibition of fatty acid β-oxidation and a reduction in energy supply.

MUT is strictly a mitochondrial enzyme. It catalyzes the isomerization of methylmalonyl-coenzyme A (CoA) to succinyl-CoA[17] and is the key enzyme for the transfer of the catabolites of branched-chain amino acids and odd-chain fatty acids into the tricarboxylic acid cycle[18]. A knockout of *Mut* in the mouse results in tubulointerstitial renal disease in response to respiratory chain dysfunction[19]. A similar interstitial nephritis was triggered by ASB in our previous study[10]. The MUT dysfunction resulting from the ASB-induced acidic shift in pI in this study may be similar to the inactivation caused by *Mut* deletion. Therefore, the ASB-induced nephrotoxicity is likely due to respiratory chain dysfunction.

NDUFA10 is a subunit of mitochondrial respiration chain complex I (NADH: ubiquinone oxidoreductase)[20]. PTMs regulate the activity and the interactive capacity of complex I subunits[21]. The phosphorylation of NDUFA10 in bovine heart has been proposed to influence the affinity of NADH binding and the activity of complex I[22]. In this study, one of the acidic isoforms of NDUFA10 was more highly expressed in the control group, in agreement with its important role in the electron transport chain of intact mitochondria. The ASB group displayed a relative reduction in this isoform, suggesting that ASB partially inhibits PTM and leads to functional decline. Complex I is the major source of superoxide[23], and impairment of complex I causes oxidative damage that is a part of the progression of different pathologies, including Parkinson's disease[24]. Although further study is needed to identify the PTM of NDUFA10 in the mouse kidney, the partial inhibition of the PTM of NDUFA10 upon treatment with ASB suggests aberrant superoxide generation by complex I. Excessive endogenous ROS can contribute to acute renal injury[13]. Hence, the ASB-induced changes in the PTM of NDUFA10 might contribute to ASB nephrotoxicity.

NDK B belongs to the *nm23* gene family and encodes nucleoside diphosphate kinase (NDK), which has multiple functions that are involved not only in cell energy conversion but also in many cellular processes[25]. In this study, NDK B was identified from two spots in the control group and one spot in the ASB group due to the ASB-induced basic shift in NDK B, suggesting a change in the function of NDK B. Both NDK B and NDK A are modified after H_2O_2 treatment[26], and Cys^{109} of NDK A was identified as the site of oxidative modification by ROS[27]. Because Cys^{109} is also present in NDK B and no other PTM of NDK B has been reported, the basic isoform of NDK B also seems to be subject to oxidative modification under physiological conditions, which would support the existence of a higher ROS level in the kidney than in other tissues[13]. Altered NDK expression is associated with the inhibition of cellular proliferation and apoptosis[28], and NDK B overexpression reduces H_2O_2-induced cell death in BAF3 cells[29]. Furthermore, a recent proteomic analysis revealed that NDK B (pI 7.6) was upregulated in neuronal nitric oxide synthase (nNOS)-knockout mice due to an increased level of superoxide[30]. Therefore, the increase in the basic isoform of NDK B (pI 7.48) in our proteomic analysis may enable its antioxidative function against superoxide triggered by ASB, which is partially supported by the increased MDA content in the ASB group.

The above proteins were all modified by ASB at the post-translational level and are all mitochondrial proteins except NDK B, a dual-localized mitochondrial protein[15]. Their modification by ASB reflects a decline or loss of mitochondrial activity in cellular energy metabolism, especially in cell respiration. Taken together, the alterations in the protein profile suggest that the mitochondrion is likely the primary target of ASB.

Proteins involved in the stress response

HSC70 is a required chaperone-mediated protein folding cofactor that belongs to the heat shock protein (HSP) 70 family. Unlike its cognate protein HSP70, which is induced only under stress, HSC70 is constitutively expressed and is involved in other housekeeping functions, including cell cycle regulation and the stress response. Depletion of the HSC70 pool has been linked to a block in the activation of caspases that inhibit apoptosis signaling[31, 32]. Attenuated HSC70 expression was also observed in ochratoxin A-induced cell death associated with ROS generation[33]. Therefore, the decrease in HSC70 after ASB administration indicates that apoptosis signaling was activated in renal cells in response to oxidative stress. In addition, PRDX6, an antioxidant enzyme, was upregulated by ASB. PRDX6 belongs to the peroxiredoxin family, and its overexpression in mice or transfected cells reduces cellular H_2O_2 levels and decreases oxidative stress-induced apoptosis[34]. The regulation of stress-responsive proteins suggests a correlation between oxidative stress and the renal toxicity of ASB that occurs via cell apoptosis. This proposal is supported by the alterations in the biochemical index, including an increase in the MDA content and a decrease in SOD activity, which suggest that a redox imbalance occurs in the mouse kidney after ASB treatment.

Upregulation of PRDX6 by superoxide

Although PRDX6 is frequently reported to increase *in vitro* in

response to cytotoxic substrates, such as glucose and H_2O_2, most efforts have failed to detect a corresponding increase *in vivo*[35, 36]. Several mechanisms for the *in vivo* upregulation of PRDX6 have been described, including the high level of superoxide caused by a lack of NO to scavenge superoxide in the nNOS-knockout mouse[30], the excessive ROS generated by complex I due to increased glutathione oxidation after ischemia-reperfusion[37], and the high level of endogenous ROS resulting from the markedly reduced GSH level in a CFTR-defective mouse lung[38]. Complex I is the major source of superoxide[23]. Furthermore, superoxide production by complex I increases in response to oxidation of the mitochondrial GSH pool[39]. From these previous studies, it has been suggested that PRDX6, which likely belongs to a core cellular antioxidative defense, is upregulated by superoxide generated by complex I. However, not all ROS inducers increase the *in vivo* expression of PRDX6. Paraquat fails to upregulate PRDX6 in the mouse lung[38]. A similar result was observed in the rat kidney after ip injection of chloroform[40]. To our knowledge, this is report of a reagent that can upregulate PRDX6 in the kidney *in vivo*.

In summary, we have identified changes in six renal mouse proteins after exposure to ASB, all of which were related to cellular energetics or the oxidative stress response. The modification of MUT and NDUFA10 is related to the dysfunction of the mitochondrial respiratory chain, and the regulation of NDK B and PRDX6 is associated with abnormal superoxide generation. Our results suggest that oxidative stress in response to superoxide production in the mitochondria plays an important role in the renal toxicity induced by ASB treatment. The proteomics data in this study provide new insights into the biochemical pathways involved in ASB nephrotoxicity, which will aid in the future reduction of ADRs to LBZ in clinical applications.

Acknowledgements

This work was supported by the Science Foundation of Zhejiang Provincial Education Administration Y201016256. We thank Dr Yue-zhi TAO and the members of his laboratory at Zhejiang Academy of Agricultural Sciences for their full support. We also thank Dr Jin-mei ZHOU for critically reading the manuscript.

Author contribution

Hong LU, Xin-yue ZHANG, and Li-ying ZHU designed the experiments; Hong LU, Xin-yue ZHANG, and Yan-quan ZHOU performed the experiments; Li-ying ZHU and Hong LU performed data analysis and prepared the manuscript; Xin WEN revised the manuscript.

References

1 Xu C, Chou GX, Wang ZT. A new diterpene from the leaves of *Andrographis paniculata* Nees. Fitoterapia 2010; 81: 610–3.
2 Rao YK, Vimalamma G, Rao CV, Tzeng YM. Flavonoids and andrographolides from *Andrographis paniculata*. Phytochemistry 2004; 65: 2317–21.
3 Chao WW, Lin BF. Isolation and identification of bioactive compounds in *Andrographis paniculata* (Chuanxinlian). Chin Med 2010; 5: 17.
4 Feng H, Ma Q, Yu L, Meng YJ. The clinical applications and adverse reaction of Lianbizhi-injection. China Medical Herald 2008; 5: 97.
5 State Food and Drug Administration [homepage on the Internet]. Beijing: The Administration; c2000–2005 [updated 2005 Apr 12; cited 2010 Nov 30]. Adverse Drug Reaction Information Bulletin vol 8; [about 1 screen]. Available from: http://www.sda.gov.cn/WS01/CL0078/11280.html.
6 Cai WP, Zhou HX, Zhu YQ, Yan F, Huang HH. The report of 10 cases of Lianbizhi-induced acute interstitial nephritis. Journal of Qiqihar Medical College 2002; 23: 297.
7 Zhao JW, Ni ZH, Cao LO, Mou S, Fang W, Zhang QY. Analysis of clinical and pathological of Lianbizhi injection-induced acute renal failure. Chinese Journal of Integrated Traditional and Western Nephrology 2005; 9: 529–31.
8 Wang HM, Du WM, Wang XY, Xu JL, Wang TC, Jin HL. Analysis of adverse reaction/event report in 70 cases of Lianbizhi-injection. Chin J Clin Pharm 2007; 16: 252–4.
9 Hu ZH, Wu CQ, Wang QJ, Wang QX, Luo YW, Yang BH, *et al*. Toxic effects of two kinds of Lianbizhi injections on rats. Adverse Drug Reactions Journal 2010; 12: 10–6.
10 Lu H, Zhang XY, Zhou YQ, Jin SS. Toxic actions of andrographolide sodium bisulfite on kidney of mice and rabbits. Chin J Pharmacol Toxicol 2010; 24: 1–5.
11 Merrick BA, Witzmann FA. The role of toxicoproteomics in assessing organ specific toxicity. EXS 2009; 99: 367–400.
12 Thongboonkerd V, Chutipongtanate S, Kanlaya R, Songtawee N, Sinchaikul S, Parichatikanond P, *et al*. Proteomic identification of alterations in metabolic enzymes and signaling proteins in hypokalemic nephropathy. Proteomics 2006; 6: 2273–85.
13 Nath KA, Norby SM. Reactive oxygen species and acute renal failure. Am J Med 2000; 109: 665–78.
14 Ofman R, Speijer D, Leen R, Wanders Ronald JA. Proteomic analysis of mouse kidney peroxisomes: identification of RP2p as a peroxisomal nudix hydrolase with acyl-CoA diphosphatase activity. Biochem J 2006; 393: 537–43.
15 Pagliarini D, Calvo S, Chang B, Sheth S, Vafai S, Ong S, *et al*. A mitochondrial protein compendium elucidates complex I disease biology. Cell 2008; 134: 112–23.
16 Gasmi L, McLennan AG. The mouse Nudt7 gene encodes a peroxisomal nudix hydrolase specific for coenzyme A and its derivatives. Biochem J 2001; 357: 33–8.
17 Fenton WA, Gravel RA, Rosenblatt DS. Disorders of propionate and methylmalonate metabolism. In: Scriver CR, Beaudet AL, Sly WS, Valle D, Childs B, Kinzler KW, *et al*, editors. The metabolic and molecular bases of inherited disease. New York: McGraw-Hill; 2001. p 2165–92.
18 Chandler RJ, Sloan J, Fu H, Tsai M, Stabler S, Allen R, *et al*. Metabolic phenotype of methylmalonic acidemia in mice and humans: the role of skeletal muscle. BMC Med Genet 2007; 8: 64.
19 Chandler RJ, Zerfas PM, Shanske S, Sloan J, Hoffmann V, DiMauro S, *et al*. Mitochondrial dysfunction in mut methylmalonic acidemia. FASEB J 2009; 23: 1252–61.
20 Carroll J, Fearnley IM, Shannon RJ, Hirst J, Walker JE. Analysis of the subunit composition of complex I from bovine heart mitochondria. Mol Cell Proteomics 2003; 2: 117–26.
21 Muñoz J, Fernández-Irigoyen J, Santamaría E, Parbel A, Obeso J, Corrales FJ. Mass spectrometric characterization of mitochondrial complex I NDUFA10 variants. Proteomics 2008; 8: 1898–908.
22 Schulenberg B. Analysis of steady-state protein phosphorylation in

mitochondria using a novel fluorescent phosphosensor dye. J Biol Chem 2003; 278: 27251–5.
23 Cadenas E, Davies KJ. Mitochondrial free radical generation, oxidative stress, and aging. Free Radic Biol Med 2000; 29: 222–30.
24 Schilling B, Aggeler R, Schulenberg B, Murray J, Row R, Capaldi R, *et al*. Mass spectrometric identification of a novel phosphorylation site in subunit NDUFA10 of bovine mitochondrial complex I. FEBS Lett 2005; 579: 2485–90.
25 Mehta A, Orchard S. Nucleoside diphosphate kinase (NDPK, NM23, AWD): recent regulatory advances in endocytosis, metastasis, psoriasis, insulin release, fetal erythroid lineage and heart failure; translational medicine exemplified. Mol Cell Biochem 2009; 329: 3–15.
26 Song EJ, Kim YS, Chung JY, Kim E, Chae SK, Lee KJ. Oxidative modification of nucleoside diphosphate kinase and its identification by matrix-assisted laser desorption/ionization time-of-flight mass spectrometry. Biochemistry 2000; 39: 10090–7.
27 Lee E, Jeong J, Kim SE, Song EJ, Kang SW, Lee KJ, *et al*. Multiple functions of nm23-h1 are regulated by oxido-reduction system. PLoS ONE 2009; 4: e7949.
28 Lombardi D, Lacombe ML, Paggi MG. nm23: unraveling its biological function in cell differentiation. J Cell Physiol 2000; 182: 144–9.
29 Arnaud-Dabernat S, Masse K, Smani M, Peuchant E, Landry M, Bourbon PM, *et al*. Nm23-M2/NDP kinase B induces endogenous c-myc and nm23-M1/NDP kinase A overexpression in BAF3 cells. Both NDP kinases protect the cells from oxidative stress–induced death. Exp Cell Res 2004; 301: 293–304.
30 Da Silva-Azevedo L, Jähne S, Hoffmann C, Stalder D, Heller M, Pries AR, *et al*. Up-regulation of the peroxiredoxin-6 related metabolism of reactive oxygen species in skeletal muscle of mice lacking neuronal nitric oxide synthase. J Physiol 2009; 587: 655–68.
31 McLaughlin B, Hartnett KA, Erhardt JA, Legos JJ, White RF, Barone FC, *et al*. Caspase 3 activation is essential for neuroprotection in preconditioning. Proc Natl Acad Sci U S A 2003; 100: 715–20.
32 Brown JE, Zeiger SLH, Hettinger JC, Brooks JD, Holt B, Morrow JD, *et al*. Essential role of the redox-sensitive kinase p66shc in determining energetic and oxidative status and cell fate in neuronal preconditioning. J Neurosci 2010; 30: 5242–52.
33 Yoon S, Cong WT, Bang Y, Lee SN, Yoon CS, Kwack SJ, *et al*. Proteome response to ochratoxin A-induced apoptotic cell death in mouse hippocampal HT22 cells. Neurotoxicology 2009; 30: 666–76.
34 Walsh B, Pearl A, Suchy S, Tartaglio J, Visco K, Phelan SA. Overexpression of Prdx6 and resistance to peroxide-induced death in Hepa1–6 cells: Prdx suppression increases apoptosis. Redox Rep 2009; 14: 275–84.
35 Morrison J. Effect of high glucose on gene expression in mesangial cells: upregulation of the thiol pathway is an adaptational response. Physiol Genomics 2004; 17: 271–82.
36 Lee CK, Kim HJ, Lee YR, So HH, Park HJ, Won KJ, *et al*. Analysis of peroxiredoxin decreasing oxidative stress in hypertensive aortic smooth muscle. Biochim Biophys Acta 2007; 1774: 848–55.
37 Eismann T, Huber N, Shin T, Kuboki S, Galloway E, Wyder M, *et al*. Peroxiredoxin-6 protects against mitochondrial dysfunction and liver injury during ischemia-reperfusion in mice. Am J Physiol Gastrointest Liver Physiol 2009; 296: G266–74.
38 Trudel S, Kelly M, Fritsch J, Nguyen-Khoa T, Thérond P, Couturier M, *et al*. Peroxiredoxin 6 fails to limit phospholipid peroxidation in lung from cftr-knockout mice subjected to oxidative challenge. PLoS ONE 2009; 4: e6075.
39 Taylor ER, Hurrell F, Shannon RJ, Lin TK, Hirst J, Murphy MP. Reversible glutathionylation of complex I increases mitochondrial superoxide formation. J Biol Chem 2003; 278: 19603–10.
40 Fujii T, Fujii J, Taniguchi N. Augmented expression of peroxiredoxin VI in rat lung and kidney after birth implies an antioxidative role. Eur J Biochem 2001; 268: 218–25.

Acta Pharmacologica Sinica (2011) 32: 895–903
 1671-4083/11 $32.00
www.nature.com/aps

Original Article

Multiple signaling pathways involved in stimulation of osteoblast differentiation by *N*-methyl-*D*-aspartate receptors activation *in vitro*

Jie-li LI[1], Lin ZHAO[1], Bin CUI[1], Lian-fu DENG[3], Guang NING[1, 2], Jian-min LIU[1, *]

[1]*Department of Endocrine and Metabolic Diseases, Shanghai Institute of Endocrine and Metabolic Diseases, Shanghai Clinical Center for Endocrine and Metabolic Diseases, Ruijin Hospital, Shanghai Jiaotong University School of Medicine, Shanghai 200025, China;* [2]*Laboratory of Endocrine & Metabolic Diseases, Institute of Health Science, Shanghai Institutes for Biological Sciences, Chinese Academy of Sciences, Shanghai 200025, China;* [3]*Shanghai Institute of Traumatology and Orthopaedics, Department of Orthopaedics, Ruijin Hospital, Shanghai Jiaotong University School of Medicine, Shanghai 200025, China*

Aim: Glutamate receptors are expressed in osteoblastic cells. The present study was undertaken to investigate the mechanisms underlying the stimulation of osteoblast differentiation by *N*-methyl-*D*-aspartate (NMDA) receptor activation *in vitro*.
Methods: Primary culture of osteoblasts was prepared from SD rats. Microarray was used to detect the changes of gene expression. The effect of NMDA receptor agonist or antagonist on individual gene was examined using RT-PCR. The activity of alkaloid phosphotase (ALP) was assessed using a commercial ALP staining kit.
Results: Microarray analyses revealed that 10 genes were up-regulated by NMDA (0.5 mmol/L) and down-regulated by MK801 (100 μmol/L), while 13 genes down-regulated by NMDA (0.5 mmol/L) and up-regulated by MK801 (100 μmol/L). Pretreatment of osteoblasts with the specific PKC inhibitor Calphostin C (0.05 μmol/L), the PKA inhibitor H-89 (20 nmol/L), or the PI3K inhibitor wortmannin (100 nmol/L) blocked the ALP activity increase caused by NMDA (0.5 mmol/L). Furthermore, NMDA (0.5 mmol/L) rapidly increased PI3K phosphorylation, which could be blocked by pretreatment of wortmannin (100 nmol/L).
Conclusion: The results suggest that activation of NMDA receptors stimulates osteoblasts differentiation through PKA, PKC, and PI3K signaling pathways, which is a new role for glutamate in regulating bone remodeling.

Keywords: bone; osteoblast; glutamate receptor; NMDA receptor; PKA; PKC; PI3K

Acta Pharmacologica Sinica (2011) 32: 895–903; doi: 10.1038/aps.2011.38; published online 20 Jun 2011

Introduction

L-Glutamate (Glu) is accepted as an excitatory amino acid neurotransmitter in the mammalian central nervous system (CNS). Extracellular levels of glutamate are determined by the glutamate transporter[1, 2]. The diverse actions of *L*-glutamate in the CNS result from the existence of multiple glutamate receptors (GluR). These have been divided into two classes, metabotropic (mGluR) and ionotropic (iGluR), according to their molecular heterologies and differing intracellular signal transduction mechanisms. The iGluRs are further classified into *N*-methyl-*D*-aspartate (NMDA), *DL*-α-amino-3-hydroxy-5-methylisoxasole-4-propionate (AMPA), and kainite(KA) receptors. NMDA receptors are glutamate-gated ion channels characterized by a very high Ca^{2+} conductance[3].

* To whom correspondence should be addressed.
E-mail liujianmin09@yahoo.com.cn
Received 2010-11-09 Accepted 2011-03-31

In mammalian bone, NMDA receptors are expressed in osteoblasts and osteoclasts as revealed by RT-PCR, *in situ* hybridization, immunohistochemistry, and electrophy-siology[4, 5]. Bone cells and neurons possess similar, and in some cases identical glutamate signaling machinery and receptors[5].

Bone loss is associated with a reduction in nerve endings that immunostain for glutamate. Glutamate-containing neuronal endings have been described in a dense and intimate network in bone tissue[6]. Chenu *et al* reported that bone loss was induced in ovarectomized (OVX) rats with a reduction in neuronal density and concluded there was a functional link between the nervous system and bone loss after ovariectomy[7]. Hinoi *et al* reported that administration of glutamate significantly prevented the decreased bone mineral density in both the femur and the tibia in ovariectomized mice *in vivo*[8]. All these findings suggest that the neurotransmitter glutamate may play a role in bone remodeling.

NMDA has been shown to promote the proliferation and

differentiation of hippocampal neural progenitor cells (NPCs) *in vitro* by activating NMDA receptors[9]. NMDA is mitogenic for MC3T3-E1 osteoblastic cells and glutamate has been reported to promote the viability of primary human osteoblasts *in vitro*[10]. Blockade of NMDA receptors in rat primary osteoblasts inhibits expression of markers of bone formation *in vitro*[4, 11]. Previously, we demonstrated that activation of NMDA receptors promoted rat primary osteoblast differentiation and that one of the possible mechanism was ERK1/2 activation[12].

In the central nervous system (CNS), activation of the Ca^{2+}-permeable NMDA receptors results in an increase in Ca^{2+} influx. The Ca^{2+} signals then activate several Ca^{2+}-dependent kinases[13]. Kinases which have been suggested to be important include protein kinases C and A (PKC and PKA), and PI3 kinase (PI3K). PKC is localized at excitatory synapses containing NMDA receptors and might be involved in NMDA-evoked ERK1/2 phosphorylation[14]. In hippocampal neurons NMDA played a neuroprotective role through the PKA signaling pathway[15], and in striatal and cortical neurons, PI3K is critically involved in NMDA receptor activation[16–18]. Thus, the above signaling pathways may positively respond to signals from ionotropic types of glutamate receptors in the CNS.

Locally elevated extracellular Ca^{2+} levels have been suggested to play a role in regulating bone remodeling. Signaling pathways such as phospholipase C (PLC), PKC, mitogen-activated protein kinase (MAPK), and PI3K have been implicated in the modification of cellular function by Ca^{2+}[19, 20]. Since these signaling pathways are involved in NMDA receptor regulation in the CNS and were also suggested to be important by our initial microarray analysis, we hypothesized that they are also involved in NMDA-induced bone remodeling. The aim of this study was to investigate the mechanism of the effects of NMDA and MK801 (the noncompetitive antagonist of NMDA receptors) on differentiation of rat primary osteoblasts.

Materials and methods

Primary cultures of osteoblasts

Osteoblasts were prepared from calvaria of 1-day-old Sprague-Dawley rats by a sequential enzymatic digestion method as described previously[21]. The bones were cut into chips and washed with calcium- and magnesium-free phosphate-buffered saline (PBS). Calvaria were incubated at 37 °C for 20 min with 0.25% trypsin and 1 h with 0.1% type II collagenase in PBS with gentle mixing. Incubation with type II collagenase was then repeated. Cells released from the bone chips were collected in α-modified minimum essential medium (α-MEM) containing 10% fetal bovine serum (FBS), 100 units/mL penicillin (Gibco) and 100 μg/mL streptomycin (Gibco), followed by centrifugation at 1000 revolutions per minute for 10 min. The resulting pellets were re-suspended in α-MEM containing 10% FBS. Cells were plated at appropriate density, and cultured at 37 °C under 5% CO_2. Culture medium was changed every 2 d.

Rat osteoblasts ($1.5\times10^5/cm^2$) were plated in 6-well plates in α-MEM containing 10% FBS, 100 units/mL penicillin, 100 μg/mL streptomycin, 50 μg/mL ascorbic acid (Sigma) and 5 mmol/L sodium β-glycerophosphate (Sigma) for measurement of differentiation markers. After 4 d of culture, cells were starved with serum-free α-MEM and 0.2% bovine serum albumin (BSA) for 12 h. Cultures were also exposed to fresh serum-free medium with 0.2% BSA with or without NMDA, MK801 (both from Tocris Cookson Ltd UK), or other inhibitors.

RNA, cDNA preparation, and quantitative real-time PCR

To ensure statistical significance of microarray analyses, cultures of osteoblasts were incubated in osteogenic medium with 0.2% BSA containing NMDA or MK801 for 48 h. Total RNA was isolated from primary rat calvarial cells with TRIzol reagent (Invitrogen). RNA (1 μg) was reverse transcribed to cDNA with the Invitrogen Superscript Kit. Corresponding probes were hybridized to Illumina GeneChip arrays and subjected to bioinformatics analyses. cDNA was amplified with the Takara SYBR Green RT-PCR kit using gene-specific primers (Table 1) in the Real-Time PCR Detection System (Roche). Quantification and normalization to GAPDH amplicons was performed. Statistical analyses were performed with Prism 5.0 (GraphPad Software, San Diego, CA).

As might be expected, many genes that have previously been demonstrated to be NMDA or MK801-regulated can be found in our lists of genes as commonly regulated in the treatment regimens (Table 2 or 3). This implies that the microarray results and analyses are reliable. To validate this further, we used quantitative real time RT-PCR to examine the effect of NMDA or MK801 on individual genes. We examined the following ten genes (*Nov, Stc1, Anxa1, Tspan8, Dab2, Nfkb2, Mmp12, Fmo1, Colec12, and Fap*) which were commonly up-regulated by NMDA and down-regulated by MK801 as shown in Table 2. We also examined thirteen genes (*Cib1, Ddit3, Gaa, Herpud1, Ninj1, Trappc2, Rpo1-2, Slc20a1, Slc3a2, Trib3, Yars, Serpinb2, and Thop1*) which were commonly down-regulated by NMDA and up-regulated by MK801 as shown in Table 3.

Gene ontology analysis

http://omicslab.genetics.ac.cn/GOEAST/php/illumina.php was applied to GO analysis. We chose only GO categories that had a *P*-value of <0.001 and a log odds-ratio of >1.5-fold.

Alkaline phosphatase synthesis

Rat calvarial osteoblasts were plated at a density of 1.5×10^5/well into 6-well culture plates. After treatments, cells were washed three times with ice-cold PBS, scraped into 0.5 mL of ice-cold 0.5% Triton X-100 solution and lysed by ultrasonication in an ice bath for 2 min. The supernatant was centrifuged at 14 000×*g* and 4 °C for 5 min, then stored frozen at -20 °C until measurement of alkaline phosphatase levels. For the determination of these levels, cell lysates were incubated in a 96-well plate with 100 μL of 0.1 mol/L $NaHCO_3$-Na_2CO_3 buffer (pH 10.0) containing 0.5% Triton X-100, with *p*-nitrophenylphosphate as substrate for 30 min at 37 °C. The absorbance

Table 1. Primer sequences used for PCRs.

Gene	Primer sequence (Forward/Reverse)	Product length (bp)	Reference
Cib1	AGTCGCCTGTCTAAGGAGCT (Forward) ATCTCCTGCTTGGTCAGGAA (Reverse)	85	NM_031145.1
Ddit3	AGGTCCTGTCCTCAGATGAAA (Forward) TAGGGATGCAGGGTCAAGAGT (Reverse)	116	NM_024134.2
Gaa	TACCGACCTCACCATCAGGAA (Forward) CTCCTGGGTGATGCCTTTGT (Reverse)	166	NM_199118.1
Herpud1	AAAAGCCAGAAGCCAGCACAA (Forward) TTGAGGAATCCCCAGGATACT (Reverse)	107	NM_053523.1
Ninj1	TCGTGGTGCTCATCTCCATCT (Forward) ATGAAAACCAGCCCCGTG (Reverse)	145	NM_012867.1
Nfkb2	ATCTGGGTGTCCTGCATGTAA (Forward) CCGTACAATGCTCAAATCCA (Reverse)	177	NM_001008349.1
Rpo1-2	ACCATCTGCAAAGAGCTCAA (Forward) TGATGGGAACATGCCAAGAA (Reverse)	166	NM_031773.1
Slc20a1	GGCAACTAGTGGCTTCGTTTT (Forward) AGACGAACCAAGACATCACAA (Reverse)	165	NM_031148.1
Slc3a2	AGAGATGGTGGCACAAGGG (Forward) TCTGGTTCTTGTGAATTGGG (Reverse)	174	NM_019283.1
Trib3	TTTTCCGACAGATGGCTAGTG (Forward) TTGTCCCACAGAGAGTCGTCT (Reverse)	189	NM_144755.2
Yars	CGTGGCCTACTTTGTACCCAT (Forward) TGCATGAAGGTCTGCAAACA (Reverse)	96	NM_001025696.1
Serpinb2	CACTCCAGGAAACCCAGAGAA (Forward) TTTGTCTCTTGCTTGTGCCT (Reverse)	129	NM_021696.1
Thop1	GGCTGACAAGAAGCTCTCAGA (Forward) TCTTTCGGGATTTTCTCCTG (Reverse)	110	NM_172075.2
Nov	TTCCTGCTCCTCCATCTCTTA (Forward) TCGGTGATATACTGGGGCA (Reverse)	115	NM_030868.2
Stc1	TGCTAAATTTGACACTCAGGG (Forward) AATGGCAAGGAAGACCTTGGA (Reverse)	106	NM_031123.2
Anxa1	ATGTTGCTGCCTTGCACAAA (Forward) TGAGCATTGGTTCTCTTGGT (Reverse)	97	NM_012904.1
Tspan8	TGGGTTTCCTGGGATGCT (Forward) ATACCTGCGGCTACTTGCAGA (Reverse)	126	NM_133526.1
Dab2	TTTGGTTATGTGTGTGGAGGA (Forward) TTCAGCCTGTTGCCCTGTTT (Reverse)	88	NM_024159.1
Mmp12	ATGAAGCGTGCGGATGTAGA (Forward) CTCCATGATCTCCAAATGCAA (Reverse)	147	NM_053963.1
Fmo1	ATGCAACCCAGTTCAACCTT (Forward) ATTGTCCAGAGACAGCGAAA (Reverse)	118	NM_012792.1
Trappc2	TGTAATTGTTGGCCACCATGA (Forward) TGACGGTGATCATCTTTGGA (Reverse)	113	NM_001024965.1
Colec12	CAGGTCCCTCAGGAGCAAT (Forward) CAAAAATTTCTTTCTCCACCG (Reverse)	159	NM_001025721.1
Fap	TTGAAGGTTACCCTGGAAGAA (Forward) TGGCTTTGTAGCTGAAACTTG (Reverse)	157	NM_138850.1
GAPDH	CTCAACTACATGGTCTACATGT (Forward) CTTCCCATTCTCAGCCTTGACT (Reverse)	132	NM_017008.3

of *p*-nitrophenol liberated in the reactive solution was read at 405 nm. Diluted cell lysates were measured at 740 nm for total protein content using the BCA method (Bio-Rad Protein Assay kit, Bio-Rad Laboratories, Richmond, CA, USA). ALP activity in the cells was normalized for total protein content of the cell lysate.

Western blotting

Cells treated with 0.5 mmol/L NMDA and wortmannin (100 nmol/L) (Cell Signaling, USA) for the indicated times were lysed and the protein concentrations were determined by Bio-Rad Protein Assay (Bio-Rad Laboratories, Richmond, CA). For Western blotting, 50 mg of total cell lysates was subjected

Table 2. The common genes up-regulated by NMDA and down-regulated by MK801 based on GO analysis.

Name	Symbol	Accession
Nephroblastoma overexpressed gene (Nov)	Nov	NM_030868.2
Stanniocalcin 1 (Stc1)	Stc1	NM_031123.2
Annexin A1 (Anxa1)	Anxa1	NM_012904.1
Tetraspanin 8 (Tspan8)	Tspan8	NM_133526.1
Disabled homolog 2 (*Drosophila*) (Dab2)	Dab2	NM_024159.1
Nuclear factor of kappa light polypeptide gene enhancer in B-cells 2, p49/p100	Nfkb2	NM_001008349.1
Matrix metallopeptidase 12 (Mmp12)	Mmp12	NM_053963.1
Flavin containing monooxygenase 1 (Fmo1)	Fmo1	NM_012792.1
Collectin sub-family member 12 (Colec12)	Colec12	NM_001025721.1
Fibroblast activation protein (Fap)	Fap	NM_138850.1

Table 3. The common genes down-regulated by NMDA and up-regulated by MK801 based on GO analysis.

Name	Symbol	Accession
Calcium and integrin binding 1 (calmyrin)	Cib1	NM_031145.1
DNA-damage inducible transcript 3	Ddit3	NM_024134.1
Glucosidase, alpha, acid	Gaa	NM_199118.1
Homocysteine-inducible, endoplasmic reticulum stress-inducible, ubiquitin-like domain member 1	Herpud1	NM_053523.1
Ninjurin 1	Ninj1	NM_012867.1
Similar to RIKEN cDNA 0610009B22 (RGD1306925)	Trappc2	NM_001024965.1
RNA polymerase 1-2	Rpo1-2	NM_031773.1
Solute carrier family 20 (phosphate transporter), member 1	Slc20a1	NM_031148.1
Solute carrier family 3 (activators of dibasic and neutral amino acid transport), member 2	Slc3a2	NM_019283.1
Tribbles homolog 3 (Drosophila)	Trib3	NM_144755.1
Tyrosyl-tRNA synthetase	Yars	NM_001025696.1
Serine (or cysteine) proteinase inhibitor, clade B, member 2	Serpinb2	NM_021696.1
Thimet oligopeptidase 1	Thop1	NM_172075.1

to SDS-polyacrylamide gel electrophoresis. The protein was transferred to polyvinylidene difluoride membranes using transfer buffer (50 mmol/L Tris, 190 mmol/L glycin, and 10% methanol) at 120 V for 2 h. The membranes were incubated with blocking buffer (50 mmol/L Tris, 200 mmol/L NaCl, 0.2% Tween 20, and 3% bovine serum albumin) overnight at 4 °C. After washing three times with washing buffer (blocking buffer without 3% bovine serum albumin) for 10 min each, the blot was incubated with primary antibody (PI3K, phosphorylated PI3K) for 12 h, followed by horseradish peroxidaselabeled secondary antibody for 1 h. The membranes were washed again, and detection was performed using an ECL kit (ECL Plus Western Blotting Detection System, GE Healthcare UK Limited, Little Chalfont, UK) and exposed to film.

Statistical analysis

Each experiment was performed with at least three independent samples. The results are expressed as the mean±SD, unless otherwise indicated. Statistical significance of the observed differences was analyzed by one-way ANOVA where appropriate. A P value <0.05 was considered statistically significant.

Results

cDNA microarray and gene ontology analysis

Genes whose expression was changed in opposite directions by NMDA and MK801 treatment were defined as being commonly up-regulated or down-regulated genes. According to the ratio values, 353 genes were up-regulated by NMDA, 106 genes down-regulated by MK801 and hence 83 genes were the commonly up-regulated genes. There were 50 genes down-regulated by NMDA, 297 genes up-regulated by MK801 and 27 were the commonly down-regulated genes (Figure 1). We then examined the significant GO categories and genes by http://omicslab.genetics.ac.cn/GOEAST/php/illumina.php. A P-value of <0.001 and a log odds-ratio >1.5-fold were selected as the significant criteria. This narrowed the numbers of genes to 10 in the group of common genes that were up-regulated by NMDA and down-regulated by MK801 (Table 2), and 13 in the group of common genes down-regulated by NMDA and up-regulated by MK801 (Figure 2, Table 3).

Effects of inhibiting PKC, PKA, and PI3K on indexes of osteoblast differentiation

From the results of the microarray analysis as well as some previously published work in other cell types, we noted several genes (*Anxa1, Mmp12, Stc1, Trib3, NF-κB, Ddit3*) involved in PKC, PKA, and PI3K signaling pathways (see discussion). To determine the involvement of PKC in NMDA-mediated osteoblast differentiation, serum-starved cells were pretreated with Calphostin C (0.05 μmol/L), a specific inhibitor of PKC, for 90 min followed by coincubation with 0.5 mmol/L NMDA for 48 h. Cell morphology was assessed using a commercial ALP staining kit. Basal levels of ALP activity were unaffected by treatment of osteoblastic cells with Calphostin C alone. However, this treatment did lead to an observable reduction in alkaline phosphatase levels (Figure 3).

To determine whether activation of PKA is involved in NMDA-induced osteoblast differentiation, cells were pretreated with the PKA inhibitor H-89 (20 nmol/L). After incubation in serum-free medium for 12 h, cells were pretreated with 20 nmol/L H-89 for 90 min, followed by coincubation with 0.5 mmol/L NMDA for 48 h. Inhibition of PKA by H-89 treatment led to a decrease in NMDA-stimulated ALP activity levels (Figure 3). The ability of this inhibitor to curtail the effects of NMDA on osteoblast differentiation suggests that PKA activation is involved in NMDA-induced osteoblast differentiation.

We further explored signal transduction components related

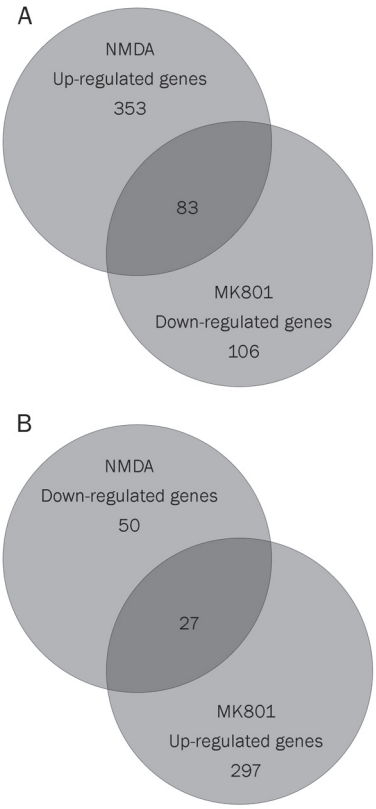

Figure 1. Number of genes changed by NMDA or MK801 treatment regimens. Genes identified by Illumina GeneChip microarray were changed with treatment by at least 1.5-fold compared to vehicle. The number of genes (both up- and down-regulated) common to both treatments is noted in the overlap of the Venn diagram.

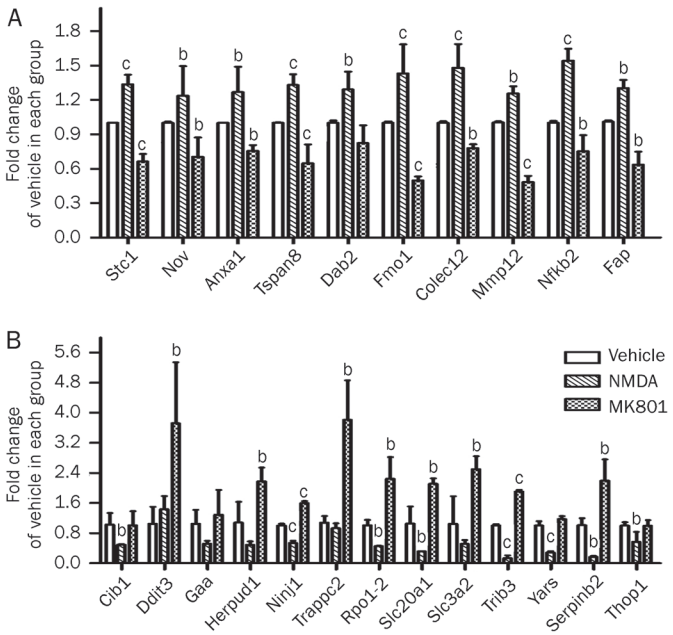

Figure 2. Verification of common genes according to GO analysis by real-time PCR. A: Genes up-regulated by NMDA and down-regulated by MK801; B: Genes down-regulated by NMDA and up-regulated by MK801. Primary calvarial osteoblasts were cultured in medium with 0.2% BSA containing 0.5 mmol/L NMDA or 100 μmol/L MK801 for 48 h. mRNAs were isolated after 48 h and subjected to quantitative real-time PCR with primers described in Table 1. Comparative threshold values represent the mean of three samples normalized to GAPDH levels. Values are relative to those obtained from the vehicle groups. $^{b}P<0.05$, $^{c}P<0.001$ by one-way ANOVA versus the vehicle groups.

to NMDA-induced osteoblast differentiation by examining the involvement of PI3K using the PI3K inhibitor wortmannin. Cells were pretreated with wortmannin (100 nmol/L) for 90 min, followed by coincubation with 0.5 mmol/L NMDA for 48 h. This treatment protocol also led to a decrease in NMDA-stimulated ALP activity levels (Figure 3). The ability of these three inhibitors to curtail the effects of NMDA on markers of osteoblast differentiation suggests that activation of PKC, PKA, and PI3K is involved in the phenomenon of NMDA-induced osteoblast differentiation.

To assess whether PI3K were activated by NMDA, we assessed phosphorylation of PI3K using phospho-antibodies against phosphorylated peptides derived from PI3K. We found that 0.5 mmol/L NMDA induced a rapid increase in PI3K phosphorylation with maximal levels at 15 min. Prolonged NMDA stimulation up to 30 min, however, resulted in a decrease of phosphorylated PI3K levels toward baseline (Figure 4A).

To determine whether activation of PI3K is involved in NMDA-induced osteoblast differentiation, cells were pretreated with the PI3K inhibitor wortmannin. After incubation in serum-free medium for 12 h, cells were pretreated with 100 nmol/L wortmannin for 90 min, followed by coincubation with 0.5 mmol/L NMDA for 15 min. Inhibition of PI3K by wortmannin treatment led to a decrease in NMDA-stimulated phosphorylated PI3K levels (Figure 4B). The ability of this inhibitor to curtail the effects of NMDA on osteoblast differentiation suggests that PI3K activation is involved in NMDA-induced osteoblast differentiation (Figure 5).

Discussion

Our data suggest that NMDA promotes osteoblast differentiation via PKA, PKC and PI3K signaling pathways. These findings also demonstrate that NMDA directly acts on and affects osteoblasts and that the NMDA receptors expressed in primary rat calvaria osteoblasts are functional.

Within the large family of iGluRs, NMDARs constitute a subfamily identifiable by a specific molecular composition and unique pharmacological and functional properties[22, 23]. The most commonly used agonist at the glutamate recognition site of NMDA receptors is NMDA itself. However, it is not a substrate that promotes glutamate uptake[24]. Activation of NMDA receptors has been shown to be important in normal expression of bone matrix proteins[4, 12]. We have previously demonstrated that NMDA increased osteoblast ALP activity and osteocalcin (OC) in a dose-dependent manner, while the NMDA receptor antagonist MK801 reduced these effects[12].

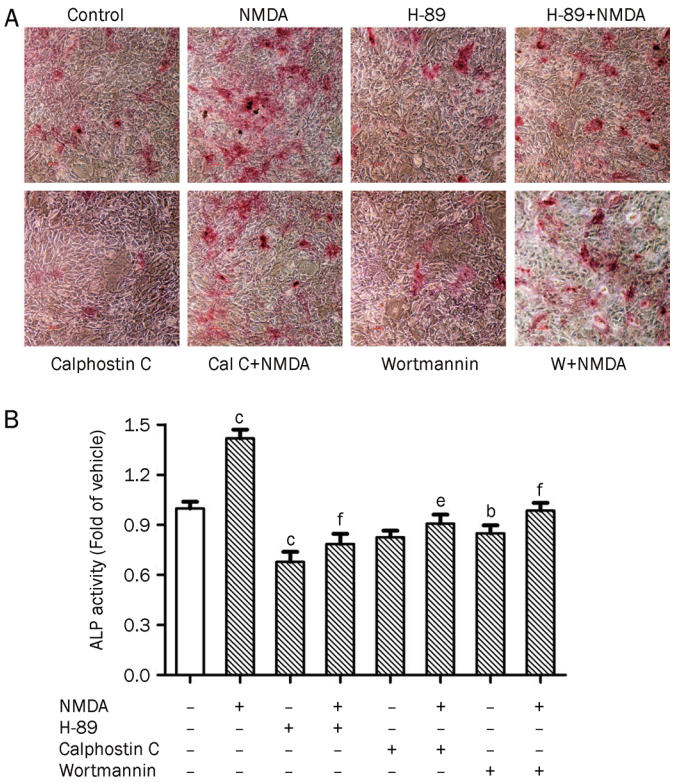

Figure 3. Effect of inhibitors of signal transduction on alkaline phosphatase levels. Cells were pretreated with vehicle or the PKA inhibitor H-89 (20 nmol/L), the PKC inhibitor Calphostin C (Cal C, 0.05 μmol/L), or the phosphatidylinositol 3-kinase (PI3K) inhibitor wortmannin (W, 100 nmol/L) for 90 min. Cells were then treated with 0.5 mmol/L NMDA for 48 h. A: ALP staining study; B: ALP activity study. Mean±SD (n=8). ^{b}P<0.05, ^{c}P<0.001 *vs* control; ^{e}P<0.05, ^{f}P<0.001 *vs* the group treated with NMDA only.

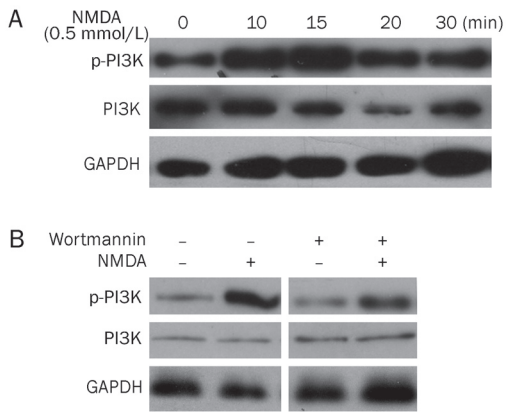

Figure 4. Effects of NMDA on PI3K activation in osteoblastic cells. Cell lysates were subjected to Western blot and incubated with PI3K or phosphorylated PI3K antibodies. (A) Cells are exposed to 0.5 mmol/L NMDA for 0, 10, 15, 20, and 30 min. PI3K was phosphorylated by NMDA and the peak reached at 15 min. (B) Cells incubated with wortmannin (100 nmol/L) for 90 min prior to treatment with 0.5 mmol/L NMDA, and then treated with or without NMDA for 15 min. The suppression of phosphorylated PI3K induced by NMDA was observed in the presence of wortmannin.

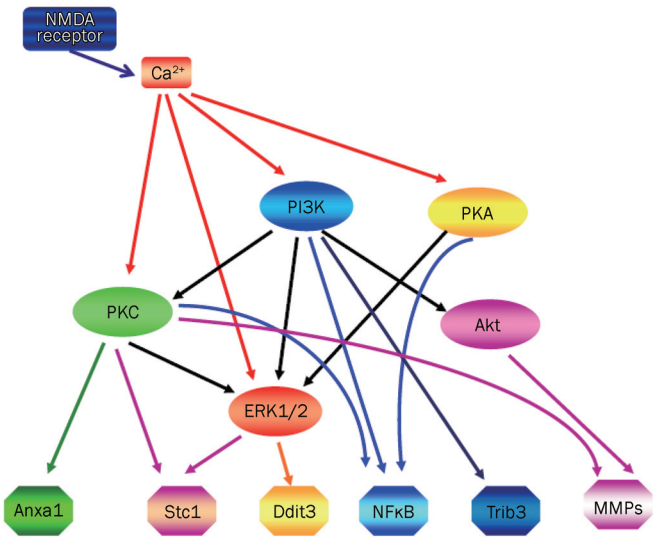

Figure 5. Schematic representations of signaling pathways from NMDA receptors to the multiple signaling system.

We have also observed that NMDA increases ALP activity and OC expression in a time-dependent manner and that the peak of this increase reached 48 h after treatment (data not shown). Together, these observations suggest that NMDA regulates osteoblast differentiation via NMDA receptors.

In the present study, we employed cDNA microarray analysis, which was expected to be more sensitive than cDNA subtraction analysis, for the detection of specific genes related to the stimulation of NMDA receptors in rat osteoblasts. Annexin 1 (Anxa1) is one member of a family of phospholipid and calcium-binding proteins of which 20 are known at present[25]. It translocates from the cytoplasm to the outer cell surface via a Ca^{2+}-dependent mechanism[26–28]. It is a substrate for protein kinase C and protein tyrosine kinases and has multiple phosphorylation sites as well as calcium and phospholipid binding properties[29]. Anxa1 was also shown to be activated as a consequence of sequential PI3K-PKC activation[30, 31]. Matrix metalloproteinases (MMPs) are a family of secreted or transmembrane zinc-dependent endopeptidases. The activation of MMP3, MMP12 and MMP13 was correlated with activation of the PI3K/Akt signaling cascade in microglial cells[32]. In epithelial cells and fibroblasts, MMP12 and MMP13 could be up-regulated in a PI3K, PKCδ and ERK1/2-dependent manner[33]. The stanniocalcins, comprising Stc1 and Stc2, are secreted homodimeric glycoprotein hormones with little homology to other proteins[34]. Stc1 was originally identified as a hormone secreted by the corpuscles of the stannius inteleost fish[35] and in fish appears to function primarily in the prevention of hypercalcaemia mediated via the ability of Stc1 to reduce calcium uptake by gills and inhibit intestinal calcium transport in the gut[36–38]. In human endothelial cells Stc1 mRNA expression was up-regulated primarily through PKC, ERK and Ca^{2+} signaling pathways[39]. Trib3 (tribbles 3) is a mammalian homologue of *Drosophila tribbles*[40–42]. Expression of Trib3 was found to be PI3K-dependent in prostate

cancer cells[43]. Furthermore, it has been suggested that the tribbles protein family is involved in regulation of the MAP kinase pathway[44]. Nuclear factor-κB (NF-κB) is a ubiquitous heterodimeric transcription factor that regulates inflammation and cell survival and differentiation[45, 46]. Many different kinases, including PKA, PKC, GSK-3β, PI3K, AKT, p38, NIK and even IKK, have been shown to induce phosphorylation of NF-κB directly or indirectly[45–47]. Regulation of NF-κB has also previously been suggested to depend on the PLCβ/PKC pathway[48, 49]. The PI3K/Akt signaling pathway seems able to positively regulate NF-κB activity[50, 51]. Studies have demonstrated that different stress response pathways mediating Ddit3 (DNA-damage inducible transcript 3) expression are regulated by protein kinases[52, 53]. Ddit3 is reported to be induced during serum starvation, glutamine deprivation, growth to confluency and upon exposure to tunicamycin, which promotes accumulation of proteins in the ER by preventing glycosylation[54]. Ddit3 protein was increased in pancreatic β-cells grown in high glucose that were exposed to U0126 to block ERK1/2 activity[55]. Our data showed Anxa1, MMP12, Stc1 and NF-κB were all up-regulated by NMDA in osteoblasts, while Trib3 and Ddit3 were down-regulated. In addition, it suggests that ERK, PKA, PKC and PI3K signaling pathways may be involved with changes of these genes' expression levels in NMDA-treated osteoblasts.

In the CNS, activation of NMDA receptors increases calcium influx, which is associated with spatial long term memory in the Morris water maze[56] through the PKA signaling pathway[56–58]. Repetitive stimulation of glutamatergic NMDA receptors result in PKA and PKC activation *in vivo*[59]. The high Ca^{2+} permeability of NMDA receptor channels in bone is a characteristic similar to that of receptors expressed in the CNS[5, 60]. Ca^{2+} flux could trigger a number of second messenger responses that could ultimately be responsible for the anabolic effects of NMDA stimulation in bone. The MAPK, PKC, PKA and PI3K signaling pathways can all be directly activated downstream of calcium influx[61]. The activation of protein kinase C (PKC) and/or protein kinase A (PKA) plays an essential role in osteoblast differentiation[62]. In our previous study, we have observed activation of the ERK1/2 signaling pathway when osteoblasts were treated with NMDA[12]. With this background information, we further pursued the results of our microarray analysis information and specifically studied the PKC, PKA and PI3K signaling pathways to see if these signaling pathways are involved in NMDA-mediated osteoblast activation, independent of ERK1/2. We found that cells staining for ALP were significantly decreased by treatment with the PKA inhibitor H-89 or the PKC inhibitor Calphostin C. However, the ALP staining cells recovered after treatment with NMDA, which suggests a mechanism for NMDA-induced osteoblast differentiation that is, at least partly, dependent on PKA and PKC signaling. NMDA increased PI3K phosphorylation which is kinetically correlated to concomitant ERK1/2 phosphorylation in rat striatal neurons[63]. It was reported that intracellular Ca^{2+}- regulated pathways signal through PI3K in osteoblasts subjected to mechanical strain[64]. The ability of the chemical inhibitor of PI3K, wortmannin, to significantly reduce NMDA-induced expression of the osteoblast differentiation marker ALP suggests that PI3K is involved in NMDA-mediated osteoblastic cell differentiation.

In summary, we have demonstrated that activation of NMDA receptors promotes osteoblast differentiation via PKA, PKC and PI3K signaling mechanisms which are independent of ERK1/2 signaling. The screening for specific genes carried out in this work allowed the discovery of signaling pathways which are associated with these genes. These findings yield new avenues by which to look for therapeutic targets in osteoporosis and provide useful direction for further investigation of the mechanisms involved.

Acknowledgments

This work is supported by the National Natural Science Foundation of China (No 30570881) and is supported partially by grants from the Division of Endocrinology and Metabolic Diseases, E-Institute of Shanghai Universities (E03007) and Shanghai Education Commission (No Y0204). We thank Genminix Informatics Ltd Co for assistance with the microarray analysis.

Author contribution

Dr Jie-li LI designed the project, performed the research and wrote the paper; Dr Lin ZHAO worked on the data for revision; Dr Bin CUI helped on detailed research work; Dr Lian-fu DENG and Dr Guang NING contributed overview advice; Dr Jian-min LIU provided fundings on all the work and designed the project.

References

1 Nakanishi N, Shneider NA, Axel R. A family of glutamate receptor genes: evidence for the formation of heteromultimeric receptors with distinct channel properties. Neuron 1990; 5: 569–81.
2 Yoneda Y, Kuramoto N, Kitayama T, Hinoi E. Consolidation of transient ionotropic glutamate signals through nuclear transcription factors in the brain. Prog Neurobiol 2001; 63: 697–719.
3 Wisden W, Seeburg PH. Mammalian ionotropic glutamate receptors. Curr Opin Neurobiol 1993; 3: 291–8.
4 Hinoi E, Fujimori S, Yoneda Y. Modulation of cellular differentiation by *N*-methyl-*D*-aspartate receptors in osteoblasts. FASEB J 2003; 17: 1532–4.
5 Gu Y, Genever PG, Skerry TM, Publicover SJ. The NMDA type glutamate receptors expressed by primary rat osteoblasts have the same electrophysiological characteristics as neuronal receptors. Calcif Tissue Int 2002; 70: 194–203.
6 Serre CM, Farlay D, Delmas PD, Chenu C. Evidence for a dense and intimate innervation of the bone tissue, including glutamate-containing fibers. Bone 1999; 25: 623–9.
7 Burt-Pichat B, Lafage-Proust MH, Duboeuf F, Laroche N, Itzstein C, Vico L, *et al*. Dramatic decrease of innervation density in bone after ovariectomy. Endocrinology 2005; 146: 503–10.
8 Hinoi E, Takarada T, Uno K, Inoue M, Murafuji Y, Yoneda Y. Glutamate suppresses osteoclastogenesis through the cystine/glutamate antiporter. Am J Pathol 2007; 170: 1277–90.
9 Joo JY, Kim BW, Lee JS, Park JY, Kim S, Yun YJ, *et al*. Activation of NMDA receptors increases proliferation and differentiation of hippocampal neural progenitor cells. J Cell Sci 2007; 120: 1358–70.

10 Fatokun AA, Stone TW, Smith RA. Hydrogen peroxide-induced oxidative stress in MC3T3-E1 cells: the effects of glutamate and protection by purines. Bone 2006; 39: 542–51.
11 Peet NM, Grabowski PS, Laketic-Ljubojevic I, Skerry TM. The glutamate receptor antagonist MK801 modulates bone resorption *in vitro* by a mechanism predominantly involving osteoclast differentiation. FASEB J 1999; 13: 2179–85.
12 Li JL, Cui B, Qi L, Li XY, Deng LF, Ning G, *et al*. NMDA enhances stretching-induced differentiation of osteoblasts through the ERK1/2 signaling pathway. Bone 2008; 43: 469–75.
13 Mabuchi T, Kitagawa K, Kuwabara K, Takasawa K, Ohtsuki T, Xia Z, *et al*. Phosphorylation of cAMP response element-binding protein in hippocampal neurons as a protective response after exposure to glutamate *in vitro* and ischemia *in vivo*. J Neurosci 2001; 21: 9204–13.
14 Wang JQ, Fibuch EF, Mao L. Regulation of mitogen-activated protein kinases by glutamate receptors. J Neurochem 2007; 100: 1–11.
15 Valera E, Sánchez-Martín FJ, Ferrer-Montiel AV, Messeguer A, Merino JM. NMDA-induced neuroprotection in hippocampal neurons is mediated through the protein kinase A and CREB (cAMP-response element-binding protein) pathway. Neurochem Int 2008; 53: 148–54.
16 Perkinton MS, Ip JK, Wood GL, Crossthwaite AJ, Williams RJ. Phosphatidylinositol 3-kinase is a central mediator of NMDA receptor signalling to MAP kinase (Erk1/2), Akt/PKB and CREB in striatal neurones. J Neurochem 2002; 80: 239–54.
17 Fuller G, Veitch K, Ho LK, Cruise L, Morris BJ. Activation of p44/p42 MAP kinase in striatal neurons via kainate receptors and PI3 kinase. Brain Res Mol Brain Res 2001; 89: 126–32.
18 Lafon-Cazal M, Perez V, Bockaert J, Marin P. Akt mediates the anti-apoptotic effect of NMDA but not that induced by potassium depolarization in cultured cerebellar granule cells. Eur J Neurosci 2002; 16: 575–83.
19 Brown EM, MacLeod RJ. Extracellular calcium sensing and extracellular calcium signaling. Physiol Rev 2001; 81: 239–97.
20 Huang Z, Cheng SL, Slatopolsky E. Sustained activation of the extracellular signal-regulated kinase pathway is required for extracellular calcium stimulation of human osteoblast proliferation. J Biol Chem 2001; 276: 21351–8.
21 Danciu TE, Adam RM, Naruse K, Freeman MR, Hauschka PV. Calcium regulates the PI3K-Akt pathway in stretched osteoblasts. FEBS Lett 2003; 536: 193–7.
22 Dingledine R, Borges K, Bowie D, Traynelis SF. The glutamate receptor ion channels. Pharmacol Rev 1999; 51: 7–61.
23 Cull-Candy SG, Leszkiewicz DN. Role of distinct NMDA receptor subtypes at central synapses. Sci STKE 2004: re16.
24 Kew JN, Kemp JA. Ionotropic and metabotropic glutamate receptor structure and pharmacology. Psychopharmacology (Berl) 2005; 179: 4–29.
25 Moss SE. Ion channels. Annexins taken to task. Nature 1995; 378: 446–7.
26 Philip JG, Flower RJ, Buckingham JC. Glucocorticoids modulate the cellular disposition of lipocortin 1 in the rat brain *in vivo* and *in vitro*. Neuroreport 1997; 8: 1871–6.
27 Taylor AD, Cowell AM, Flower J, Buckingham JC. Lipocortin 1 mediates an early inhibitory action of glucocorticoids on the secretion of ACTH by the rat anterior pituitary gland *in vitro*. Neuroendocrinology 1993; 58: 430–9.
28 Taylor AD, Christian HC, Morris JF, Flower RJ, Buckingham JC. An antisense oligodeoxynucleotide to lipocortin 1 reverses the inhibitory actions of dexamethasone on the release of adrenocorticotropin from rat pituitary tissue *in vitro*. Endocrinology 1997; 138: 2909–18.
29 Alldridge LC, Harris HJ, Plevin R, Hannon R, Bryant CE. The annexin protein lipocortin 1 regulates the MAPK/ERK pathway. J Biol Chem 1999; 274: 37620–8.
30 Solito E, Mulla A, Morris JF, Christian HC, Flower RJ, Buckingham JC. Dexamethasone induces rapid serine-phosphorylation and membrane translocation of annexin 1 in a human folliculostellate cell line via a novel nongenomic mechanism involving the glucocorticoid receptor, protein kinase C, phosphatidylinositol 3-kinase, and mitogen-activated protein kinase. Endocrinology 2003; 144: 1164–74.
31 John C, Cover P, Solito E, Morris J, Christian H, Flower R, *et al*. Annexin 1-dependent actions of glucocorticoids in the anterior pituitary gland: roles of the N-terminal domain and protein kinase C. Endocrinology 2002; 143: 3060–70.
32 Ito S, Kimura K, Haneda M, Ishida Y, Sawada M, Isobe K. Induction of matrix metalloproteinases (MMP3, MMP12, and MMP13) expression in the microglia by amyloid-beta stimulation via the PI3K/Akt pathway. Exp Gerontol 2007; 42: 532–7.
33 Shukla A, Barrett TF, Nakayama KI, Nakayama K, Mossman BT, Lounsbury KM. Transcriptional up-regulation of MMP12 and MMP13 by asbestos occurs via a PKCdelta-dependent pathway in murine lung. Faseb J 2006; 20: 997–9.
34 Wagner GF, Dimattia GE. The stanniocalcin family of proteins. J Exp Zool A Comp Exp Biol 2006; 305: 769–80.
35 Wagner GF, Hampong M, Park CM, Copp DH. Purification, characterization, and bioassay of teleocalcin, a glycoprotein from salmon corpuscles of Stannius. Gen Comp Endocrinol 1986; 63: 481–91.
36 Lafeber FP, Flik G, Wendelaar Bonga SE, Perry SF. Hypocalcin from Stannius corpuscles inhibits gill calcium uptake in trout. Am J Physiol 1988; 254: R891–6.
37 Lu M, Wagner GF, Renfro JL. Stanniocalcin stimulates phosphate reabsorption by flounder renal proximal tubule in primary culture. Am J Physiol 1994; 267: R1356–62.
38 Sundell K, Björnsson BT, Itoh H, Kawauchi H. Chum salmon (*Oncorhynchus keta*) stanniocalcin inhibits *in vitro* intestinal calcium uptake in *Atlantic cod* (Gadus morhua). J Comp Physiol [B] 1992; 162: 489–95.
39 Holmes DI, Zachary IC. Vascular endothelial growth factor regulates stanniocalcin-1 expression via neuropilin-1-dependent regulation of KDR and synergism with fibroblast growth factor-2. Cell Signal 2008; 20: 569–79.
40 Grosshans J, Wieschaus E. A genetic link between morphogenesis and cell division during formation of the ventral furrow in *Drosophila*. Cell 2000; 101: 523–31.
41 Mata J, Curado S, Ephrussi A, Rørth P. Tribbles coordinates mitosis and morphogenesis in *Drosophila* by regulating string/CDC25 proteolysis. Cell 2000; 101: 511–22.
42 Seher TC, Leptin M. Tribbles, a cell-cycle brake that coordinates proliferation and morphogenesis during *Drosophila* gastrulation. Curr Biol 2000; 10: 623–9.
43 Schwarzer R, Dames S, Tondera D, Klippel A, Kaufmann J. TRB3 is a PI 3-kinase dependent indicator for nutrient starvation. Cell Signal 2006; 18: 899–909.
44 Kiss-Toth E, Bagstaff SM, Sung HY, Jozsa V, Dempsey C, Caunt JC, *et al*. Human tribbles, a protein family controlling mitogen-activated protein kinase cascades. J Biol Chem 2004; 279: 42703–8.
45 Silverman N, Maniatis T. NF-kappaB signaling pathways in mammalian and insect innate immunity. Genes Dev 2001; 15: 2321–42.
46 Ghosh S, Karin M. Missing pieces in the NF-kappaB puzzle. Cell 2002; 109 Suppl: S81–96.
47 Sun SC, Xiao G. Deregulation of NF-kappaB and its upstream kinases in cancer. Cancer Metastasis Rev 2003; 22: 405–22.

48 Gebken J, Lüders B, Notbohm H, Klein HH, Brinckmann J, Müller PK, *et al*. Hypergravity stimulates collagen synthesis in human osteoblast-like cells: evidence for the involvement of p44/42 MAP-kinases (ERK 1/2). J Biochem 1999; 126: 676–82.
49 Shahrestanifar M, Fan X, Manning DR. Lysophosphatidic acid activates NF-kappaB in fibroblasts. A requirement for multiple inputs. J Biol Chem 1999; 274: 3828–33.
50 Ozes ON, Mayo LD, Gustin JA, Pfeffer SR, Pfeffer LM, Donner DB. NF-kappaB activation by tumour necrosis factor requires the Akt serine-threonine kinase. Nature 1999; 401: 82–5.
51 Romashkova JA, Makarov SS. NF-kappaB is a target of AKT in anti-apoptotic PDGF signalling. Nature 1999; 401: 86–90.
52 Carrier F, Zhan Q, Alamo I, Hanaoka F, Fornace AJ Jr. Evidence for distinct kinase-mediated pathways in gadd gene responses. Biochem Pharmacol 1998; 55: 853–61.
53 Papathanasiou MA, Kerr NC, Robbins JH, McBride OW, Alamo I Jr, Barrett SF, *et al*. Induction by ionizing radiation of the gadd45 gene in cultured human cells: lack of mediation by protein kinase C. Mol Cell Biol 1991; 11: 1009–16.
54 Kaufman RJ. Stress signaling from the lumen of the endoplasmic reticulum: coordination of gene transcriptional and translational controls. Genes Dev 1999; 13: 1211–33.
55 Lawrence M, Shao C, Duan L, McGlynn K, Cobb MH. The protein kinases ERK1/2 and their roles in pancreatic beta cells. Acta Physiol (Oxf) 2008; 192: 11–7.
56 Abel T, Nguyen PV, Barad M, Deuel TA, Kandel ER, Bourtchouladze R. Genetic demonstration of a role for PKA in the late phase of LTP and in hippocampus-based long-term memory. Cell 1997; 88: 615–26.
57 Huang YY, Li XC, Kandel ER. cAMP contributes to mossy fiber LTP by initiating both a covalently mediated early phase and macromolecular synthesis-dependent late phase. Cell 1994; 79: 69–79.
58 Frey U, Huang YY, Kandel ER. Effects of cAMP simulate a late stage of LTP in hippocampal CA1 neurons. Science 1993; 260: 1661–4.
59 Peng HY, Cheng YW, Lee SD, Ho YC, Chou D, Chen GD, *et al*. Glutamate-mediated spinal reflex potentiation involves ERK1/2 phosphorylation in anesthetized rats. Neuropharmacology 2008; 54: 686–98.
60 Mayer ML, Westbrook GL. Permeation and block of *N*-methyl-*D*-aspartic acid receptor channels by divalent cations in mouse cultured central neurones. J Physiol 1987; 394: 501–27.
61 Bray JG, Mynlieff M. Involvement of protein kinase C and protein-kinase A in the enhancement of L-type calcium current by GABA(B) receptor activation in neonatal hippocampus. Neuroscience 2011; 179: 62–72.
62 Carpio L, Gladu J, Goltzman D, Rabbani SA. Induction of osteoblast differentiation indexes by PTHrP in MG-63 cells involves multiple signaling pathways. Am J Physiol Endocrinol Metab 2001; 281: E489–99.
63 Mao LM, Tang QS, Wang JQ. Regulation of extracellular signal-regulated kinase phosphorylation in cultured rat striatal neurons. Brain Res Bull 2009; 78: 328–34.
64 Hinoi E, Fujimori S, Nakamura Y, Yoneda Y. Group III metabotropic glutamate receptors in rat cultured calvarial osteoblasts. Biochem Biophys Res Commun 2001; 281: 341–6.

Acta Pharmacologica Sinica (2011) 32: 904–911
 1671-4083/11 $32.00
www.nature.com/aps

Original Article

Antcin A, a steroid-like compound from *Antrodia camphorata*, exerts anti-inflammatory effect via mimicking glucocorticoids

Yi-ching CHEN[1], Ya-lin LIU[2], Feng-yin LI[2], Chi-I CHANG[3], Sheng-yang WANG[4], Kuo-yang LEE[5], Shun-lai LI[6], Yi-peng CHEN[6], Tzyy-rong JINN[7, *], Jason TC TZEN[1, 7, 8, *]

[1]Graduate Institute of Biotechnology, [2]Department of Chemistry and [4]Department of Forestry, National Chung Hsing University, Taichung 40227, Taiwan, China; [3]Graduate Institute of Biotechnology, National Pingtung University of Science and Technology, Pingtung 91201, Taiwan, China; [5]Center for General Education, Southern Taiwan University of Technology, Tainan 71005, Taiwan, China; [6]Department of Biotechnology, Southern Taiwan University of Technology, Tainan 71005, Taiwan, China; [7]School of Chinese Medicine, China Medical University, Taichung 40402, Taiwan, China; [8]Agricultural Biotechnology Research Center, Academia Sinica, Taipei 11529, Taiwan, China

Aim: To determine the active ingredient of Niuchangchih (*Antrodia camphorata*) responsible for its anti-inflammatory effects and the relevant molecular mechanisms.
Methods: Five major antcins (A, B, C, H, and K) were isolated from fruiting bodies of Niuchangchih. Structural similarity between the antcins and 2 glucocorticoids (cortisone and dexamethasone) was compared. After incubation with each compound, the cytosolic glucocorticoid receptor (GR) was examined for its migration into the nucleus. Mo lecular docking was performed to model the tertiary structure of GR associated with antcins.
Results: Incubation with cortisone, dexamethasone or antcin A (but not antcins B, C, H, and K) led to the migration of glucocorticoid receptor into the nucleus. The minimal concentration of antcin A, cortisone and dexamethasone to induce nuclear migration of glucocorticoid receptor was 10, 1, and 0.1 mol/L, respectively. The results are in agreement with the simulated binding affinity scores of these three ligands docking to the glucocorticoid receptor. Molecular modeling indicates that C-7 of antcin A or glucocorticoids is exposed to a hydrophobic region in the binding cavity of the glucocorticoid receptor, and the attachment of a hydrophilic group to C-7 of the other four antcins presumably results in their being expelled when docking to the cavity.
Conclusion: The anti-inflammatory effect of Niuchangchih is, at least, partly attributed to antcin A that mimics glucocorticoids and triggers translocation of glucocorticoid receptor into nucleus to initiate the suppressing inflammation.

Keywords: antcin A; *Antrodia camphorata*; cortisone; dexamethasone; glucocorticoid receptor; anti-inflammation

Acta Pharmacologica Sinica (2011) 32: 904–911; doi: 10.1038/aps.2011.36; published online 23 May 2011

Introduction

Niuchangchih (*Antrodia camphorata*), growing restrictedly on the inner cavity of the endemic species *Cinnamomum kanehirae* (Bull camphor tree) Hayata (Lauraceae), is a unique medicinal mushroom found in Taiwan[1]. Being a local species, Niuchangchih was originally consumed by the aborigines as a traditional prescription for the discomforts caused by alcohol drinking or exhaustion[2]. In the past few decades, fruiting bodies of Niuchangchih have been frequently recommended as a folk medicine for the treatment of liver diseases, drug intoxication, diarrhea, abdominal pain, hypertension, and tumorigenic diseases[3]. Among the therapeutic effects of Niuchangchih proposed on the basis of practical utilization and scientific investigation, anti-inflammatory effect has been positively highlighted and well-recognized by the consumers, particularly those who suffer in liver dysfunction[4–7].

The compounds identified in Niuchangchih are predominantly benzenoids, diterpenes, triterpenoids, steroids, polysaccharides, and maleic/succinic acid derivatives[8]. More than 30 steroid-like compounds (triterpenoids and steroids) identified and structurally determined from fruiting bodies of Niuchangchih represent the major constituents and account for approximately 60% of dry weight in this medicinal

* To whom correspondence should be addressed.
E-mail jinn@mail.cmu.edu.tw (Tzyy-rong JINN);
TCTZEN@dragon.nchu.edu.tw (Jason TC TZEN)
Received 2010-12-22 Accepted 2011-03-30

mushroom[9]. Among these steroid-like compounds, antcins, a unique group having ergostane skeletons, are only found in Niuchangchih to date. Anti-inflammatory, anti-insecticidal and cytotoxic activities have been observed in various antcins and their derivatives[10–16].

Glucocorticoids are a class of steroid hormones that predominantly affect the metabolism of carbohydrates[17]. They also play roles in the feedback mechanism of the immune system to repress immune activity (inflammation), and thus are used as the most important anti-inflammatory drugs as well as medicines to treat diseases caused by an overactive immune system[18, 19]. Glucocorticoids, because of their lipophilic nature, readily diffuse into the cells and initiate anti-inflammatory effects by binding to the cytosolic glucocorticoid receptor (GR). The activated glucocorticoid/GR complex migrates into the nucleus where it suppresses the expression of pro-inflammatory proteins and enhances the expression of anti-inflammatory proteins[20].

In light of the consentaneous utilization of glucocorticoids and Niuchangchih in anti-inflammation, we wondered if any constituents in this folk medicine might possess anti-inflammatory effects via the same molecular mechanism triggered by glucocorticoids. To inspect this possibility, structural similarity between two glucocorticoids (cortisone and dexamethasone) and five major antcins isolated from fruiting bodies of Niuchangchih was compared. Furthermore, translocation of GR from cytosol to the nucleus after incubation with glucocorticoids or antcins was analyzed. Molecular docking of glucocorticoids and antcins to the binding cavity of GR was simulated and compared.

Materials and methods

Chemicals and reagents

Paraformaldehyde, bovine serum albumin (BSA), dimethyl sulfoxide (DMSO), cortisone, and dexamethasone were purchased from Sigma-Aldrich (St Louis, MO, USA). Acetonitrile and phosphoric acid were supplied from Merck (Darmstadt, Germany). F-12 kaighn's modification medium, fetal bovine serum (FBS), Triton X-100, ganoderic acid A, and glycyrrhetic acid were purchased from Hyclone (Logan, UT, USA), Biological Industries (Israel), Amresco (St Louis, MO, USA), Pulin Biotech (Taipei, Taiwan, China), Extrasynthese (Genay, France), respectively.

Chromatography conditions

Niuchangchih of 3 g was extracted with methanol (5×20 mL), and the methanol extract was evaporated to a final volume of 10 mL. The sample was filtered through a 0.45 μm filter and analyzed on a liquid chromatography system coupled to a Model 600E photodiode array detector (Waters Corporation, Milford, MA, USA). Chromatographic separations were performed on a Zorbax SB-C18 column (4.6 mm×250 mm, 5 μm; Agilent, USA) with a guard column, MetaGuard Pursuit C18 (Varian, USA). The mobile phase consisted of solvent A (acetonitrile) and solvent B (0.1% phosphoric acid). A gradient procedure was used as follows: 23.5% to 30% of A for 30 min; 30% to 37% of A for 90 min; 37% to 37.3% of A for 108 min; 37.3% to 38% of A for 10 min; 38% to 47% of A for 100 min; 47% to 48.5% of A for 1 min; 48.5% to 85% of A for 95 min; 85% to 23.5% of A for 1 min. The column temperature was set at room temperature, and the injection volume was 10 μL. The flow rate was set at 1 mL/min, and the UV absorbance detection wavelength was set at 254 nm.

Preparation of antcins

The oven-dried fruiting bodies of Niuchangchih (*Antrodia camphorata*) (50 g) were extracted with methanol (3×2 L) at room temperature (7 d each)[21]. The combined extract was evaporated under reduced pressure to afford a brown residue, which was suspended in H_2O (1 L), and then extracted with EtOAc and *n*-BuOH (3×1 L) sequentially. The EtOAc fraction (10.8 g) was subjected to silica gel chromatography (60 cm×3.5 cm) using a stepwise gradient mixture of *n*-hexane and EtOAc as eluent. Ten fractions were collected as follows: 1 [3000 mL, *n*-hexane], 2 [2000 mL, *n*-hexane–EtOAc (19:1)], 3 [2000 mL, *n*-hexane–EtOAc (9:1)], 4 [2000 mL, *n*-hexane–EtOAc (17:3)], 5 [2000 mL, *n*-hexane–EtOAc (8:2)], 6 [3000 mL, *n*-hexane–EtOAc (7:3)], 7 [3000 mL, *n*-hexane–EtOAc (5:5)], 8 [3000 mL, *n*-hexane–EtOAc (4:6)], 9 [3000 mL, *n*-hexane–EtOAc (2:8)], and 10 (4000 mL, EtOAc). Fraction 5 further purified through a silica gel column (2 cm×45 cm), eluted with CH_2Cl_2–EtOAc (30:1 to 0:1) to obtain six fractions (each about 300 mL), 5A–5F. Fraction 5C was applied to semipreparative HPLC eluted with CH_2Cl_2-acetone (40:1) to yield antcin A (5.1 mg). Fraction 6 was further chromatographed on a silica gel column (2 cm×45 cm), eluted with CH_2Cl_2–EtOAc (15:1 to 0:1) to resolve into five fractions (each about 350 mL), 6A–6E. Fraction 6B was subjected to semipreparative HPLC eluted with CH_2Cl_2-acetone (20:1) to yield antcin B (9.5 mg). Fraction 6C was also subjected to semipreparative HPLC eluted with CH_2Cl_2-acetone (15:1) to yield antcin C (4.5 mg). Fraction 7 was further chromatographed on a silica gel column (2 cm×45 cm), eluted with CH_2Cl_2-methanol (50:1) to afford seven fractions (each about 300 mL), 7A–7G. Fraction 7C was subjected to semipreparative HPLC eluted with CH_2Cl_2-acetone (9:1) to yield antcin H (6.5 mg). Fraction 9 was further purified through a silica gel column (2 cm×45 cm), eluted with CH_2Cl_2–MeOH (15:1) to obtain six fractions (each about 300 mL), 9A–9F. Fraction 9E was subjected to semipreparative HPLC eluted with CH_2Cl_2–i-propanol (9:1) to yield antcin K (4.1 mg). The five purified antcins in a mixture of two epimers at C-25 were confirmed by their spectra of ^{1}H-NMR, ^{13}C-NMR and HR-EI-MS^n.

General experimental procedures

NMR spectra were recorded in $CDCl_3$ or C_5D_5N at room temperature on a Varian Mercury plus 400 NMR spectrometer, and the solvent resonance was used as internal shift reference (TMS as standard). Thin layer chromatograph was carried out on aluminum-backed silica gel 60 F_{254} plates (Merck). Silica gel (230–400 mesh ASTM, Merck) was used for column chromatography.

Detection of GR translocation to the nucleus after drug treatment

Human lung cancer cell A549 was obtained from the Bioresources Collection and Research Center, Taiwan, China. Cells were routinely cultured in the F-12k medium supplemented with 10% FBS and maintained at 37 °C in a humidified atmosphere with 5% CO_2. They were cultured on glass coverslips in 6 cm dishes at a density of 2×10^5 cells for 24 h, serum-starved for 6 h, and then treated with each of the test compounds (dissolved in DMSO) for 1 h. After treatment, cells were fixed with 4% paraformaldehyde, permeabilized with 0.5% Triton-X 100, blocked with 3% BSA in phosphate buffered saline (PBS) buffer for 30 min, and incubated with rabbit polyclonal anti-GR antibodies (1:200 dilution; Santa Cruz, CA, USA) for 2 h. After antibody incubation, cells were washed with the PBS buffer, incubated with Alexa Fluor 488 anti-rabbit IgG (1:1000 dilution; Molecular Probes, Eugene, OR, USA) for 1 h, and then stained with 0.5 μg/mL of 4′,6-diamidino-2-phenylindole (DAPI) for 1 min (Molecular Probes, Eugene, OR, USA). Cellular images were visualized in an Olympus IX71 fluorescence microscope system (Olympus, Tokyo, Japan), and photos were taken by a digital camera with UPlanSApo 60×/1.35 oil immersion objective lens.

Molecular modeling

The X-ray structure of GR in complex with deacylcortivazol (DAC), a potent glucocorticord, and steroid receptor coactivator-1 (SRC-1) (PDB code: 3BQD)[22] was used as the template for molecular docking. In order to facilitate docking process, we removed DAC and SRC-1 from GR, as well as the surrounding water molecules. Noticing that cortisone was converted to cortisol, a more active form, by 11β-hydroxysteroid dehydrogenase in liver[23], we assumed that the carbonyl group attached to C-11 of antcin A was possibly converted to a hydroxyl group in the A549 cells by their endogenous 11β-hydroxysteroid dehydrogenase activity[24]. Thus, antcin A (11β-hydroxyl form), cortisol and dexamethasone were used as GR ligands for docking simulation, and they were constructed and minimized with consistent force field[25] using the Discover Studio 2.0 (DS) package (http://accelrys.com/about/legal/)[26].

The binding cavity for GR ligands was analyzed using DS package and defined as the region of the sphere with a 16 Å radius from the center of the binding cavity, which lies in the area among Leu536, Trp600, and Met646. Docking of antcin A, cortisol and dexamethasone to GR was performed in silico by employing the CDOCKER module[27] in the DS environment. CDOCKER is a grid-based molecular docking method which employs CHARMm forcefield[28] and assigns the partial charges of the atoms with those found in Merck Molecular Force Field (MMFF)[29]. For each GR ligand studied, 300 different conformations were generated using high temperature molecular dynamics simulation and five conformations with the lowest energies were selected as the candidates for docking. The high temperature MD simulation offers all the advantages of full ligand flexibility (including bonds, angles and dihedrals) and reasonable computation time. In this study, the high temperature was set to be 1000 K. After these conformations were translated into the binding sphere, the candidate poses were created by using random rigid-body rotations followed by simulated annealing and final energy minimization, while keeping the GR structure fixed during all the above processes except the annealing. The ligand pose with the highest CDOCKER energy was selected to represent each of the studied GR ligands inside the binding cavity, and employed MMFF forcefield to minimize the final structure. In order to validate our approach, the redocking of DAC onto GR was performed and the RMSD value of the redocked DAC/GR complex compared with the X-ray one was 0.92 Å.

For the evaluation of the binding affinity, the scoring method piecewise linear potential (PLP)[30] implemented in DS was applied. PLP was reported to give reliable correlations between the binding scores and experimentally determined protein-ligand binding affinities as reported previously[31]. Two type of PLP functions are available, PLP1 and PLP2. In this study, PLP2 was adopted since it includes an extra set of parameters to describe atomic size effect, which is absent in PLP1. In this study, a hydrogen bond (X-H…Y) involves X and Y being two different electronegative atoms, such as oxygen, nitrogen and fluorine, with the distance between H and Y ranging from 1.2 up to 2.76 Å and angle of X-H-Y between 120 and 180 degrees.

Results

Purification of major antcins from fruiting bodies of Niuchangchih

Five major antcins (A, B, C, H, and K) were identified in the methanol extract of fruiting bodies of Niuchangchih, and two C-25 epimers were found in each of the five antcins (Figure 1). The five antcins were separately purified as a mixture of two C-25 epimers, and the correctness of these compounds was confirmed by comparing their spectral data of NMR and Mass (data not shown) with those of antcins described in the literatures[13, 21, 32].

Structural comparison between antcins and glucocorticoids

Structurally similar to cortisone (the major natural glucocorticoid) and dexamethasone (a synthetic glucocorticoid with

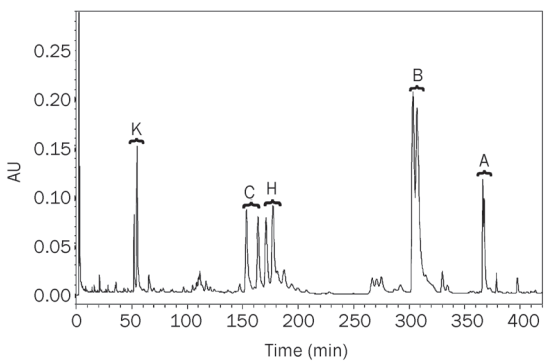

Figure 1. HPLC profile (0–420 min) of the methanol extract of Niuchangchih at 254 nm. Positions of five major antcins (A, B, C, H, and K) are indicated on top of the peaks. Two epimers are found in each antcin.

activity stronger than cortisone), antcins comprise a core steroidal backbone with carbonyl or hydroxyl groups attached to C-3 and C-11; and yet, the head groups attached to C-17 of glucocorticoids and antcins are different (Figure 2). Having a carbonyl group at C-11, cortisone is more similar to antcins than dexamethasone that possesses a hydroxyl group at C-11 and a fluoro-replacement at C-9. Among the five antcins, antcin A is more similar to cortisone than the other four antcins which have an additional carbonyl or hydroxyl group attached to C-7.

Nuclear migration of GR treated with antcins

By using two positive controls (cortisone and dexamethasone) and two negative controls (ganoderic acid A and glycyrrhetic acid), induction of GR translocation from cytosol to the nucleus was measured to evaluate if antcins could lead to a similar anti-inflammatory effect via the same mechanism triggered by glucocorticoids. The results showed that antcin A, similar to the two positive controls, led to nuclear migration of GR as the green fluorescence (indicating the localization of GR) was exclusively confined in the nuclei that were also visualized by blue fluorescence stained with DAPI (Figure 3). In contrast, green fluorescence was found diffusive in the whole cells (larger than the blue fluorescence stained with DAPI) when treated with the other four antcins or the two negative controls. To inspect the relative capability of these ligands for activating GR, three concentrations, 0.1, 1, and 10 μmol/L of antcin A, cortisone and dexamethasone were examined in the same test. The results showed that antcin A, cortisone and dexamethasone led to nuclear migration of GR at 10, 1, and 0.1 μmol/L, respectively (Figure 4). Thus, dexamethasone possessed the highest capability while antcin A had the lowest capability for activating GR. Relatively, the minimal concentration of antcin A required for nuclear migration of GR was approximately 10 times higher than that of cortisone.

Molecular modeling and docking of antcin A to GR

Molecular modeling showed that antcin A (11β-hydroxyl form) could successfully dock to the binding cavity of GR (Figure 5A). In comparison with the docking of dexamethasone and cortisol (11β-hydroxyl form converted from cortisone by 11β-hydroxysteroid dehydrogenase in liver), antcin A was found located in the same binding cavity of GR with similar orientation and interaction since these three GR ligands could be superimposed correspondingly (Figure 5B). Detailed comparison indicates that Gln642, Met646, and Tyr735 are slightly dislocated in antcin A/GR complex when compared with those in the other two complexes, and that Arg611 forming a hydrogen bond with cortisol or dexamethasone is missing in antcin A/GR. The distance between R611 and antcin A is 3.06 Å. However, for dexamethasone and cortisol, the distances are 1.62 and 1.52 Å, respectively. Consensually observed in the docking of antcin A, cortisol and dexamethasone to GR, the hydrophobic side of the steroidal backbone where C-7 is located is surrounded by hydrophobic residues in the binding cavity, including Leu608, Met604, Phe623, Ala605, Met601, Met646, Leu732, and Tyr735 (Figure 5C). Moreover, theoretical calculation showed that the binding affinity scores (PLP2 values) of antcin A, cortisol and dexamethasone to GR were -95.0, -96.4, and -104.1, respectively. These data are in agreement with the results observed in their minimal concentrations required for nuclear migration of GR (Figure 4).

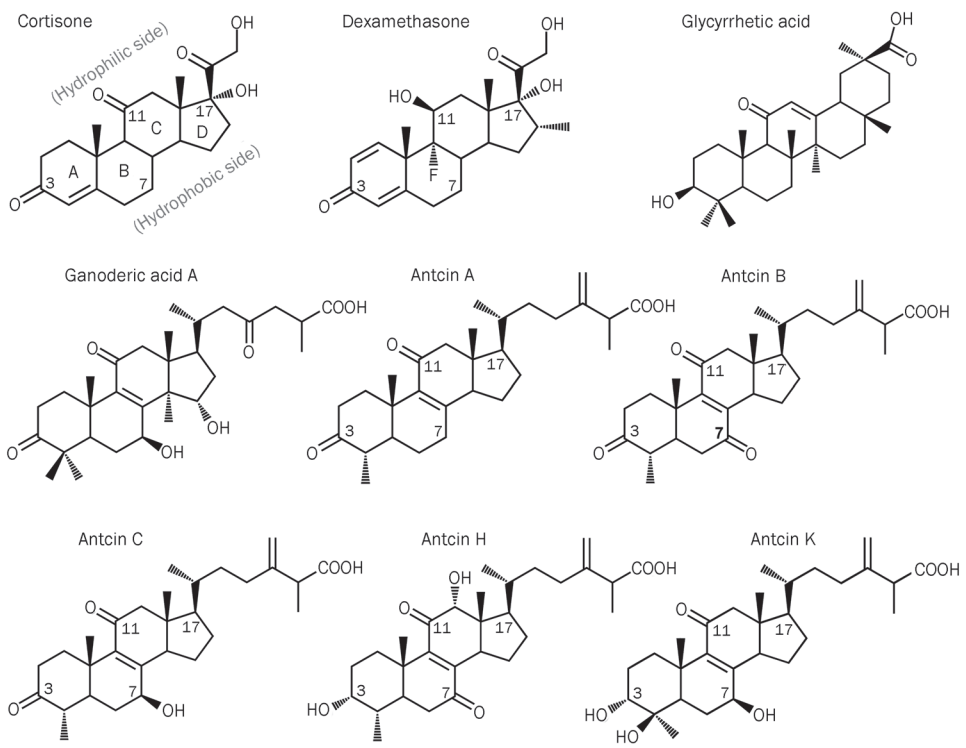

Figure 2. Chemical structures of cortisone, dexamethasone, glycyrrhetic acid, ganoderic acid A, and five major antcins (A, B, C, H, and K) of Niuchangchih.

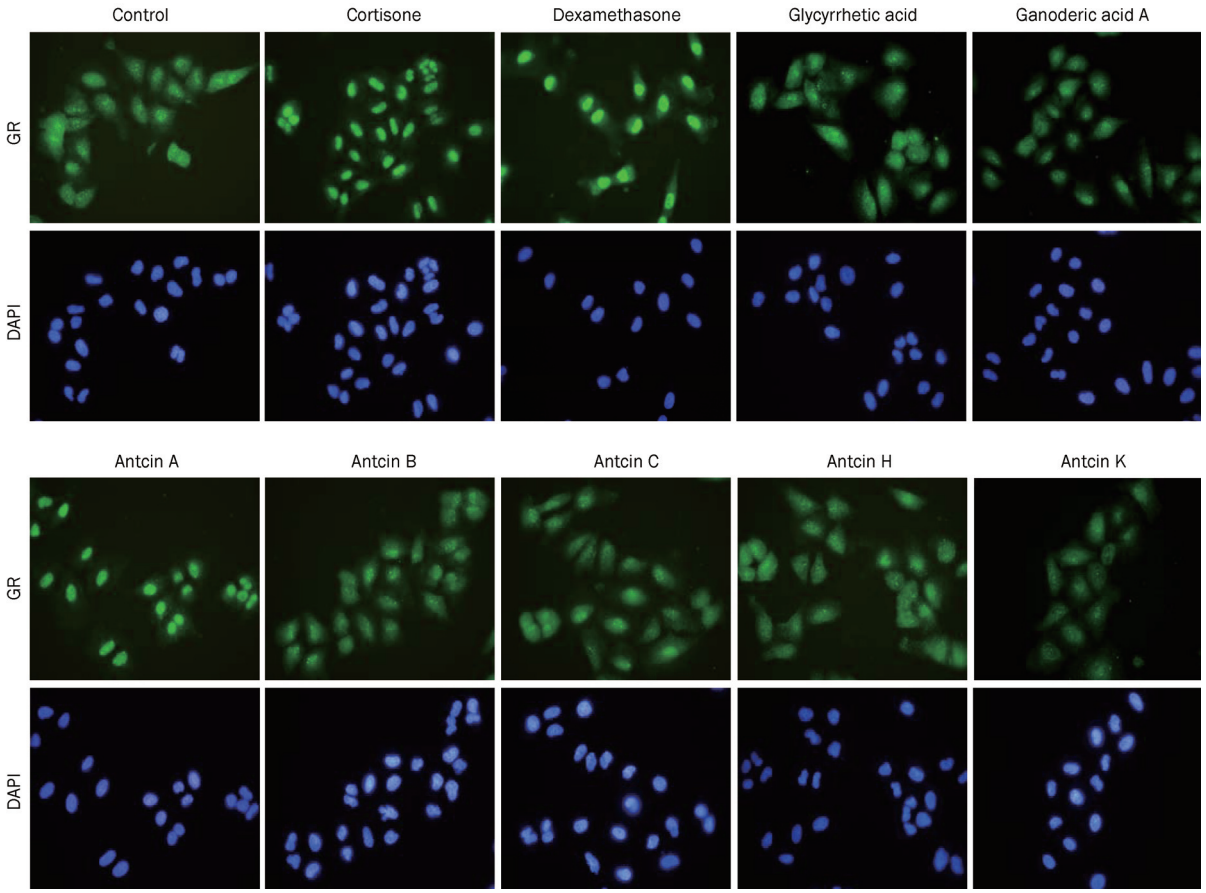

Figure 3. Nuclear migration of GR treated with various steroid-like compounds. A549 cells were treated with 10 μmol/L of two positive controls (cortisone and dexamethasone), two negative controls (ganoderic acid A and glycyrrhetic acid) and the five purified antcins. After treatment, cells were fixed, permeabilized and stained with anti-GR to check if GR translocated from cytosol to the nucleus. Localization of GR was visualized by green fluorescence of anti-GR, and nuclei were visualized by blue fluorescence stained with DAPI.

Modeling comparison between antcin A/GR and dexamethasone/GR

The validation of our docking results was also verified by examining the docking of dexamethasone to GR reported previously[33, 34]. Dexamethasone is oriented with its A ring anchored by two hydrogen bonds to the carbonyl inside the binding cavity of GR and with its D ring hanging around the cavity opening. Six residues of GR, Asn564, Gln570, Arg611, Gln642, Cys736, and Thr739 found on one side of the steroidal backbone are involved in hydrogen bonding with the specific functional groups of dexamethasone in accord with the hydrogen bonding network observed in the crystal of dexamethasone/GR complex (PDB code 1M2Z)[33]. Several distinct structural characteristics are present between antcin A and dexamethasone, mainly in their head groups attached to C-17 of the D ring. Firstly, the head group (17.3 Å) of antcin A is longer than that (12.9 Å) of dexamethasone. Furthermore, dexamethasone is neutral in its native form, but antcin A is ionic at pH 7 due to the carboxylate at the end of its head group. There are three hydrophilic groups in the head group of dexamethasone, but only one in that of antcin A. This explains why only three residues in GR, *ie* Gln570, Asn564, and Thr739, form hydrogen bonds with antcin A.

Besides the reduction in the number of hydrogen bonds, antcin A suffers two other disadvantages when compared with dexamethasone. First, as the carboxylate in the end of the long head group of antcin A forms a hydrogen bond with Thr739, it is pulled by this hydrogen bond toward the cavity opening. This shift weakens the strength of the hydrogen bonding network and causes a slight mismatch of the hydrophobic interaction pattern. Second, the replacement of the carbonyl group with methyl group in the head group pushes Gln642, Met646, and Tyr735 away from antcin A. The consequence of the dislocation of Gln642, Met646, and Tyr735 is to make the cavity opening slightly larger than that found in the dexamethasone/GR complex. Taken together, the GR binding affinity of antcin A is lower than that of dexamethasone in molecular modeling.

Discussion

In accord with their structural similarity, antcin A extracted from fruiting bodies of Niuchangchih led to GR translocation from cytosol to the nucleus as cortisone did in our experimental conditions. Molecular modeling showed that antcin A as well as glucocorticoids could stably interact with the binding

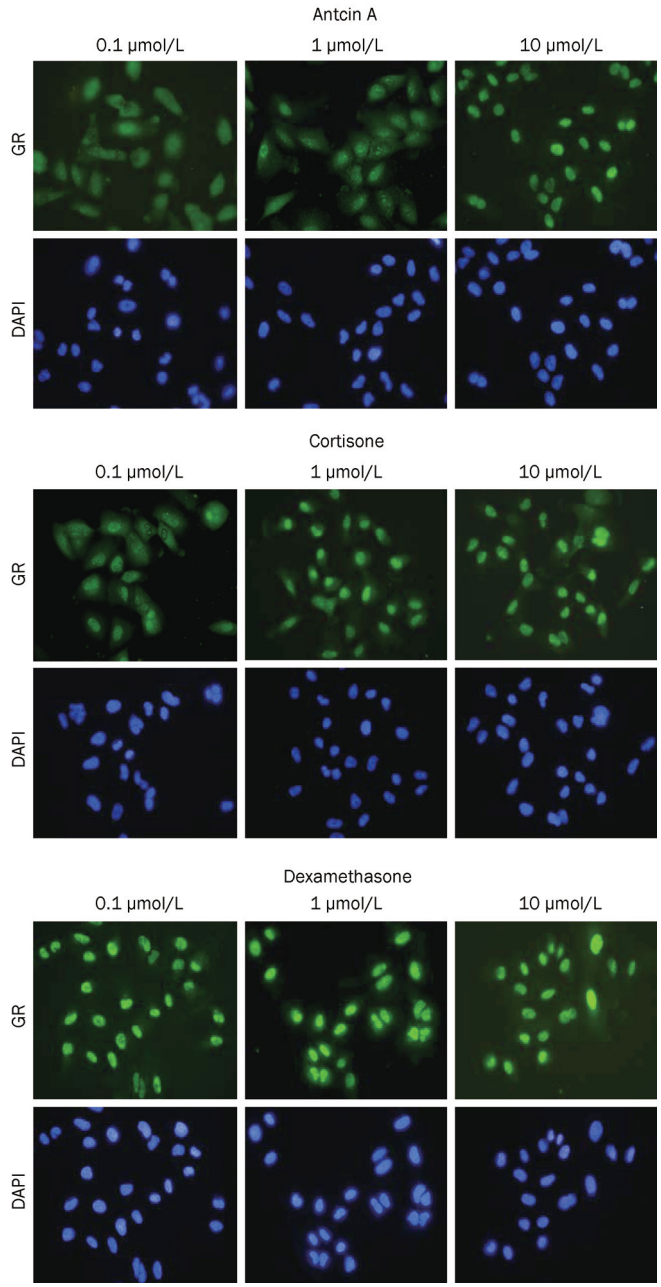

Figure 4. Nuclear migration of GR treated with antcin A, cortisone and dexamethasone at three different concentrations, 0.1, 1, and 10 μmol/L. Similar fluorescence imaging in A549 cells was visualized as described in Figure 3.

cavity of GR despite the fact that their head groups at C-17 are different. Taken together, we propose that antcin A may act as an active ingredient responsible for the anti-inflammatory effect of Niuchangchih via the same molecular mechanism triggered by glucocorticoids (Figure 6): mimicking glucocorticoids, antcin A diffuses across the cell membrane and binds to the cytosolic GR that forms a dimer after dissociated from the heat-shock protein and then translocates into the nucleus to initiate the suppression of inflammation at the gene regulation level[20].

In this study, five major antcins were isolated from fruiting bodies of Niuchangchih and examined for their possible therapeutic effects by mimicking glucocorticoids. Surprisingly, only antcin A, but not the remaining four, could lead to nuclear migration of GR. The main distinction between antcin A and the other four antcins is the additional carbonyl or hydroxyl group attached to C-7 of the latter (Figure 2). Molecular modeling indicates that C-7 of antcin A or glucocorticoids is exposed to a hydrophobic region in the binding cavity of GR (Figure 5C), and thus the other four antcins with the additional hydrophilic group attached to C-7 are presumably expelled when they approach GR. Similarly, repulsion is expected between the hydrophobic region in the binding cavity of GR and the hydrophilic hydroxyl group attached to C-7 of ganoderic acid A (a negative control in Figure 3) that possesses a head group at C-17 very similar to that of antcins. In order to demonstrate the adverse effect caused by the mismatch between the hydrophilic group attached to C-7 of the antcins and their surrounding environments in the docked complexes, the binding affinity score of antcin B was calculated, which is -89.3, higher than that of antcin A, -95. Regarding the head group, the linear chain attached to antcin A is longer than that attached to glucocorticoids and apparently reduces the binding affinity to GR. Moreover, replacement of the short head group in glucocorticoids with an additional fusion ring, *ie* the fifth ring of pentacyclic triterpenoids, seems to be unacceptable for the binding to GR as observed in the treatment with glycyrrhetic acid (Figure 3) that comprises a core steroidal backbone very similar to glucocorticoids with a hydroxyl group at C-3 and a carbonyl group at C-11.

To date, a total of 10 antcins, (A, B, C, D, E, F, G, H, I, and K) plus some of their derivatives have been identified in fruiting bodies of Niuchangchih[9]. Among the five minor ones not examined in this study, antcins D, F, G, and I, but not antcin E, possess an additional hydrophilic group attached to C-7. Therefore, we speculate that antcin E would be capable of mimicking glucocorticoids, similar to antcin A, to trigger the translocation of GR into nucleus, and thus contribute to a limited or minor extent to the anti-inflammatory effect of Niuchangchih. Furthermore, whether the other eight antcins may act as prodrugs with the additional hydrophilic group at C-7 removed by intestinal microflora or the enterohepatic circulation remains to be investigated.

In the past few decades, medicinal effects of Niuchangchih have been well-recognized by the consumers who suffer in liver dysfunction including liver cancer[8]. Recently, antcin A related compounds, particularly its methyl derivative, was demonstrated to induce apoptosis in human liver cancer cells[35]. Intracellular reactive oxygen species generation and NADPH oxidase activation were observed in the cells treated with methyl antcin A, and the apoptosis was proposed to be induced through oxidant-mediated cofilin- and Bas-triggered mitochondrial pathway. It will be an interesting task to figure out whether any cross-talk interaction is present between the apoptosis signaling pathway induced by antcin A derivatives

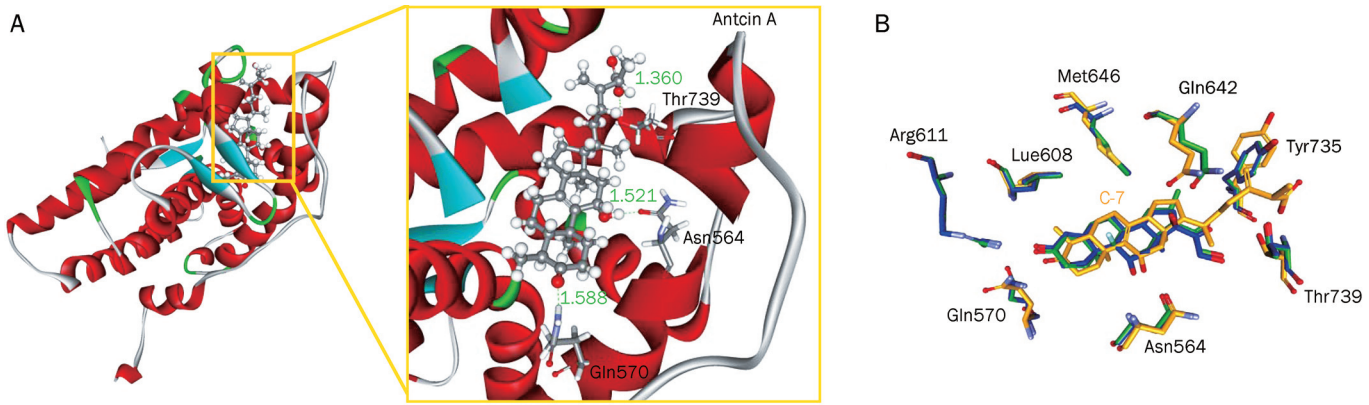

Figure 5. (A) Modeling of antcin A binding to GR. The residues around the binding cavity of GR are shown in ribbon structure, while antcin A and the three residues of GR forming hydrogen bonds with antcin A are presented in ball and stick. The distance between donor and acceptor for the three hydrogen bonds is labeled in green. (B) An overlap plot of docking structures of antcin A (yellow), cortisol (blue) and dexamethasone (green) inside the binding cavity of GR. Position of C-7 of antcin A is labeled. (C) Detailed structure of the hydrophobic residues of GR surrounding the hydrophobic side of the steroidal backbone in antcin A where C-7 is located. The hydrophobic residues in the binding cavity of GR are shown in blue wired spheres. Location of C-7 of antcin A is shown in green wire.

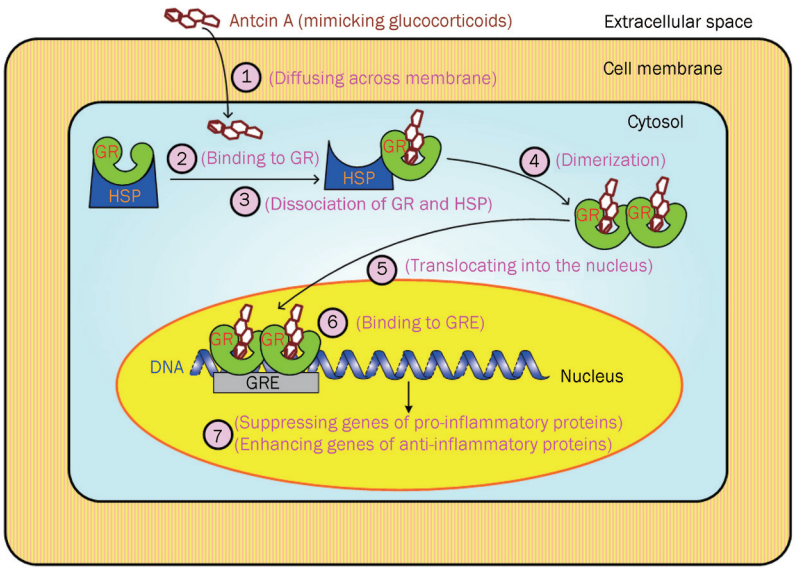

Figure 6. Proposed molecular mechanism responsible for the anti-inflammatory effect of antcin A in Niuchangchih. Step 1: Antcin A diffuses across cell membrane by its lipophilic character. Step 2: Antcin A binds to the cytosolic GR. Step 3: After binding with antcin A, GR dissociates with the heat-shock protein (HSP). Step 4: Dimerization of antcin A/GR complex. Step 5: Antcin A/GR translocates into the nucleus. Step 6: Antcin A/GR binds to glucocorticoid responsive elements (GRE) of target genes. Step 7: Regulation of gene expression, such as suppressing the expression of pro-inflammatory proteins and enhancing the expression of anti-inflammatory proteins, leads to the anti-inflammatory effect.

and the anti-inflammatory signaling pathway induced by antcin A/GR complex, particularly in liver cells.

Although glucocorticoids are effective anti-inflammatory drugs, short-term side effects, such as insomnia, euphoria and, mania as well as long-term side effects, such as Cushing's syndrome, truncal weight gain, osteoporosis, and glaucoma have been observed[18]. The underlying molecular mechanisms for these side effects are complex, distinct and only partly understood; they are presumably mediated via transactivation and/or transrepression on a case-by-case basis. Searching for new

drugs that exert the anti-inflammatory effect with no or low side effects is an on-going task. It remains to be investigated whether the utilization of antcin A at therapeutic dosage for anti-inflammation leads to the same or different side effects comparable with those of glucocorticoids.

Acknowledgements

Project was supported by a grant to Jason TC TZEN from the National Science Council, Taiwan, China (No 98-2622-B-005-007-CC3).

Author contribution

Jason TC TZEN and Tzyy-rong JINN designed research; Yi-ching CHEN, Ya-lin LIU, Chi-I CHANG, Sheng-yang WANG performed research; Kuo-yang LEE, Shun-lai LI, and Yi-peng CHEN contributed new analytical tools and reagents; Jason TC TZEN and Feng-yin LI wrote the paper.

References

1 Wu SH, Ryvarden L, Chang TT. *Antrodia camphorata* ("niu-chang-chih"), new combination of a medicinal fungus in Taiwan. Bot Bull Acad Sin 1997; 38: 273–5.
2 Su CH. Health Guardian Angel: *Antrodia camphorata*. 1 st ed. Taipei (China): EKS Book Publishing Co; 2002.
3 Chen CJ, Su CH, Lan MH. Study on solid cultivation and bioactivity of *Antrodia camphorata*. Fung Sci 2001; 16: 65–72.
4 Hseu YC, Wu FY, Wu JJ, Chen JY, Chang WH, Lu FJ, *et al*. Anti-inflammatory potential of *Antrodia Camphorata* through inhibition of iNOS, COX-2 and cytokines via the NF-kappaB pathway. Int Immunopharmacol 2005; 5: 1914–25.
5 Shen YC, Wang YH, Chou YC, Chen CF, Lin LC, Chang TT, *et al*. Evaluation of the anti-inflammatory activity of zhankuic acids isolated from the fruiting bodies of *Antrodia camphorata*. Planta Med 2004; 70: 310–4.
6 Liu DZ, Liang HJ, Chen CH, Su CH, Lee TH, Huang CT, *et al*. Comparative anti-inflammatory characterization of wild fruiting body, liquid-state fermentation, and solid-state culture of *Taiwanofungus camphoratus* in microglia and the mechanism of its action. J Ethnopharmacol 2007; 113: 45–53.
7 Huang CH, Chang YY, Liu CW, Kang WY, Lin YL, Chang HC, *et al*. Fruiting body of Niuchangchih (*Antrodia camphorata*) protects livers against chronic alcohol consumption damage. J Agric Food Chem 2010; 58: 3859–66.
8 Ao ZH, Xu ZH, Lu ZM, Xu HY, Zhang XM, Dou WF. Niuchangchih (*Antrodia camphorata*) and its potential in treating liver diseases. J Ethnopharmacol 2009; 121: 194–212.
9 Geethangili M, Tzeng YM. Review of pharmacological effects of *Antrodia camphorata* and its bioactive compounds. Evid Based Complement Alternat Med 2011; 2011; 212641. doi:10.1093/ecam/nep108.
10 Cherng IH, Wu DP, Chiang HC. Triterpenoids from *Antrodia cinnamomea*. Phytochemistry 1996; 41: 263–67.
11 Shen YC, Chen CF, Wang YH, Chang TT, Chou CJ. Evaluation of the immuno-modulating activity of some active principles isolated from the fruiting bodies of *Antrodia camphorata*. Chin Pharm J 2003; 55: 313–8.
12 Shen CC, Wang YH, Chang TT, Lin LC, Don MJ, Hou YC, *et al*. Anti-inflammatory ergostanes from the basidiomata of *Antrodia salmonea*. Planta Med 2007; 73: 1208–13.
13 Chen CH, Yang SW, Shen YC. New steroid acids from *Antrodia cinnamomea*, a fungal parasite of *Cinnamomum micranthum*. J Nat Prod 1995; 58: 1655–61.
14 Chen JJ, Lin WJ, Liao CH, Shieh PC. Anti-inflammatory benzenoids from *Antrodia camphorata*. J Nat Prod 2007; 70: 989–92.
15 Male KB, Rao YK, Tzeng YM, Montes J, Kamen A, Luong JH. Probing inhibitory effects of *Antrodia camphorata* isolates using insect cell-based impedance spectroscopy: inhibition *vs* chemical structure. Chem Res Toxicol 2008; 21: 2127–33.
16 Yeh CT, Rao YK, Yao CJ, Yeh CF, Li CH, Chuang SE, *et al*. Cytotoxic triterpenes from *Antrodia camphorata* and their mode of action in HT-29 human colon cancer cells. Cancer Lett 2009; 285: 73–9.
17 Rose AJ, Vegiopoulos A, Herzig S. Role of glucocorticoids and the glucocorticoid receptor in metabolism: insights from genetic manipulations. J Steroid Biochem Mol Biol 2010; 122: 10–20.
18 De Bosscher K, Haegeman G, Elewaut D. Targeting inflammation using selective glucocorticoid receptor modulators. Curr Opin Pharmacol 2010; 10: 497–504.
19 Schacke H, Docke WD, Asadullah K. Mechanisms involved in the side effects of glucocorticoids. Pharmacol Ther 2002; 96: 23–43.
20 Revollo JR, Cidlowski JA. Mechanisms generating diversity in glucocorticoid receptor signaling. Ann N Y Acad Sci 2009; 1179: 167–78.
21 Cherng IH, Chiang HC, Cheng MC, Wang Y. Three new triterpenoids from *Antrodia cinnamomea*. J Nat Prod 1995; 58: 365–71.
22 Suino-Powell K, Xu Y, Zhang C, Tao YG, Tolbert WD, Simons SS Jr, *et al*. Doubling the size of the glucocorticoid receptor ligand binding pocket by deacylcortivazol. Mol Cell Biol 2008; 28: 1915–23.
23 Chapman KE, Coutinho AE, Gray M, Gilmour JS, Savill JS, Seckl JR. The role and regulation of 11beta-hydroxysteroid dehydrogenase type 1 in the inflammatory response. Mol Cell Endocrinol 2009; 301: 123–31.
24 Sai S, Esteves CL, Kelly V, Michailidou Z, Anderson K, Coll AP, *et al*. Glucocorticoid regulation of the promoter of 11beta-hydroxysteroid dehydrogenase type 1 is indirect and requires CCAAT/enhancer-binding protein-beta. Mol Endocrinol 2008; 22: 2049–60.
25 Lifson S, Warshel A. Consistent force field for calculations of conformations, vibrational spectra, and enthalpies of cycloalkane and n-alkane molecules. J Chem Phys 1968; 49: 5116–29.
26 Accelrys Software Inc, Discovery studio modeling environment, Release 2.0, San Diego: Accelrys Software Inc, 2007.
27 Wu G, Robertson DH, Brooks CL 3rd, Vieth M. Detailed analysis of grid-based molecular docking: A case study of CDOCKER-A CHARMm-based MD docking algorithm. J Comput Chem 2003; 24: 1549–62.
28 Brooks BR, Bruccoleri RE, Olafson BD, States DJ, Swaminathan S, Karplus M. CHARMM: A program for macromolecular energy minimization and dynamics calculations. J Comp Chem 1983; 4: 187–217.
29 Halgren TA. Merck Molecular Force Field. II. MMFF94 van der Waals and electrostatic parameters for intermolecular interactions. J Comp Chem 1996; 17: 520–52.
30 Gehlhaar DK, Verkhivker GM, Rejto PA, Sherman CJ, Fogel DB, Fogel LJ, *et al*. Molecular recognition of the inhibitor AG-1343 by HIV-1 protease: conformationally flexible docking by evolutionary programming. Chem Biol 1995; 2: 317–24.
31 Wang R, Lu Y, Wang S. Comparative evaluation of 11 scoring functions for molecular docking. J Med Chem 2003; 46: 2287–303.
32 Shen CC, Kuo YC, Huang RL, Lin LC, Don MJ, Chang TT, *et al*. New ergostane and lanostane from *Antrodia camphorata*. J Chin Med 2003; 14: 247–58.
33 Bledsoe RK, Montana VG, Stanley TB, Delves CJ, Apolito CJ, McKee DD, *et al*. Crystal structure of the glucocorticoid receptor ligand binding domain reveals a novel mode of receptor dimerization and coactivator recognition. Cell 2002; 110: 93–105.
34 Kauppi B, Jakob C, Farnegardh M, Yang J, Ahola H, Alarcon M, *et al*. The three-dimensional structures of antagonistic and agonistic forms of the glucocorticoid receptor ligand-binding domain: RU-486 induces a transconformation that leads to active antagonism. J Biol Chem 2003; 278: 22748–54.
35 Hsieh YC, Rao YK, Wu CC, Huang CY, Geethangili M, Hsu SL, *et al*. Methyl antcinate A from *Antrodia camphorata* induces apoptosis in human liver cancer cells through oxidant-mediated cofilin- and Bax-triggered mitochondrial pathway. Chem Res Toxicol 2010; 23: 1256–67.

Acta Pharmacologica Sinica (2011) 32: 912–920
 1671-4083/11 $32.00
www.nature.com/aps

Original Article

Inhibition of hypoxia-inducible carbonic anhydrase-IX enhances hexokinase II inhibitor-induced hepatocellular carcinoma cell apoptosis

Su-jong YU[1], Jung-hwan YOON[1, *], Jeong-hoon LEE[1], Sun-jung MYUNG[1], Eun-sun JANG[1], Min-sun KWAK[1], Eun-ju CHO[1], Ja-june JANG[2], Yoon-jun KIM[1], Hyo-suk LEE[1]

[1]Department of Internal Medicine and Liver Research Institute and [2]Pathology, Seoul National University College of Medicine, Seoul 110–744, Korea

Aim: The hypoxic condition within large or infiltrative hypovascular tumors produces intracellular acidification, which could activate many signaling pathways and augment cancer cell growth and invasion. Carbonic anhydrase-IX (CA-IX) is an enzyme lowering pH. This study is to examine whether hypoxia induces CA-IX in hepatocellular carcinoma (HCC) cells, and to evaluate its clinical implication in HCC patients.

Methods: Human HCC cell lines (Huh-7 and HepG2 cells) were used, and cell growth was assessed using MTS assay. CA-IX expression and apoptotic/kinase signaling were evaluated using immunoblotting. The cells were transfected with CA-IX-specific siRNA, or treated with its inhibitor 4-(2-aminoethyl) benzenesulfonamide (CAI#1), and/or the hexokinase II inhibitor, 3-bromopyruvate (3-BP). A clinic pathological analysis of 69 patients who underwent an HCC resection was performed using a tissue array.

Results: Incubation of HCC cells under hypoxia (1% O_2, 5% CO_2, 94% N_2) for 36 h significantly increased CA-IX expression level. CAI#1 (400 μmol/L) or CA-IX siRNA (100 μmol/L) did not influence HCC cell growth and induce apoptosis. However, CAI#1 or CA-IX siRNA at these concentrations enhanced the apoptosis induced by 3-BP (100 μmol/L). This enhancement was attributed to increased ER stress and JNK activation, as compared with 3-BP alone. Furthermore, a clinic pathological analysis of 69 HCC patients revealed that tumor CA-IX intensity was inversely related to E-cadherin intensity.

Conclusion: Inhibition of hypoxia-induced CA-IX enhances hexokinase II inhibitor-induced HCC apoptosis. Furthermore, CA-IX expression profiles may have prognostic implications in HCC patients. Thus, the inhibition of CA-IX, in combination with a hexokinase II inhibitor, may be therapeutically useful in patients with HCCs that are aggressively growing in a hypoxic environment.

Keywords: hepatocellular carcinoma; hypoxia; intracellular acidification; carbonic anhydrase-IX; hexokinase II; apoptosis

Acta Pharmacologica Sinica (2011) 32: 912–920; doi: 10.1038/aps.2011.24; published online 13 Jun 2011

Introduction

Hepatocellular carcinoma (HCC) is one of the most aggressive malignancies originating from the diseased liver[1–3]. HCCs are characteristically hypervascular; therefore, transarterial chemoembolization (TACE) is considered one of the favorable treatment options for unresectable HCCs. However, cells that survive in HCC nodules despite TACE treatment, which confers a robust hypoxic insult, sometimes grow more rapidly than those in neighboring nodules[4]. Moreover, HCCs occasionally exhibit an infiltrating rather than mass-forming growth pattern[5, 6], and these advanced infiltrative HCCs seldom show hypervascularity, grow more rapidly, and have a poorer prognosis than mass-forming hypervascular tumors. Therefore, hypoxia seems to promote signals that allow HCC cells to survive and proliferate in a hypoxic environment[7].

In the hypoxic state, a glycolytic system replaces oxidative phosphorylation as a salvage pathway for generating adenosine triphosphate[7]. Many glycolytic enzymes and glucose transporters are induced by hypoxia inducible factor-1 (HIF-1) through hypoxia response elements in their promoters[8]. HIF-1 also induces the two lactate dehydrogenase isoforms, LDH-5 and LDH-A, and pyruvate dehydrogenase kinase 1. These lactate dehydrogenase isoforms convert pyruvate to lactate, and pyruvate dehydrogenase kinase 1 prevents pyruvate from entering the tricarboxylic acid cycle, which enables the switch to a glycolytic metabolism[8]. Furthermore, hexokinase (HK) is the first enzyme in this pathway and is essential for maintaining the high glycolytic phenotype[9]. We

* To whom correspondence should be addressed.
E-mail yoonjh@snu.ac.kr
Received 2010-11-28 Accepted 2011-02-28

previously demonstrated that hypoxia stimulates HCC cell growth by inducing HK II expression[7], and *in vivo* HK II inhibition reveals an anti-tumor effect through the induction of apoptosis[10]. Glycolysis produces excessive amounts of lactate and carbon dioxide (CO_2) as by-products. However, these waste products are not efficiently removed, due to the high tumor interstitial pressure and defective vasculature[11, 12], and the resulting acidic milieu causes transient intracellular acidification, which is incompatible with cell growth and survival. Thus, tumor cells that are either located within the hypovascular tumor or reside in the center of large tumors are exposed to a hypoxia-induced acidic microenvironment; however, cancer cells adapt to this acidic setting and continue to grow.

Carbonic anhydrase-IX (CA-IX) is a transmembrane protein with a catalytic site in the extracellular space, and it is involved in lowering pH by expediting the pericellular metabolism of CO_2 in a collaboration with bicarbonate transporters[13]. In response to hypoxia, HIF-1 directly activates *CA9* gene transcription and up-regulates CA-IX protein expression[8]. Although CA-IX is expressed in few normal tissues, it is expressed in many cancers, and its overexpression was reported to be related to poor prognosis[14, 15]. Based on this knowledge, we postulated that CA-IX is one of the possible mechanisms by which HCC adapts to the acidic tumor milieu. Therefore, in this study, we aimed to examine whether CA-IX is induced by hypoxia in HCC cells, and we evaluated its clinical implications in HCC patients.

Materials and methods

Cell culture

Huh-7 and HepG2 cells, which were derived from a well-differentiated HCC, were used in this study. Cells were grown in DMEM supplemented with 10% fetal bovine serum, streptomycin (100 mg/L), and penicillin (100 U/mL). Cell proliferation assays were performed using 3% fetal bovine serum, and the other experiments were performed using cells that were serum-starved overnight to avoid serum inducing signals. Depending on the specific experiment, cells were incubated either under standard culture conditions (20% O_2 and 5% CO_2 at 37 °C) or under hypoxic conditions (1% O_2, 5% CO_2, and 94% N_2 at 37 °C).

Chemicals and reagents

3-Bromopyruvate (3-BP) and carbonic anhydrase inhibitor (CAI) #1 sulfonamide [4-(2-aminoethyl)-benzenesulfonamide] were obtained from Sigma-Aldrich, Inc (St Louis, MO, USA). SP600125 (a c-Jun NH_2-terminal kinase (JNK) inhibitor) was obtained from Biomol Research Laboratories (Plymouth Meeting, PA, USA).

Cell proliferation

The CellTiter 96 Aqueous One Solution cell proliferation assay (Promega, Madison, WI, USA) was used to measure cell proliferation. In this assay, dehydrogenase enzymes convert the colorimetric MTS reagent [3,4-(5-dimethylthiazole-2-yl)-5-(3-carboxymethoxyphenyl)-2-(4-sulfophenyl)-2H-tetrazolium salt] into soluble formazan in only the metabolically active and proliferating cells. After each treatment, 20 μL of dye solution was added to each well of a 96-well plate, which was then incubated for 2 h. Afterward, the 490 nm absorbance was measured with an ELISA plate reader (Molecular Devices, Sunnyvale, CA, USA).

Quantitation of apoptosis

The levels of apoptosis were evaluated using the nuclear binding dye 4′,6-diamidino-2-phenylindole dihydrochloride (DAPI) to measure apoptotic cells by fluorescence microscopy (Zeiss, Germany). The cells were treated with DAPI for 30 min and evaluated by fluorescence microscopy. Apoptotic cells were defined as those containing nuclear fragmentation and condensed chromatin. The percentage of apoptotic cells was calculated as the ratio of apoptotic cells to total counted cells ×100. For each treatment, a minimum of 400 cells was counted.

Immunoblot assay

Cells were lysed for 20 min on ice in lysis buffer (50 mmol/L Tris-HCl, pH 7.4, 1% Nonidet P-40, 0.25% sodium deoxycholate, 150 mmol/L NaCl, 1 mmol/L EDTA, 1 mmol/L phenylmethylsulfonyl fluoride, 1 mmol/L Na_3VO_4, 1 mmol/L NaF, and 1 μg/mL each of aprotinin, leupeptin, and pepstatin), and they were centrifuged at 14 000×*g* for 10 min at 4 °C. Samples were resolved by sodium dodecyl sulfate polyacrylamide gel electrophoresis, transferred to nitrocellulose membranes, blotted with appropriate primary antibodies, and incubated with peroxidase-conjugated secondary antibodies (Biosource International, Camarillo, CA, USA). Bound antibodies were visualized using a chemiluminescent substrate (ECL; Amersham, Arlington Heights, IL, USA) and exposed to Kodak X-OMAT film. The primary antibodies used included mouse anti-CA-IX and mouse anti-phospho-eukaryotic initiation factor 2α (eIF2α), which were obtained from Santa Cruz Biotechnology, Inc (Santa Cruz, CA, USA), and rabbit anti-caspase 7, rabbit anti-caspase 8, rabbit anti-caspase 9, mouse anti-phospho-JNK, rabbit anti-phospho-p42/44, and rabbit anti-phospho-Akt, which were obtained from Cell Signaling Technology Inc (Danvers, MA, USA). Rabbit anti-E-cadherin was obtained from BD Transduction Laboratories (San Jose, CA, USA). An image analyzer (LAS-1000; Fuji Photo Film, Tokyo, Japan) was used to detect images, and densitometric analyses were performed using Image Gauge software (Fuji Photo Film). Arbitrary units were calculated by densitometric scanning of the intensity of CA-IX relative to actin intensity, setting the 0 h data point to 1.

Small interfering RNA (siRNA) transfection

CA-IX-specific siRNA was obtained from Dharmacon (Lafayette, CO, USA). Huh-7 and HepG2 cells were transfected with CA-IX-specific siRNA and incubated at concentrations ranging from 0 to 200 μmol/L, in a hypoxic state. Cells were lysed after 24 h, and immunoblot analysis was performed with anti-CA-IX and anti-actin antibodies.

Tissue array and immunohistochemical analyses of surgical specimens

We retrospectively evaluated HCC tissue specimens from 69 HCC patients (male, 89.9%; mean age 52±9 years) who had undergone TACE followed by surgical resection at Seoul National University Hospital, Seoul, Korea, between June 1994 and December 1998. The study protocol was approved by the Institutional Review Board of Seoul National University Hospital.

Tumor specimens from each patient were processed into 10% neutral formalin fixed, paraffin-embedded blocks. Tumor staging was evaluated in accordance with the American Joint Committee on Cancer (AJCC) staging system, 6th edition[16]. All tumors were histologically diagnosed, graded according to Edmondson's scale, and grouped as either low grade (I or II) or high grade (III or IV). Tumors were also stratified by multiplicity and the presence or absence of microscopic vascular invasion. For immunohistochemical staining, all specimens were evaluated using a tissue-array method. Core tissue biopsies (2 mm in diameter) were taken from individual paraffin embedded tissues (donor blocks) and arranged in a new recipient paraffin block (tissue array block) using a trephine apparatus (Superbiochips Laboratories, Seoul, Korea). Immunohistochemical staining was performed with E-cadherin (BD Transduction Laboratories) and CA-IX (Santa Cruz Biotechnology Inc) antibodies, using a streptavidin peroxidase-based procedure after microwave antigen retrieval. The immunoreactive intensity for each case was scored as none, weak, moderate, or strong. The extent of immunoreactivity was scored as less than one-third or more than one-third for E-cadherin, and it was scored as less than 10%, 10% to 50%, or more than 50% for CA-IX. Histological examinations were performed by an experienced pathologist (Ja-june JANG) who was unaware of any clinical information.

Statistical analysis

All cell-based experimental data were acquired from at least three independent experiments, with a minimum of three separate isolations, and were expressed as the mean±standard deviation (SD). Statistical evaluations of numeric variables in each group were conducted using the Mann-Whitney *U* test. The clinicopathological data were analyzed using the chi-square test. All statistical analyses were performed using SPSS version 17.0 (SPSS, Inc, Chicago, IL, USA). Statistical significance was defined as a P value less than 0.05.

Results

Hypoxia induced CA-IX expression in HCC cells

We first investigated whether CA-IX expression is hypoxia-inducible in HCC cells. For this purpose, the two different human HCC cell lines were serum starved and cultured in a hypoxic state. Hypoxia increased CA-IX expression in both Huh-7 and HepG2 cells (Figure 1A). This finding suggests that HCC cells do express CA-IX and that its expression is hypoxia-inducible in different cell lines.

The effect of CA-IX inhibition on HCC cellular growth or apoptotic cell death

To inhibit CA-IX, either its expression was suppressed by siRNA transfection (Figure 1B) or its activity was inhibited by sulfonamide, a carbonic anhydrase inhibitor #1 (CAI#1). Both CA-IX siRNA and CAI#1 treatment failed to suppress HCC cell growth under normoxic or hypoxic culture conditions (P>0.05) (Figure 1C). In addition, neither CA-IX siRNA nor CAI#1 treatment significantly induced HCC cell apoptosis under hypoxic culture conditions (P>0.05) (Figure 1D). These observations indicate that changes in CA-IX expression or activity do not affect HCC cell growth or survival.

Enhanced HK II inhibitor-induced apoptosis by CA-IX inhibition in HCC cells

Because hypoxia induces both HK II[7] and CA-IX[13] expression through HIF-1, we hypothesized that simultaneously blocking these two enzymes would enhance 3-BP-induced apoptosis in HCC cells under hypoxic conditions. When HCC cells that were CA-IX-inhibited with either siRNA or CAI#1 were treated with 3-BP under hypoxic conditions, apoptosis was significantly enhanced compared to cells treated with 3-BP alone (Figure 2A). However, this enhancement was not observed in cells similarly treated under normoxic culture conditions (Figure 2B). Thus, these findings demonstrate that the enhancement of 3-BP-induced HCC cell apoptosis by CA-IX inhibition is hypoxia specific.

Mechanism of apoptosis enhancement by CA-IX inhibition

To explore possible mechanisms of enhanced 3-BP-induced apoptosis through CA-IX inhibition, we next explored which apoptotic signaling pathway was more activated in 3-BP/CAI#1-treated cells compared to cells treated with 3-BP alone. When cells were treated with both 3-BP and CAI#1, the activation of caspases 9 and 7 was more prominent than in cells treated with 3-BP alone (Figure 2C), indicating that the activation of the mitochondrial apoptotic signaling pathway is enhanced by CA-IX inhibition. We then explored kinase signals that are known to regulate apoptosis and found that pro-apoptotic JNK was more promptly and potently activated in cells treated with 3-BP and CAI#1 than in cells treated with 3-BP alone, whereas prosurvival signals such as p42/44 and Akt were unaffected (Figure 2D). Because JNK activation might depend on endoplasmic reticulum (ER) stress, we evaluated whether ER stress is activated in 3-BP and CAI#1-treated cells. Indeed, eIF2α phosphorylation, which indicates ER stress activation, was prominent in these cells (Figure 2D). Finally, we examined whether JNK activation participated in 3-BP-induced apoptosis enhancement by CA-IX inhibition and found that JNK inhibition did attenuate this enhancement (Figure 2E). Therefore, these findings collectively suggest that CA-IX inhibition may induce ER stress-dependent JNK activation in 3-BP-treated HCC cells and thus enhance apoptotic cell death in these cells.

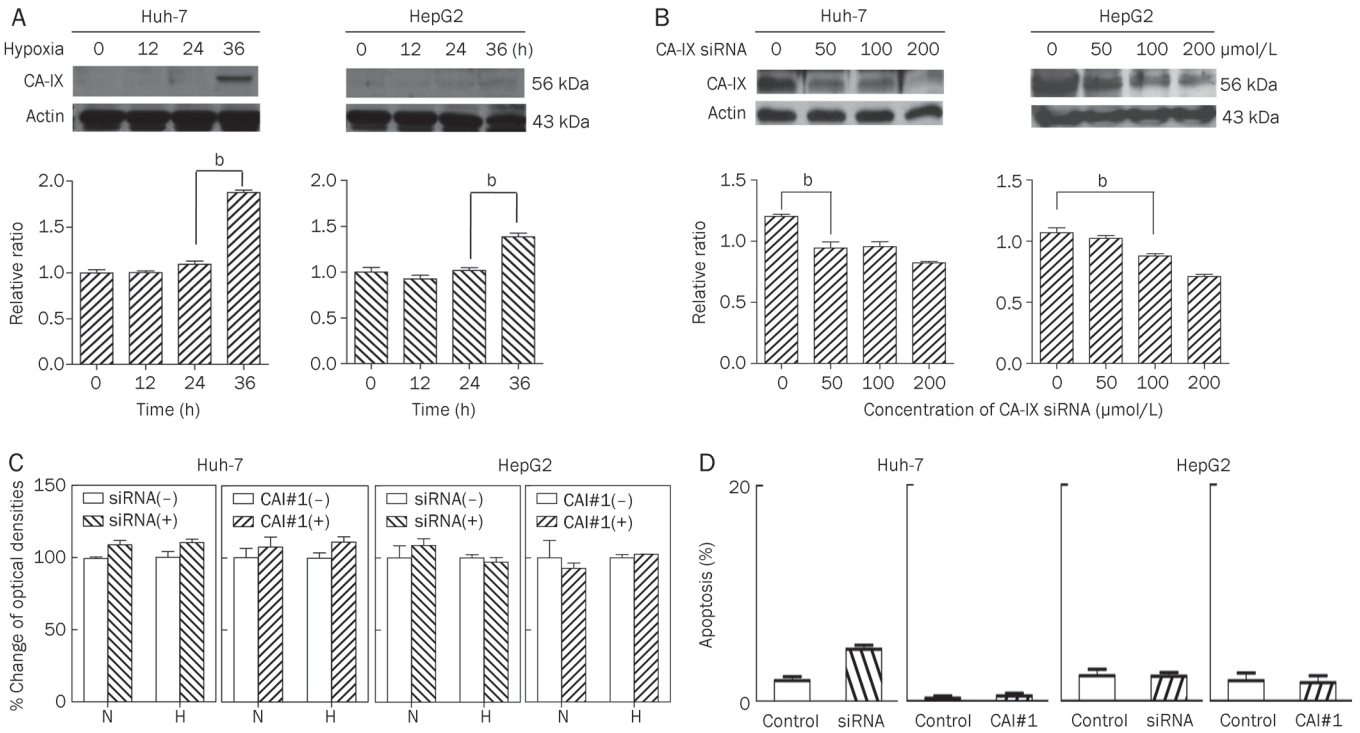

Figure 1. Hypoxia-induced CA-IX expression and the effect of its inhibition in human HCC cell lines. (A) Hypoxia increased CA-IX expression in HCC cells. Huh-7 and HepG2 cells were cultured under hypoxic conditions for the indicated times. Equivalent amounts of proteins were immunoblotted using anti-CA-IX and anti-actin antibodies. Densitometric analyses were performed, and data are expressed as the mean±SD of relative intensity ratios of CA-IX to actin. $^{b}P<0.05$ *vs* 24 h. (B) CA-IX expression was efficiently reduced by CA-IX-specific siRNA in a dose-dependent manner. Huh-7 and HepG2 cells were transfected with CA-IX siRNA for 24 h and incubated at concentrations ranging from 0 to 200 μmol/L in a hypoxic state. Cells were lysed after 24 h, and immunoblot analysis was performed using anti-CA-IX and anti-actin antibodies. Densitometric analyses were performed and data were expressed as the mean±SD of relative intensity ratios of CA-IX to actin. $^{b}P<0.05$ *vs* 0 μmol/L. (C) Inhibition of CA-IX expression failed to influence the HCC cell growth. Huh-7 and HepG2 cells were treated with either CA-IX siRNA (0 and 100 μmol/L) or CAI#1 (0 and 1 mmol/L) for 24 h with 3% fetal bovine serum under normoxic or hypoxic culture conditions. Cell growth was determined using the MTS assay. (D) Inhibition of CA-IX expression failed to modulate HCC cell apoptosis. Huh-7 and HepG2 cells were serum starved for 15 h and then treated with CA-IX siRNA (0 and 100 μmol/L) or CAI#1 (0 and 400 μmol/L). Apoptotic cells were DAPI stained, visualized by fluorescent microscopy, and counted after 4 and 6 h of hypoxia, respectively. Data were expressed as the mean±SD. siRNA, CA-IX siRNA; N, normoxia; H, hypoxia.

Prognostic implications of CA-IX expression in HCC patients

Because we found that CA-IX modulation may be therapeutically important in HCC cells, particularly under hypoxic conditions, and could also confer a potent survival signal to cells, we next evaluated whether CA-IX is expressed in human HCC tissues and, if so, whether its expression is linked to patient prognosis. For this purpose, we employed a tissue array and performed clinicopathological analysis using HCC tissues from 69 patients who had undergone TACE prior to surgical resection because TACE may powerfully activate hypoxia-induced signals in HCC cells. Of the 69 specimens, 48, 17, and 4 cases showed none, weak, or moderate CA-IX cell membrane immunoreactivity, respectively. Representative cases are shown in Figure 3A. The clinicopathological findings are summarized in Table 1. Following clinicopathological analysis, there was no correlation between the extent of CA-IX immunoreactivity and clinicopathological variables (Table 2). However, we found that tumoral CA-IX intensity was inversely related to E-cadherin intensity (Figure 3B, Table 3). E-cadherin is representative of classic cadherins, and its down-regulation has been frequently associated with invasiveness, metastasis, and a poor prognosis in a variety of human cancers, including HCC[17, 18]. This finding suggests that CA-IX expression in HCC tissues may have prognostic implications in HCC patients.

Decreased E-cadherin expression by CA-IX in HCC cells

We next evaluated whether E-cadherin expression levels are affected by modulation of CA-IX expression *in vitro*. When CA-IX expression was suppressed by siRNA in HCC cells, E-cadherin expression increased (Figure 3C). This finding is compatible with that of a previous study, in which CA-IX was found to decrease E-cadherin levels in the Madin-Darby Canine kidney cell line[19], and our results show that tumoral CA-IX intensity is inversely related to E-cadherin intensity. Altogether, these findings suggest that the induction of CA-IX expression may attenuate E-cadherin expression, thus leading to epithelial-mesenchymal transition potentiating invasiveness

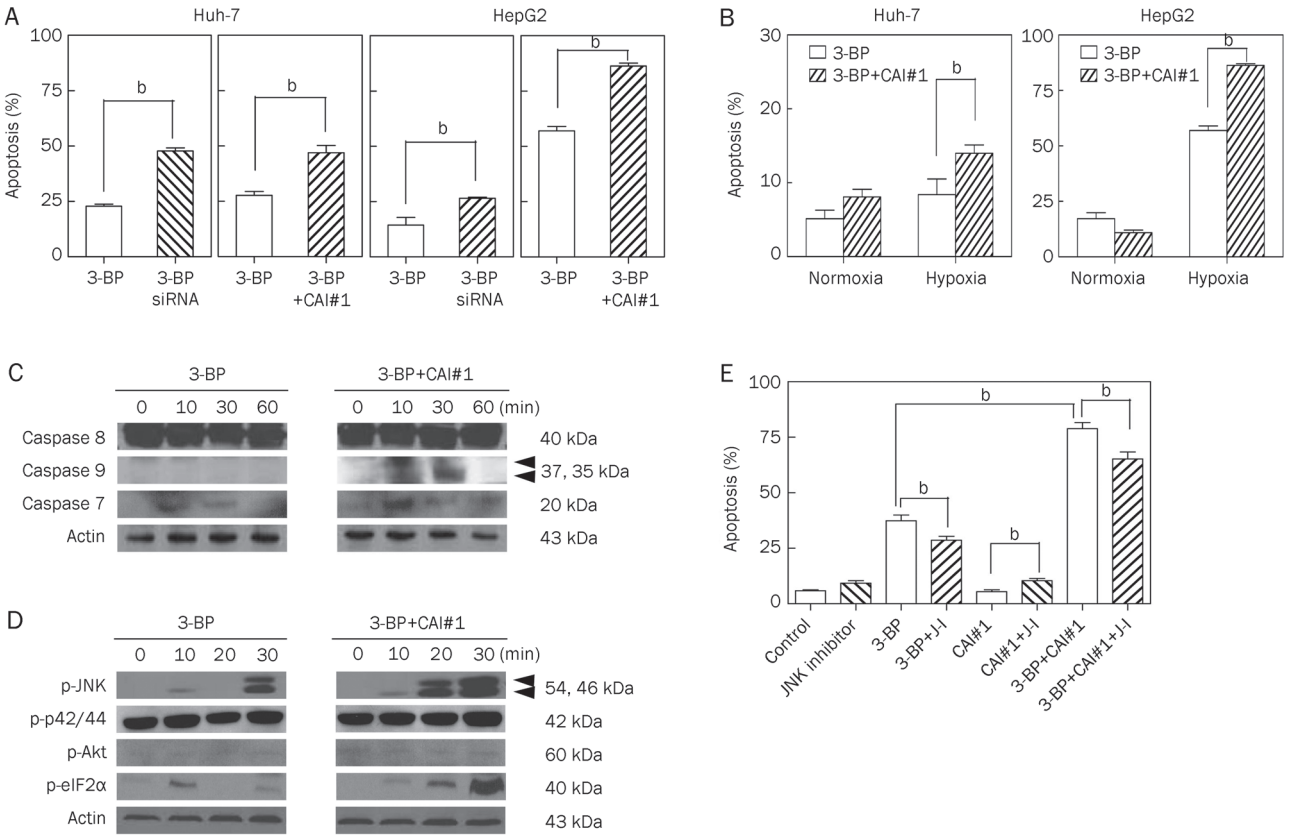

Figure 2. Effect of CA-IX inhibition on 3-BP-induced apoptosis in hypoxic HCC cells. (A) CA-IX inhibition enhances 3-BP-induced apoptosis in hypoxic HCC cells. Huh-7 and HepG2 cells were serum starved for 15 h and then treated with 3-BP (100 μmol/L) in the presence or absence of either CA-IX siRNA (0 and 100 μmol/L) or CAI#1 (0 and 400 μmol/L) for 24 h. Apoptotic cells were counted by DAPI staining and fluorescent microscopy after 4 and 6 h of hypoxia, respectively. (B) Apoptosis enhancement by CA-IX inhibition is a hypoxia-specific phenomenon. Huh-7 and HepG2 cells were serum starved for 24 h either under normoxic or hypoxic conditions and then treated with 3-BP (100 μmol/L) in the presence or absence of CAI#1 (0 and 1 mmol/L) for 5 h. Apoptotic cells were then counted by DAPI staining and fluorescent microscopy. (C) The activation of caspases 7 and 9 was more prominent in 3-BP/CAI#1-treated cells than in cells treated with 3-BP alone, and (D) CA-IX inhibition induces ER stress-dependent JNK activation. Huh-7 cells were serum starved, cultured under hypoxic conditions, and then treated with 3-BP (100 μmol/L) in the presence or absence of CAI#1 (0 and 1 mmol/L) for the indicated times. Cells were lysed and immunoblot analysis was performed using anti-caspase 7, anti-caspase 8, anti-caspase 9, anti-phospho-JNK, anti-phospho-p42/44, anti-phospho-Akt, anti-phospho-eIF2α, and anti-actin antibodies. (E) JNK activation participates in 3-BP-induced apoptosis enhancement by CA-IX inhibition. Huh-7 cells were serum starved for 24 h under hypoxic culture conditions and then treated with 3-BP (0 and 100 μmol/L) in the presence or absence of CAI#1 (0 and 1 mmol/L) and/or JNK inhibitor (0 and 10 μmol/L) for 6 h. Apoptotic cells were counted by DAPI staining and fluorescent microscopy. Data were expressed as the mean±SD. $^{b}P<0.05$. siRNA, CA-IX siRNA; J–I, JNK inhibitor.

and metastasis.

Discussion

The principal findings of this study relate to hypoxia-induced activation of an intracellular pH maintenance mechanism in human HCC cells. Specifically, this study demonstrates that hypoxia stimulates the expression of CA-IX in HCC cells. Furthermore, although CA-IX inhibition alone failed to induce significant HCC cell growth suppression or apoptosis, CA-IX inhibition enhanced 3-BP-induced apoptotic cell death mediated by ER stress-dependent JNK activation. In addition, HCC tissues express CA-IX, and tumoral CA-IX intensity is inversely related to E-cadherin intensity, thus potentiating invasiveness and metastasis. Each of these findings is discussed in further detail below.

Among CA isoenzymes, it has become clear that CA-IX is the most important enzyme for tumorigenesis and prognostication in various tumors including pancreatic[20] and rectal[15] cancers. In the liver, it has been reported that 78% of cholangiocarcinomas show a positive reaction for CA-IX, whereas HCCs show a weak immunoreactivity in only 33% of cases[21]. Furthermore, in contrast to other malignancies, the prognostic role of CA-IX in HCC has not been fully elucidated. In the present study, we observed that CA-IX is expressed in different HCC cell lines under hypoxic culture conditions. This finding suggests that CA-IX may participate in intracellular pH maintenance under innate intratumoral hypoxic conditions or during hypoxic insult such as that induced by TACE. However, HCC cell death or growth was not significantly affected by CA-IX inhibition alone. This can be explained by

Table 1. Baseline characteristics of the HCC patients.

Variable		*n* (%)
Age (year)	<50	28 (40.6)
	≥50	41 (59.4)
Sex	Male	62 (89.9)
	Female	7 (10.1)
Child-Pugh class	A	69 (100)
Etiology of chronic hepatitis	HBV	50 (72.5)
	HCV	8 (11.6)
	HBV + HCV	4 (5.8)
	Non-HBV, Non-HCV	7 (10.1)
AJCC T stage*	T1	51 (73.9)
	T2 or T3	18 (26.1)
Tumor multiplicity	Yes	3 (4.3)
	No	66 (95.7)
Vascular invasion	Yes	18 (26.1)
	No	51 (73.9)
Edmondson's grade	Low (I or II)	37 (53.6)
	High (III or IV)	32 (46.4)
E-cadherin intensity	None to weak	29 (42.0)
	Moderate to strong	40 (58.0)
E-cadherin extent	<1/3	28 (40.6)
	≥1/3	41 (59.4)
CA-IX intensity	None	48 (69.6)
	Weak	17 (24.6)
	Moderate	4 (5.8)
CA-IX extent	None	48 (69.6)
	<0%	7 (10.1)
	10%, <50%	11 (16.0)
	≥50%, ≤100%	3 (4.3)

* According to the American Joint Committee on Cancer staging system (6th edition, 2002).
HBV, hepatitis B virus; HCV, hepatitis C virus; CA-IX, carbonic anhydrase-IX.

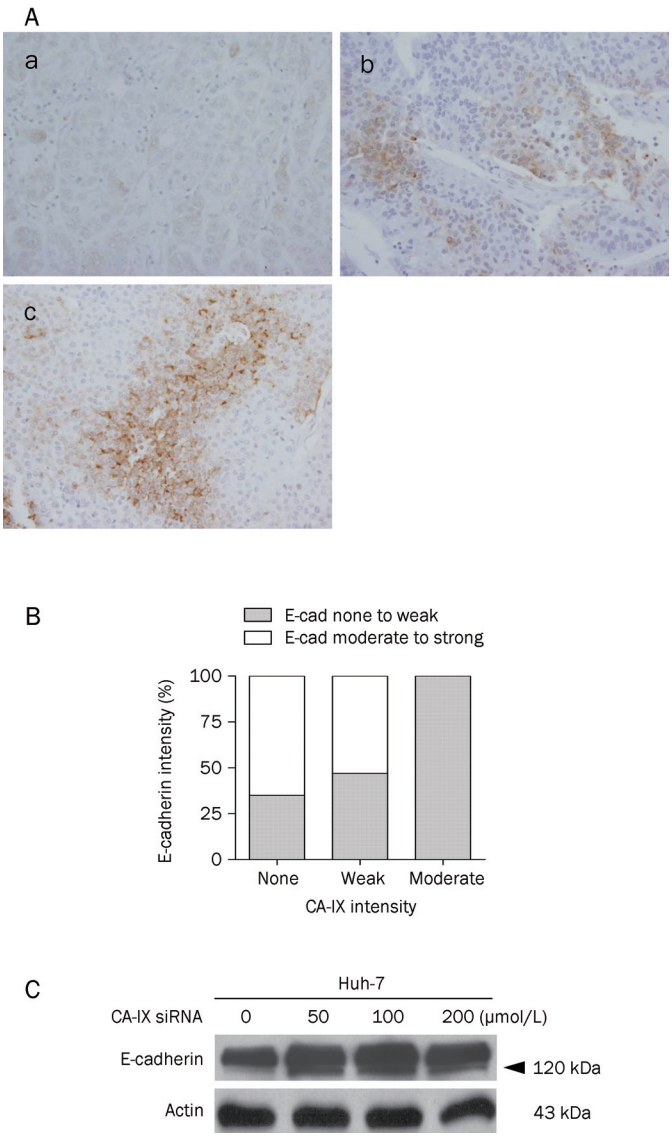

Figure 3. CA-IX expression in HCC tumor tissues and its prognostic implications in HCC patients. (A) Representative immunohistochemical staining showed (a) no, (b) weak, and (c) moderate CA-IX immunoreactivity in human HCC tumor tissues. Original magnification ×400. (B) HCC tumoral CA-IX intensity is inversely related to E-cadherin intensity. Statistical significance was analyzed using the chi-square test. P=0.024. (C) E-cadherin expression increases when CA-IX is inhibited. Huh-7 cells were transfected with CA-IX siRNA for 24 h and incubated at concentrations ranging from 0 to 200 μmol/L in a hypoxic state for 24 h. Cells were then lysed, and immunoblot analysis was performed using anti-E-cadherin and anti-actin antibodies. E-cad, E-cadherin.

the fact that tumor cells can regulate their cytoplasmic pH via the Na^+/H^+ exchanger, the H^+/monocarboxylate transporter, and the vacuolar H^+/ATP pump in addition to CA-IX[8].

Because hypoxia induces both HK II[7] and CA-IX[13] expression through HIF-1, we postulated that simultaneously blocking these two enzymes could enhance 3-BP-induced apoptosis in HCC cells. Indeed, we confirmed that 3-BP-induced HCC cell apoptosis was significantly enhanced by CA-IX inhibition and that this enhancement was hypoxia specific. This finding indicates that a combinatorial strategy is more effective for HCCs under hypoxic conditions, such as in advanced infiltrative HCCs, which seldom show hypervascularity, grow more rapidly, and have a poorer prognosis than mass-forming hypervascular subtypes.

We explored the possible mechanism of apoptosis enhancement by CA-IX inhibition and found that the activation of caspases 9 and 7 by 3-BP/CAI#1 was more prominent than the activation induced by 3-BP alone, which suggests that activation of mitochondrial apoptotic signaling is augmented by CA-IX inhibition. In addition, we found that the proapoptotic JNK was more promptly and potently activated in cells treated with both 3-BP and a CA-IX inhibitor compared to cells treated with 3-BP alone. JNK performs a crucial role in modulating the function of proapoptotic proteins placed in the mitochondria[22]. JNK has been shown to be required for the release of cytochrome *c* from the inner membrane space of mitochondria. Released cytochrome *c*, in combination with apoptotic peptidase activating factor 1 and caspase 9, forms apoptosomes that trigger the caspase 9 cascade[23]. It has been previously

Table 2. Relationships between the extent of CA-IX immunoreactivity and clinicopathological variables.

	CA-IX extent *n* (% within CA-IX extent)				
	None	<10%	≥10%, <50%	≥50%, ≤100%	*P**
Age (year)					
<50	17 (35.4)	4 (57.1)	7 (63.6)	0 (0)	0.490
≥50	31 (64.6)	3 (42.9)	4 (36.4)	3 (100)	
Sex					
Male	44 (91.7)	6 (85.7)	9 (81.8)	3 (100)	0.618
Female	4 (8.3)	1 (14.3)	2 (18.2)	0 (0)	
Viral hepatitis					
HBV	35 (72.9)	5 (71.4)	9 (81.8)	1 (33.3)	0.360
HCV	6 (12.5)	1 (14.3)	0 (0)	1 (33.3)	
HBV+HCV	2 (4.2)	0 (0)	2 (18.2)	0 (0)	
Non-HBV, Non-HCV	5 (10.4)	1 (14.3)	0 (0)	1 (33.3)	
AJCC T stage†					
T1	36 (75.0)	5 (71.4)	7 (63.6)	3 (100)	0.979
T2 or T3	12 (25.0)	2 (28.6)	4 (36.4)	0 (0)	
Tumor multiplicity					
Yes	2 (4.2)	1 (14.3)	0 (0)	0 (0)	0.674
No	46 (95.8)	6 (85.7)	11 (100)	3 (100)	
Vascular invasion					
Yes	13 (27.1)	1 (14.3)	4 (36.4)	0 (0)	0.785
No	35 (72.9)	6 (85.7)	7 (63.6)	3 (100)	
Edmondson's grade					
Low (I or II)	26 (54.2)	3 (42.9)	5 (45.5)	3 (100)	0.669
High (III or IV)	22 (45.8)	4 (57.1)	6 (54.5)	0 (0)	
E-cadherin intensity					
None-to-weak	17 (35.4)	4 (57.1)	6 (54.5)	2 (66.7)	0.108
Moderate-to-strong	31 (64.6)	3 (42.9)	5 (45.5)	1 (33.3)	
E-cadherin extent					
<1/3	19 (39.6)	3 (42.9)	4 (36.4)	2 (66.7)	0.672
≥1/3	29 (60.4)	4 (57.1)	7 (63.6)	1 (33.3)	

* The chi-square test was used for group comparisons.
† According to the American Joint Committee on Cancer staging system (6th edition, 2002).
HBV, hepatitis B virus; HCV, hepatitis C virus; CA-IX, carbonic anhydrase-IX.

Table 3. Relationships between the intensity of CA-IX immunoreactivity and clinicopathological variables.

	CA-IX intensity *n* (% within CA-IX intensity)			
	No staining	Weak	Moderate	*P**
Age (year)				
<50	17 (35.4)	9 (52.9)	2 (50.0)	0.238
≥50	31 (64.6)	8 (47.1)	2 (50.0)	
Sex				
Male	44 (91.7)	15 (88.2)	3 (75.0)	0.325
Female	4 (8.3)	2 (11.8)	1 (25.0)	
Viral hepatitis				
HBV	35 (72.9)	11 (64.6)	4 (100)	0.808
HCV	6 (12.5)	2 (11.8)	0 (0)	
HBV+HCV	2 (4.2)	2 (11.8)	0 (0)	
Non-HBV, Non-HCV	5 (10.4)	2 (11.8)	0 (0)	
AJCC T stage†				
T1	36 (75.0)	13 (76.5)	2 (50.0)	0.495
T2 or T3	12 (25.0)	4 (23.5)	2 (50.0)	
Tumor multiplicity				
Yes	2 (4.2)	1 (5.9)	0 (0)	0.931
No	46 (95.8)	16 (94.1)	4 (100)	
Vascular invasion				
Yes	13 (27.1)	3 (17.6)	2 (50.0)	0.825
No	35 (72.9)	14 (82.4)	2 (50.0)	
Edmondson's grade				
Low (I or II)	26 (54.2)	9 (52.9)	2 (50.0)	0.869
High (III or IV)	22 (45.8)	8 (47.1)	2 (50.0)	
E-cadherin intensity				
None to weak	17 (35.4)	8 (47.1)	4 (100)	0.024
Moderate to strong	31 (64.6)	9 (52.9)	0 (0)	
E-cadherin extent				
<1/3	19 (39.6)	6 (35.3)	3 (75.0)	0.443
≥1/3	29 (60.4)	11 (64.7)	1 (25.0)	

* The chi-square test was used for group comparisons.
† According to the American Joint Committee on Cancer staging system (6th edition, 2002).
HBV, hepatitis B virus; HCV, hepatitis C virus; CA-IX, carbonic anhydrase-IX.

reported that phosphorylated CA-IX could cooperate with the regulatory subunit of phosphatidylinositol 3 kinase and induce Akt activation, which could participate in cancer progression[24]. However, in contrast to this previous study, phosphorylation of both the prosurvival Akt and p42/44 MAPK were not affected by 3-BP or 3-BP+CA-IX inhibitor treatment in the present study.

In a recent study, it was reported that 3-BP may induce ER stress and thereby cause apoptosis in human HCC cell lines[25]. Because ER stress induction may activate JNK[8, 26], we next evaluated whether ER stress is more activated in cells treated with 3-BP and a CA-IX inhibitor than in cells treated with 3-BP alone, and we found that eIF2α phosphorylation was more prominent in cells treated with 3-BP and a CA-IX inhibitor. ER stress sensors initiate an unfolded protein response (UPR) that results in the phosphorylation of its main substrate, eIF2α,

and direct binding of the eIF2α-dependent translationally regulated gene activating transcription factor 4 to the *CA9* promoter[27]. These data suggest that 3-BP-induced ER stress can trigger CA-IX expression as one of the UPRs that reduces ER stress. Thus, the simultaneous inhibition of CA-IX and HK II may disturb ER stress alleviation, thereby leading to ER stress escalation, subsequent JNK activation, and apoptosis enhancement through the mitochondrial activation of caspases 9 and 7. Indeed, in the present study, we observed that JNK inhibition attenuated apoptosis enhancement.

Acidic extracellular pH inhibits the binding of cells to CA-IX, suggesting that the CA-IX adhesion ability can be modulated by the tumor milieu[28]. CA-IX has also been implicated in intercellular adhesion[19]. In this previous study, it was found that CA-IX is localized with the key adhesion molecule E-cadherin, internalizes in response to the same external stimuli as E-cadherin, and reduces cell-to-cell adhesion by destabilizing the association between E-cadherin and the cytoskeleton through a method that involves direct binding of CA-IX to β-catenin[19]. In the present study, tumoral CA-IX intensity was found to be inversely related to E-cadherin intensity, increases of E-cadherin intensity may predict a favorable prognosis[29]. Furthermore, when CA-IX expression was suppressed by siRNA, E-cadherin expression was increased. The ability of CA-IX to adhere to β-catenin[19] is consistent with the suggestion that hypoxia can promote tumor invasion by decreasing E-cadherin-mediated intercellular adhesion, offering the possibility that CA-IX participates in epithelial-mesenchymal transition[30, 31]. Moreover, an alkaline intracellular pH and an acidic extracellular pH have been hypothesized to increase tumor growth[32]. Thus, in CA-IX-expressing HCCs, CA-IX inhibition could be therapeutically useful for reducing tumor survival or invasiveness and metastasis.

This study demonstrates that the inhibition of hypoxia-inducible CA-IX enhances 3-BP-induced HCC cell apoptosis and that CA-IX expression profiles may have prognostic implications in HCC patients. Thus, the blockage of CA-IX in combination with hexokinase II inhibitor treatment may be therapeutically useful in patients with large or infiltrative hypovascular HCCs that are aggressively growing in a hypoxic environment.

Acknowledgements

This study was funded, in part, by the Korea Health 21 R&D Project [No 0412-CR01-0704-0001], by a Seoul National University Hospital Research Grant [03-2010-021-0], and by a grant from the Liver Research Foundation of Korea. The authors thank Ms Sung-hee LEE and Ms Soo-mi LEE for excellent technical assistance.

Author contribution

Su-jong YU and Jung-hwan YOON designed the research; Su-jong YU, Eun-sun JANG, Min-sun KWAK, and Eun-ju CHO performed the research; Su-jong YU, Sun-jung MYUNG, and Jung-hwan YOON analyzed the data; Ja-june JANG performed histological examinations; Jung-hwan YOON, Jeong-hoon LEE, Yoon-jun KIM, and Hyo-suk LEE critically revised the manuscript for important intellectual content; Su-jong YU wrote the paper.

References

1 Liang TJ, Jeffers LJ, Reddy KR, de Medina M, Parker IT, Cheinquer H, *et al.* Viral pathogenesis of hepatocellular carcinoma in the United States. Hepatology 1993; 18: 1326–33.
2 Colombo M, de Franchis R, Del Ninno E, Sangiovanni A, de Fazio C, Tommasini M, *et al.* Hepatocellular carcinoma in Italian patients with cirrhosis. N Engl J Med 1991; 325: 675–80.
3 Koike K. Role of hepatitis viruses in multistep hepatocarcinogenesis. Dig Liver Dis 2001; 33: 2–6.
4 Tezuka M, Hayashi K, Kubota K, Sekine S, Okada Y, Ina H, *et al.* Growth rate of locally recurrent hepatocellular carcinoma after transcatheter arterial chemoembolization: comparing the growth rate of locally recurrent tumor with that of primary hepatocellular carcinoma. Dig Dis Sci 2007; 52: 783–8.
5 Trevisani F, Caraceni P, Bernardi M, D'Intino PE, Arienti V, Amorati P, *et al.* Gross pathologic types of hepatocellular carcinoma in Italian patients. Relationship with demographic, environmental, and clinical factors. Cancer 1993; 72: 1557–63.
6 Weinstein-Oppenheimer CR, Henriquez-Roldan CF, Davis JM, Navolanic PM, Saleh OA, Steelman LS, *et al.* Role of the Raf signal transduction cascade in the *in vitro* resistance to the anticancer drug doxorubicin. Clin Cancer Res 2001; 7 : 2898–907.
7 Gwak GY, Yoon JH, Kim KM, Lee HS, Chung JW, Gores GJ. Hypoxia stimulates proliferation of human hepatoma cells through the induction of hexokinase II expression. J Hepatol 2005; 42: 358–64.
8 Pastorekova S, Zatovicova M, Pastorek J. Cancer-associated carbonic anhydrases and their inhibition. Curr Pharm Des 2008; 14: 685–98.
9 Bustamante E, Morris HP, Pedersen PL. Energy metabolism of tumor cells. Requirement for a form of hexokinase with a propensity for mitochondrial binding. J Biol Chem 1981; 256: 8699–704.
10 Kim W, Yoon JH, Jeong JM, Cheon GJ, Lee TS, Yang JI, *et al.* Apoptosis-inducing antitumor efficacy of hexokinase II inhibitor in hepatocellular carcinoma. Mol Cancer Ther 2007; 6: 2554–62.
11 Helmlinger G, Sckell A, Dellian M, Forbes NS, Jain RK. Acid production in glycolysis-impaired tumors provides new insights into tumor metabolism. Clin Cancer Res 2002; 8: 1284–91.
12 Fukumura D, Jain RK. Tumor microenvironment abnormalities: causes, consequences, and strategies to normalize. J Cell Biochem 2007; 101: 937–49.
13 Pastorekova S, Ratcliffe PJ, Pastorek J. Molecular mechanisms of carbonic anhydrase IX-mediated pH regulation under hypoxia. BJU Int 2008; 101: 8–15.
14 Swinson DE, Jones JL, Richardson D, Wykoff C, Turley H, Pastorek J, *et al.* Carbonic anhydrase IX expression, a novel surrogate marker of tumor hypoxia, is associated with a poor prognosis in non-small-cell lung cancer. J Clin Oncol 2003; 21: 473–82.
15 Korkeila E, Talvinen K, Jaakkola PM, Minn H, Syrjanen K, Sundstrom J, *et al.* Expression of carbonic anhydrase IX suggests poor outcome in rectal cancer. Br J Cancer 2009; 100: 874–80.
16 Greene FL, American Joint Committee on Cancer, American Cancer Society. AJCC cancer staging handbook : from the AJCC cancer staging manual. 6th ed. New York Springer; 2002.
17 Endo K, Ueda T, Ueyama J, Ohta T, Terada T. Immunoreactive E-cadherin, alpha-catenin, beta-catenin, and gamma-catenin proteins in hepatocellular carcinoma: relationships with tumor grade, clinicopathologic parameters, and patients' survival. Hum Pathol 2000; 31: 558–65.

18 Berx G, Cleton-Jansen AM, Nollet F, de Leeuw WJ, van de Vijver M, Cornelisse C*, et al.* E-cadherin is a tumour/invasion suppressor gene mutated in human lobular breast cancers. EMBO J 1995; 14: 6107–15.
19 Svastova E, Zilka N, Zat'ovicova M, Gibadulinova A, Ciampor F, Pastorek J*, et al.* Carbonic anhydrase IX reduces E-cadherin-mediated adhesion of MDCK cells via interaction with beta-catenin. Exp Cell Res 2003; 290: 332–45.
20 Kivela AJ, Parkkila S, Saarnio J, Karttunen TJ, Kivela J, Parkkila AK*, et al.* Expression of transmembrane carbonic anhydrase isoenzymes IX and XII in normal human pancreas and pancreatic tumours. Histochem Cell Biol 2000; 114: 197–204.
21 Saarnio J, Parkkila S, Parkkila AK, Pastorekova S, Haukipuro K, Pastorek J*, et al.* Transmembrane carbonic anhydrase, MN/CA IX, is a potential biomarker for biliary tumours. J Hepatol 2001; 35: 643–9.
22 Aoki H, Kang PM, Hampe J, Yoshimura K, Noma T, Matsuzaki M*, et al.* Direct activation of mitochondrial apoptosis machinery by c-Jun N-terminal kinase in adult cardiac myocytes. J Biol Chem 2002; 277: 10244–50.
23 Dhanasekaran DN, Reddy EP. JNK signaling in apoptosis. Oncogene 2008; 27: 6245–51.
24 Dorai T, Sawczuk IS, Pastorek J, Wiernik PH, Dutcher JP. The role of carbonic anhydrase IX overexpression in kidney cancer. Eur J Cancer 2005; 41: 2935–47.
25 Ganapathy-Kanniappan S, Geschwind JF, Kunjithapatham R, Buijs M, Syed LH, Rao PP*, et al.* 3-Bromopyruvate induces endoplasmic reticulum stress, overcomes autophagy and causes apoptosis in human HCC cell lines. Anticancer Res 2010; 30: 923-35.
26 Szegezdi E, Logue SE, Gorman AM, Samali A. Mediators of endoplasmic reticulum stress-induced apoptosis. EMBO Rep 2006; 7: 880–5.
27 van den Beucken T, Magagnin MG, Savelkouls K, Lambin P, Koritzinsky M, Wouters BG. Regulation of Cited2 expression provides a functional link between translational and transcriptional responses during hypoxia. Radiother Oncol 2007; 83: 346–52.
28 Zavadova Z, Zavada J. Carbonic anhydrase IX (CA IX) mediates tumor cell interactions with microenvironment. Oncol Rep 2005; 13: 977–82.
29 Lin Q, Li M, Shen ZY, Xiong LW, Pan XF, Gen JF*, et al.* Prognostic impact of vascular endothelial growth factor-A and E-cadherin expression in completely resected pathologic stage I non-small cell lung cancer. Jpn J Clin Oncol 2010; 40: 670–6.
30 Beavon IR. Regulation of E-cadherin: does hypoxia initiate the metastatic cascade? Mol Pathol 1999; 52: 179–88.
31 Sanchez-Tillo E, Lazaro A, Torrent R, Cuatrecasas M, Vaquero EC, Castells A*, et al.* ZEB1 represses E-cadherin and induces an EMT by recruiting the SWI/SNF chromatin-remodeling protein BRG1. Oncogene 2010; 29: 3490–500.
32 Martinez-Zaguilan R, Seftor EA, Seftor RE, Chu YW, Gillies RJ, Hendrix MJ. Acidic pH enhances the invasive behavior of human melanoma cells. Clin Exp Metastasis 1996; 14: 176–86.

Acta Pharmacologica Sinica (2011) 32: 921–929
 1671-4083/11 $32.00
www.nature.com/aps

Original Article

A novel positive feedback loop involving FASN/p-ERK1/2/5-LOX/LTB4/FASN sustains high growth of breast cancer cells

Nan HU[1, #], Yu LI[1, #], Yu ZHAO[1], Qi WANG[2], Jia-cong YOU[1], Xiao-dong ZHANG[2, *], Li-hong YE[1, *]

[1]Department of Biochemistry, the Key Laboratory of Bioactive Materials, Ministry of Education; [2]Department of Cancer Research, Key Laboratory of Molecular Microbiology and Technology of Ministry of Education, Institute for Molecular Biology and Biochemistry, College of Life Sciences, Nankai University, Tianjin 300071, China

Aim: To investigate the endogenous signaling pathways associated with high proliferation potential of breast cancer cells.
Methods: Breast cancer cell lines LM-MCF-7 and MCF-7 with high and low proliferation capability were used. The promoter activity of fatty acid synthase (FASN) was examined using luciferase reporter gene assay. The expression level of FASN mRNA was measured using RT-PCR and real time PCR, respectively. The level of leukotriene B4 (LTB4) was determined with ELISA. The expression levels of 5-lipoxygenase (5-LOX) was analyzed using RT-PCR and Western blot, respectively. 5-Bromo-20-deoxyuridine (BrdU) incorporation assay was used to study the proliferation of LM-MCF-7 and MCF-7 cells.
Results: The promoter activity of FASN was significantly higher in LM-MCF-7 cells than MCF-7 cells. Treatment of LM-MCF-7 cells with ERK1/2 inhibitor PD98059 (30–50 μmol/L) or LOX inhibitor NDGA (25 μmol/L) abolished the activation of FASN. Moreover, treatment of LM-MCF-7 cells with the specific 5-LOX inhibitor MK-886 (20–40 μmol/L) or 5-LOX siRNA (50–100 nmol/L) decreased the promoter activity of FASN. The level of LTB4, the final metabolite produced by 5-LOX, was significantly higher in LM-MCF-7 cells than MCF-7 cells. Administration of exogenous LTB4 (1–10 nmol/L) was able to stimulate the promoter activity of FASN in MCF-7 cells. Treatment of LM-MCF-7 cells with the FASN inhibitor cerulenin (10 μmol/L) reduced all the levels of p-ERK1/2, 5-LOX, and LTB4. Treatment of LM-MCF-7 cells with cerulenin, PD98059, or MK-886 abolished the proliferation. Administration of exogenous LTB4 (10 nmol/L) significantly increased BrdU incorporation in MCF-7cells.
Conclusion: These results suggest a novel positive feedback loop involving FASN/p-ERK1/2/5-LOX/LTB4/FASN contributes to the sustaining growth of breast cancer LM-MCF-7 cells.

Keywords: breast cancer; extracellular signal-regulated kinase; fatty acid synthase; 5-lipoxygenase; leukotriene B4; cell proliferation

Acta Pharmacologica Sinica (2011) 32: 921–929; doi: 10.1038/aps.2011.40; published online 6 Jun 2011

Introduction

Monod and Jacob reported that the feedback loops were present in eukaryotic signal transduction system in 1961[1]. In the network of signaling transduction, the positive feedback loop regulation plays important roles in determining the progressive nature of malignant cancer cells including cell proliferation[2–5]. Extracellular signal-regulated kinase 1/2 (ERK1/2), a major cellular proliferation signaling pathway, is involved in many positive feedback loops. Previously, we reported a positive feedback between the phosphorylated ERK1/2 (p-ERK1/2) and cyclooxygenases (COX)/lipoxygenases (LOX)[6]. Kim *et al*[7] discovered a positive feedback loop between Wnt and ERK pathways. It has also been reported that there is a regulatory loop between fatty acid synthase (FASN) and ERK pathway dependent on the HER1/HER2[8]. Cheng *et al*[9] identified a positive feedback loop in which Ras signaling promoted CD44v6 splicing, and CD44v6 then sustained late Ras signaling. Moreover, ERK occurs crosstalk with other pathways, including activated stress activated protein kinase (SAPK)-p38[10], phosphatidylinositol 3-kinase (PI3K)[11], Wnt[12] and myosin light-chain kinase (MLCK)[13]. Thus, p-ERK1/2 may serve as a key hub in the network.

FASN is a 250−270 kDa multifunctional, homodimeric enzyme responsible for energy storage by converting excess carbohydrate to fatty acids that are then sterified to store triacylglycerols[14]. Under normal physiological conditions,

# These two authors contributed equally to this work.
* To whom correspondence should be addressed.
E-mail yelihong@nankai.edu.cn (Li-hong YE);
zhangxd@nankai.edu.cn (Xiao-dong ZHANG)
Received 2011-02-14 Accepted 2011-03-29

expression of FASN is tightly regulated in breast tissues, whereas deregulation of FASN occurs in cancer cells contributing to exacerbated lipogenesis required for highly proliferating cancer cell population[15]. The pharmacological and RNAi mediated inhibition of FASN leads to growth inhibition and cell apoptosis in several experimental models, suggesting that FASN may be a promising therapeutic target for cancer therapy[16]. Therefore, we are interested in the intracellular growth signaling pathways that are associated with FASN in breast cancer cells.

The contribution of arachidonic acid metabolites to cancer progression is becoming the focus of intense research, with the involvement of both COX and LOX pathways[17]. The LOX pathway has different isoenzymes, including 5-LOX, which converts arachidonic acid to hydroxyeicosatetraenoic acids or leukotrienes[18]. 5-LOX is often overexpressed in multiple tumor types and is involved in proliferation, survival, and apoptosis of cancer cells[19]. Leukotriene B4 (LTB4), the final metabolite in the 5-LOX pathway, is able to enhance proliferation, increase survival and suppress the apoptosis of human cells. Blockade of the LTB4-signaling pathway induced apoptosis via the inhibition of ERK1/2 activation in colon cancer cells[20]. However, the mechanisms that 5-LOX/LTB4 promotes breast cancer cell growth remain unclear.

Previously, our laboratory established a metastatic subclone from the MCF-7 breast cancer cell line, called LM-MCF-7, which was derived from a lung metastasis of a severe combined immunodeficient (SCID) mouse[21]. *In vivo* and *in vitro* experiments showed that LM-MCF-7 had high malignant phenotype in cell proliferation and migration[22]. The two cell lines, having the similar genetic background, provide excellent parallel models for investigating the molecular mechanisms underlying the sustained proliferation of breast cancer cells.

In the present study, we investigate the signal transduction pathway that maintains the growth of breast cancer cells using the parallel MCF-7/LM-MCF-7 breast cancer cell lines. We report a novel positive cascade loop in the network. Our data show that p-ERK1/2 is one of key hubs in the network. This finding provides new insight into the mechanisms of network regulation in breast cancer cells.

Materials and methods

Cell culture

MCF-7 and LM-MCF-7 cells were cultured in RPMI-1640 (Gibco, USA) medium supplemented with 10% fetal calf serum (Gibco, USA), 100 U/mL penicillin, 100 mg/mL streptomycin and 1% glutamine. Cultures were incubated at 37 °C in a humidified atmosphere with 5% CO_2.

Reagents

MK-886 (an inhibitor of 5-LOX), NDGA (an inhibitor of LOX), indomethacin (Indo, an inhibitor of COX), PD98059 (a p42/44 MAPK inhibitor), SKF525A (a CYP450 inhibitor) and LTB4 were purchased from Sigma-Aldrich (USA). Pertussis toxin (PTX, an inhibitor of a Gi/o protein) was purchased from List Biological Laboratories Inc (USA). Cerulenin (an inhibitor of FASN) was purchased from Fermentek Ltd (Israel). The enzyme immunoassay kit for measurement of LTB4 was purchased from Adlitteram Diagnostic Laboratories (USA).

Small interfering RNA and plasmids transfection

The reporter construct, pFASN-WT-Luc, containing the promoter of FASN was kindly provided by Dr Qiang LIU (University of Saskatchewan, Canada). The small siRNAs (siRNAs) targeting human 5-LOX mRNA (NM_000698, 315 to 335) and human FASN mRNA (NM_004104.4, 1210 to 1231) and control siRNA were designed and synthesized by RiboBio (Guangzhou, China). The transfection with RNAi reagents and different dose of plasmids were performed using Lipofectamine 2000 (Invitrogen, USA) according to the manufacturer's protocol, respectively.

Treatments of tumor cells

Cells were cultured in 24-well plates for 24 h, and then were recultured in serum-free medium for 12 h. In brief, LM-MCF-7 cells were treated with PTX (30 ng/mL or 50 ng/mL), Indo (25 μmol/L), PD98059 (30, 50 μmol/L), NDGA (25 μmol/L), SKF 525A (a CYP450 inhibitor, 50 μmol/L) and AG112 (20, 40 mmol/L) for 4 h, respectively. In addition, MCF-7 cells were cultured for 48 h, followed by treatment with 50% or 100% conditioned media from LM-MCF-7 and the LM-MCF-7 cells treated with NDGA (25 μmol/L) for 24 h. MCF-7 cells were treated with LTB4 (0.1 or 10 nmol/L) for different period of time. MCF-7 cells were treated with LTB4 10 nmol/L, followed by treatment with MK-886 (5, 10, or 20 μmol/L) for 6 h. LM-MCF-7 cells were treated with cerulenin (2.5, 5, or 10 μmol/L) for 12 h. The treated cells were examined by using luciferase reporter gene assay, reverse transcription polymerase chain reaction (RT-PCR), immunoblot analysis and enzyme-linked immunosorbent (ELISA), respectively, as described below.

RNA isolation, RT-PCR and quantitative real-time PCR

Total RNA isolation, RT-PCR and quantitative real-time PCR were performed as previously described[23]. Briefly, total RNA of cells was isolated using TRIzol reagent (Invitrogen, USA) according to the manufacturer's instructions. First-strand cDNA was synthesized with PrimeScript reverse transcriptase (TaKaRa Bio, China) and oligo (dT). After reverse transcription reaction, PCR and real-time PCR were performed by an ABI PRISM 7000 sequence detection system according to the manufacturer's instructions using double stranded DNA specific flurophore SYBR Green (Promega, USA). We included specific primers for FASN (forward primer, 5′-GGT CTT GAG AGA TGG CTT GC-3′ and reverse primer, 5′-AAT TGG CAA AGC CGT AGT TG-3′), 5-LOX (forward primer, 5′-CCC GGG GCA TGG AGA GCA-3′ and reverse primer, 5′-GCG GTC GGG CAG CGT GTC-3′). As a control, GAPDH was amplified with specific primers (forward primer, 5′-CAT CAC CAT CTT CCA GGA GCG-3′ and reverse primer, 5′-TGA CCT TGC CCA CAG CCT TG-3′). The conditions of PCR were as follows: 94 °C for 10 min, followed by 35 cycles of amplifications

including 94 °C for 30 s, 52 °C for 45 s, and 72 °C for 45 s, and a final extension at 72 °C for 10 min. The conditions of real-time PCR were as follows: 95 °C for 10 s, 95 °C for 5 s, 53 °C annealing for 1 min, 72 °C for 15 s, followed by 45 cycles. There is no nonspecific amplification determined by dissolved curves. There are three samples in each group. The real-time PCR results were reported as the fold induction of relative light units for the treatment over vehicle after normalization to GAPDH expression.

Luciferase reporter gene assay

Treated MCF-7 and LM-MCF-7 cells grown in 24-well plates were cotransfected with 0.3 μg of a plasmid encoding firefly luciferase under the control of wild-type FASN promoter, and 0.05 μg of pRL-SV40 encoding Renilla luciferase (rLuc) (Promega, USA). Reporter luciferase assay was performed 48 h after transfection with Dual Luciferase Assay reagents (Promega, USA) using a TD 20/20 luminometer (Turner Designs). The luciferase readings of each sample were normalized against the rLuc levels. All of the data shown in this study were obtained from three independent experiments.

Western blot analysis

Cells were washed with cold phosphate-buffered saline (PBS) for 3 times and lysed in RIPA cell lysis buffer (10 mmol/L HEPES pH 7.4, 0.15 mol/L NaCl, 1 mmol/L $MgCl_2$, 1 mmol/L $CaCl_2$, 1 mmol/L dithiothreitol, 0.1% sodium dodecylsulfate, 0.1% NP-40, and 20 μg/mL leupeptin). Protein concentrations were estimated using Bradford reagent (Bio-Rad, USA). Equal amount of total protein was loaded for immunoblotting. Following SDS-PAGE, resolved proteins were electrotransfered on PVDF membrane (Millipore, USA). The membrane was blocked overnight in TBS containing 0.1% Tween-20 (TBST) and 5% skim milk. The membrane was then probed with primary antibody in TBST for 2 h at room temperature or overnight at 4 °C , followed by three 15 min TBST washes at room temperature. Incubation with the secondary antibody was done for 1 h and three 10 min TBST washes were given prior to chemiluminiscence detection using ECL substrate (Amersham Biosciences, UK). The primary antibodies for Western blot followed a dilution below mouse anti-p-ERK1/2 monoclonal antibody (1:1000 dilution, Cell Signaling Technology, Danvers, MA, USA), rabbit anti-5-LOX monoclonal antibody (1:500 dilution, Santa Cruz Biotechnology), mouse anti-human β-actin monoclonal antibody (1:20 000 dilution, Sigma). The data were analyzed by applying Glyco Band-Scan software. All of the data shown in this study were obtained from three independent experiments.

Enzyme-linked immunosorbent assay (ELISA)

The amount of LTB4, a metabolite of 5-LOX, was determined by ELISA assay according to the instructions provided by the manufacturer. The concentration of LTB4 was normalized to total protein. The concentrations of LTB4 in these extracts were determined using a protein assay method (Bio-Rad).

BrdU incorporation assay

The detailed 5-Bromo-20-deoxyuridine (BrdU) incorporation assay procedure was described as previously[13]. In brief, LM-MCF-7 and MCF-7 cells were seeded in 6-well culture plate and were grown overnight prior to treatment. LM-MCF-7 cells were treated with 2.5, 5, and 10 μmol/L cerulenin for 8 h, or with 10 and 20 μmol/L MK-886 for 8 h, respectively. MCF-7 cells were treated with 1 and 10 nmol/L LTB4 for 8 h. All groups (n=3, in every group) were incubated with fresh medium containing 10 μmol/L BrdU (Sigma) for 4 h prior to immunofluorescence staining with mouse anti-BrdU antibody. The cells were fixed for 15 min with 4% paraformaldehyde in PBS. After 1 h incubation with PBS containing 2 mol/L HCl to denature DNA, cover slips were washed 3 times with 0.5% bovine serum albumin (BSA) and 0.5% Tween 20 in PBS, and incubated overnight (4 °C) with a mouse anti-BrdU antibody (NeoMarkers, Fremont, CA, USA) at 1:300 dilution. Reactions were developed using fluorescein isothiocyanate (FITC)-conjugated goat anti-mouse IgG (Dako, Glostrup, Denmark) at 1:100 dilution for BrdU staining. The BrdU labeling index was assessed by point counting through a Nikon TE200 inverted microscope (Nikon, Tokyo, Japan) using a 40×objective lens. About 700–800 nuclei were counted in 6–8 representative fields. The labeling index was expressed as the number of positively labeled nuclei/total number of nuclei. Propidium iodine (PI) (Sigma) (50 μg/mL) was used to stain nuclei as the control to all cells in each group.

Statistical analysis

Statistical analysis was performed using SigmaPlot 2001 (Systat Software Inc, Richmond, CA, USA http://www.systat.com). Statistical significance was assessed by comparing the mean values (±SD) using a Student's t test or χ^2 test.

Results

p-ERK1/2 and LOX are involved in the upregulation of FASN

It has been reported that FASN is associated with the progression of many kinds of tumor and it is primarily regulated at the transcriptional level. Then, we examined the promoter activities of FASN in MCF-7 and LM-MCF-7 cells with different metastatic ability. Our data showed that the promoter activity of FASN was much higher in LM-MCF-7 cells with high proliferation capability relative to MCF-7 cells using pFASN-WT-Luc, a FASN promoter-luciferase reporter (Figure 1A, P<0.05 *vs* MCF-7 cells, Student's t test). To identify the signaling pathways involved in FASN, we undertook a screen of several cellular proliferation signaling pathways by treatment with different inhibitors in LM-MCF-7 cells. Our data showed that 30 μmol/L and 50 μmol/L PD98059 (a p42/44 MAPK inhibitor) and 25 μmol/L NDGA (a LOX inhibitor) significantly decreased the promoter activity of FASN. However, no modulation was observed after the addition of 30 ng/mL and 50 ng/mL PTX (a Gi/o protein inhibitor), 20 μmol/L and 40 μmol/L AG112 (a specific EGFR kinase inhibitor), 25 μmol/L indomethacin (Indo, a COX inhibitor) and 50 μmol/L

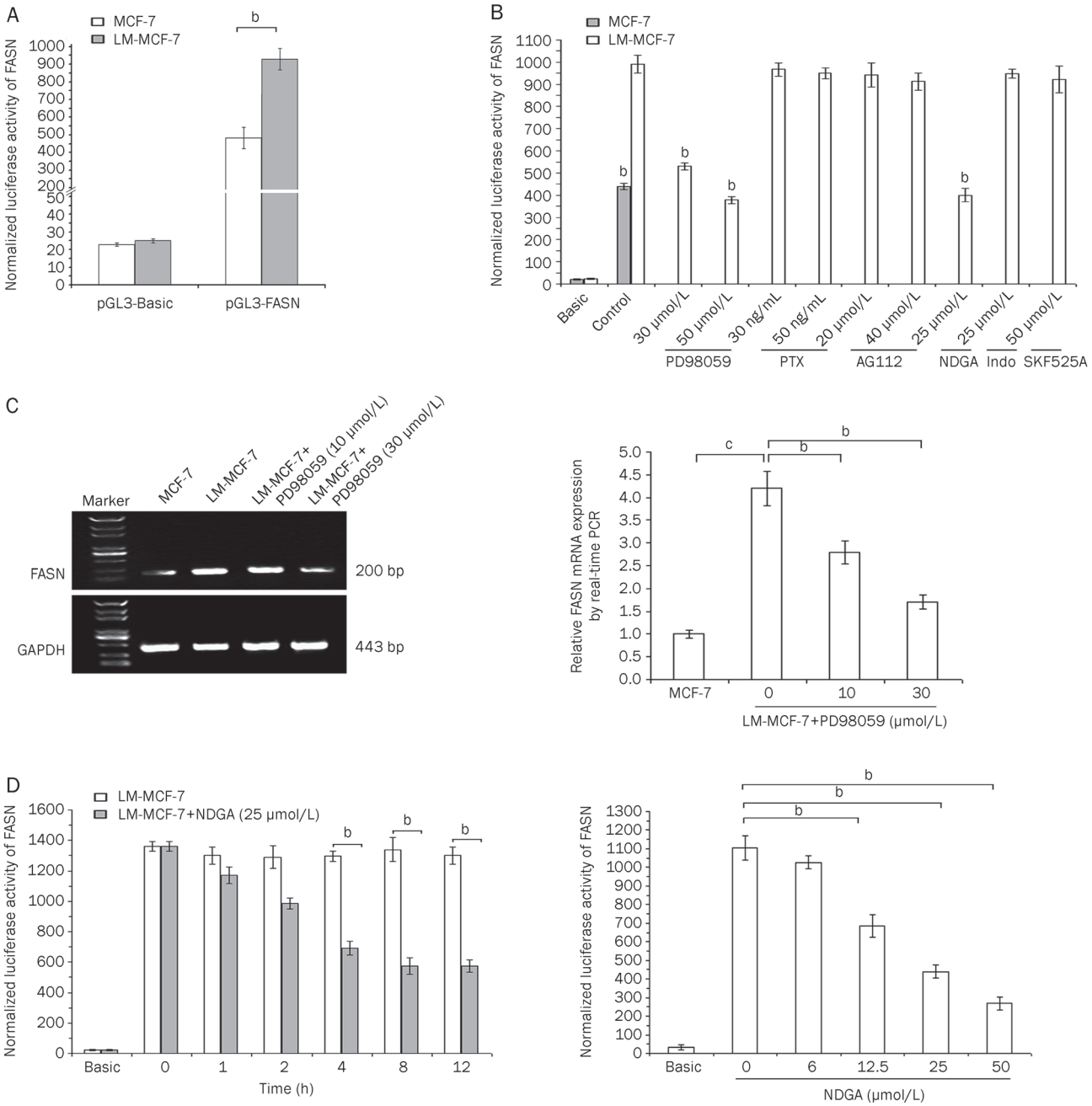

Figure 1. p-ERK1/2 and LOX are responsible for the upregulation of FASN. (A) The promoter activity of FASN was examined by luciferase reporter gene assay in MCF-7 and LM-MCF-7 cells ($^bP<0.05$ *vs* MCF-7 cells, Student's *t* test). (B) The promoter activity of FASN was examined by luciferase reporter gene assay in LM-MCF-7 cells treated with PD98059 (a p42/44 MAPK inhibitor), PTX (a Gi/o protein inhibitor), AG112 (a specific EGFR kinase inhibitor), NDGA (an inhibitor of LOX), Indo (indomethacin, a COX inhibitor), and SKF525A (a CYP450 inhibitor), respectively ($^bP<0.05$ *vs* LM-MCF-7 cells, Student's *t* test). (C) The expression of FASN mRNA was measured by RT-PCR and real time PCR, respectively, after treatment with PD98059 ($^bP<0.05$; $^cP<0.01$ *vs* LM-MCF-7 cells, Student's *t* test). (D) The promoter activity of FASN was examined by luciferase reporter gene assay in LM-MCF-7 cells treated with NDGA ($^bP<0.05$ *vs* LM-MCF-7 cells, Student's *t* test). All data are obtained from at least three independent experiments. Bars indicate the standard deviations.

SKF525A (a CYP450 inhibitor), respectively (Figure 1B, $P<0.05$ *vs* LM-MCF-7 cells, Student's *t* test). Furthermore, RT-PCR and quantitative real time PCR showed that PD98059 reduced mRNA level of FASN in a dose-dependent manner in LM-MCF-7 cells (Figure 1C, $P<0.05$; $P<0.01$ *vs* LM-MCF-7 cells, Student's *t* test). We also found that NDGA reduced the promoter activity of FASN in a dose- and time-dependent manner (Figure 1D, $P<0.05$ *vs* LM-MCF-7 cells, Student's *t* test). Thus, these data suggest that p-ERK1/2 and LOX are upstream activators of FASN.

p-ERK1/2 activates 5-LOX

Our previous finding showed that PD98059 treatment led to a decrease of 5-LOX expression in breast cancer cells[6]. Here, we confirmed the results in the two cell lines as determined by RT-PCR and Western blot analysis, respectively (data not shown).

5-LOX/LTB4 activates FASN

Next, we investigated whether 5-LOX was involved in the upregulation of FASN. We treated LM-MCF-7 cells with increasing concentration of MK-886 (a specific 5-LOX inhibitor) for 6 h. Our finding showed that MK-886 was able to decrease the expression of FASN in a dose-dependent manner in LM-MCF-7 cells by luciferase reporter gene assays, RT-PCR and real-time PCR, respectively (Figure 2A–2B, $P<0.05$; $P<0.01$ *vs* LM-MCF-7 cells, Student's *t* test). In addition, we found that siRNA targeting the mRNA of 5-LOX could significantly

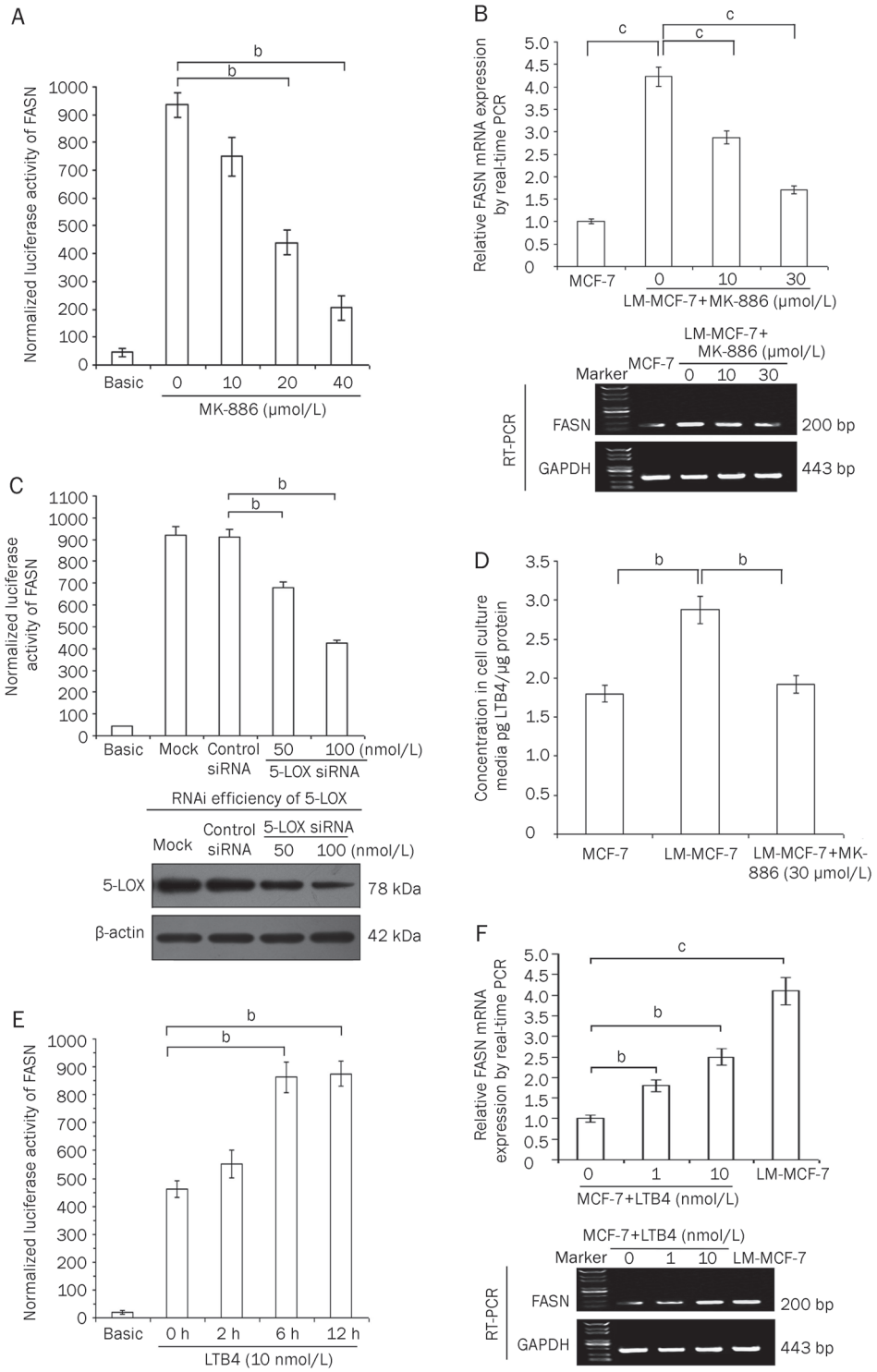

Figure 2. 5-LOX/LTB4 activates FASN. (A) The promoter activity of FASN was examined by luciferase reporter gene assay in LM-MCF-7 cells treated with MK-886 ($^bP<0.05$ *vs* LM-MCF-7 cells, Student's *t* test). (B) The mRNA levels of FASN was examined by RT-PCR and real time PCR in LM-MCF-7 cells treated with MK-886 ($^cP<0.01$ *vs* LM-MCF-7 cells, Student's *t* test). (C) LM-MCF-7 cells were transfected with 5-LOX siRNA (50 or 100 nmol/L) or control siRNA for 48 h. Then, the promoter activities of FASN were examined by luciferase reporter gene assay ($^bP<0.05$ *vs* control siRNA, Student's *t* test). In parallel, the protein levels of 5-LOX were analyzed with Western blot analysis. (D) The levels of LTB4 were determined by ELISA in the conditioned media from MCF-7, LM-MCF-7, and LM-MCF-7 cells treated with MK-886, respectively ($^bP<0.05$ *vs* LM-MCF-7 cells, Student's *t* test). (E) The promoter activity of FASN was examined by luciferase reporter gene assay in MCF-7 cells treated with exogenous LTB4 ($^bP<0.05$ *vs* MCF-7 cells, Student's *t* test). (F) The mRNA levels of FASN was examined by RT-PCR and real time PCR in MCF-7 cells treated with exogenous LTB4 ($^bP<0.05$, $^cP<0.01$ *vs* MCF-7 cells, Student's *t* test). All data are obtained from at least three independent experiments. Bars indicate the standard deviations.

reduce the promoter activity of FASN in a dose-dependent manner in LM-MCF-7 cells as well (Figure 2C, $P<0.05$ *vs* control siRNA, Student's *t* test). Then, we determined the amount of LTB4, the final metabolite of 5-LOX, in the conditioned media of MCF-7 and LM-MCF-7 cells. ELISA analysis showed that the levels of released LTB4 were higher in the conditioned media from LM-MCF-7 cells than that in the conditioned media from MCF-7 cells. However, this elevation could be abolished by pretreatment with MK-886 (Figure 2D, $P<0.05$ *vs* LM-MCF-7 cells, Student's *t* test). Accordingly, we examined whether LTB4 was responsible for high level of FASN. The administration of exogenous LTB4 was able to enhance the promoter activity of FASN in a time-dependent manner by luciferase reporter gene assay in MCF-7 cells (Figure 2E, $P<0.05$ *vs* MCF-7 cells, Student's *t* test). Meanwhile, LTB4 significantly increased the FASN expression by RT-PCR and real-time PCR in the cells (Figure 2F, $P<0.05$; $P<0.01$ *vs* MCF-7 cells, Student's *t* test). 5-HETE, one of 5-LOX important products, has direct proliferating activity on a subset of cancers[24]. To demonstrate whether 5-HETE contributes to the upregulation of FASN, we examined the effect of 5-HETE on FASN promoter activity. Our data showed that the treatment with 5-HETE in MCF-7 cells failed to activate the promoter activity of FASN (data not shown). Thus, it suggests that 5-LOX/LTB4, but not 5-HETE, is responsible for the upregulation of FASN.

LTB4/FASN activates the p-ERK1/2/5-LOX in a positive feedback manner

Given several studies revealed that the effects of LTB4 were mediated through MEK/ERK pathway[25–27], we speculated whether LTB4 could activate p-ERK1/2/5-LOX in a positive feedback manner in breast cancer MCF-7 cells. Interestingly, Western blot analysis showed that administration of exogenous LTB4 was able to increase the expression levels of p-ERK1/2 and 5-LOX in a dose-dependent manner (Figure 3A). In addition, we also investigated whether FASN could activate p-ERK1/2/5-LOX/LTB4 signaling in a positive

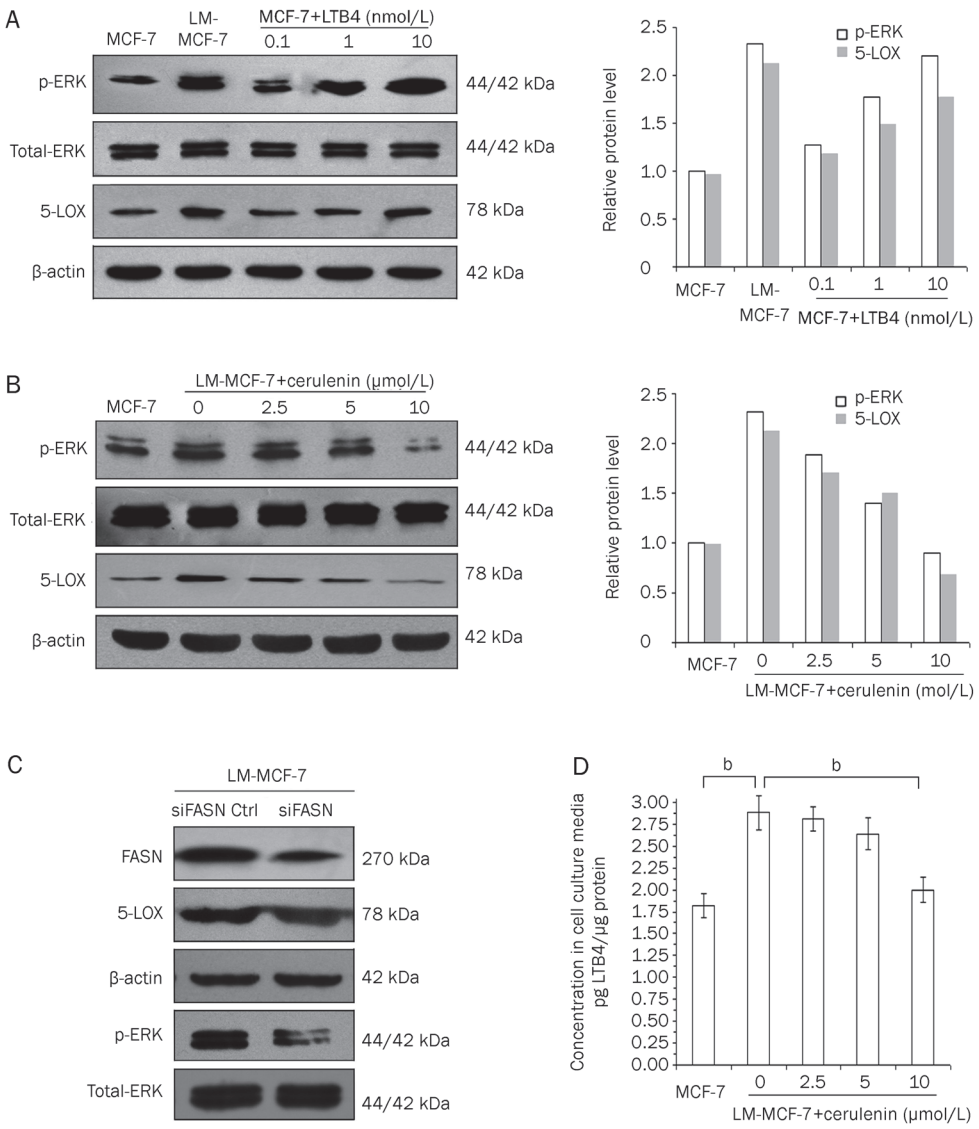

Figure 3. LTB4/FASN activates the p-ERK1/2/5-LOX in a positive feedback manner. (A) The expression levels of p-ERK1/2 and 5-LOX were examined by Western blot analysis in MCF-7 cells treated with exogenous LTB4. Histogram shows the results by applying Glyco Band-Scan software. (B) The expression levels of p-ERK1/2 and 5-LOX were examined by Western blot analysis in LM-MCF-7 cells treated with cerulenin, an inhibitor of FASN. Histogram shows the results by applying Glyco Band-Scan software. (C) The expression levels of FASN, p-ERK1/2 and 5-LOX were examined by Western blot analysis in LM-MCF-7 cells treated with siRNA targeting FASN mRNA. (D) The levels of released LTB4 were examined by ELISA assay in the conditioned media from LM-MCF-7 cells treated with cerulenin ($^bP<0.05$ *vs* LM-MCF-7 cells, Student's *t* test). All data are obtained from at least three independent experiments. Bars indicate the standard deviations.

feedback manner. The treatment with cerulenin, an inhibitor of FASN, could greatly decrease the levels of p-ERK1/2 and 5-LOX in a dose-dependent manner in LM-MCF-7 cells (Figure 3B). Silencing of FASN with siRNA targeting FASN mRNA could also significantly reduce the levels of p-ERK1/2 and 5-LOX (Figure 3C). Furthermore, cerulenin decreased the levels of LTB4 in a dose-dependent manner in LM-MCF-7 cells (Figure 3D, $P<0.05$ *vs* LM-MCF-7 cells, Student's *t* test), suggesting that LTB4/FASN activates the signaling of p-ERK1/2/5-LOX in a positive feedback manner.

A positive feedback loop of FASN/p-ERK1/2/5-LOX/LTB4/FASN maintains growth of breast cancer cells

Taken together, we summarize that FASN/p-ERK1/2/5-LOX/LTB4/FASN results in a positive feedback loop. Then, we investigated the effect of the loop on keeping the growth of breast cancer cells by BrdU incorporation assay. Our results revealed that the treatment with cerulenin (or PD98059, MK-886) abolished the proliferation of LM-MCF-7 cells (Figure 4A, $P<0.05$ *vs* LM-MCF-7 cells, Student's *t* test). The administration of exogenous LTB4 significantly increased BrdU labeling index of MCF-7 cells (Figure 4B, $P<0.05$ *vs* MCF-7 cells, Student's *t* test). Thus, it suggests that the novel positive feedback loop of FASN/p-ERK1/2/5-LOX/LTB4/FASN is responsible for maintaining the growth of breast cancer cells.

Discussion

Previously, we reported that breast cancer cells grew faster in a positive feedback manner involving activated ERK and COX/LOX[6]. However, the endogenous signaling pathways associated with high proliferation potential of breast cancer cells remain unclear. Indeed, we are interested in the network regulation involving positive feedback loop manner in sustaining tumor growth. In this study, we focused on the investigation of positive feedback loop.

FASN is a complex multifunctional enzyme that plays a central role in endogenous lipogenesis in mammals[28, 29]. It has been reported that the overexpression of FASN together with a high proliferative index of breast cancer cells are associated with a nine-fold increased risk of patient mortality[30]. Accordingly, we examined the level of FASN by comparing breast cancer cell lines with different proliferative capability. Our data showed that the level of FASN promoter activity was positively correlated with the high proliferative ability

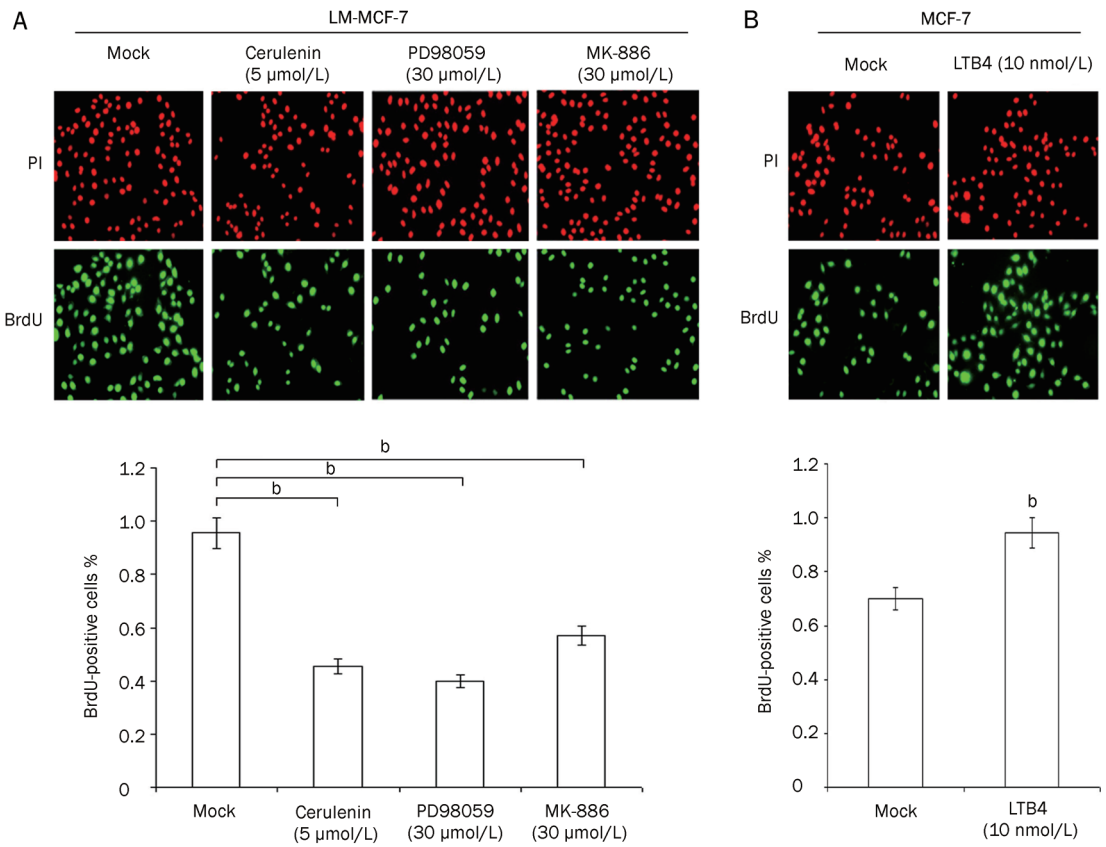

Figure 4. A positive feedback loop of FASN/p-ERK1/2/5-LOX/LTB4/FASN maintains growth of breast cancer cells. (A) The proliferation of LM-MCF-7 cells was examined by BrdU incorporation assay after treatment with cerulenin, PD98059, or MK-886, respectively. Histogram shows the positive rates of BrdU-positive cells ($^bP<0.05$ *vs* LM-MCF-7 cells, Student's *t* test). (B) The proliferation of MCF-7 cells was examined by BrdU incorporation assay after treatment with exogenous LTB4. Histogram shows the positive rates of BrdU-positive cells ($^bP<0.05$ *vs* MCF-7 cells, Student's *t* test). BrdU positive cell was stained with FITC-conjugated goat anti-mouse IgG (green). Nuclei were stained with 50 μg/mL propidium iodine (PI) (red). All data are obtained from at least three independent experiments. Bars indicate the standard deviations.

(Figure 1A). Thus, we need to answer the upstream activators of FASN in breast cancer cells. Several studies have demonstrated the involvement of ERK1/2 pathways in regulating FASN expression in cancer cells[31, 32]. It has been reported that LOX or its metabolites are able to stimulate tumor cell proliferation[33]. In agreement, we identified that p-ERK1/2 and LOX were upstream regulators of FASN (Figure 1B–1D).

Several studies have reported that 5-LOX is able to enhance cell proliferation and increase cell survival[19, 34]. A recent study found that the expression levels of FASN and 5-LOX played important roles in mediating breast cancer formation[35]. Our previous observation showed that ERK1/2 activation increased the expression of 5-LOX in breast cancer cells[6]. In this text, we confirmed the data (data not shown). Activation of ERK1/2 and overexpression of 5-LOX are frequently observed in various human tumors[36, 37]. Thus, we conclude that p-ERK1/2 activates 5-LOX in breast cancer cells. The final product of the 5-LOX pathway is LTB4, which is able to enhance tumor growth, including enhancing proliferation and suppressing apoptosis in human cancer cells[38]. Therefore, we present a hypothesis that a link between 5-LOX metabolism and FASN may contribute to sustaining high proliferation rate of breast cancer cells. Interestingly, we found that the blockade of 5-LOX with MK-886 or siRNAs was able to significantly decrease the expression level of FASN in LM-MCF-7 cells (Figure 2A–2C). Then, we examined the amount of LTB4 in the conditioned media from breast cancer cells. Our data showed that the level of LTB4 was higher in the cellular extracts from LM-MCF-7 cells relative to MCF-7 cells, which was abolished by the treatment with MK-886 (Figure 2D). Interestingly, the administration of exogenous LTB4 was able to enhance the expression of FASN (Figure 2E–2F). Moreover, we examined the effect of 5-HETE, another product of 5-LOX, on FASN. Our data showed that 5-HETE failed to activate the promoter activity of FASN in MCF-7 cells. Thus, we conclude that 5-LOX/LTB4, but not 5-HETE, is responsible for the upregulation of FASN.

Currently, feedback mechanisms have been implicated in the carcinogenesis. Our previous study showed that 5-LOX plays an important role in the activation of ERK1/2[39]. Studies by Tong *et al*[25] have shown that the growth stimulatory effect of LTB4 is mediated at least through MEK/ERK pathway in human pancreatic cancer cells. Consistently, we here report a novel positive feedback loop involving FASN/p-ERK1/2/5-LOX/LTB4/FASN that is responsible for the sustained high proliferation of breast cancer cells (Figures 3, 4).

Taken together, we conclude that a novel positive feedback loop involving FASN/p-ERK1/2/5-LOX/LTB4/FASN sustains a high proliferative potential of breast cancer cells, in which p-ERK1/2 is one of key hubs in the network. Our finding provides a new insight into the mechanism involving the high growth ability of breast cancer cells.

Acknowledgements

The authors thank Dr Qiang LIU (University of Saskatchewan, Canada) for providing plasmid of pFASN-WT-Luc. This work was supported in part by National Basic Research Program of China (973 Program, No 2007CB914802, 2007CB914804, and 2009CB521702), National Natural Scientific Foundation of China (No 81071623 and 30770826) and Tianjin Natural Scientific Foundation (No 08JCZDJC20700).

Author contribution

Li-hong YE and Xiao-dong ZHANG designed the research; Nan HU, Yu LI, Yu ZHAO, Qi WANG, and Jia-cong YOU performed the experiments; Li-hong YE, Xiao-dong ZHANG, and Nan HU analyzed data and wrote the paper.

References

1 Monod J, Jacob F. Teleonomic mechanisms in cellular metabolism, growth, and differentiation. Cold Spring Harb Symp Quant Biol 1961; 26: 389–401.
2 Wanzel M, Russ AC, Kleine-Kohlbrecher D, Colombo E, Pelicci PG, Eilers M. A ribosomal protein L23-nucleophosmin circuit coordinates Mizl function with cell growth. Nat Cell Biol 2008; 10: 1051–61.
3 Li H, Xu LL, Masuda K, Raymundo E, McLeod DG, Dobi A, *et al*. A feedback loop between the androgen receptor and a NEDD4-binding protein, PMEPA1, in prostate cancer cells. J Biol Chem 2008; 283: 28988–95.
4 Wang HQ, Altomare DA, Skele KL, Poulikakos PI, Kuhajda FP, Di Cristofano A, *et al*. Positive feedback regulation between AKT activation and fatty acid synthase expression in ovarian carcinoma cells. Oncogene 2005; 24: 3574–82.
5 Rasola A, Fassetta M, De Bacco F, D'Alessandro L, Gramaglia D, Di Renzo MF, *et al*. A positive feedback loop between hepatocyte growth factor receptor and beta-catenin sustains colorectal cancer cell invasive growth. Oncogene 2007; 26: 1078–87.
6 You J, Mi D, Zhou X, Qiao L, Zhang H, Zhang X, *et al*. A positive feedback between activated extracellularly regulated kinase and cyclooxygenase/lipoxygenase maintains proliferation and migration of breast cancer cells. Endocrinology 2009; 150: 1607–17.
7 Kim D, Rath O, Kolch W, Cho KH. A hidden oncogenic positive feedback loop caused by crosstalk between Wnt and ERK pathways. Oncogene 2007; 26: 4571–9.
8 Vazquez-Martin A, Colomer R, Brunet J, Lupu R, Menendez JA. Overexpression of fatty acid synthase gene activates HER1/HER2 tyrosine kinase receptors in human breast epithelial cells. Cell Prolif 2008; 41: 59–85.
9 Cheng C, Yaffe MB, Sharp PA. A positive feedback loop couples Ras activation and CD44 alternative splicing. Genes Dev 2006; 20: 1715–20.
10 Estrada Y, Dong J, Ossowski L. Positive crosstalk between ERK and p38 in melanoma stimulates migration and *in vivo* proliferation. Pigment Cell Melanoma Res 2009; 22: 66–76.
11 Bradley EW, Ruan MM, Vrable A, Oursler MJ. Pathway crosstalk between Ras/Raf and PI3K in promotion of M-CSF-induced MEK/ERK-mediated osteoclast survival. J Cell Biochem 2008; 104: 1439–51.
12 Hu T, Li C. Convergence between Wnt-beta-catenin and EGFR signaling in cancer. Mol Cancer 2010; 9: 236.
13 Zhou X, Liu Y, You J, Zhang H, Zhang X, Ye L. Myosin light-chain kinase contributes to the proliferation and migration of breast cancer cells through cross-talk with activated ERK1/2. Cancer Lett 2008; 270: 312–27.
14 Flavin R, Peluso S, Nguyen PL, Loda M. Fatty acid synthase as a potential therapeutic target in cancer. Future Oncol 2010; 6: 551–62.
15 Little JL, Kridel SJ. Fatty acid synthase activity in tumor cells. Subcell

Biochem 2008; 49: 169–94.
16 Lupu R, Menendez JA. Pharmacological inhibitors of fatty acid synthase (FASN) — catalyzed endogenous fatty acid biogenesis: a new family of anti-cancer agents? Curr Pharm Biotechnol 2006; 7: 483–93.
17 Maloberti PM, Duarte AB, Orlando UD, Pasqualini ME, Solano AR, Lopez-Otin C, *et al*. Functional interaction between acyl-CoA synthetase 4, lipooxygenases and cyclooxygenase-2 in the aggressive phenotype of breast cancer cells. PLoS One 2010; 5: e15540.
18 Catalano A, Procopio A. New aspects on the role of lipoxygenases in cancer progression. Histol Histopathol 2005; 20: 969–75.
19 Chen X, Sood S, Yang CS, Li N, Sun Z. Five-lipoxygenase pathway of arachidonic acid metabolism in carcino-genesis and cancer chemoprevention. Curr Cancer Drug Targets 2006; 6: 613–22.
20 Ihara A, Wada K, Yoneda M, Fujisawa N, Takahashi H, Nakajima A. Blockade of leukotriene B4 signaling pathway induces apoptosis and suppresses cell proliferation in colon cancer. J Pharmacol Sci 2007; 103: 24–32.
21 Ye LH, Wu LY, Guo W, Ma HT, Zhang XD. Screening of a sub-clone of human breast cancer cells with high metastasis potential. Zhonghua Yi Xue Za Zhi 2006; 86: 61–5.
22 Ye LH, You JC, Guo W, Xu SF, Wu LY, Qi RZ, *et al*. Investigation of discrepant proteins between two breast cancer cell lines with different metastatic abilities. Ai Zheng 2006; 25: 823–7.
23 Cui W, Zhang Y, Hu N, Shan C, Zhang S, Zhang W, *et al*. MiRNA-520b and miR-520e sensitize breast cancer cells to complement attack via directly targeting 3'UTR of CD46. Cancer Biol Ther 2010; 10: 232–41.
24 Hayashi T, Nishiyama K, Shirahama T. Inhibition of 5-lipoxygenase pathway suppresses the growth of bladder cancer cells. Int J Urol 2006; 13: 1086–91.
25 Tong WG, Ding XZ, Talamonti MS, Bell RH, Adrian TE. LTB4 stimulates growth of human pancreatic cancer cells via MAPK and PI-3 kinase pathways. Biochem Biophys Res Commun 2005; 335: 949–56.
26 Sanchez-Galan E, Gomez-Hernandez A, Vidal C, Martin-Ventura JL, Blanco-Colio LM, Munoz-Garcia B, *et al*. Leukotriene B4 enhances the activity of nuclear factor-kappaB pathway through BLT1 and BLT2 receptors in atherosclerosis. Cardiovasc Res 2009; 81: 216–25.
27 Woo CH, You HJ, Cho SH, Eom YW, Chun JS, Yoo YJ, *et al*. Leukotriene B(4) stimulates Rac-ERK cascade to generate reactive oxygen species that mediates chemotaxis. J Biol Chem 2002; 277: 8572–8.
28 Kridel SJ, Lowther WT, Pemble CWt. Fatty acid synthase inhibitors: new directions for oncology. Expert Opin Investig Drugs 2007; 16: 1817–29.
29 Mashima T, Seimiya H, Tsuruo T. *De novo* fatty-acid synthesis and related pathways as molecular targets for cancer therapy. Br J Cancer 2009; 100: 1369–72.
30 Lupu R, Menendez JA. Targeting fatty acid synthase in breast and endometrial cancer: An alternative to selective estrogen receptor modulators? Endocrinology 2006; 147: 4056–66.
31 Yang YA, Han WF, Morin PJ, Chrest FJ, Pizer ES. Activation of fatty acid synthesis during neoplastic transformation: role of mitogen-activated protein kinase and phosphatidylinositol 3-kinase. Exp Cell Res 2002; 279: 80–90.
32 Menendez JA, Colomer R, Lupu R. Why does tumor-associated fatty acid synthase (oncogenic antigen-519) ignore dietary fatty acids? Med Hypotheses 2005; 64: 342–9.
33 Menna C, Olivieri F, Catalano A, Procopio A. Lipoxygenase inhibitors for cancer prevention: promises and risks. Curr Pharm Des 2010; 16: 725–33.
34 Avis I, Hong SH, Martinez A, Moody T, Choi YH, Trepel J, *et al*. Five-lipoxygenase inhibitors can mediate apoptosis in human breast cancer cell lines through complex eicosanoid interactions. FASEB J 2001; 15: 2007–9.
35 Wei N, Wang B, Zhang QY, Mi MT, Zhu JD, Yu XP, *et al*. Effects of different dietary fatty acids on the fatty acid compositions and the expression of lipid metabolic-related genes in mammary tumor tissues of rats. Nutr Cancer 2008; 60: 810–25.
36 Pidgeon GP, Lysaght J, Krishnamoorthy S, Reynolds JV, O'Byrne K, Nie D, *et al*. Lipoxygenase metabolism: roles in tumor progression and survival. Cancer Metastasis Rev 2007; 26: 503–24.
37 Steinmetz R, Wagoner HA, Zeng P, Hammond JR, Hannon TS, Meyers JL, *et al*. Mechanisms regulating the constitutive activation of the extracellular signal-regulated kinase (ERK) signaling pathway in ovarian cancer and the effect of ribonucleic acid interference for ERK1/2 on cancer cell proliferation. Mol Endocrinol 2004; 18: 2570–82.
38 Bachi AL, Kim FJ, Nonogaki S, Carneiro CR, Lopes JD, Jasiulionis MG, *et al*. Leukotriene B4 creates a favorable microenvironment for murine melanoma growth. Mol Cancer Res 2009; 7: 1417–24.
39 Shan C, Xu F, Zhang S, You J, You X, Qiu L, *et al*. Hepatitis B virus X protein promotes liver cell proliferation via a positive cascade loop involving arachidonic acid metabolism and p-ERK1/2. Cell Res 2010; 20: 563–75.

Acta Pharmacologica Sinica (2011) 32: 930–938
 1671-4083/11 $32.00
www.nature.com/aps

Original Article

Establishment of platform for screening insulin-like growth factor-1 receptor inhibitors and evaluation of novel inhibitors

Lin-jiang TONG[1, 2, #], Hua XIE[2, #], Ting PENG[2], Xiao-feng LIU[3], Xian-liang XIN[2], Xun HUANG[2], Si-meng CHEN[2], Hong-yan LIU[2], Hong-lin LI[3], Mei-yu GENG[2], Ming YIN[1, *], Jian DING[2, *]

[1]School of Pharmacy, Shanghai Jiao Tong University, Shanghai 200240, China; [2]State Key Laboratory of Drug Research, Division of Antitumor Pharmacology, Shanghai Institute of Materia Medica, Chinese Academy of Sciences, Shanghai 201203, China; [3]Shanghai Key Laboratory of Chemical Biology, School of Pharmacy, East China University, Shanghai 200237, China

Aim: The insulin-like growth factor-1 receptor (IGF1R) is over-expressed in a wide variety of tumors and contributes to tumor cell proliferation, metastasis and drug resistance. The aim of this study was to establish a sensitive screening platform to identify novel IGF1R inhibitors.

Methods: The catalytic domain of IGF1R was expressed using the Bac-to-Bac baculovirus expression system. The screening platform for IGF1R inhibitors was established based on ELISA. The binding profile of IGF1R with the inhibitors was predicted with molecular docking and then subjected to the surface plasmon resonance (SPR) approach. The growth inhibition of cancer cells by the inhibitors was assessed with MTT assay. Apoptosis was analyzed using flow cytometry and Western blotting.

Results: A naturally occurring small molecule compound hematoxylin was identified as the most potent inhibitor (IC_{50} value=1.8±0.1 μmol/L) within a library of more than 200 compounds tested. Molecular simulation predicted the possible binding mode of hematoxylin with IGF1R. An SPR assay further confirmed that hematoxylin bound directly to IGF1R with high binding affinity ($Kd=4.2\times10^{-6}$ mol/L). In HL-60 cancer cells, hematoxylin inactivated the phosphorylation of IGF1R and downstream signaling and therefore suppressed cell proliferation. Mechanistic studies revealed that hematoxylin induced apoptosis in HL-60 cells via both extrinsic and intrinsic pathways.

Conclusion: A simple, sensitive ELISA-based screening platform for identifying IGF1R inhibitors was established. Hematoxylin was identified as a promising IGF1R inhibitor with effective antitumor activity that deserves further investigation.

Keywords: insulin like growth factor 1 receptor (IGF1R); anticancer drug; enzyme-linked immunosorbent assay (ELISA); hematoxylin; cell proliferation; apoptosis; HL-60 cell line

Acta Pharmacologica Sinica (2011) 32: 930–938; doi: 10.1038/aps.2011.23; published online 6 Jun 2011

Introduction

Insulin-like growth factor 1 receptor (IGF1R) belongs to the insulin receptor (IR) family of receptor tyrosine kinase and is composed of two α and two β subunits[1, 2]. The extracellular α subunit is responsible for ligand binding, whereas the β subunit consists of a transmembrane domain and a cytoplasmic tyrosine kinase domain. The receptor is predominantly activated by IGF-I and IGF-II, but it can also be activated by insulin at a much lower affinity (500–1000 fold less). Ligand binding activates intrinsic tyrosine kinase activity, resulting in trans-β subunit autophosphorylation and stimulation of signaling cascades, including phosphatidylinositol 3-kinase (PI3K)/AKT and mitogen-activated protein kinase (MAPK) pathways. Activation of these pathways has been reported to result in cellular proliferation, survival, transformation, metastasis, and angiogenesis. Deregulation of the IGF1/IGF1R axis has been implicated in the development and progression of several cancers, including myeloma, breast, prostate, colon, ovarian, and lung cancer[3]. Increased expression of IGF1R and its ligands correlates with poor prognosis, reduced survival and drug resistance. Thus, the IGF1/IGF1R axis has become a promising target for anticancer drug development[4, 5].

Several approaches have been employed to target IGF1R, which include monoclonal antibodies, antisense oligonucleotides, IGF1R siRNA, and small molecule inhibitors. To date, more than 25 candidates have been identified at various stages of development; these candidates are predominantly small

# These authors contributed equally to this work.
* To whom correspondence should be addressed.
E-mail suozhang@mail.shcnc.ac.cn (Jian DING);
myin@sjtu.edu.cn (Ming YIN)
Received 2010-11-24 Accepted 2011-03-07

molecule inhibitors and monoclonal antibodies that target IGF1R[6]. For example, CP-751871[7], a fully human monoclonal antibody specific for IGF1R, is in phase III clinical trial as a component of combination therapies for the treatment of non-small cell lung cancer (NSCLC). Nordihydroguaiaretic acid Insm-18/NGDA[8], a dual inhibitor of IGF1R and human epidermal growth factor receptor 2 (HER2), is in phase II clinical trial for the treatment of prostate cancer. In addition, several small molecule IGF1R inhibitors are currently in clinical or preclinical development, including picropodophyllin (PPP)[9], NVP-AEW541[10], AG-1024[11], BMS-536942[12], BMS-554417[13], and NVP-ADW742[14]. However, none of these inhibitors has been approved by the FDA for clinical uses. Meanwhile, with an increasing number of compounds available for screening, tremendous efforts have been made toward finding novel inhibitors as anti-tumor candidates. These efforts highlight the importance of establishing an efficient screening platform to identify and develop novel IGF1R inhibitors.

Here, we established a simple and effective screening model to identify potential IGF1R inhibitors. Several novel inhibitors were identified from the library, and hematoxylin stood out as a distinct compound that can suppress IGF1R activities both at an enzymatic level and in intact cells and inhibit the proliferation of HL-60 human cancer cells. Moreover, hematoxylin induces caspase-dependent apoptosis in cancer cells via both extrinsic and intrinsic pathways.

Materials and methods

Agents

A compound library is maintained in our laboratory. I-OMe-AG 538, a known IGF1R inhibitor, was purchased from Calbiochem (San Diego, CA, USA). Stock solutions of the compounds were prepared in DMSO at a concentration of 10 mmol/L, stored in aliquots at -20 °C, and thawed immediately prior to use. Insulin receptor tyrosine kinase was purchased from Millipore.

Cell culture

The *Spodoptera frugiperda* (Sf9) and *Trichoplusia ni* (T ni) insect cell lines were kind gifts from Dr Jia LI (National Center for Drug Screening, Chinese Academy of Sciences, Shanghai, China) and Prof Xiang-fu WU (Institute of Biochemistry and Cell Biology, Chinese Academy of Sciences, Shanghai, China), respectively. Cells were cultured in modified TNM-FH medium (Sigma) supplemented with 10% fetal bovine serum (Gibco-BRL) and 50 μg/mL gentamicin. Cultures were grown as monolayers in stationary flasks at 27 °C.

The HL-60 human leukemia cell line was obtained from the American Type Culture Collection (Rockville, MD, USA) and cultured in RPMI-1640 (Gibco-BRL) supplemented with 10% fetal bovine serum, 4 mmol/L glutamine, 100 units/mL penicillin and 100 μg/L streptomycin in a humidified atmosphere of 95% air and 5% CO_2 at 37 °C.

Cloning and expression of the IGF1R catalytic domain

Full length human IGF1R was purchased from Addgene. The catalytic domain (amino acids 999–1274) of IGF1R (IGF1R-CD) was obtained by PCR. The primers used for amplification included sense (5′-CGCGGATCCGATCACCATGAGCCGGGAAC-3′) and antisense (5′-CCGGAATTCAAGGAGACCTCCCGGAAGC-3′) oligonucleotides containing *Bam*H I and *Eco*R I sites, respectively. The PCR reaction was performed in a Peltier Thermal Cycler-200 with Pyrobest DNA Polymerase (TaKaRa Biotechnology Co, Ltd) using the following conditions: 94 °C for 5 min, then 30 cycles of 94 °C for 1 min, 55 °C for 1 min, 72 °C for 3 min, followed by a final elongation at 72 °C for 10 min. Amplified cDNA was digested with *Bam*H I/*Eco*R I and subcloned into the corresponding restriction sites of pAcGP67-A (Invitrogen). The correct cDNA was confirmed by DNA sequencing. Recombinant Bacmid DNA was prepared following the Bac-to-Bac baculovirus expression system manual (Invitrogen) and subsequently transfected into T ni cells using the CELLFECTIN reagent (Invitrogen). Transfection mixtures were removed after a 5 h incubation, and TNM-FH medium was added. Culture supernatants containing baculovirus were harvested at 72 h postinfection by centrifugation at 500×*g* for 5 min and transferred into a fresh tube. Next, T ni cells were infected with the baculovirus at 27 °C for 72 h, when expression levels of IGF1R were highest. T ni cells were harvested at 4 °C at 500×*g* for 5 min and washed with ice-cold phosphate buffered saline (PBS). Finally, cells were re-spun as above and quickly frozen at -80 °C after discarding the supernatant.

Purification of IGF1R-CD from T ni cells

The desired amount of Ni-NTA resin (QIAGEN) was packed into a disposable column (QIAGEN), which was equilibrated as recommended by the manufacturer. T ni cell pellets were resuspended and lysed in ice-cold lysis buffer [50 mmol/L Tris-HCl (pH 8.5), 5 mmol/L 2-mercaptoethanol, 100 mmol/L KCl, 1 mmol/L PMSF, and 1% Nonidet P-40]. Cells were sonicated (15 s pulses at 30 s intervals with an output power level of 10 W), cell lysates were centrifuged at 10000×*g* for 10 min at 4 °C, and supernatants were loaded onto a preequilibrated column. The column was washed with ice-cold buffer A [20 mmol/L Tris-HCl (pH 8.5), 500 mmol/L KCl, 20 mmol/L imidazole, 5 mmol/L 2-mercaptoethanol, and 10% (*v*/*v*) glycerol] and buffer B [20 mmol/L Tris-HCl (pH 8.5), 1 mol/L KCl, 5 mmol/L 2-mercaptoethanol, and 10% (*v*/*v*) glycerol] until the OD_{280} returned to baseline. Proteins were eluted with ice-cold buffer C [20 mmol/L Tris-HCl (pH 8.5), 100 mmol/L KCl, 100 mmol/L imidazole, 5 mmol/L 2-mercaptoethanol, and 10% (*v*/*v*) glycerol]. The active fraction containing the enzyme was divided into aliquots, rapidly frozen, and stored at -80 °C.

Protein determination and detection

Protein concentrations were determined using the BCA Kit method. To identify proteins expressed in the T ni cells, cell extracts, flow-through samples and purified proteins were resolved on 10% SDS-polyacrylamide gels and either stained with Coomassie blue dye or gently rocked with an anti-His-Tag antibody overnight at 4 °C. In the latter procedure, the

antibody-protein complexes were captured on protein A agarose beads (Boehringer Mannheim) for 2 h at 4 °C, and the proteins were then boiled off in the presence of *DL*-dithiothreitol (DTT). After the proteins were separated by electrophoresis and transferred to a nitrocellulose membrane (Amersham Life Sciences), the blot was probed with an anti-IGF1R antibody (Upstate Biotechnology) and visualized with an enhanced chemiluminescence detection reagent (Pierce).

Protein kinase assays

IGF1R-CD tyrosine kinase activity was determined by an enzyme-linked-immunosorbent assay (ELISA) in 96-well plates pre-coated with 2.5 μg/well poly(Glu, Tyr)$_{4:1}$ (Sigma) as a substrate. Fifty microliters of 10 μmol/L ATP solution diluted in reaction buffer [50 mmol/L HEPES, pH 7.4, 20 mmol/L $MgCl_2$, 0.1 mmol/L Na_3VO_4, and 1 mmol/L DTT] was added to each well, and the reaction was initiated by the addition of increasing concentrations of IGF1R tyrosine kinase. After incubation for 1 h at 37 °C, the plate was washed three times with phosphate buffered saline containing 0.1% Tween 20 (PBST). Next, 100 μL of antiphosphotyrosine (PY99; 1:1000 dilution) antibody was added. After 0.5 h incubation at 37 °C, the plate was washed three times and goat anti-mouse IgG horseradish peroxidase (100 μL of a 1:2000 dilution) diluted in PBST containing 5 mg/mL BSA was added. The plate was reincubated at 37 °C for 0.5 h and washed as before. Finally, 100 μL of color development solution (0.03% H_2O_2 and 2 mg/mL *o*-phenylenediamine in 0.1 mol/L citrate buffer, pH 5.4) was added and the plate was incubated at room temperature until color emerged. The reaction was terminated by the addition of 50 μL of 2 mol/L H_2SO_4, and the A_{492} was measured using a multiwell spectrophotometer (SpectraMax 190, Molecular Devices). Similar assays were performed with varying concentrations of IGF1R-CD tyrosine kinase, ATP, Poly (Glu, Tyr)$_{4:1}$, Mg^{2+}, and Mn^{2+}. IR tyrosine kinase activity was detected by ELISA as described above.

Screening of IGF1R inhibitors

The IGF1R inhibitors were screened in 96-well plates pre-coated with 2.5 μg/well poly(Glu, Tyr)$_{4:1}$. Each well was treated with 50 μL of 10 μmol/L ATP solution and 1 μL of compound at varying concentrations. The known IGF1R inhibitor, I-OMe-AG 538, was used as a positive control, and 0.1% (*v*/*v*) DMSO was utilized as the negative control. Experiments at each concentration were performed in duplicate. The reaction was initiated by adding 49 μL of IGF1R-CD diluted in reaction buffer, and the A_{492} was measured as described above. The inhibition rate (%) was calculated using the equation [1-($A_{492\ treated}$ / $A_{492\ control}$)]×100%. The IC_{50} values were determined from the results of at least three independent tests.

Surface plasmon resonance (SPR) analysis

The kinetics and specificity of the binding reactions between hematoxylin and IGF1R were performed with the ProteOn XPR36 (Bio-Rad). Briefly, IGF1R was immobilized on GLM sensor chips by amine coupling according to the protocol described in the application handbook. To assess real-time binding capacity, 100 μL of soluble hematoxylin was injected over the sensor chip surface with the immobilized IGF1R and then washed with HBS-EP buffer for 5 min. The sensor chip surface was then regenerated using 60 μL NaCl (2 mol/L). All binding experiments were performed at 25 °C with a constant flow rate of 50 μL/min PBST. For binding affinity assessment, the association phase was allowed to proceed to equilibrium. To correct for nonspecific binding and bulk refractive index change, a blank channel (FC2) without IGF1R was employed as a control for each experiment. Sensorgrams for all binding interactions were recorded in real time and analyzed after subtracting the values from the blank channel. Changes in mass due to the binding response were recorded as resonance units (RU). Binding kinetics and affinities were determined with ProteOn software 2.1.1.

Molecular docking

The 3D conformation of hematoxylin was generated based on the 2D structures from PubChem (http://pubchem.ncbi.nlm.nih.gov/, accessed on 2009.12.11) (id 10603) using LigPrep (version 2.0, Schrödinger, LLC, NY, USA, 2005), and all of the stereo configurations were manually checked. The crystal structure of IGF1R (PDB code 1IR3) was prepared with the Protein Preparation Wizard workflow of Schrodinger (version 1.0, Schrödinger, LLC, NY, USA, 2005) with all crystal water molecules and binding ATP removed and all hydrogen atoms added. Molecular docking was performed using Glide (version 4.0, Schrödinger, LLC, NY, USA, 2005). The grid-enclosing box was centered on the centroid of co-complexed ligand (ANP) to enclose residues located within 20.0 Å around the ATP binding site, and a scaling factor of 1.0 was set to van der Waals (VDW) radii of those receptor atoms with the partial atomic charge less than 0.25. The extra-precision (XP) mode of Glide was used, and the top ranked poses of hematoxylin (ranked by lowest Glide Score) were retained after visual analysis.

In vitro antiproliferation assay

Cell proliferation was evaluated using the MTT assay as previously described[15]. Briefly, cells were seeded into 96-well plates and grown for 24 h. The cells were then treated with or without different concentrations of hematoxylin and grown for a further 72 h. At the end of exposure, 20 μL of MTT (5 g/L) was added to each well and the plates were incubated at 37 °C for 4 h. Then a "triplex solution" (10% SDS-5% isobutanol-12 mmol/L HCl) was added and the plates were incubated at 37 °C for 12 h. The plates were then measured at 570 nm using a multiwell spectrophotometer (SpectraMax 190, Molecular Devices). The cell growth inhibition rate was calculated by the equation [1–(A_{570} treated/A_{570} control)]×100 %. The IC_{50} value was obtained by the Logit method and was determined from the results of at least 3 independent tests.

DAPI staining assay

DAPI staining was performed as described previously[16].

Briefly, HL-60 cells (3×10^5 cells/mL) were seeded into six-well plates and treated with different concentrations of hematoxylin for the indicated times. The cells were harvested and fixed with 4% paraformaldehyde for 30 min at room temperature. After cells were washed with PBS by centrifugation at 1000×*g* for 5 min, 2 μL DAPI (5 μg/mL) was added to the fixed cells for 5 min, after which they were examined by fluorescence microscopy. Apoptotic cells were identified by condensation and fragmentation of chromatin.

Flow cytometry assay

To evaluate the apoptosis-inducing activity of hematoxylin, HL-60 cells were plated at a density of 3×10^5 cells/mL into six-well plates and incubated with or without the indicated concentrations of hematoxylin for 24 h. The cells were then harvested and fixed in 70% ethanol and stored at 4 °C overnight. Afterward, the cells were stained in PBS containing 40 μg/mL RNase and 10 μg/mL propidium iodide (PI) at room temperature in the dark for 30 min. Subsequently, the cells were analyzed using a FACS-Calibur cytometer (Becton Dickinson, San Jose, CA, USA). The cells undergoing apoptosis were obtained from the distinct sub-G_1 region of the DNA distribution histograms. At least 10 000 events were counted for each sample.

Western blot analysis

HL-60 cells (3×10^5 cells/mL) were seeded into six-well plates and exposed to hematoxylin at various concentrations for 24 h. After treatment, the cells were collected and suspended in lysis buffer (100 mmol/L Tris-HCl, pH 6.8, 200 mmol/L DTT, 4% SDS, 0.2% bromophenol blue, and 20% glycerol). The cell lysate was cleared by centrifugation at 14 000 revolutions per minute for 15 min. Lysate proteins were resolved by 7.5% sodium dodecyl sulfate polyacrylamide gel electrophoresis (SDS-PAGE) and transferred to nitrocellulose membranes. The membranes were incubated for 1 h in 5% milk, followed by 2 h of incubation with primary antibodies. The membranes were washed three times with PBS (with 0.1% Tween-20) and then incubated with the respective peroxidase-conjugated secondary antibody for 1 h. The membranes were washed again, developed using enhanced chemiluminescence (ECL, Amersham Biosciences), and exposed to Kodak X-Omat BT film.

Statistical analysis

Data shown were mean±SD from three independent experiments.

Results

Expression and purification of human IGF1R-CD

The catalytic domain of the human IGF1R cDNA was subcloned into the pAcGP67-A vector for generation of a histidine $(His)_6$-tagged fusion protein. The proteins were purified and detected as described in Materials and methods. The time-course analysis of protein expression revealed maximal levels at 3 d post-infection (data not shown), and the protein concentration was approximately 1.5 g/L. The $(His)_6$-IGF1R-CD fusion protein was observed as a major band migrating with an apparent molecular weight of 31 kDa (Figure 1A), which is consistent with the expected size of the protein. When the elution fraction was probed by an antibody specifically raised against IGF1R, the corresponding immunoreactive band was detected with the same molecular weight (Figure 1B).

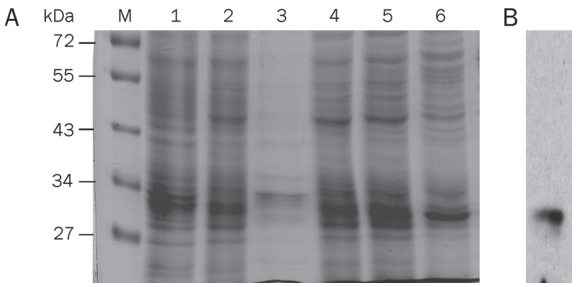

Figure 1. SDS-polyacrylamide gel analysis of purified IGF1R-CD. (A) IGF1R-CD was Ni-NTA column purified from T ni insect cells, and the purity of the fusion protein was examined in aliquots from different steps of the purification. Lane 1, whole infected cell lysate; Lane 2, supernatant sample; Lane 3, cell debris after lysis; Lane 4, wash step fraction; Lane 5, elution step fraction 1; Lane 6, elution step fraction 2; M, molecular weight marker. Proteins were separated by 15% SDS-PAGE, and stained with Coomassie blue dye. (B) Parallel samples were immunoprecipitated using a polyclonal antibody against His-Tag and then Western blotted with an anti-IGF1R antibody.

Kinase activity of IGF1R-CD

To determine the kinase activity of IGF1R-CD and the kinase concentration required for the phosphorylation of substrate, we used an ELISA assay. The peptide substrate employed in this test is a random copolymer of glutamic acid and tyrosine [poly(Glu, Tyr)$_{4:1}$][17]. Varying quantities of IGF1R-CD were mixed with a fixed amount of ATP (5 μmol/L) and then added to 96-well plates pre-coated with 20 μg/mL of poly(Glu, Tyr)$_{4:1}$. As illustrated in Figure 2A, the phosphorylation state of the substrates increased with rising concentrations of IGF1R-CD protein kinase, reaching a high level (A_{490}=1.0) upon exposure to 0.75 μg of IGF1R-CD protein kinase. Consequently, 0.75 μg of IGF1R-CD protein kinase per well was used as a defined concentration in the subsequent screening. Next, we investigated the effects of the concentrations of both ATP and the peptide substrate on the phosphorylation reaction. The results in Figure 2B and 2C clearly demonstrated a positive correlation between kinase activity and the substrate concentrations, releasing the optimal concentrations of ATP and poly(Glu, Tyr)$_{4:1}$ in the kinase assay at 5 μmol/L and 20 μg/mL, respectively.

Divalent cation is required for substrate phosphorylation

Substrate phosphorylation by a kinase requires the presence of divalent cations. The interactions among these factors are complex. The kinases are either activated or inactivated upon binding to such divalent cations as Mg^{2+} or Mn^{2+}. ATP usually coordinates with Mg^{2+} and Mn^{2+} to form ATP-Mg and ATP-

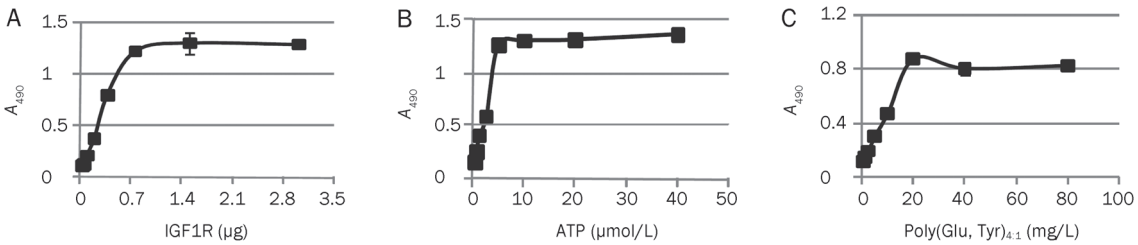

Figure 2. ELISA assays determining the phosphorylation of a synthetic peptide. (A) Plot of A_{490} *vs* IGF1R quantity illustrating the relationship between substrate phosphorylation status and IGF1R level. (B) Plot of A_{490} *vs* ATP concentration, and (C) Plot of A_{490} *vs* concentration of synthetic substrate poly(Glu,Tyr)$_{4:1}$, used to determine the optimal concentration of substrate in the screening model. Data shown were mean±SD from three independent experiments.

Mn, which serve as the actual substrates in phosphorylation. Accordingly, we examined the effects of divalent cation concentrations on the rate of substrate phosphorylation catalysis by IGF1R-CD. As shown in Figure 3A and 3B, with increases in their concentrations, the kinase activities were increased accordingly within a certain range of Mg^{2+} or Mn^{2+} concentration. Optimal kinase activity was observed at 10 mmol/L and 0.05 mmol/L for Mg^{2+} and Mn^{2+}, respectively.

Screening of IGF1R kinase inhibitors

We have identified the optimal concentration of key factors in our screening model. We then used the compound I-OMe-AG 538, a well known IGF1R inhibitor, as the positive control to determine the efficiency of the model. As illustrated in Figure 3C, I-OMe-AG 538 inhibited the IGF1R-CD kinase activity in a concentration-dependent manner, with an IC_{50} value of 0.175 μmol/L. These data are consistent with a previous report[18], illustrating that the model established in the present study can be used for the identification of IGF1R inhibitors.

The optimized IGF1R-based ELISA assay was then used to screen more than 200 compounds featuring a wide variety of chemical structures. The primary screening was performed at a single concentration of 10 μmol/L of each compound. Subsequently, all primary hits demonstrating at least 30% inhibition relative to control were retested, and the IC_{50} values were calculated. Eventually, eight potential inhibitors were characterized (data not shown). Notably, hematoxylin, a widely used nuclear dye, was revealed to be one of the most potent inhibitors of IGF1R. This compound effectively inhibited the IGF1R activity in a dose-dependent manner, with an IC_{50} value of 1.8±0.1 μmol/L (Figure 4A).

Hematoxylin binds to the kinase domain of IGF1R

Because hematoxylin was identified as a novel IGF1R inhibitor, we then wanted to know whether its inhibitory activity on IGF1R was associated with direct engagement with tyrosine kinases. An SPR assay was employed to assess the interaction between hematoxylin and IGF1R. For this assay, hematoxylin was immobilized on CM-5 sensor chips. The response of binding units of hematoxylin to IGF1R was recorded as described in Materials and methods. As shown in Figure 4B, hematoxylin was noted to bind to IGF1R in a concentration-dependent manner with high affinity, yielding the equilibrium dissociation constant (Kd) of 4.2×10^{-6} mol/L. The results demonstrated that hematoxylin could bind directly to IGF1R-CD.

Docking analysis of hematoxylin with IGF1R tyrosine kinase domain

To further explore the binding profiles of the compound, a binding model of hematoxylin with the IGF1R tyrosine kinase domain was simulated by molecular docking. The results in Figure 4C indicated that hematoxylin occupies the adenine pocket of the ATP binding site of IGF1R. The binding orientation of one catechol moiety is located at the hinge region through hydrogen bonds with the backbone of the conserved residues among the kinase family (Glu 1077 and Met 1079). Two hydrogen bonds exist between the other catechol moiety and carboxylates of Asp 1150 of the Asp-Phe-Gly (DFG) motif

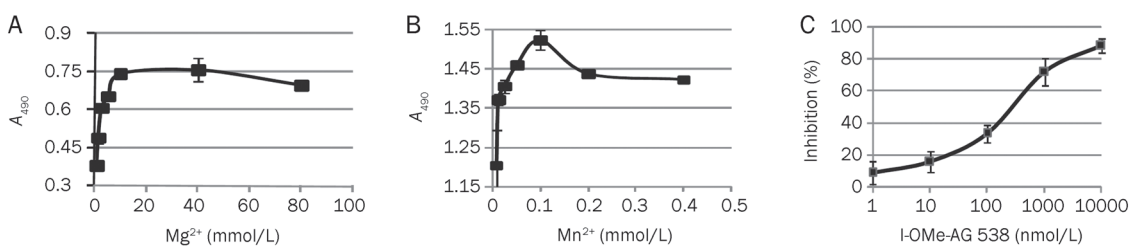

Figure 3. Titration of the divalent cations and determination of IGF1R inhibitory activity of I-OMe-AG 538 in the established screening model. (A-B) Plot of A_{490} *vs* concentrations of divalent cations, used to determine the metal requirement for catalysis of substrate phosphorylation. (C) Effect of positive IGF1R inhibitor, I-OMe-AG 538, on IGF1R tyrosine kinase activity. Data shown were mean±SD from three independent experiments.

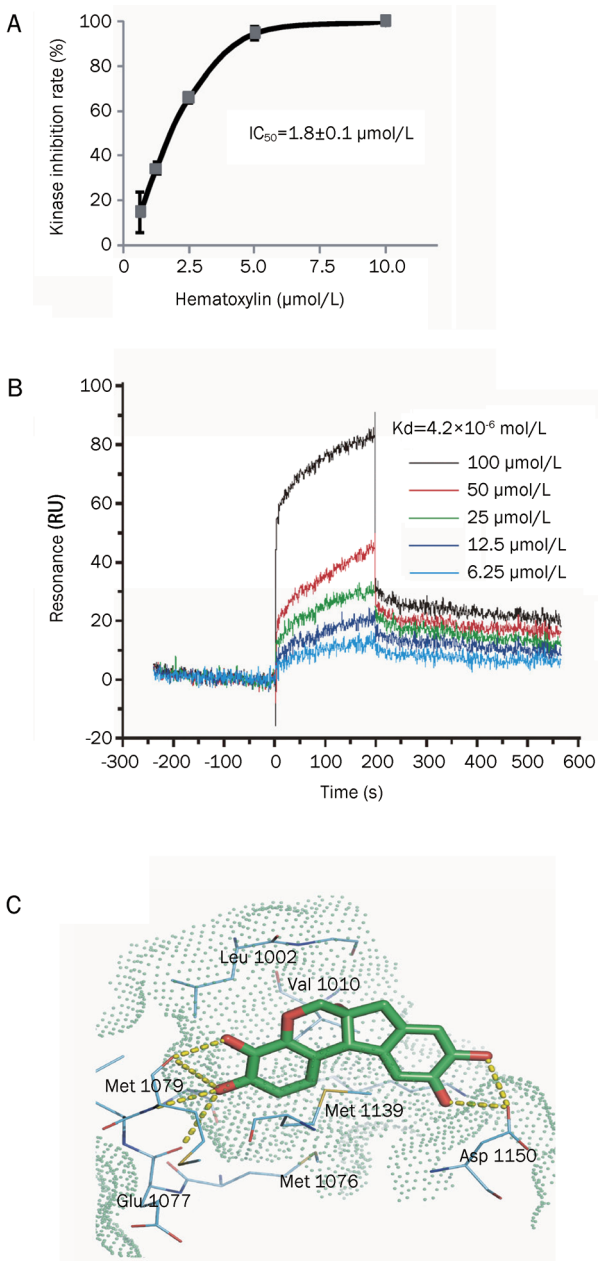

Figure 4. Hematoxylin inhibits IGF1R activity *in vitro* and binds directly to IGF1R-CD. (A) Inhibitory activity of hematoxylin on IGF1R detected by ELISA assay. Tests were performed three times independently. (B) Hematoxylin binds to IGF1R-CD. SPR assay was performed as described in Materials and methods. (C) The binding mode of hematoxylin to the kinase domain of IGF1R predicted by molecular docking. The ligand (green carbon) and residues (cyan carbon) are represented as sticks and lines, respectively. The yellow dashed lines denote the hydrogen bonds and the oxygen atoms are colored in red. The molecular surface of the binding site was shown as green dots. The structure figure was prepared using PyMol (www.pymol.org). Data shown were mean±SD from three independent experiments.

of the activation loop. Multiple hydrophobic interactions and van der Waals (VDW) contacts to the ATP binding site were also observed, including Leu 1002, Val 1010, Met 1139, and Met 1076. The docking results indicated that the hematoxylin formed a good interaction with the IGF1R active site, which may underlie the direct binding of the compound to IGF1R.

Hematoxylin potently inhibits the kinase activity of the insulin receptor (IR) tyrosine kinase

Because the insulin receptor is highly homologous to IGF1R, we further determined the effect of hematoxylin on the kinase activity of IR using an ELISA assay. As shown in Table 1, hematoxylin potently inhibited the kinase activity of IR *in vitro* with an IC_{50} value of 0.67±0.10 μmol/L, which is lower than that of hematoxylin on IGF1R. I-OMe-AG 538 was used as a positive control.

Table 1. Inhibitory effect of hematoxylin on the kinase activity of IR. Data shown were mean±SD from three independent experiments.

Compound	IC_{50} (μmol/L)
Hematoxylin	0.67±0.10
I-OMe-AG 538	0.21±0.12

Hematoxylin inhibits proliferation and IGF1R phosphorylation in HL-60 human leukemia cells

Next, we selected HL-60 human leukemia cells, which naturally express high levels of IGF1R, to test the inhibitory effects of hematoxylin on cell proliferation. As illustrated in Figure 5A, hematoxylin inhibited the proliferation of HL-60 cells in a concentration-dependent manner. Moreover, this compound inhibited IGF-induced IGF1R phosphorylation in a dose-dependent manner (Figure 5B), with the maximal effects obtained at 10 μmol/L of hematoxylin. Hematoxylin also decreased the phosphorylation of AKT and Erk1/2, the downstream signaling pathways of IGF1R. Together with the data described above, we conclude that hematoxylin at least partially inhibited cell proliferation via blocking the activation of IGF1R and subsequent downstream signaling.

Hematoxylin induces apoptosis in HL-60 cells

Because IGF1R signaling prevents apoptosis through the PI3K-AKT pathway[19], we next wanted to address whether hematoxylin induces apoptosis in HL-60 cells.

We first observed morphological changes in apoptosis induced by hematoxylin using DAPI staining. As illustrated in Figure 6A, treatment with hematoxylin at 20 μmol/L for 24 h induced marked apoptotic changes in HL-60 cells compared to the control cells, as evidenced by the appearance of fragmented chromatin and apoptotic bodies.

For further confirmation, we quantified apoptotic cells using flow cytometry analysis. As shown in Figure 6B, the fraction of cells in sub G_1/G_0 increased in a dose-dependent manner after hematoxylin treatment for 24 h. Approximately 10% of the HL-60 cells underwent apoptosis upon exposure to hema-

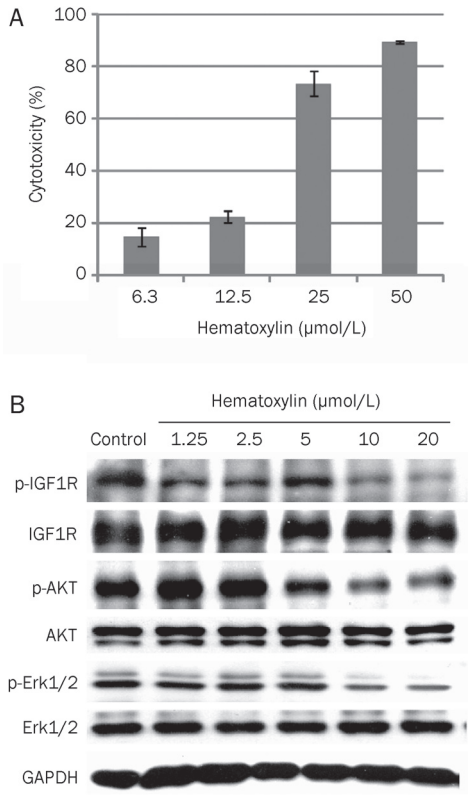

Figure 5. Effect of hematoxylin on the proliferation and the phosphorylation of IGF1R and downstream signaling pathways in HL-60 cells. (A) Growth inhibition of HL-60 cells by hematoxylin. Cells were treated with the indicated concentrations of hematoxylin for 72 h. Cell viability was determined by sulforhodamine B assay. The tests were repeated three times independently. (B) Hematoxlyin inhibits the phosphorylation of IGF1R and the activation of downstream signaling pathways in HL-60 cells. Cells were cultured in the presence of different doses of hematoxylin for 24 h and harvested. Whole cell lysates were assayed for different proteins by immunoblotting. A representative anti-GAPDH immunoblot is shown as a loading control. Data shown were mean±SD from three independent experiments.

toxylin (1.25 μmol/L), which increased to more than 23% with hematoxylin concentrations up to 20 μmol/L.

Hematoxylin activates caspase -3, -8, and -9 and induces PARP cleavage

We further evaluated whether hematoxylin induced apoptosis in a caspase-dependent manner. The results clearly showed that caspase-3 was activated after exposure to hematoxylin, as shown by a decrease in the procaspase-3 band and an increase in the cleaved caspase-3 band (Figure 6C). In addition, hematoxylin exposure resulted in PARP cleavage, a downstream target of caspase, in a dose-dependent fashion (Figure 6C).

To gain further insights into the mechanisms involved in the activation of caspase-3, the effects of hematoxylin on caspase-8 and caspase-9 were preferentially determined. As shown in Figure 6C, we found that both caspase-8 and caspase-9 were obviously cleaved after hematoxylin treatment, suggesting the involvement of both the extrinsic and the intrinsic apoptosis pathways.

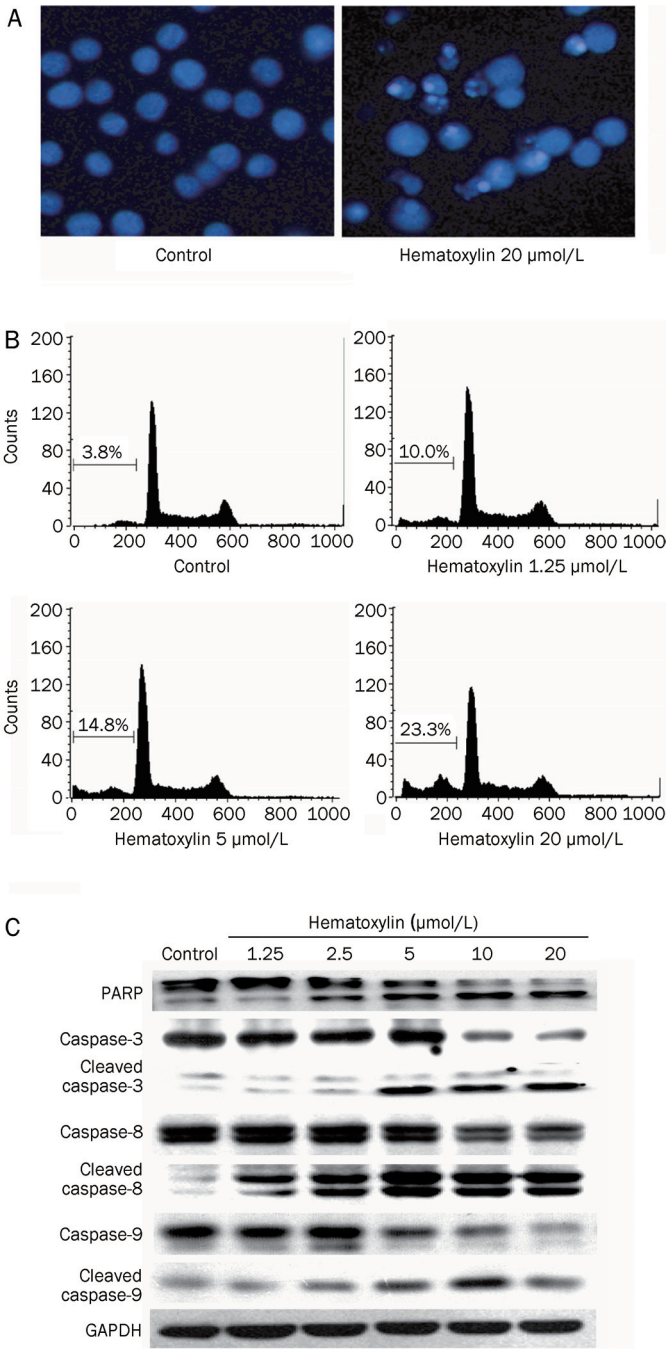

Figure 6. Hematoxylin induces apoptosis in HL-60 cells via both intrinsic and extrinsic apoptosis pathways. (A) DAPI staining assay. DAPI-stained nuclei of cells untreated or treated with 20 μmol/L hematoxylin were observed using a microcopy (×200). (B) PI staining for flow cytometry. Cells were treated with hematoxylin for 24 h at indicated concentrations and then analyzed using FACS after they were fixed by 70% ethanol and stained with PI. Sub G_0/G_1 DNA content of cells were indicated. (C) Hematoxylin modulates the expression of apoptosis-related proteins. After treatment with or without desired concentration of hematoxylin for 24 h, cells were collected and assayed by Western blotting analysis.

Discussion

IGF1R signaling pathway is activated in many types of cancers due to aberrant expression of IGF1R or its ligands (such as IGF-I and IGF-II) and/or by decreased levels of the binding proteins. Disruption of IGF1R signaling is an attractive approach for blocking tumor growth and metastasis[1, 3]. However, the efficient identification of novel IGF1R small molecule inhibitors primarily hinges on the availability of effective and feasible screening methods. Accumulating evidence has supported the notion that the catalytic domain accurately reflects the nature of the intact receptor. In the present study, the catalytic domain of IGF1R (IGF1R-CD) was successfully cloned and expressed using the Bac-to-Bac expression system. Using this active fragment, we developed a successful model for screening IGF1R inhibitors based on the phosphorylation of the IGF1R-CD substrate. ELISA, a widely used specific assay for the detection and quantification of antigens or antibodies without radioactive pollution, was employed in this assay. The reliability and feasibility of this method were validated by reference IGF1R inhibitors, followed by screening of 200 compounds for IGF1R inhibition activity. Of these compounds, eight compounds were identified as exhibiting inhibitory effects on IGF1R in the low micromolar to micromolar range. Hematoxylin, a well-known dye, stood out as a potent inhibitor of IGF1R at both the enzymatic and the cellular level. Molecular docking combined with SPR analysis revealed that hematoxylin binds to IGF1R with high affinity through hydrogen bonding to the hinge region of the ATP binding site and hydroxylation to the catalytic site.

Moreover, we found that hematoxylin exhibits potent inhibition of the IR kinase activity. IR is a receptor tyrosine kinase that is 84% homologous to the IGF1R kinase domain and 100% homologous in the ATP binding cleft. IR is primarily involved in the response to insulin and uptake of glucose into cells. Due to the high homology between the two receptors, inhibitors and antibodies directed at IGF1R often also affect IR signaling, resulting in potential side effects, such as diabetes and cardiotoxicity. However, insulin, acting via IR, has been recognized as able to stimulate proliferation of breast cancer cells, and increased levels of insulin have been related to an increased risk of different types of human cancer[20–22]. Moreover, IGF-II, the ligand of IGF1R, also binds with high affinity to IR and IGF1R/IR hybrid receptors. Thus, targeting IGF1R itself, but not IR, may not be adequate to inhibit IGF action. An ideal anti-IGF strategy would target both IGF1R and IR only in tumor cells and leave host IR in insulin target tissues (liver, muscle, and fat) unaffected[5, 23]. Because our results demonstrate that hematoxylin can inhibit the kinase activities of both of IGF1R and IR, this compound deserves further investigation *in vivo* to evaluate target inhibition.

Activation of the IGF1R signaling pathway is involved in the growth, invasion and metastasis of cancer cells[5]. IGF1R has several survival signals, including PI3K/AKT/mTOR and Ras/MEK/MAPK pathways, which are able to protect cancer cells from apoptosis. Simultaneous inactivation of two of these pathways is required to inhibit the capacity of IGF1R to protect cancer cells from apoptotic injuries. In HL-60 human leukemia cancer cells, we found that hematoxylin inhibits the activation of IGF1R and downstream signaling. Importantly, such blockage of these signaling pathways eventually contributed to the subsequent induction of apoptosis and inhibition of cell proliferation. In addition, because our studies have proven that hematoxylin can inhibit multiple targets (including EGFR, FGFR, c-Met, and so on), inhibition of the downstream signaling pathways in HL-60 cells may result not only from the IGF1R inhibition but also from the inhibition of multiple kinases.

Detailed mechanistic studies indicated that caspases were involved in hematoxylin-induced apoptosis, as evidenced by the fact that hematoxylin is capable of activating caspase-3 and the downstream target, PARP. Caspase-driven cascades are activated through the membrane death-receptor pathway utilizing caspase-8 or through the mitochondrial pathway relying on the activation of caspase-9[24, 25]. In congruence with this notion, we found that that both caspase-8 and caspase-9 were activated after hematoxylin treatment, suggesting that both the extrinsic and the intrinsic apoptosis pathways are involved in hematoxylin-induced apoptosis.

Several small molecular tyrosine kinase inhibitors (TKIs) have been launched into marketing and numerous candidates are under clinical or preclinical evaluation. However, several candidates have failed in clinical trials due to the complex nature of the crosstalk and signaling bypasses downstream of the targeted protein tyrosine kinase (PTK). PTK inhibitors with broad-spectrum specificity are increasingly expected to demonstrate a better clinical benefit than selective agents[26]. Some multi-targeted PTK inhibitors approved by the FDA/EMEA, such as sorafenib[27] and sunitinib[28], are marked as a new generation of PTK inhibitor drugs. We have previously reported that hematoxylin is a multi-targeted inhibitor of several tyrosine kinases, including c-Src, c-Met, FGFR1, EGFR, VEGFR, PDGFR, and c-Kit [29]. These data, together with the newly recognized function of hematoxylin as a potent inhibitor of IGF1R, suggest that hematoxylin may be a promising therapeutic agent for the treatment of cancer.

In summary, we established an ELISA-based IGF1R inhibitor screening platform. Our new method will simplify the future identification of other IGF1R inhibitors, and using this approach, hematoxylin has emerged as a promising candidate for further investigation.

Acknowledgements

This work was financially supported by the Key New Drug Creation and Manufacturing Program (2009ZX09103-001 and 2009ZX09103-102), a grant from the Shanghai Science and Technology Committee (10431902600), and a grant from the Shanghai Key Lab of Chemical Biology (SKLCB-2008-03).

Author Contribution

Hua XIE, Ming YIN, and Jian DING designed research; Linjiang TONG, Hua XIE, and Ting PENG performed research; Xun HUANG, Si-meng CHEN, and Hong-yan LIU contributed

the protein expression; Xian-liang XIN performed the SPR experiment; Xiao-feng LIU and Hong-lin LI performed the molecular docking; Hua XIE, Lin-jiang TONG, Mei-yu GENG, and Jian DING wrote the paper.

References

1 Laviola L, Natalicchio A, Giorgino F. The IGF-I signaling pathway. Curr Pharm Des 2007; 13: 663–9.
2 Adams TE, Epa VC, Garrett TP, Ward CW. Structure and function of the type 1 insulin-like growth factor receptor. Cell Mol Life Sci 2000; 57: 1050–93.
3 Pollak MN, Schernhammer ES, Hankinson SE. Insulin-like growth factors and neoplasia. Nat Rev Cancer 2004; 4: 505–18.
4 Samani AA, Yakar S, LeRoith D, Brodt P. The role of the IGF system in cancer growth and metastasis: overview and recent insights. Endocr Rev 2007; 28: 20–47.
5 Sachdev D, Yee D. Disrupting insulin-like growth factor signaling as a potential cancer therapy. Mol Cancer Ther 2007; 6: 1–12.
6 Dransfield DT, Cohen EH, Chang Q, Sparrow LG, Bentley JD, Dolezal O, *et al*. A human monoclonal antibody against insulin-like growth factor-II blocks the growth of human hepatocellular carcinoma cell lines *in vitro* and *in vivo*. Mol Cancer Ther 2010; 9: 1809–19.
7 Iwasa T, Okamoto I, Suzuki M, Hatashita E, Yamada Y, Fukuoka M, *et al*. Inhibition of insulin-like growth factor 1 receptor by CP-751871 radiosensitizes non-small cell lung cancer cells. Clin Cancer Res 2009; 15: 5117–25.
8 Blecha JE, Anderson MO, Chow JM, Guevarra CC, Pender C, Penaranda C, *et al*. Inhibition of IGF-1R and lipoxygenase by nordihydroguaiaretic acid (NDGA) analogs. Bioorg Med Chem Lett 2007; 17: 4026–9.
9 Ohshima-Hosoyama S, Hosoyama T, Nelon LD, Keller C. IGF-1 receptor inhibition by picropodophyllin in medulloblastoma. Biochem Biophys Res Commun 2010; 399: 727–32.
10 Gariboldi MB, Ravizza R, Monti E. The IGFR1 inhibitor NVP-AEW541 disrupts a pro-survival and pro-angiogenic IGF-STAT3-HIF1 pathway in human glioblastoma cells. Biochem Pharmacol 2010; 80: 455–62.
11 Chu CH, Huang CY, Lu MC, Lin JA, Tsai FJ, Tsai CH, *et al*. Enhancement of AG1024-induced H9c2 cardiomyoblast cell apoptosis via the interaction of IGF2R with Galpha proteins and its downstream PKA and PLC-beta modulators by IGF-II. Chin J Physiol 2009; 52: 31–7.
12 Haluska P, Carboni JM, TenEyck C, Attar RM, Hou X, Yu C, *et al*. HER receptor signaling confers resistance to the insulin-like growth factor-I receptor inhibitor, BMS-536924. Mol Cancer Ther 2008; 7: 2589–98.
13 Haluska P, Carboni JM, Loegering DA, Lee FY, Wittman M, Saulnier MG, *et al*. *In vitro* and *in vivo* antitumor effects of the dual insulin-like growth factor-I/insulin receptor inhibitor, BMS-554417. Cancer Res 2006; 66: 362–71.
14 Martins AS, Mackintosh C, Martin DH, Campos M, Hernandez T, Ordonez JL, *et al*. Insulin-like growth factor I receptor pathway inhibition by ADW742, alone or in combination with imatinib, doxorubicin, or vincristine, is a novel therapeutic approach in Ewing tumor. Clin Cancer Res 2006; 12: 3532–40.
15 Liu X, Xie H, Luo C, Tong L, Wang Y, Peng T, *et al*. Discovery and SAR of thiazolidine-2,4-dione analogues as insulin-like growth factor-1 receptor (IGF-1R) inhibitors via hierarchical virtual screening. J Med Chem 2010; 53: 2661–5.
16 Xie H, Qin YX, Zhou YL, Tong LJ, Lin LP, Geng MY, *et al*. GA3, a new gambogic acid derivative, exhibits potent antitumor activities *in vitro* via apoptosis-involved mechanisms. Acta Pharmacol Sin 2009; 30: 346–54.
17 Guo XN, Zhong L, Zhang XH, Zhao WM, Zhang XW, Lin LP, *et al*. Evaluation of active recombinant catalytic domain of human ErbB-2 tyrosine kinase, and suppression of activity by a naturally derived inhibitor, ZH-4B. Biochim Biophys Acta 2004; 1673: 186–93.
18 Blum G, Gazit A, Levitzki A. Development of new insulin-like growth factor-1 receptor kinase inhibitors using catechol mimics. J Biol Chem 2003; 278: 40442–54.
19 Shelton JG, Steelman LS, White ER, McCubrey JA. Synergy between PI3K/Akt and Raf/MEK/ERK pathways in IGF-1R mediated cell cycle progression and prevention of apoptosis in hematopoietic cells. Cell Cycle 2004; 3: 372–9.
20 Mulligan AM, O'Malley FP, Ennis M, Fantus IG, Goodwin PJ. Insulin receptor is an independent predictor of a favorable outcome in early stage breast cancer. Breast Cancer Res Treat 2007; 106: 39–47.
21 Goodwin PJ, Ennis M, Pritchard KI, Trudeau ME, Koo J, Madarnas Y, *et al*. Fasting insulin and outcome in early-stage breast cancer: results of a prospective cohort study. J Clin Oncol 2002; 20: 42–51.
22 Kaaks R, Lukanova A. Energy balance and cancer: the role of insulin and insulin-like growth factor-I. Proc Nutr Soc 2001; 60: 91–106.
23 Buck E, Gokhale PC, Koujak S, Brown E, Eyzaguirre A, Tao N, *et al*. Compensatory insulin receptor (IR) activation on inhibition of insulin-like growth factor-1 receptor (IGF-1R): rationale for cotargeting IGF-1R and IR in cancer. Mol Cancer Ther 2010; 9: 2652–64.
24 Kim KS. Multifunctional role of Fas-associated death domain protein in apoptosis. J Biochem Mol Biol 2002; 35: 1–6.
25 Green DR, Reed JC. Mitochondria and apoptosis. Science 1998; 281: 1309–12.
26 Gossage L, Eisen T. Targeting multiple kinase pathways: a change in paradigm. Clin Cancer Res 2010; 16: 1973–8.
27 Iyer R, Fetterly G, Lugade A, Thanavala Y. Sorafenib: a clinical and pharmacologic review. Expert Opin Pharmacother 2010; 11: 1943–55.
28 Goodman VL, Rock EP, Dagher R, Ramchandani RP, Abraham S, Gobburu JV, *et al*. Approval summary: sunitinib for the treatment of imatinib refractory or intolerant gastrointestinal stromal tumors and advanced renal cell carcinoma. Clin Cancer Res 2007; 13: 1367–73.
29 Lin LG, Xie H, Li HL, Tong LJ, Tang CP, Ke CQ, *et al*. Naturally occurring homoisoflavonoids function as potent protein tyrosine kinase inhibitors by c-Src-based high-throughput screening. J Med Chem 2008; 51: 4419–29.

Acta Pharmacologica Sinica (2011) 32: 939–946
 1671-4083/11 $32.00
www.nature.com/aps

Original Article

Anti-cancer effects of p21WAF1/CIP1 transcriptional activation induced by dsRNAs in human hepatocellular carcinoma cell lines

Zhi-ming WU[1, #], Chun DAI[2, #], Ying HUANG[3, #], Cui-fang ZHENG[3], Qiong-zhu DONG[2], Guan WANG[2], Xiao-wen LI[2], Xiao-fei ZHANG[2], Bin LI[1], Gang CHEN[1, *]

[1]Department of Surgery, Jinshan Hospital, Fudan University, Shanghai 200540, China; [2]Liver Cancer Institute and Zhongshan Hospital, Fudan University, Shanghai 200032, China; [3]Children's Hospital of Fudan University, Shanghai 201102, China

Aim: To investigate the anti-cancer effects of p21WAF1/CIP1 transcriptional activation induced by dsRNAs in hepatocellular carcinoma (HCC) cell lines.
Methods: HCC cell lines BEL7402, SMMC-7721, MHCC97L, MHCC97H, and MHCCLM3 were used. HCC cells were treated with dsP21-322 (50 nmol/L), dsControl (50 nmol/L), siP21 (50 nmol/L), or mock transfection. The expression of p21 was detected using quantitative PCR and Western blot. The effects of RNA activation on HCC cells were determined using cell viability assays, apoptosis analyses and clonogenic survival assays. Western blot was also conducted to detect the expression of Bcl-xL, survivin, cleaved caspase-3, cleaved caspase-9 and cleaved PARP.
Results: At 72 to 120 h following the transfection, dsP21-322 markedly inhibited the viability of HCC cells and clone formation. At the same times, dsP21-322 caused a significant increase in HCC cell apoptosis, as demonstrated with cytometric analysis. The phenomena were correlated with decreased expression levels of the anti-apoptotic proteins Bcl-xL, survivin, and increased expression of cleaved caspase-3, cleaved caspase-9 and cleaved PARP.
Conclusion: RNA-induced activation of p21 gene expression may have significant therapeutic potential for the treatment of hepatocellular carcinoma and other cancers.

Keywords: hepatocellular carcinoma; small activating RNA (saRNA); RNA-induced gene activation (RNAa); p21WAF1/CIP1; cell viability; apoptosis

Acta Pharmacologica Sinica (2011) 32: 939–946; doi: 10.1038/aps.2011.28; published online 13 Jun 2011

Introduction

Hepatocellular carcinoma (HCC) is one of the most common and aggressive malignancies worldwide, ranking among the top five leading causes of cancer death in the world, and is the second highest cause in China[1, 2]. HCC now accounts for over 626 000 new cases annually[1], and the incidence has more than doubled over the last two decades[3]. Whereas the incidence of HCC has been steadily increasing, the emergence of new and effective therapeutic agents remains relatively stagnant. High mortality rates are due to the severity of underlying liver disease, late diagnosis resulting in advanced stage disease, lack of effective treatment options, and disease progression even after surgical therapies or locoregional procedures[4]. Even in well-selected patients with operable disease, the long-term prognosis is still unsatisfactory because of frequent recurrences after resection. Therefore, there is a great need for novel treatments and better interventions for HCC.

Noncoding RNA (ncRNA) molecules, such as small interfering RNA (siRNA), microRNAs (miRNAs), and short-hairpin RNAs (shRNAs), were recognized initially for their powerful ability to down-regulate specific genes at both the post-transcriptional[5–7] and the transcriptional levels[8, 9]. Other reports have claimed the opposite effect[10–14]. Li *et al* reported that double stranded RNA (dsRNA) molecules could induce sequence-specific transcriptional gene activation, termed this phenomenon RNA-induced gene activation (RNAa) and termed the molecules small activating RNAs (saRNA)[10]. Although two mechanistic models related to RNA activation have been proposed[10–16], very little is known about what makes one molecule a silencer and another an activator [17]. Nevertheless, what is becoming clear is that RNAa has the

# These authors contributed equally to this study.
* To whom correspondence should be addressed.
E-mail chgan305@126.com
Received 2010-11-20 Accepted 2011-03-15

potential to be a powerful biological tool and could lead to new therapies for diseases such as cancer[18, 19]. Among those genes that can be modulated through RNAa[10–14], the p21WAF1/CIP1 (p21) gene product is special because it is a potent cyclin-dependent kinase inhibitor that binds to and inhibits the activity of cyclin-CDK2 or cyclin-CDK4 complexes. It thus functions as a regulator of cell cycle progression at the G_1 stage[20]. The p21 gene product may also play a regulatory role in S-phase DNA replication and DNA damage repair by interacting with proliferating cell nuclear antigen (PCNA), a DNA polymerase accessory factor[21]. Although the role of p21 in apoptosis is still controversial, with contradictory findings of both stimulation and inhibition of apoptosis[22], there are studies indicating that p21 also possesses pro-apoptotic functions against cancer[19, 23]. Previous studies have also shown that decreased p21 expression may be involved in a variety of carcinomas, especially in cases of altered p53 expression[24, 25]. Therefore, p21 is a potential candidate for RNAa-mediated cancer therapy.

In this study, we sought to investigate the anticancer effects of RNAa-mediated p21 activation in HCC cells. Our study has shown that up-regulation of p21 triggered by an saRNA resulted in the significant inhibition of proliferation and survival and in the induction of apoptosis in HCC cells.

Materials and methods

dsRNAs

dsP21-322, 21 nucleotides long, corresponding to the promoter region of p21, was designed as described previously by Li *et al*[10]. siP21, which targets p21 mRNA, was designed with the BLOCK-iT™ RNAi Designer (Invitrogen, Carlsbad, CA, USA). A dsRNA lacking significant homology to all known human sequences (dsControl) was used as a non-specific control. The dsRNAs were chemically synthesized by Genepharma (Shanghai, China). All dsRNA sequences are listed in Table 1.

Table 1. Sequences for dsRNAs and PCR primers.

dsRNA/Primer	Sequence (5′–3′)
dsP21-322 S	CCA ACU CAU UCU CCA AGU A[dT][dT]
dsP21-322 AS	UAC UUG GAG AAU GAG UUG G[dT][dT]
dsP21+271 S	GAA CUU CGA CUU UGU CAC CGA GAC A
dsP21+271 AS	UGU CUC GGU GAC AAA GUC GAA GUU C
dsControl S	ACU UAC GAG UGA CAG UAG A[dT][dT]
dsControl AS	UCU ACU GUC ACU CGU AAG U[dT][dT]
GAPDH-For	GCA CCG TCA AGG CTG AGA AC
GAPDH-Rev	TGG TGA AGA CGC CAG TGG A
P21-For	AAG ACC ATG TGG ACC TGT CAC TGT
P21-Rev	GAA GAT CAG CCG GCG TTT G

S, sense; AS, antisense; For, forward; Rev, reverse.

Cell culture and transfection

The human hepatoma cell lines BEL7402, SMMC-7721, MHCC97L, MHCC97H, and MHCCLM3 used in this study were a generous gift from the Liver Cancer Institute and Zhongshan Hospital, Fudan University (Shanghai, China). MHCC97L, MHCC97H, and MHCCLM3 cell lines were established from the same parent human HCC cell line of MHCC97 in the Liver Cancer Institute and Zhongshan Hospital, Fudan University. Cells were grown in Dulbecco's modified Eagle's medium (DMEM) containing 10% FBS, penicillin (100 units/mL), and streptomycin (0.1 mg/mL) and were incubated at 37 °C in a humidified incubator under an atmosphere of 5% CO_2. The day before transfection, cells were plated in growth medium without antibiotics at a density of 50% to 70%. The dsRNA was transfected at a concentration of 50 nmol/L using Lipofectamine 2000 (Invitrogen, Carlsbad, CA, USA) according to the manufacturer's instructions.

The cultures were collected 48 or 72 h later, cells were counted to determine viability, and mRNA and protein were obtained.

Cell viability assay

Phase-contrast images of treated cells were taken with an Olympus X51 microscope (Olympus, Tokyo, Japan) at 40× magnification. Cell viability was measured by a colorimetric assay based on the cleavage of the tetrazolium salt WST-1 by mitochondrial dehydrogenases (cell proliferation reagent WST-1; Molecular Biochemicals, Mannheim, Germany). MHCCLM3 cells were seeded onto 96-well culture plates at approximately 6000–8000 cells in 200 μL DMEM medium with 10% FBS. Cells were cultured for 24 h under 5% CO_2 at 37 °C. After overnight incubation, cells were treated with dsP21-322 (50 nmol/L), siP21 (50 nmol/L), dsControl (50 nmol/L), or mock transfection. Twelve hours later, the incubation medium was removed and replaced with 200 μL fresh medium with 10% FBS. At various time points following transfection (24, 48, 72, 96, or 120 h), 10 μL WTS-1 was added to each well. After incubation at 37 °C for 2 h, viable cells were detected by measuring absorbance at 440 nm using a SpectraMax M5 microplate reader (Molecular Devices, Sunnyvale, CA, USA). Cell viability was expressed as a percentage of the absorbance of cells after transfection at various time points relative to the values before transfection. Cells present 24 h after seeding were considered 100% viable. The reduction in viability of dsP21-322 or dsControl-treated MHCCLM3 cells was compared to the mock transfection group. The dsP21-322 and dsControl treatment groups were compared to the mock transfection group to obtain *P* values. Each assay was repeated three times.

Apoptosis assay

Cells were plated in 6-well plates at a density of 0.5×10^6 cells/mL and incubated overnight. Transfections were performed and then cells were incubated for 12 h before changing the transfection medium to fresh medium containing 10% FBS. Cells were harvested at 72 h following transfection, washed twice with pre-chilled PBS, and resuspended in 100 μL 1× binding buffer at a concentration of 1×10^6 cells/mL. Annexin V and PI double-staining was performed using an Annexin

V-FITC Apoptosis Detection Kit (BD Biosciences, San Jose, CA, USA) according to the manufacturer's protocol. Cell apoptosis analysis was performed by an EPICS ALTRA Flow Cytometry System with CXP Software (Beckman Coulter, Fullerton, CA, USA) within 1 h.

Quantitative PCR

Total RNA was extracted from cells by TRIzol (Invitrogen) after 48 h of transfection (mock, 50 nmol/L dsControl, 50 nmol/L dsP21-322 or 50 nmol/L siP21) and reverse transcription was performed with a PrimeScript RT reagent Kit (Takara Biotechnology, Dalian, China). qRT-PCR was performed with SYBR Green PCR reagent kits (Toyobo Co, Osaka, Japan) at a constant annealing temperature (64 °C) according to the manufacturer's protocol. Specific primer sets used in the real-time PCR directed against human p21 and GAPDH were designed and generated by Takara Biotechnology Co (Dalian, China) (listed in Table 1). Data were recorded and analyzed using the real-time PCR analysis software Bio-Rad iQ5. Endogenous gene expression was normalized to GAPDH levels in the cells.

Western blot analysis

Cells were harvested at 72 h following dsRNAs treatment as described above and then washed and lysed with M-PER extraction buffer (Pierce Biotechnology) containing protease inhibitors. Protein lysates, quantified using a BCA assay (Sangon Biotech Co, Ltd, Shanghai, China), were separated on reducing SDS-polyacrylamide gels and transferred to polyvinyl difluoride membranes (PVDF, Millipore). The membranes were blocked with 5% nonfat milk TBS buffer for 2 h at room temperature and incubated with primary antibodies overnight at 4 °C. Beta-actin levels were used to normalize loading. Primary immunoblotting antibodies (anti-Bcl-xL rabbit monoclonal antibody, anti-p21WAF1/CIP1 rabbit monoclonal antibody, anti-survivin rabbit monoclonal antibody, anti-cleaved caspase-9 rabbit polyclonal antibody, anti-cleaved caspase-3 rabbit polyclonal antibody, anti-cleaved PARP rabbit polyclonal antibody, or anti-β-actin antibody) were obtained from Cell Signaling Technology (Cell Signaling, Beverly, MA, USA) and used at 1:1000 dilutions. The first antibody exposure was followed by incubation with an anti-rabbit IgG, HRP-linked secondary antibody (Cell Signaling, Beverly, MA, USA). Antigen-antibody complexes were visualized by an enhanced chemiluminescence detection method (ECL kit, Thermo, Waltham, MA, USA).

Clonogenic survival assay

The day before transfection, MHCCLM3 cells were plated as single-cell suspensions at a density of 5000 cells per well in a 6-well plate. Cells were transfected 2 times with 50 nmol/L dsRNA (dsControl and dsP21-322) or mock transfection using Lipofectamine 2000 (Invitrogen, Carlsbad, CA, USA) at 24 h intervals, and the transfection medium was replaced with normal complete medium after 6 h and changed every three days. At d 12, the medium was removed and colonies were stained with 0.5% *w/v* crystal violet solution for 30 min. Images were taken for analysis using a single-lens reflex digital camera (K100D Super Pentax, Japan).

Statistical analysis

All experiments were performed at least three times. Statistical significance of the differences between various treatment groups and controls was calculated by applying Student's two-tailed *t*-test. The level of statistical significance was set at $P<0.05$.

Results

dsP21-322 induced p21 gene expression in HCC cell lines

A dsRNA targeting the p21 gene promoter at position-322 relative to the transcription start site (dsP21-322)[10] (Figure 1A) and a nonspecific control dsRNA (dsControl), which lacked significant homology to all known human sequences, were transfected into HCC cell lines of BEL7402, SMMC-7721, MHCC97L, MHCC97H, and MHCCLM3. After 48 and 72 h, mRNA and protein were obtained and analyzed by real-time quantitative PCR and Western blotting, respectively. As shown in Figure 1B, at 48 h, dsP21-322 caused a significant increase in p21 mRNA expression. Compared with mock transfections, the increases were 2.9-, 2.6-, 2.8-, 3.2-, and 4.0-fold higher in BEL7402, SMMC-7721, MHCC97L, MHCC97H, and MHCCLM3 cells, respectively ($P<0.05$, Figure 1B). Western blot analysis revealed that the levels of p21 protein elevated significantly when compared with mock and dsControl transfection, strongly correlating to the observed increase in p21 mRNA levels (Figure 1C). Although BEL7402, SMMC-7721 and MHCC97H cells had high baseline levels of p21 (Figure 1D), a moderate and consistent increase in p21 expression after dsP21-322 treatment was observed at both the mRNA and the protein levels. These results were reproducible in at least three independent experiments.

To determine whether activation of p21 by saRNA was dose- and time-dependent, concentration gradient and time-response studies were performed with MHCCLM3 cells. Figure 2A shows the up-regulation of p21 with various concentrations of dsP21-322 for 3 d. MHCCLM3 cells were transfected with 50 nmol/L dsP21-322 for the indicated lengths of time (Figure 2B). These data indicated that dsP21-322 exerted a significant activating effect upon MHCCLM3 cells in a dose- and time-dependent manner.

dsP21-322 inhibited HCC cell proliferation and survival

After transfection, mock-transfected and dsControl-transfected cells maintained healthy growth, whereas cells transfected with dsP21-322 gradually lost viability after d 2. Morphological changes were also observed (Figure 3A). There were more rounded floating cells in the supernatant of cells transfected with dsP21-322 while the adherent cells had become enlarged and flattened with decreased cell density. Typical apoptotic morphological changes were also seen, in which cells became smaller, rounded, and deformed with nuclear condensation.

Further quantitation performed in MHCCLM3 cells by WST-1 colorimetric assay demonstrated that the dsP21-322

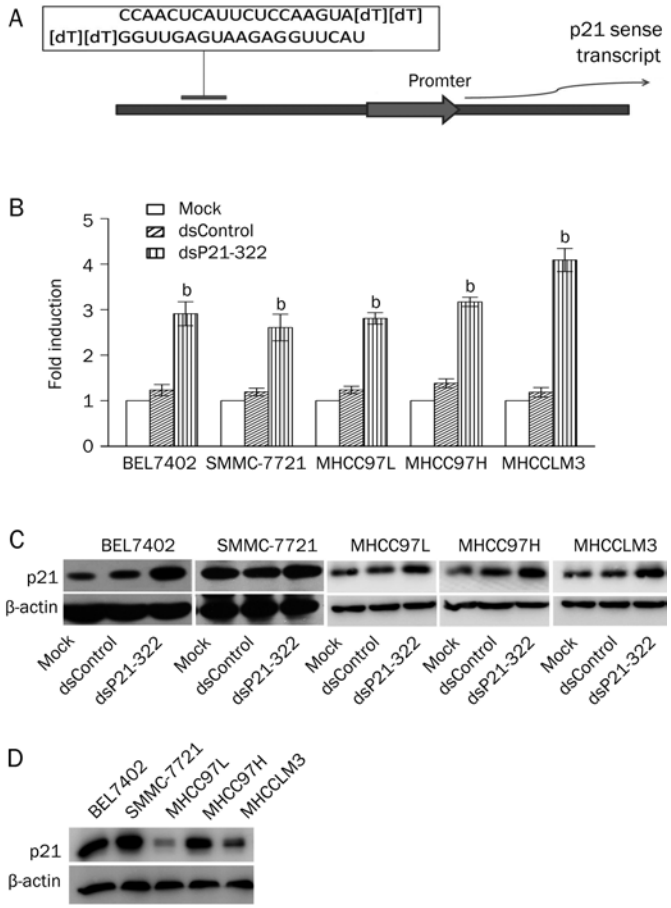

Figure 1. Effects of dsRNAs targeting the p21 gene promoter on p21 mRNA and protein levels in HCC cell lines. (A) A schematic diagram showing the target sequence positions of dsP21-322 relative to the transcriptional start site. (B) Induction of p21 mRNA expression was detected by real-time quantitative RT-PCR. HCC cells were transfected with 50 nmol/L dsP21-322 and dsControl for 2 d. Mock transfections were also done in the absence of saRNA. Expression levels were measured as fold-induction relative to mock transfections. The results were normalized to GAPDH and presented as mean±SD of three independent experiments. $^{b}P<0.05$ *vs* mock transfections. (C) The induction of p21 protein levels were detected by Western blot analysis at 72 h following dsRNA treatment, as described above. A representative blot is shown from three independent experiments with identical results. Beta-actin levels were also detected and served as endogenous controls. (D) Detection of p21 protein levels in the HCC cell lines of BEL7402, SMMC-7721, MHCC97L, MHCC97H, and MHCCLM3.

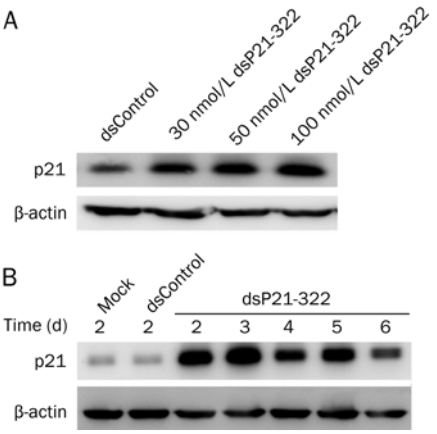

Figure 2. Concentration dependence and the time course of activation by dsP21-322 in MHCCLM3 cells. (A) Western blot analysis showing the levels of p21 protein after transfection with various concentrations of dsRNAs into MHCCLM3 cells. A representative blot is shown from three independent experiments with identical results. (B) MHCCLM3 cells were treated with 50 nmol/L dsP21-322, dsControl or mock transfection at various time points (2–6 d). p21 protein and beta-actin expression were detected by Western blotting.

transfection induced a significant loss in cell viability. As shown in Figure 3B, there were detectable reductions in MHCCLM3 cell viability after dsP21-322 transfection at a concentration of 50 nmol/L. After 48 h, proliferation of the dsP21-322 transfection group decreased dramatically from 65.9% to 20.1%. The time point of the strong growth-inhibitory effect substantially correlated with the kinetics of RNAa. By contrast, viability of the mock group and dsControl group decreased slightly during the 48 h after transfection, after which they recovered. These observations indicated that dsP21-322 was an effective inhibitor of HCC cell growth, and this inhibitory effect was time dependent.

The clonogenic survival assay or colony formation assay is a widely used method to determine the effectiveness of other cytotoxic agents. It tests every cell in the population for its ability to undergo "unlimited" division[26]. After 12 d of incubation, colonies were stained and photographed. As shown in Figure 3C, no colony formation was observed in cells transfected with dsP21-322, while numerous colonies were stained in both mock and dsControl-transfected cells. These results were consistent with a previous report in T24 bladder cancer cells[18].

Previous studies have shown that survivin expression was strongly correlated with the proliferation index in HCC tissues, and overexpression of survivin resulted in both significant cell proliferation and survival promotion in carcinoma cells[27]. Hence, to determine whether the decrease in cell viability and survival in the induction of p21 by RNAa occurred through a survivin-dependent pathway, changes in the levels of survivin were investigated after treatment. As can be seen in Figure 3D, a dramatic decrease in survivin protein levels was found in the dsP21-322-treated group when compared with the control groups. The data showed that the up-regulation of p21 strongly correlated with decreased survivin levels in MHCCLM3 cells.

dsP21-322 significantly increased apoptosis and levels of apoptosis-related proteins in HCC cells

The extent of apoptosis was quantified by flow-cytometric analysis of saRNA-treated cells labeled with PI and annexin V. As shown in Figure 4A, treatment of SMMC-7721 and MHCCLM3 cells with 50 nmol/L dsP21-322 for 72 h resulted in 9.11% and 23.91% of total cells becoming apoptotic, respectively. In the mock and dsControl-transfected SMMC-7721

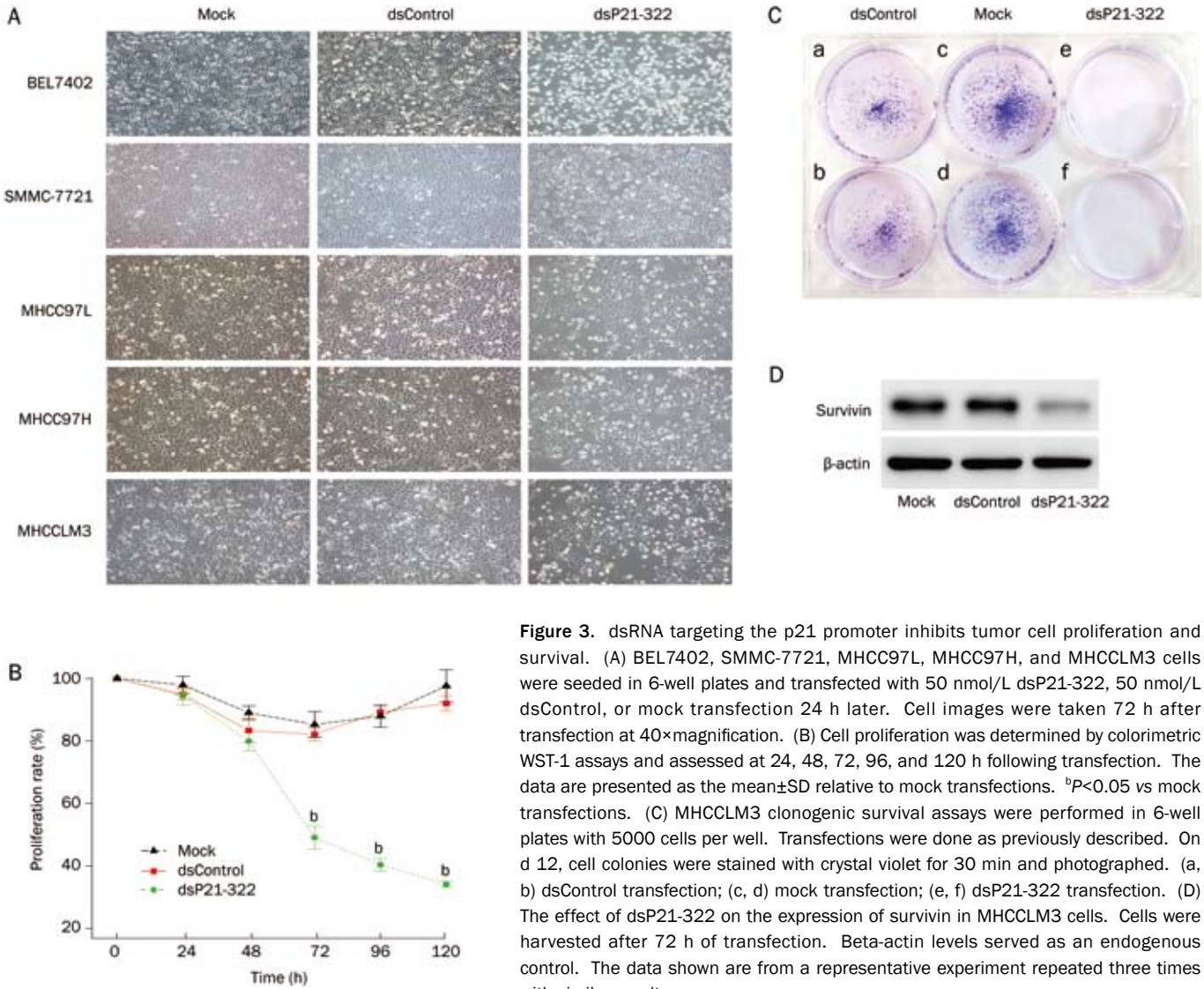

Figure 3. dsRNA targeting the p21 promoter inhibits tumor cell proliferation and survival. (A) BEL7402, SMMC-7721, MHCC97L, MHCC97H, and MHCCLM3 cells were seeded in 6-well plates and transfected with 50 nmol/L dsP21-322, 50 nmol/L dsControl, or mock transfection 24 h later. Cell images were taken 72 h after transfection at 40×magnification. (B) Cell proliferation was determined by colorimetric WST-1 assays and assessed at 24, 48, 72, 96, and 120 h following transfection. The data are presented as the mean±SD relative to mock transfections. $^{b}P<0.05$ *vs* mock transfections. (C) MHCCLM3 clonogenic survival assays were performed in 6-well plates with 5000 cells per well. Transfections were done as previously described. On d 12, cell colonies were stained with crystal violet for 30 min and photographed. (a, b) dsControl transfection; (c, d) mock transfection; (e, f) dsP21-322 transfection. (D) The effect of dsP21-322 on the expression of survivin in MHCCLM3 cells. Cells were harvested after 72 h of transfection. Beta-actin levels served as an endogenous control. The data shown are from a representative experiment repeated three times with similar results.

and MHCCLM3 cells, 2.78% and 3.26%, and 10.59% and 12.67%, were found to be apoptotic, respectively. These results revealed that treatment of SMMC-7721 and MHCCLM3 cells with dsP21-322 resulted in a significant increase in apoptosis.

Cells undergoing apoptosis follow a death program by inhibiting the anti-apoptosis protein Bcl-xL and activating a hierarchy of caspases. Caspase-9 and caspase-3 are at least partially responsible for the proteolytic cleavage of many key proteins, such as the nuclear enzyme poly (ADP-ribose) polymerase (PARP), which plays a central role in the execution phase of cell apoptosis. In our study, besides a remarkable decrease in Bcl-xL, significant increases in cleaved caspase-9 and caspase-3 as well as cleaved PARP were observed in the dsP21-322-transfected MHCCLM3 cells (Figure 4B). Such significant changes in apoptosis execution further confirm the observed features of the apoptotic phenotype and the results from the flow cytometry assay.

p21 knockdown by siP21 resulted in the induction of proliferation and inhibition of apoptosis in MHCCLM3 cells

To confirm the role of p21 in the inhibition of proliferation and the induction of apoptosis, a siRNA strategy was used to knockdown expression of p21 in MHCCLM3 cells. The siRNA knockdown efficiency of p21 mRNA expression was 83% after 48 h of transfection (Figure 5A). Figure 5B showed that p21 levels decreased significantly in the siP21 transfection group. Next, cell viability and apoptosis assays were used to investigate the effect of p21 knockdown on the growth of MHCCLM3 cells. As shown in Figure 5C, inhibition of p21 expression is sufficient to promote survival and cell proliferation in 50 nmol/L siP21-transfected cells. Similar results were obtained with a flow cytometry assay, where 8.46% of the total cells became apoptotic 72 h after treatment of MHCCLM3 cells with 50 nmol/L siP21, which was substantially lower than the mock and dsControl groups, whose apoptotic rates were

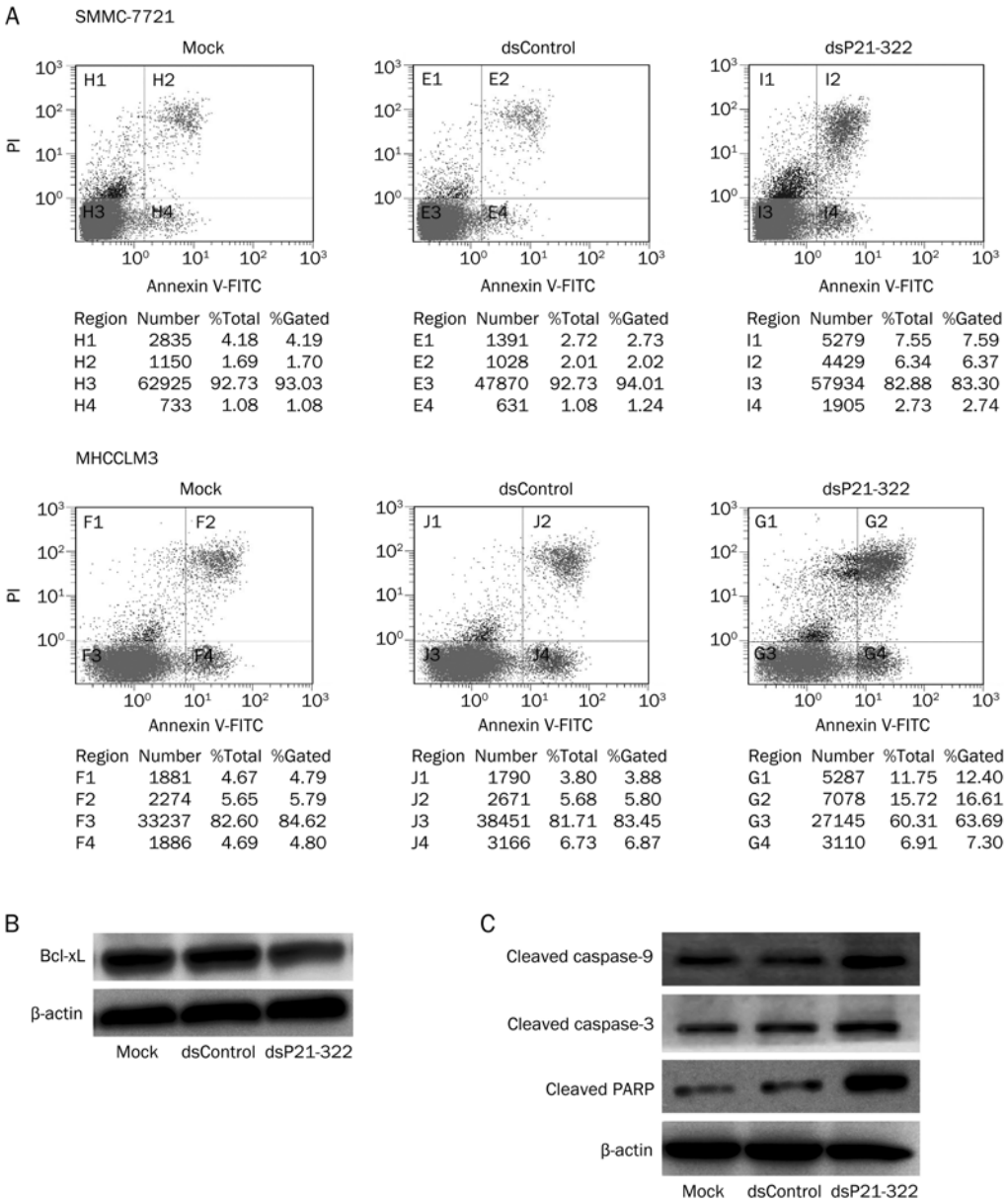

Figure 4. dsP21-322 transfection-induced apoptosis in HCC cells. (A) SMMC-7721 or MHCCLM3 cells were double-stained with annexin V and PI 72 h after treatment with dsP21-322 (50 nmol/L), dsControl (50 nmol/L), or mock transfection and analyzed by flow cytometry. Gate settings distinguished between live (bottom left), necrotic (top left), early apoptotic (bottom right), and late apoptotic (top right) cells. (B) Changes in the levels of Bcl-xL anti-apoptotic gene products in MHCCLM3 cells 72 h after treatment with 50 nmol/L dsP21-322. (C) Effects of dsP21-322 transfection-activated p21 levels on cleavage of apoptosis-related proteins caspase-3, caspase-9, and poly (ADP-ribose) polymerase (PARP). Beta-actin levels served to normalize loading. The data shown are from a representative experiment repeated three times with similar results.

12.76% and 13.67%, respectively (Figure 5D). These findings further confirm that the role of the *p21* gene in growth control of MHCCLM3 cells is mediated by an apoptotic mechanism.

Discussion

RNA activation in human cells was first observed with dsRNAs targeted to the promoters of E-cadherin, vascular endothelial growth factor (VEGF), and p21 and was confirmed in studies on the progesterone receptor (PR)[11]. Subsequently, microRNA-373 was found to induce expression of E-cadherin and cold-shock domain-containing protein C2 (CSDC2) with complementary promoter sequences[12]. When it comes to the exact mechanism underlying dsRNA induced RNAa, several models have been reported or proposed, including transcriptional activation by directly targeting the transcriptional start site of the desired gene[10, 12] or the activating siRNAs-mediated loss of an endogenous repressor antisense non-coding RNA, resulting in a loss of epigenetic regulation for the sense/mRNA partner, which ultimately resulted in a marked increase in transcription[15, 28]. However, due to the lack of a deeper understanding of the detailed mechanism of RNAa, more research will certainly be required. Regardless, what is becoming clear is that small RNAs can be used to mediate the activation of a wide array of genes. RNAa offers a promising new therapeutic strategy for diseases that can be corrected by stimulating gene expression[18, 19].

In our study, we found that dsP21-322 can cause a 2.6- to 4-fold increase in p21 mRNA levels in BEL7402, SMMC-7721, MHCC97L, MHCC97H, and MHCCLM3 cells. We also noticed that, although the BEL7402, SMMC-7721, and MHCC97H cells normally expressed high levels of p21, a moderate and consistent increase in p21 levels occurred after dsP21-322 treatment.

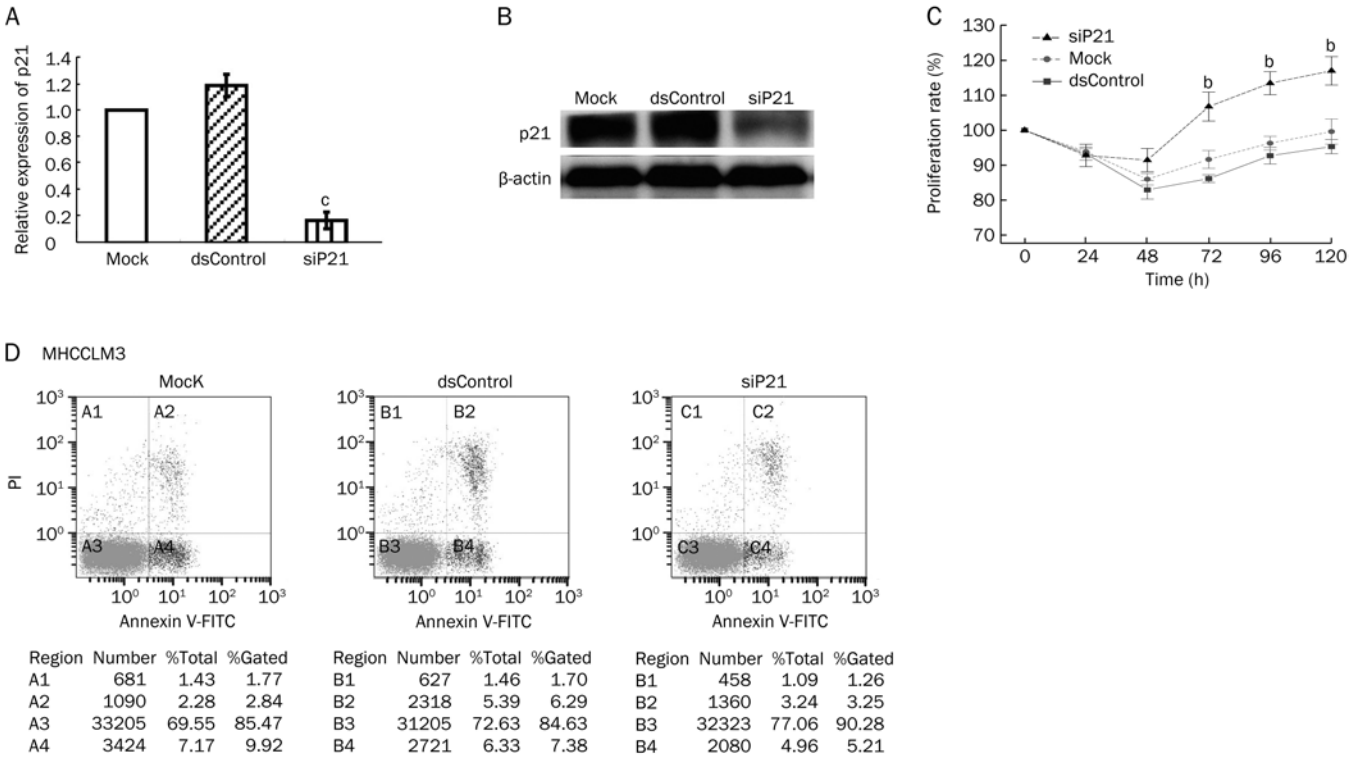

Region	Number	%Total	%Gated
A1	681	1.43	1.77
A2	1090	2.28	2.84
A3	33205	69.55	85.47
A4	3424	7.17	9.92

Region	Number	%Total	%Gated
B1	627	1.46	1.70
B2	2318	5.39	6.29
B3	31205	72.63	84.63
B4	2721	6.33	7.38

Region	Number	%Total	%Gated
B1	458	1.09	1.26
B2	1360	3.24	3.25
B3	32323	77.06	90.28
B4	2080	4.96	5.21

Figure 5. Effects of p21 knockdown on cell proliferation and apoptosis of MHCCLM3 cells. Either 48 or 72 h after cells were treated with siP21 (50 nmol/L), dsControl (50 nmol/L), or mock transfection, messenger RNA levels (A) were determined by qPCR analysis, and Western blot (B) was used to analyze p21 knockdown efficiency. Cell proliferation (C) and apoptosis (D) were assessed as described previously. $^{b}P<0.05$ *vs* mock transfections.

Data from both time- and concentration-dependence experiments in MHCCLM3 cells showed that the stimulatory effect of dsP21-322 was quite potent. Those results revealed that RNAa can be manipulated to up-regulate gene expression in hepatocellular carcinoma. To our knowledge, this is the first report that demonstrates dsRNA-mediated gene activation in HCC, which suggests that RNAa may be used to manipulate genes, especially tumor suppressor genes (TSG), in the treatment of HCC.

Clonogenic assays permit the study of the effectiveness of drugs or radiation on the survival and proliferation of cells[26]. The results from our study in the clonogenic assay indicate that colony formation in MHCCLM3 cells was completely inhibited by the up-regulation of p21, which is in agreement with the findings of the study by Zhong *et al* in bladder cancer cells[18]. However, the proliferation assay showed that dsP21-322-transfected cells decreased proliferation by approximately 70%. This discrepancy may be because, in the clonogenic assay, MHCCLM3 cells were transfected twice with 50 nmol/L dsRNA (dsControl and dsP21-322) or without dsRNA (mock transfection) using Lipofectamine 2000 (Invitrogen) at 24 h intervals. In addition, a density of 5000 cells per well also limited the survival of single cells in the clonogenic assay.

Survivin, a unique member of the inhibitors-of-apoptosis gene family, is characterized by its abundant expression in transformed cells and a variety of human cancers. However, it is barely detectable in terminally differentiated normal cells or tissues[29]. Besides inhibiting apoptosis in cells exposed to diverse apoptotic stimuli[29], survivin was found to promote cell proliferation in human HCC cells by interacting with cyclin-dependent kinase4 (CDK4)[30]. In the current study, a significant decrease in survivin levels was found following dsP21-322 transfection, which is consistent with the inhibition of proliferation and survival. This suggests that the dsRNA-induced stimulation of p21 may lead to decreased survival of HCC cells through a survivin-dependent mechanism. However, the causality and association between p21 and survivin need to be explored in future studies.

Through the proliferation assay, as well as the clonogenic assay, our study has shown that dsP21-322 can significantly inhibit the growth of HCC cells. These effects may be due mainly to the action of p21 as a potent cyclin-dependent kinase inhibitor (CKI) that binds to and inhibits the activity of cyclin-CDK2 or -CDK4 complexes. Thus, it functions as a mediator of cell-cycle G_1-phase arrest in response to a variety of stress stimuli[31, 32].

There have been contradictory results claiming both the promotion and the inhibition of apoptosis by p21[22, 23]. Our results showed that apoptosis was increased both early and late after transfection, which was also consistent with a previous study on bladder cancer[19]. The decrease in Bcl-xL as well as the activation of caspase proteins contributed to the effect of p21 up-regulation in HCC cell lines. Then knockdown of p21 by siRNA resulted in the reverse of proliferation and the

reduction of apoptosis, which supports the role of p21 in the induction of apoptosis and the inhibition of proliferation.

In summary, transfection with dsP21-322 decreased cell viability, inhibited colony formation, and induced apoptosis of HCC cells. Evidence supports the hypothesis that a loss of survivin and activation of the caspase pathway ultimately results in the observed anti-cancer effects in the HCC cell lines.

Taken together, the induction of p21 by small RNA molecules targeted to the promoter regions of p21 can cause anticancer effects in HCC cell lines. These results show that RNAa is also activated in HCC cells, pointing to a potential therapeutic use for dsRNA-induced gene activation in HCC.

Acknowledgements

This work was supported by grants from both the Shanghai Natural Science Fund (Grant No 08ZR1402400) and the Fudan University Institute of Biomedical Science Opening Fund (Grant No IBS0837). We wish to express our deepest gratitude and indebtedness to Prof Lun-xiu QIN, Zhongshan Hospital, the Liver Cancer Institute, Fudan University, Shanghai, for his generous help throughout the entire course of this project, without which it would not have been possible for us to complete this work.

Author contribution

Gang CHEN designed research; Zhi-ming WU, Chun DAI, and Cui-fang ZHENG performed research; Ying HUANG, Qiong-zhu DONG, Guan WANG, Xiao-wen LI, Xiao-fei ZHANG, and Bin LI contributed new analytical tools and data analysis; Zhi-ming WU wrote the paper.

References

1 Parkin DM, Bray F, Ferlay J, Pisani P. Global cancer statistics, 2002. CA Cancer J Clin 2005; 55: 74–108.
2 He J, Gu DF, Wu XG, Reynolds K, Duan XF, Yao CH, *et al*. Major causes of death among men and women in China. N Engl J Med 2005; 353: 1124–34.
3 Hashem BE, Andrew CM. Rising incidence of hepatocellular carcinoma in the United States. N Engl J Med 1999; 340: 745–50.
4 Bruix J, Sherman M. Management of hepatocellular carcinoma. Hepatology 2005; 42: 1208–36.
5 Fire A, Xu SQ, Montgomery MK, Kostas SA, Driver SE, Mello CC. Potent and specific genetic interference by double-stranded RNA in *Caenorhabditis elegans*. Nature 1998; 391: 806–11.
6 Eulalio A, Huntzinger E, Izaurralde E. Getting to the root of miRNA-mediated gene silencing. Cell 2008; 132: 9–14.
7. Paddison PJ, Caudy AA, Bernstein E ,Hannon GJ, Conklin DS. Short hairpin RNAs (shRNAs) induce sequence-specific silencing in mammalian cells. Genes Dev 2002; 16: 948–58.
8 Morris KV, Chan SWL, Jacobsen SE, Looney DJ. Small interfering RNA-induced transcriptional gene silencing in human cells. Science 2004; 305: 1289–92.
9 Khraiwesh B, Asif MA, Seumel GI, Ossowski S, Weigel D, Reski R. Transcriptional control of gene expression by microRNAs. Cell 2010; 140: 111–22.
10 Li LC, Okino ST, Zhao H, Pookot D, Place RF, Urakami S, *et al*. Small dsRNAs induce transcriptional activation in human cells. Proc Natl Acad Sci U S A 2006; 103: 17337–42.
11 Janowski BA, Younger ST, Hardy DB, Ram R, Huffman KE, Corey DR. Activating gene expression in mammalian cells with promoter-targeted duplex RNAs. Nat Chem Biol 2007; 3: 166–73.
12 Place RF, Li LC, Pookot D, Noonan EJ, Dahiya R. MicroRNA-373 induces expression of genes with complementary promoter sequences. Proc Natl Acad Sci U S A 2008; 105: 1608–13.
13 Turunen MP, Lehtola T, Heinonen SE, Assefa GS, Korpisalo P, Gienary R, *et al*. Efficient regulation of VEGF expression by promoter-targeted lentiviral shRNAs based on epigenetic mechanism: A novel example of epigenetherapy. Circ Res 2009; 105: 604–9.
14 Huang V, Qin Y, Wang J, Wang XL, Place RF, Lin GT, *et al*. RNAa is conserved in mammalian cells. PLoS One 2010; 5: e8848
15 Morris KV, Santoso S, Turner AM, Pastori C, Hawkins PG. Bidirectional Transcription directs both transcriptional gene activation and suppression in human cells. PLoS Genet 2008; 4: e1000258.
16 Schwartz JC, Younger ST, Nguyen NB, Hardy DB, Monia BP, Corey DR, *et al*. Antisense transcripts are targets for activating small RNAs. Nat Struct Mol Biol 2008; 15: 842–8.
17 Garber K. Small RNAs reveal an activating side. Science 2006; 341: 741–2.
18 Zhong C, Place RF, Jia ZJ, Pookot D, Dahiya R, Li LC. Antitumor effect of dsRNA-induced p21WAF1/CIP1 gene activation in human bladder cancer cells. Mol Cancer Ther 2008; 7: 698–703.
19 Yang K, Zheng XY, Qin J, Wang YB, Bai Y, Mao QQ, *et al*. Up-regulation of p21WAF1/CIP1 by saRNA induces G_1-phase arrest and apoptosis in T24 human bladder cancer cells. Cancer Lett 2008; 265: 206–14.
20 Sekiguchi T, Hunter T. Induction of growth arrest and cell death by overexpression of the cyclin-Cdk inhibitor p21 in hamster BHK21 cells. Oncogene 1998; 16: 369–80.
21 Waga S, Hannon GJ, Beach D, Stillman B. The p21 inhibitor of cyclin-dependent kinases controls DNA replication by interaction with PCNA. Nature 1994; 369: 574–8.
22 Gorospe M, Wang X, Guyton KZ, Holbrook NJ. Protective role of p21(WAF1/CIP1)against prost agland in A2-mediated apoptosis of Human colorectal carcinoma cells. Mol Cell Biol 1996; 16: 6654–60.
23 Gartel AL, Tyner AL. The role of the cyclin-dependent kinase inhibitor p21 in apoptosis. Mol Cancer Ther 2002; 1: 639–49.
24 Shi YZ, Hui AM, Takayama T, Li X, Makuuchi M. Reduced p21WAF1/CIP1 protein expression is predominantly related to altered p53 in hepatocellular carcinomas. Br J Cancer 2000; 83: 50–5.
25 Hui AM, Kanai Y, Sakamoto M, Tsuda H, Hirohashi S. Reduced $p21^{WAF1/CIP1}$ expression and p53 mutation in hepatocellular carcinomas. Hepatology 1997; 25: 575–9.
26 Franken NAP, Rodermond HM, Stap J, Haveman J, Bree CV. Clonogenic assay of cells *in vitro*. Nat Protoc 2006; 1: 2315–9.
27 Ito T, Shiraki K, Sugimoto K, Yamanaka T, Fujikawa K, Ito M, *et al*. Survivin promotes cell proliferation in human hepatocellular carcinoma. Hepatology 2000; 31: 1080–5.
28 Schwartz JC, Younger ST, Nguyen NB, Hardy DB, Monia BP, *et al*. Antisence transcripts are targets for activating small RNAs. Nat Struct Mol Biol 2008; 15: 842–8.
29 Sah NK, Khan Z, Khan GJ, Bisen PS. Structural, functional and therapeutic biology of survivin. Cancer Lett 2006; 244: 164–71
30 Ambrosini G, Adida C, Altieri DC. A novel anti-apoptosis gene, survivin, expressed in cancer and lymphoma. Nat Med 1997; 3: 917–21.
31 Serrano M, Hannon GJ, Beach D. A new regulatory motif in cell-cycle control causing specific inhibition of cyclin D/CDK4. Nature 1993; 366: 704–7.
32 Harper JW, Adami GR, Wei N, Keyomarsi K, Elledge SJ. The p21cdk-interacting protein Cip1 is a potent inhibitor of G_1 cyclin-dependent kinases. Cell 1993; 75: 805–16.

Acta Pharmacologica Sinica (2011) 32: 947–955

www.nature.com/aps

Original Article

No association between polymorphisms and haplotypes of *COL1A1* and *COL1A2* genes and osteoporotic fracture in postmenopausal Chinese women

Wei-wei HU, Jin-wei HE, Hao ZHANG, Chun WANG, Jie-mei GU, Hua YUE, Yao-hua KE, Yun-qiu HU, Wen-zhen FU, Miao LI, Yu-juan LIU, Zhen-lin ZHANG*

Metabolic Bone Disease and Genetic Research Unit, Department of Osteoporosis and Bone Diseases, Shanghai Jiao Tong University Affiliated Sixth People's Hospital, Shanghai 200233, China

Aim: To study whether genetic polymorphisms of *COL1A1* and *COL1A2* genes affected the onset of fracture in postmenopausal Chinese women.
Methods: SNPs in *COL1A1* and *COL1A2* genes were identified via direct sequencing in 32 unrelated postmenopausal Chinese women. Ten SNPs were genotyped in 1252 postmenopausal Chinese women. The associations were examined using both single-SNP and haplotype tests using logistic regression.
Results: Twenty four (4 novel) and 28 (7 novel) SNPs were identified in *COL1A1* and *COL1A2* gene, respectively. The distribution frequencies of 2 SNPs in *COL1A1* (rs2075554 and rs2586494) and 3 SNPs in *COL1A2* (rs42517, rs1801182, and rs42524) were significantly different from those documented for the European Caucasian population. No significant difference was observed between fracture and control groups with respect to allele frequency or genotype distribution in 9 selected SNPs and haplotype. No significant association was found between fragility fracture and each SNP or haplotype. The results remained the same after additional corrections for other risk factors such as weight, height, and bone mineral density.
Conclusion: Our results show no association between common genetic variations of *COL1A1* and *COL1A2* genes and fracture, suggesting the complex genetic background of osteoporotic fractures.

Keywords: *COL1A1*; *COL1A2*; polymorphism; bone fracture; osteoporosis

Acta Pharmacologica Sinica (2011) 32: 947–955; doi: 10.1038/aps.2011.37; published online 23 May 2011

Introduction

Osteoporotic fracture is the most serious clinical consequence of osteoporosis. It is a major cause of the public health burden associated with osteoporosis due to the high rates of morbidity and mortality in the elderly and the tremendous health care costs[1, 2]. The incidence of osteoporotic fracture is increasing rapidly in Asian countries[3, 4]. The incidence for all osteoporotic fractures and hip fractures was 635/100 000 and 123/100 000 person-years in southern Chinese men, respectively[5]. Therefore, the elucidation of ways to prevent osteoporotic fracture is an important goal. The most common osteoporotic fracture sites are the hip, wrist and spine[6].

Most studies demonstrate a heritability of 50%–80% for bone mineral density (BMD), but fracture heritability has been estimated to be less than 50%[7, 8]. The risk for osteoporotic fracture is complex and is regulated by both environmental and genetic factors. To date, most genetic studies have focused on surrogate phenotypes of osteoporotic fracture, such as BMD, bone size, bone geometry parameters and bone turnover markers, to search for genes that underlie the susceptibility to osteoporotic fracture[9]. Although the measurement of BMD has been the best method to identify the risk for osteoporotic fracture, a meta-analysis for the predictive ability of the measurement for hip fracture was reported a false positive rate of 15% and a detection rate of only 50%[10]. Another study found that the association between genetic variations and wrist fracture was largely independent of BMD[8]. Many studies have focused on the relationship between candidate genes and BMD, but some studies have found that candidate genes are associated with an increased risk for osteoporotic fracture independently of BMD[11, 12], and the genetic correlation between these surrogate phenotypes and osteoporotic fracture is very low[8, 13]. The underlying genetic factors that cause susceptibility to osteoporotic fracture are generally unknown;

* To whom correspondence should be addressed.
E-mail ZZL2002@medmail.com.cn
Received 2011-01-27 Accepted 2011-03-28

therefore, the underlying genetic associations with osteoporotic fracture were assessed in the present study. Due to low fracture heritability[7, 13] and difficulty associated with recruiting a large number of individuals with the same fracture type, until now, few studies have performed a direct genetic evaluation of osteoporotic fracture using a case-control method.

Considering the important role of collagen type I in the bone matrix, genes that are related to type I collagen are potential candidates for osteoporotic fracture. Type I collagen acts by binding to two collagen chains, α_1 and α_2, which are encoded by the *COL1A1* and *COL1A2* genes, respectively[14]. There are common polymorphisms in *COL1A1*: Sp1 (rs1800012) in intron 1, -1997G/T (rs1107946) and -1663in/de1T (rs2412298) have been extensively studied because of their association with the risk for osteoporosis[12, 15–18]. Of note, the Sp1 polymorphism is associated with a modest reduction of BMD and a significant increase in the risk for osteoporotic fracture, particularly vertebral fracture[12, 16, 18]. A recent meta-analysis of clinical studies has confirmed that the Sp1 polymorphism is associated with a higher prevalence of fractures among heterozygote (Ss) and homozygote (ss) in comparison to wild type individuals (SS) and that *COL1A1* "s" allele has a stronger association with the risk for fracture than with BMD[19]. However, the Sp1 polymorphism has not been found in the Chinese population[20, 21]. The relationship between *COL1A2* genotypes and osteoporosis is less well characterized than that between *COL1A1* genotypes and osteoporosis. A number of studies have found an association between GT-repeat polymorphisms, *Msp* I, *Pvu* II, and *Eco*R I of the *COL1A2* gene and BMD[22, 23] or bone size[24]. However, there are few studies selected osteoporotic fracture as a direct phenotype. Therefore, additional data are required to confirm the potential role of collagen type I genes in the pathogenesis of osteoporotic fracture. In the present study, we aimed to investigate whether the genetic polymorphisms in the *COL1A1* and *COL1A2* genes affected the onset of osteoporotic fracture independently of clinical risk factors in postmenopausal Chinese women.

Materials and methods

Subjects

The study was approved by the Ethics Committee of the Shanghai Jiao Tong University Affiliated Sixth People's Hospital. All of the subjects included in the study were recruited from a local population in Shanghai City by the Department of Osteoporosis and Bone Diseases, Shanghai Jiao Tong University Affiliated Sixth People's Hospital from 2006 to 2009. All of the subjects signed informed consent documents before participating in the project. After signing, the subjects were assisted with the completion of a structured questionnaire that included information regarding anthropometric variables, lifestyle and medical history. A physical checkup and routine serum examination were performed, and all of the subjects were found to be in good health. Secondary causes of osteoporosis were excluded. Postmenopausal women who had experienced early menopause (before 45 years of age) and those who had undergone ovariectomy or were receiving estrogen replacement therapy or antiosteoporotic drugs were excluded.

Volunteers were recruited from communities in Xuhui district, Shanghai, China and cases of vertebral fractures that were detected by radiographs were screened. Among patients who were seeking medical treatment in the outpatient department, Colles' and hip fractures (including femoral neck fractures and trochanter fractures) were found on the radiographs. The diagnosis was performed by orthopedic surgeons and radiologists according to the information provided by X-rays. In total, 1252 unrelated subjects (627 cases of fragility fracture in the case group and 625 cases in the control group) of postmenopausal Han women between the ages of 45 and 80 years were selected for inclusion in the study. The inclusion criteria for fragility fracture cases were as follows: (i) age <80 years and onset age >45 years; (ii) minimal fractures, usually due to falls from standing height or less; (iii) fracture site location in the lumbar spine, hip and radius; (iv) a diagnosis of osteoporotic fracture identified and confirmed by radiographs that were interpreted by orthopedic surgeons or radiologists and by the Genant semiquantitative method to assess vertebral fractures[25]. There were 668 fracture times in the fracture group (Table 1): 419 cases were vertebral fractures (composition ratio of 62.7%), 156 cases were Colles' fractures (composition ratio of 22.4%) and 93 cases were hip fractures (composition ratio of 13.9%). All of the subjects with a fracture were considered to have primary osteoporosis. The inclusion criteria for control subjects were an age <80 years, an onset age >45 years and a lack of any fracture history. The exclusion criteria were same as those described in our previously reported study[26].

Table 1. Details of the fracture sites in the case subjects.

Fracture site	Age (years)	No of fractures
Vertebral fracture (including thoracic and lumbar regions)	70.9±9.0	419
Hip fracture	70.6±9.7	93
Colles' fracture	68.8±9.2	156

BMD measurements

The BMD (g/cm^2) of the left proximal femur (if the individual had a left hip fracture, the right proximal femur was measured) including the total hip, the femoral neck, the trochanter, and Ward's triangle were measured using dual-energy X-ray absorptiometry (DXA) on a Hologic QDR 2000 (Hologic, Bedford, MA, USA) and a Lunar Prodigy GE densitometer (Lunar Corp, Madison, WI, USA). Both of the scanners were calibrated daily, and the coefficient of variability (CV) values for the DXA measurements at L1-4, the total hip, and the femoral neck were 0.9%, 0.8%, and 1.93%, respectively, for the Hologic QDR 2000[26] and 1.39%, 0.7%, and 2.22%, respectively, for the Lunar Prodigy[27]. The long-term reproducibility of the DXA

data during the trial, which was based on phantom measurements that were repeated weekly, was 0.45%. Height and weight were measured using standardized equipment.

Sequencing analysis of the *COL1A1* and *COL1A2* genes

Genomic DNA was isolated from peripheral blood leukocytes using conventional methods. Single nucleotide polymorphisms (SNP) screening was conducted by DNA sequencing of the entire gene sequence in 32 unrelated healthy postmenopausal Chinese women using the ABI Prism 3730 DNA Analyzer (Applied Biosystems, Foster City, CA, USA). The primers used for the amplification and sequencing analysis were designed based on GenBank sequences (reference sequence of *COL1A1* mRNA: NM_000088.3 and *COL1A2* mRNA: NM_000089.3). Sequence variants were verified using the Phred/Phrap/Consed package and Polyphred[28, 29].

SNP selection and genotyping

According to the sequencing analysis of the *COL1A1* and *COL1A2* genes and specific criteria, ten SNPs in two genes were selected. SNPs in the two genes were selected based on the following criteria: (i) degree of heterozygosity (minor allele frequency (MAF) >10%); (ii) r^2=0.8; (iii) denoted as tagSNPs; (iv) amino acid mutations, missense mutations: rs1800215 (Ala1075Thr) and rs42524 (Pro549Ala), and synonymous mutations: rs1801182 (Thr29Thr) and rs1800248 (Gly1045Gly). Based on these criteria, we selected five SNPs in the *COL1A1* gene, including SNP 3 (rs2075554), SNP 7 (rs2586494), SNP 18 (rs1800215), SNP 19 (rs2586488) and SNP 23 (rs2277632), and five SNPs in *COL1A2*, including SNP 1 (rs1801182), SNP 9 (rs42517), SNP 18 (rs42524), SNP 19 (rs421587), and SNP 27 (rs1800248). Ten SNPs were genotyped using the TaqMan assay, for which the primer and probe sequences were optimized using the SNP Assay-by-Design service provided by Applied Biosystems. The genotype for every sample was named according to the ratio of the fluorescence intensities of the two dyes. The reactions were performed with a Mx3000P Real-Time PCR System (Stratagene, CA, USA) using 20 ng of genomic DNA in a 5-μL reaction volume per well.

LD and haplotype analysis

Haplotypes were constructed from the population genotype data using the algorithm of Stephens with the Phase program version 2.0.2[30]. The linkage disequilibrium block structure was examined using Haploview version 3.2[31]. We examined Lewontin's D' and the LD coefficient r^2 between all of the pairs of biallelic loci. The genotype and haplotype frequencies were calculated for 32 unrelated subjects and 1252 postmenopausal women.

Statistical analysis

Statistical analyses were performed using SPSS version 11.0 (SPSS, Chicago, IL, USA). The allele frequencies for each SNP were calculated by counting the alleles, and the Hardy-Weinberg equilibrium was assessed by Chi-squared analysis.

Because of the different DXA devices that were used to measure BMD in the 1252 subjects (some were measured by Hologic QDR 2000 and others by Lunar Prodigy GE), the absolute BMD values could not be compared. Therefore, we transformed the absolute value determined for the femoral neck BMD to a Z-score of the neck BMD using the BMD reference database for a previously reported Shanghai population[26, 27].

The age, height, weight, and femoral neck BMD (Z-score) for the nine genotypes in the two groups were analyzed by analysis of variance (ANOVA). Analysis of covariance (ANCOVA) was used to analyze the association of the nine genotypes or haplotypes with femoral neck BMD while simultaneously adjusting the height, weight, and years since menopause (YSM) as covariates. A Chi-squared analysis was used to test the differences among the nine SNP genotype frequencies between the case and control groups. By adjusting for age, height, weight, and YSM and BMD as risk factors, a logistic regression was used to analyze the association of the nine genotypes or haplotypes with the risk for osteoporotic fracture. P<0.05 was considered statistically significant in all of the analyses.

Results

Basic characteristics of the subjects

1252 postmenopausal women were included in the study: 627 osteoporotic fracture cases and 625 controls. The basic characteristics of the study subjects are shown in Table 2. Differences in age, height, weight, YSM and femoral neck BMD (Z-score) were found in the two groups according to a *t*-test analysis. The average age in the case group [(70.4±9.2) years] was older than that in the control group [(60.6±6.7) years] (P<0.01); the average height in the case group [(151.6±6.9) cm] was less than that in the control group [(155.3±5.6) cm] (P<0.01); the average weight in the case group [(55.7±9.7) kg] was lower than that in the control group [(57.6±8.3) kg] (P<0.01); the average femoral neck BMD was lower in the case group (Z-score: -0.42±1.07) than in the control group (Z-score: -0.08±0.97) (P<0.01); and YSM was longer in the case group [(16.9±7.1) years] than in the control group [(15.1±6.6) years] (P<0.05). No significant differences were observed between the two groups with respect to BMI (P>0.05).

SNP genotyping and linkage disequilibrium

SNPs were genotyped for a sample of 32 unrelated individuals who were randomly selected among 1252 subjects in our population, and 24 and 28 SNPs were identified in the *COL1A1* and *COL1A2* genes, respectively. Twenty SNPs in the *COL1A1* gene were found in dbSNP of the NCBI database, but four SNPs were novel. Twenty-one SNPs in the *COL1A2* gene were found in dbSNP of the NCBI database, but seven SNPs were novel. All of the SNPs demonstrated MAF of >1.0% in our population, and the genotype frequencies of these SNPs did not deviate from Hardy-Weinberg equilibrium (P>0.05; Tables 3 and 4). The frequencies of each SNP are shown in Tables 3 and 4. According to these genotype frequencies and the above mentioned criteria, five SNPs (rs2075554, rs2586494, rs1800215, rs2586488, and rs2277632) in the *COL1A1* gene and five SNPs

Table 2. Basic characteristics of the study subjects. Data are the mean±SD (range).

Trait	Cases (*n*=627)	Controls (*n*=625)	*P* value
Age (year)	70.4±9.2 (46.0–82.5)	60.6±6.7 (45.0–81.8)	<0.001
Height (cm)	151.6±6.9 (131.0–170.5)	155.3±5.6 (135.6–169.0)	<0.001
Weight (kg)	55.7±9.7 (34.0–88.0)	57.6±8.3 (35.4–87.0)	<0.001
BMI (kg/cm^2)	24.2±3.7 (13.2–38.2)	23.9±3.1 (14.6–39.5)	0.107
Years since menopause (year)	16.9±7.1 (0.8–31.6)	15.1±6.6 (0.6–30.1)	0.030
Femoral neck BMD (Z-score)	-0.42±1.07 (-3.78–3.29)	-0.08±0.97 (-2.90–3.71)	<0.001

Table 3. Positions and frequencies of *COL1A1* gene polymorphisms in the Chinese population (*n*=32).

SNP name	Loci	SNP	SNP in dbSNP	Genotype frequencies (%, N)		
SNP1	471+195T>C	C/T	Novel	TT (71.8, 23)	CT (28.2, 9)	
SNP2		C/T	rs35231764	TT (71.8, 23)	CT (25, 8)	CC (3.2, 1)
SNP3		A/G	rs2075554	AG (53.1, 17)	GG (37.5, 12)	AA (9.4, 3)
SNP4		A/C	rs2075555	CC (43.8, 14)	CA (46.9, 15)	AA (9.4, 3)
SNP5		A/G	rs2141279	GG (56.3, 18)	AG (37.5, 12)	AA (6.2, 2)
SNP6		A/G	rs2734281	AG (53.1, 17)	AA (28.1, 9)	GG (18.8, 6)
SNP7		T/G	rs2586494	TT (34.4, 11)	GT (43.8, 14)	GG (21.8, 7)
SNP8		A/G	rs2253369	AG (43.8, 14)	AA (43.8, 14)	GG (12.4, 4)
SNP9		C/T	rs1007086	CT (46.9, 15)	TT (37.5, 12)	CC (15.6, 5)
SNP10		C/G	rs41316671	GG (71.8, 23)	CG (18.8, 6)	CC (9.4, 3)
SNP11		C/T	rs2696247	TC (43.8, 14)	TT (43.8, 14)	CC (12.4, 4)
SNP12	2028+27G>A	A/G	Novel	GG (93.8, 30)	GA (6.2, 2)	
SNP13		C/G	rs2075556	GC (43.8, 14)	GG (43.8, 14)	CC (12.4, 4)
SNP14		T/G	rs2075558	GG (75.0, 24)	TT (12.6, 4)	TG (12.4, 4)
SNP15	2559+27C>T	T/C	Novel	CC (93.8, 30)	CT (6.2, 2)	
SNP16		C/G	rs2075559	CG (46.9, 15)	CC (34.4, 11)	GG (18.7, 6)
SNP17	2949C>A	A/C	Novel	CC (93.8, 30)	CA (6.2, 2)	
SNP18		A/G	rs1800215	AG (53.2, 17)	GG (46.8, 15)	
SNP19		C/T	rs2586488	TC (43.8, 14)	TT (34.4, 11)	CC (21.8, 7)
SNP20		T/C	rs2277634	CC (93.8, 30)	CT (6.2, 2)	
SNP21		T/C	rs41316715	CC (90.6, 29)	CT (9.4, 3)	
SNP22		T/C	rs2277633	CC (93.8, 30)	CT (6.2, 2)	
SNP23		T/C	rs2277632	TC (53.1, 17)	TT (28.1, 9)	CC (18.8, 6)
SNP24		A/G	rs2249492	GG (37.5, 12)	AG (43.8, 14)	AA (18.7, 6)

(rs1801182, rs42517, rs42524, rs421587, and rs1800248) in the *COL1A2* gene were subsequently measured.

The data for ten SNPs in the *COL1A1* and *COL1A2* genes are summarized in Table 5. Among those SNPs, rs1800215 in the *COL1A1* gene deviated from Hardy-Weinberg equilibrium, as determined by chi-squared analysis (χ^2=85.63, *P*<0.001), and therefore, this SNP was excluded from the subsequent statistical analysis. The genotype frequencies of the other nine SNPs did not deviate significantly from Hardy-Weinberg equilibrium (*P*>0.05). The LD patterns of *COL1A1* and *COL1A2* are shown in Figures 1 and 2. In the *COL1A1* gene, based on the D′ values (D′=0.87), we identified one block with a high LD that ranged from intron 44 to intron 48 and included rs2586488 and rs2277632 (Figure 1A). When the haplotypes were reconstructed with the inclusion of rs2586488 and rs2277632, four potential haplotypes were obtained for the *COL1A1* gene (Figure 1B). In the *COL1A2* gene, only a single LD block was identified based on the D′ values (D′=0.87), and it ranged from exon 3 to exon 47 and included rs1801182, rs42517, rs42524, rs421587, and rs1800248 (Figure 2A). When the haplotypes were reconstructed with the inclusion of these five SNPs in the *COL1A2* gene, six possible haplotypes were obtained (Figure 2B).

Association between SNP and haplotype and BMD in postmenopausal women

There were no differences in the femoral neck BMD values (Z-score) determined for the 9 SNP genotypes according to an ANOVA analysis (data not shown). The results for the association between the *COL1A1* and *COL1A2* genotypes and BMD were determined by ANCOVA. Following an adjustment for height, weight and YSM as covariates, no significant results

Table 4. Positions and frequencies of *COL1A2* gene polymorphisms in the Chinese population (*n*=32).

SNP name	Loci	SNP	SNP in dbSNP	Genotype frequencies (%, N)		
SNP1		C/T	rs1801182	TT (46.9, 15)	CT (40.6, 13)	CC (12.5, 4)
SNP2	96+112A>G	A/G	Novel	AA (93.8, 30)	AG (6.2, 2)	
SNP3	97-119C>G	C/G	Novel	CC (84.4, 27)	CG (15.6, 5)	
SNP4		A/G	rs4729131	GG (46.9, 15)	GA (46.9, 15)	AA (6.2, 2)
SNP5		C/T	rs1800222	TT (46.9, 15)	CT (40.6, 13)	CC (12.5, 4)
SNP6		A/T	rs405946	AA (78.1, 25)	AT (22.9, 7)	
SNP7		A/G	rs406226	AA (78.1, 25)	AG (22.9, 7)	
SNP8		C/T	rs28417792	CT (43.8, 14)	CC (43.8, 14)	TT (12.4, 4)
SNP9		A/G	rs42517	AG (46.9, 15)	AA (46.9, 15)	GG (6.2, 2)
SNP10	739-96T>C	C/T	Novel	TT (93.8, 30)	CT (6.2, 2)	
SNP11		C/T	rs42518	TT (78.1, 25)	CT (22.9, 7)	
SNP12		A/G	rs28754326	GG (93.8, 30)	GA (6.2, 2)	
SNP13		C/T	rs42519	TT (75, 24)	CT (25, 8)	
SNP14		A/G	rs2521206	AG (46.9, 15)	AA (28.1, 9)	GG (25.0, 8)
SNP15		T/C	rs52520	TT (78.1, 25)	CT (22.9, 7)	
SNP16		A/G	rs34026686	GG (78.1, 25)	AG (22.9, 7)	
SNP17		A/G	rs412777	AA (50.0, 16)	AG (50.0, 16)	
SNP18		C/G	rs42524	GG (75, 24)	CG (25, 8)	
SNP19		A/G	rs421587	AA (71.9, 23)	AG (28.1, 9)	
SNP20		A/G	rs2301643	GG (78.1, 25)	AG (22.9, 7)	
SNP21		T/G	rs1800238	GG (43.8, 14)	GT (37.5, 12)	TT (19.7, 6)
SNP22	2296-82C>T	C/T	Novel	CC (93.8, 30)	CT (6.2, 2)	
SNP23		A/G	rs42530	AA (53.1, 17)	AG (40.7, 13)	GG (6.2, 2)
SNP24	3105+15G>C	C/G	Novel	GG (93.8, 30)	CG (6.2, 2)	
SNP25	3105+43G>A	A/G	Novel	GG (78.1, 25)	AG (22.9, 7)	
SNP26		C/T	rs13590724	TT (78.1, 25)	CT (22.9, 7)	
SNP27		C/T	rs1800248	CC (75, 24)	CT (25, 8)	
SNP28	3712-13C>T	C/T	Novel	CC (93.8, 30)	CT (6.2, 2)	

Table 5. Characteristics of the analyzed SNPs. MAF: minor allele frequency in the whole sample.

Gene name	SNP name	Allele	Location	Amino acid change	MAF (Hapmap-HCB)	MAF (Hapmap-CEU)	MAF (This study)
COL1A1	rs2075554	A/G	Intron 11	None	0.411	0.190	0.335
	rs2586494	A/G	Intron 16	None	0.467	0.175	0.5
	rs1800215	A/C	Exon 44	Ala1075Thr	0.000	0.026	0.287
	rs2586488	A/G	Intron 44	None	0.467	0.353	0.458
	rs2277632	A/G	Intron 48	None	0.378	0.208	0.371
COL1A2	rs1801182	C/T	Exon 3	None	0.289	0.008	0.381
	rs 42517	A/G	Intron 12	None	0.329	0.276	0.27
	rs 42524	G/C	Exon 28	Pro549Ala	0.056	0.202	0.068
	rs 421587	A/G	Intron 28	None	0.193	0.308	0.165
	rs1800248	T/C	Exon 47	None	0.102	0.125	0.103

were obtained for the association between each SNP and the femoral neck BMD (data not shown). Using ANCOVA to analyze the association of the haplotypes with femoral neck BMD, we failed to detect any differences in femoral neck BMD among the various haplotypes (data not shown).

SNP and haplotype analyses for osteoporotic fractures

Using Chi-squared analysis, no differences were observed between the case and control groups with respect to the nine SNP genotype frequencies (Table 6). The same method was used to evaluate differences between the case and control

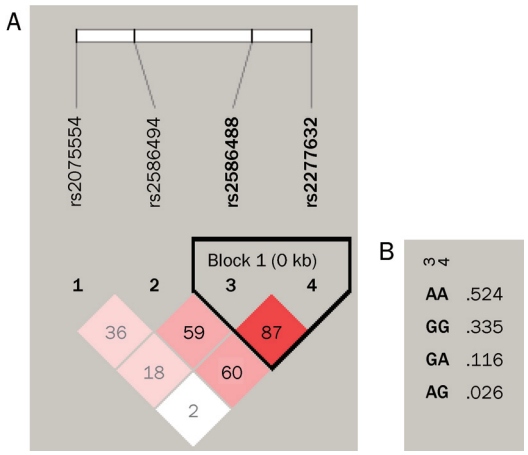

Figure 1. LD patterns for the *COL1A1* gene in 1252 subjects. Squares in red indicate a strong LD. Values in the cells represent the pairwise degrees of LD indicated by D'×100 when D'<1. (A) 1 to 4 represent rs2075554, rs2586494, rs2586488, and rs2277632, respectively. (B) Haplotype frequencies for the *COL1A1* gene.

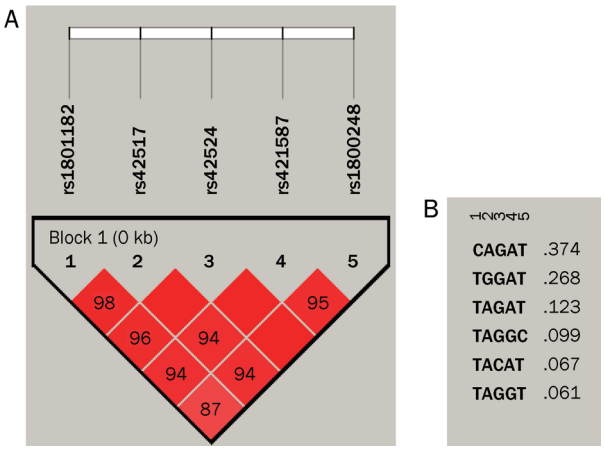

Figure 2. LD patterns for the *COL1A2* gene in 1252 subjects. Squares in red indicate a strong LD. Values in the cells represent the pairwise degrees of LD indicated by D'×100 when D'<1. (A) 1 to 5 represents rs1801182, rs42517, rs42524, rs421587, and rs1800248, respectively. (B) Haplotype frequencies for the *COL1A2* gene.

Table 6. Frequencies of the nine SNPs.

Gene name	SNP		Genotype, N (%) Cases	Genotype, N (%) Controls	χ^2	*P* value
COL1A1	rs2075554	AA	80 (12.8)	72 (11.5)	0.486	0.784
		AG	266 (42.6)	267 (42.8)		
		GG	279 (44.6)	285 (45.7)		
	rs2586494	AA	155 (24.7)	166 (26.6)	0.898	0.638
		AC	305 (48.7)	304 (48.6)		
		CC	167 (26.6)	155 (24.8)		
	rs2586488	AA	193 (30.8)	182 (29.1)	0.705	0.703
		AG	296 (47.2)	310 (49.6)		
		GG	138 (22.0)	133 (21.3)		
	rs2277632	AA	258 (41.1)	248 (39.7)	0.329	0.848
		AG	279 (44.5)	284 (45.4)		
		GG	90 (14.4)	93 (14.9)		
COL1A2	rs1801182	CC	89 (14.2)	101 (16.1)	1.658	0.437
		CT	297 (47.4)	276 (44.2)		
		TT	240 (38.3)	248 (39.7)		
	rs42517	AA	336 (53.7)	337 (53.9)	1.321	0.517
		AG	246 (39.3)	234 (37.4)		
		GG	44 (7.0)	54 (8.6)		
	rs42524	GG	543 (86.7)	545 (87.2)	2.319	0.314
		CG	81 (12.9)	74 (11.8)		
		CC	2 (0.3)	6 (1.0)		
	rs421587	AA	435 (69.5)	441 (70.6)	0.820	0.664
		AG	163 (27.8)	163 (26.1)		
		GG	93 (2.7)	21 (3.4)		
	rs1800248	TT	509 (81.3)	497 (79.5)	0.833	0.659
		TC	108 (17.3)	120 (19.2)		
		CC	9 (1.4)	8 (1.3)		

groups with respect to the nine SNP allele frequencies, but no differences were detected (data not shown). Following an adjustment for age, height, weight, YSM, and BMD as risk factors, we failed to find any significant associations between

osteoporotic fracture and each SNP according to a logistic regression (data not shown). We further investigated the relationship between various haplotypes and osteoporotic fracture using logistic regression. No significant association was found between any of the haplotypes and osteoporotic fracture (Table 7). However, height, weight and femoral neck BMD (Z-score) were found to be risk factors for osteoporotic fracture (Table 7). Meanwhile, we investigated the relationship between various haplotypes and vertebral, wrist and hip fracture using logistic regression, respectively. Also no significant association was found between any of the haplotypes and various sites fracture (data not shown).

To eliminate the age differences that might be produced by false-negative results, we matched 627 cases in the fracture group to 625 cases in the control group. After matching the two groups according to age, 813 postmenopausal women among the 1252 cases were included (402 cases of fragility fracture in the case group and 411 cases in the control group). And we used the same method as the above statistical analyses to analyze association between polymorphisms and haplotypes in *COL1A1* and *COL1A2* genes and osteoporotic fracture in 813 postmenopausal women. No differences were found in neck BMD among the various SNPs or any haplotypes (data not shown). No significant association was found between polymorphisms or any of the haplotypes and osteoporotic fracture (data not shown).

Discussion

This study is the first to report the distribution by DNA sequencing of the entire *COL1A1* and *COL1A2* genes in healthy postmenopausal Chinese women. In the present study, we found four novel SNPs in the *COL1A1* gene and seven novel SNPs in the *COL1A2* gene and that the distribution frequencies of two SNPs in *COL1A1* (rs2075554 and rs2586494) and three SNPs in *COL1A2* (rs42517, rs1801182, and rs42524) were significantly different from those documented for the European Caucasian population shown in the HapMap database. This result suggests that the allele distribution of the two gene frequencies differs among various ethnicities.

The extent to which genetic information can improve the prognosis of a fracture is largely unknown. Based on the importance of collagen type I in the bone matrix, we explored the associations of the *COL1A1* and *COL1A2* genes with osteoporotic fracture in postmenopausal Chinese women.

The *COL1A1* gene has been widely studied in previous reports, but inconsistent results have been obtained, even for the same allele. For example, some studies have found that the Sp1 polymorphism in the *COL1A1* gene contributes to susceptibility to vertebral fracture or BMD[12, 15, 16, 18], but other studies have reported that there is no such association[20, 21]. These discordant findings may be due to the inclusion of study subjects from populations with different ethnicities. Due to the lack of the Sp1 polymorphism in Chinese women[20, 21], this SNP was not evaluated in the present study. Few studies have investigated the association among other SNPs (excluding the Sp1 polymorphism) in *COL1A1* and osteoporotic fracture or BMD[16, 17]. Gareia-Giralt *et al*[16] found two novel SNPs, -1997G/T (rs1107946), and -1663in/de1T (rs2412298), in *COL1A1* that were located in the upstream regulatory region of the gene in postmenopausal Spanish women; the authors suggested that -1997G/T had a significant association with BMD. Jin *et al*[17] found that the -1997G/T, -1663in/delT, and +1245G/T polymorphisms affected BMD and that the binding of several regulatory factors (Nmp4 and Osterix) regulated the transcription of *COL1A1*. In the present study, we evaluated four SNPs in the *COL1A1* gene (rs2075554, rs2586494, rs2586488, and rs2277632) and failed to find an association between single-SNP or haplotype analysis and osteoporotic fracture.

Until now, most studies have investigated the association between SNPs in *COL1A2* and BMD or other surrogate phenotypes[22–24, 32]. To our knowledge, this is the first study to investigate the association of *COL1A2* with osteoporotic fracture. Our results revealed that there was no individual SNP

Table 7. Haplotype analyses to assess osteoporotic fractures. OR: odds ratio.

	Variant	B	SE	*P* value	OR	95% CI for OR	
						Lower	Upper
	Height	-0.101	0.011	0.000	0.904	0.884	0.924
	Weight	0.022	0.008	0.008	1.022	1.006	1.038
	Femoral neck BMD (Z-score)	-0.349	0.070	0.000	0.705	0.615	0.809
COL1A1	Haplo1-AA	0.019	0.341	0.922	1.001	0.520	1.917
	Haplo2-GG	0.145	0.244	0.587	1.135	0.702	1.878
	Haplo3-GA	0.128	0.199	0.530	1.147	0.778	1.693
	Haplo4-AG	0.104	0.206	0.521	1.127	0.759	1.606
COL1A2	Haplo1-CAGAT	-0.090	0.246	0.695	0.952	0.581	1.455
	Haplo2-TGGAT	-0.080	0.235	0.737	0.923	0.571	1.501
	Haplo3-TAGAT	0.020	0.120	0.867	1.020	0.806	1.291
	Haplo4-TAGGC	-0.023	0.090	0.807	0.975	0.823	1.160
	Haplo5-TACAT	-0.138	0.209	0.589	0.889	0.595	1.367
	Haplo6-TAGGT	-0.099	0.267	0.700	0.923	0.637	1.537

or any of haplotypes in *COL1A2* associated with osteoporotic fracture. Lindahl *et al*[23] discovered interactions between the *COL1A2* gene and BMD in older men from Sweden, the United Kingdom and Hong Kong (n=2004). Their results demonstrated that rs42524 was significantly associated with BMD and older men with a CC or GG genotype had a higher BMD than men who carried the CG genotype. In the present study, the same SNP was evaluated and failed to demonstrate any association with BMD or the risk for osteoporotic fracture in postmenopausal women. These inconsistent findings may be explained by the use of study subjects with different ethnicities and genders. Lau *et al*[22] found that *Pvu* II and *Eco*R I in the *COL1A2* gene was associated with BMD in elderly men in Hong Kong, but they did not find any association between these two SNPs and BMD in 450 postmenopausal women. Lei *et al*[24] analyzed *Msp* I in the *COL1A2* gene and osteoporosis according to another phenotype (bone size). Using the quantitative transmission disequilibrium test (QTDT) in Chinese population, they found that this SNP was associated with femoral neck bone size. These studies, which were performed in Chinese population, used BMD or bone size as the study phenotype, in contrast to the use of osteoporotic fracture as the phenotype in the present study. Therefore, our results cannot be compared with the above findings obtained for the Chinese population.

A shortcoming of association studies is the recognition of population admixtures that yield false-positive or false-negative genetic effects for complex traits, which can have significant adverse effects on the results[33]. To eliminate the age stratification that might be produced by false-negative or false-positive results, we matched 402 cases in the fracture group to 411 cases in the control group. But we also did not find differences in neck BMD among the various SNPs or any haplotypes, and also failed to find significant association between polymorphisms or any of the haplotypes and osteoporotic fracture.

Although osteoporotic fracture is a heritable trait, many studies have also indicated that fracture is partly governed by genetic factors that are distinct from bone mineralization as measured by the BMD[8, 10, 11, 13]. Tran *et al*[34] also found that genetic profiling could enhance the predictive accuracy of fracture prognosis by comparison of clinical risk factors and 50 genes in 858 men and 1358 women with fragility fractures. Because fractures typically occur later in life, it is difficult to study the genetics of the osteoporotic fracture phenotype[11, 13, 35]. Therefore, quantitative risk factors such as BMD, bone geometry parameters and bone turnover markers are used to predict the risk for osteoporotic fractures[9, 10]. However, it is important to note that none of these surrogate phenotypes are ideal for a genetic study[36], because these phenotypes could not entirely replace osteoporotic fractures. Furthermore, recent genome-wide association study (GWAS) showed that rs4355801 near the *TNFRSF11B* (osteoprotegerin) gene and rs3736228 in the *LRP5* gene were associated with BMD, only rs3736228 was associated with the risk of osteoporotic fractures identified in 314 075 SNPs in 6463 people[37]. This study also did not find associations between SNPs in *COL1A1* and *COL1A2* genes and osteoporotic fracture or BMD[37], and was accordant with our result.

One of the strengths of the present study was that the fracture data obtained for the case group was verified by hospital radiographs rather than comprising a collection of self-reported fractures. Another strength was that the SNPs in our study were gotten in the sequencing analysis of *COL1A1* and *COL1A2* genes in postmenopausal Chinese women. Our study has several limitations. First, because we selected the most informative SNPs, which demonstrated a high MAF and r^2, some causal variants (such as rare SNPs) might have been overlooked. Second, a number of other risk factors were not taken into account, such as the fall frequency.

In conclusion, we tested the association between SNPs and haplotypes in *COL1A1* and *COL1A2* genes with osteoporotic fracture in postmenopausal Chinese women. Our results failed to find the association between each of the 9 SNPs and haplotypes in *COL1A1* and *COL1A2* genes and osteoporotic fracture. Although our findings must be confirmed in other populations, the present results suggest that the common genetic variants in *COL1A1* and *COL1A2* are not major contributors to the risk for osteoporotic fracture in postmenopausal Chinese women. To confirm whether the SNPs in *COL1A1* and *COL1A2* can be used as a genetic means of determining the risk for osteoporotic fracture requires a large number of sample cases from populations that comprise different ethnicities and ages. In addition, lower and rare SNPs information in these two genes needs further research.

Acknowledgements

The study was supported by the National Natural Science Foundation of China (No 30570891, 30771019, 30800387, 81070692, and 81000360), the Program of Shanghai awarded to the chief scientist (No 08XD1403000) and STCSM10DZ1950100.

Author contribution

Wei-wei HU measured all SNPs, carried out all statistical analyses and drafted the manuscript. Zhen-lin ZHANG conceived and designed the study and revised the manuscript. Jin-wei HE guided the work of the genetics laboratory and guaranteed and confirmed the quality of the genetic data. Chun WANG, Hao ZHANG, and Hua YUE guided the work of the genetics laboratory. Jie-mei GU, Wen-zhen FU, Yun-qiu HU, Miao LI, and Yu-juan LIU carried out the field work including sample and data collection. Yao-hua KE coordinated the DNA sample collection. All authors read and approved the final manuscript.

References

1 Cummings SR, Melton LJ. Epidemiology and outcomes of osteoporotic fractures. Lancet 2002; 359: 1761–7.
2 Burge R, Dawson-Hughes B, Solomon DH, Wong JB, King A, Tosteson A. Incidence and economic burden of osteoporosis-related fractures in the United States, 2005–2025. J Bone Miner Res 2007; 22: 465–75.

3 Xu L, Cummings SR, Qin MW, Zhao XH, Chen XS, Michael N, *et al*. Vertebral fractures in Beijing, China: the Beijing Osteoporosis Project. J Bone Miner Res 2000; 15: 2019–25.
4 Lau EM, Lee JK, Suriwongpaisal P, Saw SM, Das De S, Khir A, *et al*. The incidence of hip fracture in four Asian countries: the Asian Osteoporosis Study (AOS). Osteoporos Int 2001; 12: 239–43.
5 Bow CH, Tsang SW, Loong CH, Soong CS, Yeung SC, Kung AW. Bone mineral density enhances use of clinical risk factors in predicting ten-year risk of osteoporotic fractures in Chinese men: the Hong Kong Osteoporosis Study. Osteoporos Int DOI: 10.1007/s00198-010-1490-0.
6 Consensus development conference: diagnosis, prophylaxis, and treatment of osteoporosis. Am J Med 1993; 94: 646–50.
7 Michaelsson K, Melhus H, Ferm H, Ahlbom A, Pedersen NL. Genetic liability to fractures in the elderly. Arch Intern Med 2005; 165: 1825–30.
8 Deng HW, Chen WM, Recker S, Stegman MR, Li JL, Davies KM, *et al*. Genetic determination of Colles' fracture and differential bone mass in women with and without Colles' fracture. J Bone Miner Res 2000; 15: 1243–52.
9 Wang JT, Guo Y, Yang TL, Xu XH, Dong SS, Li M, *et al*. Polymorphisms in the estrogen receptor genes are associated with hip fractures in Chinese. Bone 2008; 43: 910–4.
10 Chen Y, Shen H, Yang F, Liu PY, Tang N, Recker RR, *et al*. Choice of study phenotype in osteoporosis genetic research. J Bone Miner Metab 2009; 27: 121–6.
11 Garnero P, Munoz F, Borel O, Sornay-Rendu E, Delmas PD. Vitamin D receptor gene polymorphisms are associated with the risk of fractures in postmenopausal women, independently of bone mineral density. J Clin Endocrinol Metab 2005; 90: 4829–35.
12 Nguyen TV, Esteban LM, White CP, Grant SF, Center JR, Gardiner EM, *et al*. Contribution of the collagen I alpha1 and vitamin D receptor genes to the risk of hip fracture in elderly women. J Clin Endocrinol Metab 2005; 90: 6575–9.
13 Deng HW, Mahaney MC, Williams JT, Li J, Conway T, Davies KM, *et al*. Relevance of the genes for bone mass variation to susceptibility to osteoporotic fractures and its implications to gene search for complex human diseases. Genet Epidemiol 2002; 22: 12–25.
14 Retief E, Parker MI, Retief AE. Regional chromosome mapping of human collagen genes alpha 2(I) and alpha 1(I) (COLIA2 and COLIA1). Hum Genet 1985; 69: 304–8.
15 Tran BN, Nguyen ND, Center JR, Eisman JA, Nguyen TV. Enhancement of absolute fracture risk prognosis with genetic marker: the collagen I alpha 1 gene. Calcif Tissue Int 2009; 85: 379–88.
16 Garcia-Giralt N, Nogues X, Enjuanes A, Puig J, Mellibovsky L, Bay-Jensen A, *et al*. Two new single-nucleotide polymorphisms in the COL1A1 upstream regulatory region and their relationship to bone mineral density. J Bone Miner Res 2002; 17: 384–93.
17 Jin H, van't Hof RJ, Albagha OM, Ralston SH. Promoter and intron 1 polymorphisms of COL1A1 interact to regulate transcription and susceptibility to osteoporosis. Hum Mol Genet 2009; 18: 2729–38.
18 Jin H, Evangelou E, Ioannidis JP, Ralston SH. Polymorphisms in the 5′ flank of COL1A1 gene and osteoporosis: meta-analysis of published studies. Osteoporos Int 2011; 22: 911–21.
19 Mann V, Ralston SH. Meta-analysis of COL1A1 Sp1 polymorphism in relation to bone mineral density and osteoporotic fracture. Bone 2003; 32: 711–7.
20 Lambrinoudaki I, Kung AW. Absence of high-risk "s" allele associated with osteoporosis at the intronic SP1 binding-site of collagen I alpha1 gene in Southern Chinese. J Endocrinol Invest 2001; 24: 499–502.
21 Lei SF, Deng FY, Liu XH, Huang QR, Qin Y, Zhou Q, *et al*. Polymorphisms of four bone mineral density candidate genes in Chinese populations and comparison with other populations of different ethnicity. J Bone Miner Metab 2003; 21: 34–42.
22 Lau EM, Choy DT, Li M, Woo J, Chung T, Sham A. The relationship between COL1A1 polymorphisms (Sp1) and COL1A2 polymorphisms (Eco R1 and Puv II) with bone mineral density in Chinese men and women. Calcif Tissue Int 2004; 75: 133–7.
23 Lindahl K, Rubin CJ, Brandstrom H, Karlsson MK, Holmberg A, Ohlsson C, *et al*. Heterozygosity for a coding SNP in COL1A2 confers a lower BMD and an increased stroke risk. Biochem Biophys Res Commun 2009; 384: 501–5.
24 Lei SF, Deng FY, Xiao SM, Chen XD, Deng HW. Association and haplotype analyses of the COL1A2 and ER-alpha gene polymorphisms with bone size and height in Chinese. Bone 2005; 36: 533–41.
25 Genant HK, Wu CY, van Kuijk C, Nevitt MC. Vertebral fracture assessment using a semiquantitative technique. J Bone Miner Res 1993; 8: 1137–48.
26 Zhang ZL, He JW, Qin YJ, Hu YQ, Li M, Zhang H, *et al*. Association between myostatin gene polymorphisms and peak BMD variation in Chinese nuclear families. Osteoporos Int 2008; 19: 39–47.
27 Gao G, Zhang ZL, Zhang H, Hu WW, Huang QR, Lu JH, *et al*. Hip axis length changes in 10,554 males and females and the association with femoral neck fracture. J Clin Densitom 2008; 11: 360–6.
28 Gordon D, Abajian C, Green P. Consed: a graphical tool for sequence finishing. Genome Res 1998; 8: 195–202.
29 Ewing B, Hillier L, Wendl MC, Green P. Base-calling of automated sequencer traces using phred. I. Accuracy assessment. Genome Res 1998; 8: 175–85.
30 Stephens M, Smith NJ, Donnelly P. A new statistical method for haplotype reconstruction from population data. Am J Hum Genet 2001; 68: 978–89.
31 Barrett JC, Fry B, Maller J, Daly MJ. Haploview: analysis and visualization of LD and haplotype maps. Bioinformatics 2005; 21: 263–5.
32 Lei SF, Deng FY, Dvornyk V, Liu MY, Xiao SM, Jiang DK, *et al*. The $(GT)_n$ polymorphism and haplotype of the COL1A2 gene, but not the $(AAAG)_n$ polymorphism of the PTHR1 gene, are associated with bone mineral density in Chinese. Hum Genet 2005; 116: 200–7.
33 Deng HW. Population admixture may appear to mask, change or reverse genetic effects of genes underlying complex traits. Genetics 2001; 159: 1319–23.
34 Tran BN, Nguyen ND, Nguyen VX, Center JR, Eisman JA, Nguyen TV. Genetic profiling and individualized prognosis of fracture. J Bone Miner Res 2011; 26: 414–9.
35 Andrew T, Antioniades L, Scurrah KJ, Macgregor AJ, Spector TD. Risk of wrist fracture in women is heritable and is influenced by genes that are largely independent of those influencing BMD. J Bone Miner Res 2005; 20: 67–74.
36 Karasik D, Hsu YH, Zhou Y, Cupples LA, Kiel DP, Demissie S. Genome-wide pleiotropy of osteoporosis-related phenotypes: the framingham study. J Bone Miner Res 2010; 25: 1555–63.
37 Richards JB, Rivadeneira F, Inouye M, Pastinen TM, Soranzo N, Wilson SG, *et al*. Bone mineral density, osteoporosis, and osteoporotic fractures: a genome-wide association study. Lancet 2008; 371: 1505–12.

Acta Pharmacologica Sinica (2011) 32: 956–966
 1671-4083/11 $32.00
www.nature.com/aps

Original Article

Tissue-specific alterations in expression and function of P-glycoprotein in streptozotocin-induced diabetic rats

Lu-lu ZHANG, Liang LU, Shi JIN, Xin-yue JING, Dan YAO, Nan HU, Li LIU, Ru DUAN, Xiao-dong LIU*, Guang-ji WANG, Lin XIE

Key Laboratory of Drug Metabolism and Pharmacokinetics, China Pharmaceutical University, Nanjing 210009, China

Aim: To investigate the changes of expression and function of P-glycoprotein (P-GP) in cerebral cortex, hippocampus, liver, intestinal mucosa and kidney of streptozocin-induced diabetic rats.
Methods: Diabetic rats were prepared via a single dose of streptozocin (65 mg/kg, ip). *Abcb1*/P-GP mRNA and protein expression levels in tissues were evaluated using quantitative real time polymerase chain reaction (QRT-PCR) analysis and Western blot, respectively. P-GP function was investigated via measuring tissue-to-plasma concentration ratios and body fluid excretion percentages of rhodamine 123.
Results: In 5- and 8-week diabetic rats, *Abcb1a* mRNA levels were significantly decreased in cerebral cortices and intestinal mucosa, but dramatically increased in hippocampus and kidney. In liver, the level was increased in 5-week diabetic rats, and decreased in 8-week diabetic rats. *Abcb1b* mRNA levels were increased in cerebral cortex, hippocampus and kidney, but reduced in liver and intestinal mucosa in the diabetic rats. Western blot results were in accordance with the alterations of *Abcb1a* mRNA levels in most tissues examined. P-GP activity was markedly decreased in most tissues of diabetic rats, except kidney tissues.
Conclusion: Alterations in the expression and function of *Abcb1*/P-GP under diabetic conditions are tissue specific, *Abcb1* specific and diabetic duration-dependent.

Keywords: diabetes mellitus; ABC superfamily transporter; *Abcb1*/P-GP gene; P-glycoprotein; rhodamine 123; insulin

Acta Pharmacologica Sinica (2011) 32: 956–966; doi: 10.1038/aps.2011.33; published online 20 Jun 2011

Introduction

Diabetes mellitus (DM), which is mainly a glucose metabolism disorder, is associated with the development and progression of pathological changes in various organ systems. Several reports have shown that diabetes may also alter the pharmacokinetic behavior of many drugs[1–3], and these changes are generally associated with alterations in functional proteins, including cytochrome P450s (CYP450s) and efflux transporters, which participate in the absorption, metabolism, distribution and excretion of drugs.

The efflux transporters mainly belong to the ABC superfamilies, which comprise P-glycoprotein (P-GP), breast cancer resistance protein (BCRP) and multidrug resistance-associated proteins (MRPs). P-GP is expressed in various tissues, including brain, lung, liver, kidney, gastrointestinal tract, skin and muscle tissue[4, 5], and it is considered an important component of the blood-brain barrier (BBB), blood-placenta barrier, blood-testis barrier and other biological barriers *in vivo*[6, 7]. Moreover, P-GP may efflux many substrates, including anticancer agents, calcium channel blockers, antibiotics, cardiac glycosides and immunosuppressants[5, 8]. Therefore, concomitant administration of drugs usually has been shown to cause drug-drug interactions via the inhibition of P-GP mediated transport[9]. For example, Liu *et al* reported that the level of nimodipine in the rat brain was markedly increased after co-administration of cyclosporin A[10].

Previous studies have also demonstrated that P-GP expression and function are affected by pathophysiological conditions, such as cancer, diabetes, chronic renal failure and non-alcoholic fatty liver disease[11–13]. Yu *et al* found that the intestines of streptozocin (STZ)-induced diabetic rats had higher effective permeabilities of five protoberberine alkaloids, which was accompanied by lowered levels of P-GP protein, indicating an impairment of P-GP function and expression under diabetic conditions[14]. Liu *et al* discovered that diabetes may cause an increase in phenobarbital distribution in the mouse

* To whom correspondence should be addressed.
E-mail xdliu@cpu.edu.cn
Received 2011-01-20 Accepted 2011-03-23

brain following an enhancement of the pharmacological activity of phenobarbital in the central nervous system (CNS), suggesting that diabetes may suppress P-GP function and expression in the brains of mice[15]; however, the patterns of P-GP alterations appear to be complicated and controversial in certain tissue types. Several reports have demonstrated that diabetes may decrease P-GP function and expression in the brain and intestines[14, 16, 17], while it also may induce increases in the liver or kidney[18, 19]. All of the results that have been published indicate that P-GP alterations under diabetic conditions are tissue specific.

We used STZ-induced diabetic rats as a model to verify our hypothesis. The mRNA and protein expression levels of P-GP in the indicated tissues were estimated by QRT-PCR analysis and Western blot, respectively. P-GP function was assessed by measuring the distribution and excretion of rhodamine 123 (Rho123). In addition, the effects of insulin treatment on changes in P-GP expression and function induced by diabetes were also investigated.

Materials and methods

Reagents

Blood glucose reagent kits were purchased from Jiancheng Biotech Co (Nanjing, China). Insulin was purchased from Wanbang Pharmaceutical Co (Xuzhou, China). Primers for the *Abcb1a/1b* and *β-actin* genes used in QRT-PCR analysis were provided by Realgene Bio-Technologies, Inc (Shanghai, China). The P-glycoprotein monoclonal antibody C219 was obtained from Calbiochem-Novabiochem (Seattle, WA, USA). Streptozocin (STZ), rhodamine 123 (Rho123), pentobarbital and protease inhibitor cocktail were all purchased from Sigma Chemical Co (St Louis, MO, USA). All other reagents were commercially available and were of analytical grade. STZ was dissolved in 0.1 mol/L sodium citrate buffer (pH 4.5). Both Rho123 and pentobarbital were dissolved in physiological saline before use.

Animals

Male Sprague-Dawley rats, weighing 180–200 g, were purchased from Sino-British Sippr/BK Laboratory Animal Ltd (Shanghai, China). Rats were housed under controlled environmental conditions (temperature, 23±1 °C; humidity, 55%±5%) and kept under a 12-h light/dark cycle; commercial food and water were freely available. All animal experiments were performed under a license granted by Jiangsu Science and Technology Office (China) with approval from the Animal Ethics Committee of China Pharmaceutical University. Every effort was made to minimize stress to the animals.

Diabetic model and insulin treatment

Diabetes was induced in rats by a single injection of STZ (65 mg/kg, ip). The age-matched normal control rats were injected with vehicle. Development of diabetes was confirmed by measuring fasting blood glucose (FBG) levels using a reagent kit. Rats with FBG levels higher than 11.1 mmol/L on d 7 after STZ injection were considered diabetic[15]. The STZ-induced hyperglycemic state is considered a type 1 DM model[20].

The STZ-induced diabetic rats were divided into two groups: diabetic rats and insulin-treated diabetic rats. Insulin (4×10^4 U/L) was subcutaneously administered to rats at 10 $U\cdot kg^{-1}\cdot d^{-1}$ twice a day for either 5 or 8 weeks. The diabetic rats and age-matched normal control rats received only vehicle. By the end of 5 weeks, half of the whole rats from each group were randomly chosen for measuring *Abcb1* mRNA and P-GP protein levels, as well as P-GP activity in the cerebral cortex, hippocampus, liver, intestinal mucosa and kidney following the determination of FBG. The remaining rats continued to be treated for another 3 weeks and then were subjected to the same experiments, as mentioned above.

QRT-PCR analysis

QRT-PCR analysis was used to measure *Abcb1* mRNA levels in the rat cerebral cortex, hippocampus, liver, intestinal mucosa and kidney. The experimental rats were sacrificed under ether anesthesia, and the indicated tissues were quickly obtained. Each tissue, weighing 50 mg, was homogenized under ice-cold conditions. The QRT-PCR procedure was conducted as previously described[21–23]. Briefly, 2 μg of total RNA from each original sample was converted into cDNA for each individual QRT-PCR assay with a 38-cycle three-step PCR using the ABI Prism 7000 thermocycler. The PCR primer sequences are shown in Table 1. Amplifications were performed in a 20 μL reaction mixture containing 2.0 μL of 10×PCR buffer, 2.0 μL of 25 mmol/L $MgCl_2$, 0.4 μL of 10 mmol/L deoxyribonucleoside triphosphate, 250 nmol/L of the appropriate forward and reverse primers (*Abcb1a/1b* and *β-actin*), and SYBR green I (Molecular Probes, OR, USA). For normalization of the gene levels, *β-actin* was used to correct minor variations in the input RNA amount or inefficiencies of the reverse transcription. The results were calculated according to the manufacturer's instructions[24].

Western blotting

Western blotting was used for the assessment of P-GP protein expression in the rat cerebral cortex, hippocampus, liver, intestinal mucosa and kidney according to the method previously

Table 1. Primer characteristics of *Abcb1a*, *Abcb1b*, and *β-actin*.

Gene	GeneBank	Amplicon (bp)	Sequence forward	Sequence reverse
Abcb1a	AF257746	351	5′-GCCCTGTTCTTGGACTGT-3′	5′-GGCCGTGATAGCTTTCTT-3′
Abcb1b	AY082609	351	5′-GCCCATCCTGTTTGACTG-3′	5′-CGCTTCCTGGACGACCTT-3′
β-actin	NM_007393.3	365	5′-TGACGTGGACATCCGCAAAG-3′	5′-CTGGAAGGTGGACAGCGAGG-3′

described[25]. Rats were sacrificed under ether anesthesia, and the indicated tissues were quickly obtained. Each tissue, weighing 100 mg, was homogenized and lysed in lysis buffer containing 10 mmol/L Tris-HCl (pH 7.5), 1 mmol/L EGTA, 1 mmol/L $MgCl_2$, 1 mmol/L mercaptoethanol, 1% glycerol and protease inhibitor cocktail (1 mmol/L dithiothreitol, 2 mmol/L phenylmethylsulfonyl fluoride). Lysates were incubated on ice for 30 min and centrifuged at 13 000×*g* for 10 min at 4 °C. The supernatants were obtained as membrane fractions for Western blot. Protein concentrations in the solution were measured by the Bio-Rad Protein Assay. An aliquot of each tissue sample was diluted with a volume of 4×sodium dodecyl sulfate (SDS) sample buffer containing 0.1 mol/L Tris-HCl (pH 6.8), 4% SDS, 200 mmol/L dithiothreitol, 20% glycerol, and 0.2% bromophenol blue. Proteins (25 μg per lane) were separated by electrophoresis on 8% SDS-polyacrylamide gels. After electrophoresis, the proteins were electrophoretically transferred to nitrocellulose membranes. Membranes were blocked in phosphate-buffered saline containing 0.1% Tween-20 (PBST) and 5% dried skim milk for 60 min at room temperature and washed three times for 15 min in PBST. Then the membranes were incubated with the primary monoclonal antibody C219, which was diluted 500-fold in PBST overnight at 4 °C. After removal of the primary antibody, membranes were washed with PBST, incubated with the appropriate HRP-conjugated goat anti-mouse secondary antibody at room temperature for another 1 h and washed again three times in PBST. The transferred proteins were incubated with enhanced chemiluminescence substrate solution for 5 min, according to the manufacturer's instructions, and visualized with autoradiography X-ray film. The relative levels were quantified densitometrically with Quantity One Software (Bio-Rad Laboratories, Richmond, CA, USA) and calculated according to the reference bands of the protein glyceraldehyde phosphate dehydrogenase (GAPDH).

Tissue distribution of Rho123

To elucidate the changes in P-GP function in the rat cerebral cortex, hippocampus, liver, intestinal mucosa and kidney, Rho123 (0.2 mg/kg) was intravenously administered to the rats. At 45 min after administration, the rats were sacrificed under light ether anesthesia, and then the indicated tissues and blood samples were harvested to measure the concentrations of Rho123[16].

Biliary excretion, intestinal fluid excretion and urinary excretion of Rho123

To confirm the changes in P-GP function in the rat liver, intestinal mucosa and kidney, we analyzed biliary excretion, intestinal fluid excretion and urinary excretion. On the day of the experiment, several rats from each group were randomly chosen and immediately housed in individual metabolic cages following the injection of Rho123 (0.2 mg/kg, iv). Urine was collected from 0 to 6 h, 0 to 12 h, and 0 to 24 h.

To evaluate the biliary excretion and intestinal exsorption of Rho123, *in situ* single pass perfusion was performed, as previously described[14]. Rats were anesthetized by an intraperitoneal injection of pentobarbital sodium (45 mg/kg). The small intestine was exposed by midline abdominal incision. The end of the proximal ileum (about 4 cm above the junction with the cecum) was cannulated with import-resistant silicone tubing (id 1 mm). The end of distal ileum (just above the junction with the caecus) was cannulated with silicone tubing (id 4 mm) as well. The bile duct was also cannulated with polyethylene tubing (PE10). Intestinal segments were perfused at a constant rate (0.2 mL/min) by a pump with physiological saline. Then the intestines were returned to the abdominal cavity. The abdomen was covered with saline-saturated gauze to maintain the moisture levels. The rats immediately received Rho123 (0.2 mg/kg) via the tail vein following the surgery. Then bile samples and intestinal fluid samples were collected every 30 min up to 180 min. At the same time, blood was collected via the jugular vein, and plasma from the samples was obtained by centrifugation. The plasma, bile, intestinal fluid and urine samples were stored at -20 °C until further analysis. The accumulated excretion percentages were calculated, and the area under curve of plasma concentration ($AUC_{0\text{–}180\ min}$) was estimated using the linear trapezoidal rule.

Sample assays

The concentrations of Rho123 in the tissues, bile, intestinal fluid, urine and plasma were measured by HPLC according to the method previously described[15, 25]. The HPLC system consisted of a Shimadzu LC-10Avp system (Shimadzu, Japan), Diamonsil C18, 150 mm×4.6 mm id, a 5 μm particle size column (Richmond Hill, ON, USA) and a fluorescence detector ($RF\text{-}10A_{XL}$) set at an excitation wavelength of 485 nm and an emission wavelength of 546 nm. One hundred microliters of plasma, bile, intestinal fluid, urine and tissue homogenate were vortexed with 300 μL methanol for 10 min. After centrifugation, 200 μL of the supernatant was taken out and centrifuged again. Twenty microliters of the supernatant was injected into the HPLC system. The mobile phase consisted of 0.1% glacial acetic acid (pH 4.0) and acetonitrile (7:3, *v/v*), and the flow rate was set at 1.0 mL/min. The lowest limits of quantitation of Rho123 were 1.0 ng/g in the brain; 12.5 ng/g in the liver; 50 000 ng/g in the intestinal mucosa; 125.0 ng/g in the kidney; 7.8×10^{-2} g/L in the bile; 3.1×10^{-3} g/L in the intestinal fluid; 3.1×10^{-2} g/L in the urine; and 1.6×10^{-2} g/L in the plasma. The recoveries were higher than 85%, and the relative standard deviations of the intra-day and inter-day in samples were lower than 10%.

Statistical analyses

Results were expressed as the mean±standard deviation (SD). The overall differences among groups were determined by one-way analysis of variance (ANOVA). If the differences were significant, they were estimated using the Student–Newman-Keuls multiple comparison *post hoc* test. A *P*-value of less than 0.05 indicates a significant difference.

Results

Physiological and biochemical parameters of experimental rats

The physiological and biochemical parameters of the rats 5 or 8 weeks after streptozotocin or vehicle treatment were measured and listed in Table 2. Compared with the age-matched normal control rats, lower body weights and higher levels of blood glucose were found in STZ-induced diabetic rats (P<0.01). Insulin treatment reversed the changes induced by diabetes (P<0.01).

Table 2. Effects of diabetes and insulin treatment on body weight and blood glucose of experimental rats.

Treatment time	Parameters	Control	Diabetes	Diabetes+ insulin
5-week	body weight (g)	392±21	193±7^{c}	308±18^{f}
	blood glucose (mmol/L)	6.7±0.9	31.7±2.9^{c}	6.7±3.1^{f}
8-week	body weight (g)	438±14	223±28^{c}	370±22^{f}
	blood glucose (mmol/L)	6.5±1.1	31.0±2.9^{c}	4.7±3.0^{f}

The insulin-treated rats (Diabetes+insulin) were subcutaneouly administered insulin at 10 U·kg^{-1}·d^{-1} twice a day for consecutive 5 or 8 weeks. The STZ-induced diabetic rats (Diabetes) and age-matched normal control rats (Control) only received vehicle. Data are shown as mean±SD of twenty rats. ^{c}P<0.01 *vs* control group; ^{f}P<0.01 *vs* diabetic group.

Levels of *Abcb1* mRNA

In rodents, *Abcb1*/P-GP exists as two functional isoforms that are encoded by two different genes: *Abcb1a* and *Abcb1b*. QRT-PCR was used to measure levels of *Abcb1a/1b* mRNA in the indicated tissues. mRNA levels of these genes were normalized to the cycle threshold values for the housekeeping gene *β-actin*. The results show that *Abcb1a* mRNA levels are tissue specific (Figure 1). Among the indicated tissues of age-matched normal control rats, the highest levels were found in the cerebral cortex and the lowest levels were located in the kidney. The levels of *Abcb1a* mRNA in the brain also varied among different regions; for example, *Abcb1a* mRNA levels in the cerebral cortex were significantly higher than those in the hippocampus. The induction of diabetes resulted in tissue-specific and duration-dependent changes in the *Abcb1a* mRNA levels. *Abcb1a* mRNA levels were clearly down-regulated in the cerebral cortices and intestinal mucosa of diabetic rats, while up-regulations were observed in the hippocampi and kidneys of these rats. In the liver, increased *Abcb1a* mRNA levels were found in 5-week diabetic rats, but clear decreases were noted in 8-week diabetic rats. We postulated that insu-

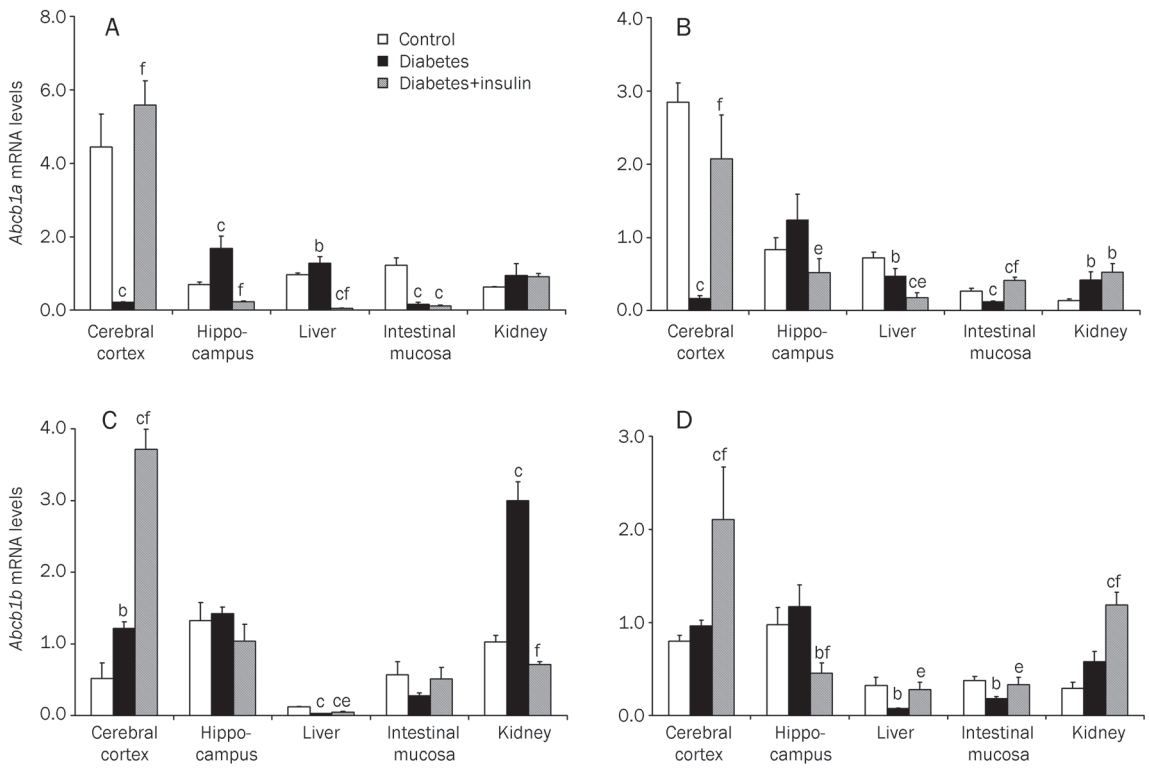

Figure 1. Effects of diabetes on *Abcb1a/1b* mRNA levels in the rat cerebral cortex, hippocampus, liver, intestinal mucosa and kidney. Insulin-treated rats (■, Diabetes+insulin) were subcutaneously administered insulin at a concentration of 10 U·kg^{-1}·d^{-1} twice a day consecutively for 5 or 8 weeks. STZ-induced diabetic rats (■, Diabetes) and age-matched normal control rats (□, Control) only received vehicle. Relative staining intensity for *Abcb1a* mRNA levels in the indicated tissues of 5-week (A) and 8-week (B) experimental rats and *Abcb1b* mRNA levels in the indicated tissues of 5-week (C) and 8-week (D) experimental rats are presented. Each data point represents the mean±SD of four rats. ^{b}P<0.05, ^{c}P<0.01 *vs* control group; ^{e}P<0.05, ^{f}P<0.01 *vs* diabetic group.

lin treatment might improve the altered *Abcb1a* mRNA levels induced by diabetes in tissue-specific and duration-dependent manners. It was evident that insulin treatment blocks the down-regulation of *Abcb1a* mRNA levels in the cerebral cortices of diabetic rats. Conversely, insulin treatment further suppressed *Abcb1a* mRNA levels in the hippocampus and liver of diabetic rats, which led to lower levels of *Abcb1a* mRNA in the hippocampus and liver of insulin-treated rats compared to age-matched normal control rats. We also observed that insulin treatment only improved *Abcb1a* mRNA levels in the intestinal mucosa of 8-week diabetic rats. The levels of *Abcb1a* mRNA in the kidneys of diabetic rats were not improved by insulin treatment.

Abcb1b mRNA levels were also different among various tissues. In the age-matched normal control rats, the levels in the hippocampus were the highest and the levels in the liver were the lowest. We also noted that the levels of *Abcb1b* mRNA in various tissues were quite different from those of *Abcb1a* mRNA in the same tissues. For example, in the cerebral cortex, the *Abcb1b* mRNA levels were significantly lower than the levels of *Abcb1a* mRNA. Diabetes also altered *Abcb1b* mRNA levels in a tissue-specific manner. Clear decreases were found in the intestinal mucosa and livers of diabetic rats, while up-regulations were present in the cerebral cortices and kidneys. However, diabetes did not affect *Abcb1b* mRNA levels in the hippocampus. Insulin treatment resulted in differential effects on *Abcb1b* mRNA levels in various tissues. Insulin treatment further increased *Abcb1b* mRNA levels in the cerebral cortex but suppressed its levels in the hippocampus of diabetic rats, causing lower levels of *Abcb1b* mRNA in the hippocampus compared with age-matched normal control rats. We also found that insulin treatment partly blocked the down-regulation of *Abcb1b* mRNA levels in the intestinal mucosa and liver of diabetic rats. The effects of insulin treatment on *Abcb1b* mRNA levels in the kidneys of diabetic rats were dependent on the duration of diabetes. Insulin treatment reversed the up-regulation of *Abcb1b* mRNA levels in 5-week diabetic rats, but further enhanced *Abcb1b* mRNA levels of 8-week diabetic rats.

Expression of P-GP protein

Western blotting was used to investigate P-GP protein expression in the indicated tissues. The results revealed a band of 170 kDa that corresponded to P-GP. We found that the effects of diabetes on P-GP expression were also tissue specific (Figure 2). Up-regulations were observed in the hippocampus and kidney of diabetic rats, but clear decreases in P-GP expression were shown in the cerebral cortex, liver and intestinal mucosa. These findings were in good accordance with the changes in *Abcb1a* mRNA levels in most tissues. Although *Abcb1b* mRNA levels were increased in the cerebral cortex of diabetic rats, lowered total expression of P-GP protein was still found, indicating that *Abcb1b* mRNA has minor contributions to P-GP expression in the cerebral cortex. Similarly, up-regulation of *Abcb1a* mRNA levels was found in the liver of diabetic rats, but P-GP expression was decreased, suggesting that *Abcb1a* mRNA has a nominal contribution to P-GP expression in the liver. Insulin treatment partly reversed the alterations induced by diabetes in most tissues. Nevertheless, insulin treatment further enhanced P-GP expression in the kidneys of 8-week diabetic rats.

Tissue distribution of Rho123

To investigate whether the alterations of P-GP expression induced by diabetes affected P-GP functional activity, Rho123 distribution in the indicated tissues was estimated. The tissue-to-plasma concentration ratio (*ie*, K_p) was calculated as an index of P-GP functional activity. The results (Table 3) indicate that diabetes increased the concentrations of Rho123 in most tissues, leading to higher tissue-to-plasma concentration ratios. However, a lower tissue-to-plasma concentration ratio was found in the kidneys of 8-week diabetic rats. We also noted that the extent of changes in the tissue-to-plasma concentration ratios of 5-week diabetic rats was higher than that of 8-week diabetic rats. Insulin treatment also partly reversed the changes in P-GP functional activity induced by diabetes.

Biliary excretion, intestinal fluid excretion and urinary excretion of Rho123

The functional activities of P-GP in the liver, intestinal mucosa and kidney were further evaluated by measuring the biliary excretion, intestinal fluid excretion and urinary excretion of Rho123, respectively. The plasma $AUC_{0\text{–}180\ min}$ was also estimated. The results show that plasma $AUC_{0\text{–}180\ min}$ was not affected in 5-week diabetic rats, but lower exposure of Rho123 was found in the plasma of 8-week diabetic rats (Figure 3). A clear decrease in biliary excretion of Rho123 was observed in diabetic rats; however, intestinal fluid excretion of Rho123 in diabetic rats had only an indistinctive downward trend. In contrast, diabetes increased urinary excretion of Rho123. The results indicate that diabetes may decrease P-GP function in the liver and intestinal mucosa, but it increases P-GP function in the kidney, which is in agreement with the P-GP expression findings. Five-week insulin treatment further enhanced the decreases in biliary excretion and intestinal fluid excretion of Rho123, but 8-week insulin treatment reversed the declines induced by diabetes. However, insulin treatment did not improve the effect on Rho123 urinary excretion in 8-week diabetic rats.

Discussion

The present study was undertaken to investigate the effects of diabetes on P-GP expression and function in the cerebral cortex, hippocampus, liver, intestinal mucosa and kidney. The results clearly demonstrate that alterations in P-GP expression and function under diabetic conditions were tissue specific and diabetic duration dependent.

Our QRT-PCR analysis (Figure 1) showed that *Abcb1* mRNA levels are tissue specific. The highest level of *Abcb1a* mRNA was found in the cerebral cortex of age-matched normal control rats, while the kidneys had the lowest levels of *Abcb1a* mRNA. We also found that the levels of *Abcb1b* mRNA were

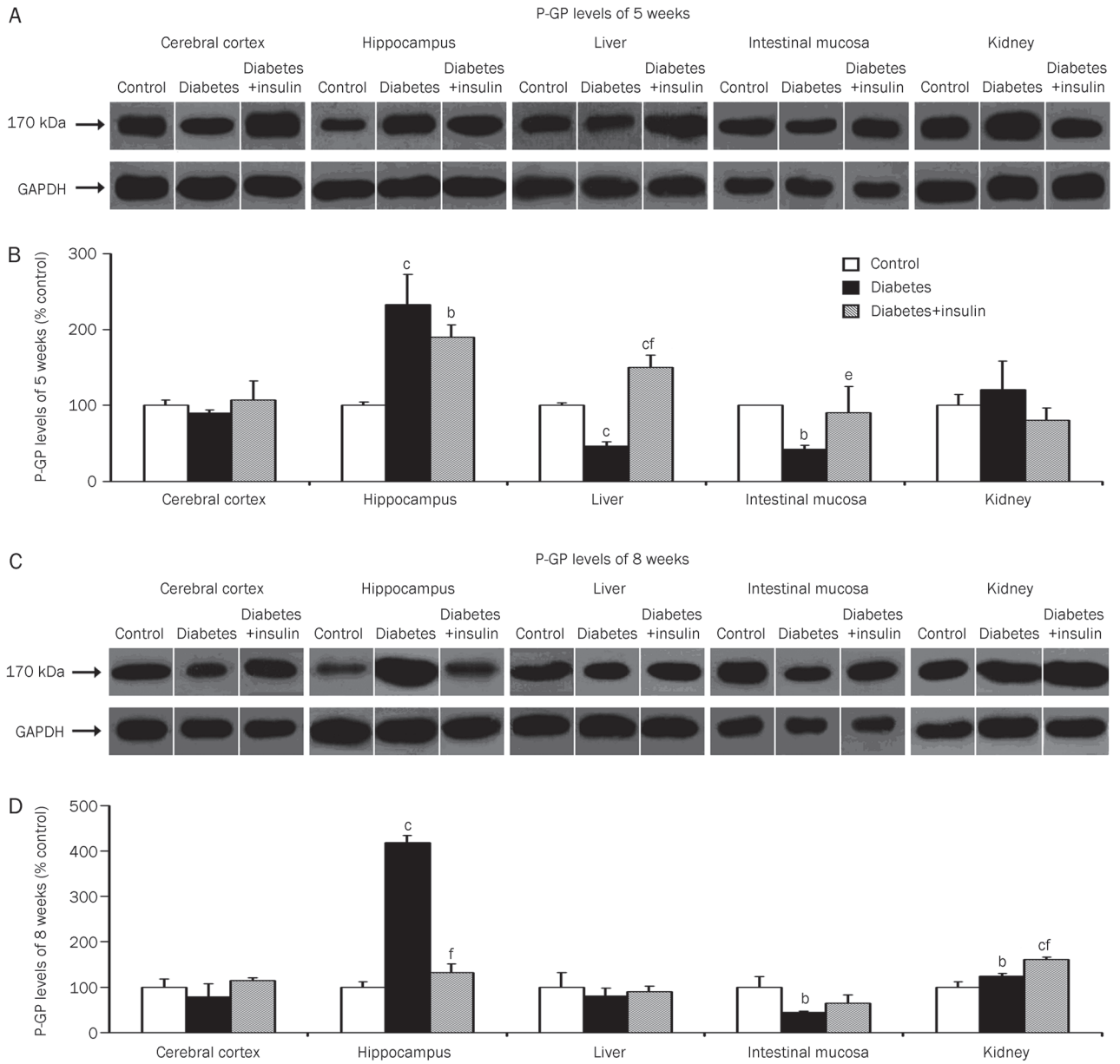

Figure 2. Effects of diabetes on P-GP protein levels in the rat cerebral cortex, hippocampus, liver, intestinal mucosa and kidney. Insulin-treated rats (■, Diabetes+insulin) were subcutaneously administered insulin at a concentration of 10 U·kg^{-1}·d^{-1} twice a day consecutively for 5 or 8 weeks. STZ-induced diabetic rats (■, Diabetes) and age-matched normal control rats (□, Control) only received vehicle. Representative Western blots of P-GP in the indicated tissues of 5-week (A) and 8-week (C) experimental rats and the ratio of relative intensities of P-GP in the indicated tissues of 5-week (B) and 8-week (D) experimental rats are described. Each band corresponding to 170 kDa was analyzed. Data are shown as the mean±SD of four rats. $^{b}P<0.05$, $^{c}P<0.01$ *vs* control group; $^{e}P<0.05$, $^{f}P<0.01$ *vs* diabetic group.

quite different from those of *Abcb1a* mRNA in the corresponding tissues. The effects of diabetes on *Abcb1* mRNA levels were also tissue specific, *Abcb1* specific and diabetic duration dependent. Clear down-regulations of *Abcb1a* mRNA levels were observed in the cerebral cortex and intestinal mucosa of diabetic rats. On the contrary, up-regulations of *Abcb1a* mRNA levels were noted in the kidney and hippocampus. However, the changes in the *Abcb1a* mRNA levels in the livers of diabetic rats were dependent on the duration of diabetes. *Abcb1a* mRNA levels were increased in 5-week diabetic rats but decreased in 8-week diabetic rats in the liver. However, we found that the alterations in *Abcb1b* mRNA levels were different from *Abcb1a* mRNA levels. Although decreases in *Abcb1b* mRNA levels were observed in the liver and intestinal mucosa, increased levels of *Abcb1b* mRNA were shown in the cerebral cortex and kidney of diabetic rats. In the hippocampus, the *Abcb1b* mRNA levels were not significantly affected by diabetes. Surprisingly, *Abcb1b* mRNA levels increased

Table 3. Effects of diabetes on Rho123 distribution in cerebral cortex, hippocampus, liver, intestinal mucosa and kidney of experimental rats.

	Control	Diabetes	Diabetes+insulin
5-week			
Plasma (ng/mL)	44.4±5.5	30.6±1.8[c]	45.6±4.0[f]
Cerebral cortex (ng/g)	4.28±0.14	5.15±0.43[b]	3.80±0.26[f]
K_p (cerebral cortex, mL/g)	0.09±0.01	0.17±0.01[c]	0.09±0.01[f]
Hippocampus (ng/g)	4.62±0.63	6.26±1.32	7.11±2.59
K_p (hippocampus, mL/g)	0.11±0.02	0.21±0.02[c]	0.14±0.06
Liver (ng/g)	52.5±17.3	187.1±47.5[c]	87.6±45.4[f]
K_p (liver, mL/g)	1.16±0.26	6.17±1.41[c]	1.87±0.87[f]
Intestinal mucosa (ng/g)	451 811±68 825	527 034±14 232	275 987±76 654[b]
K_p (intestinal mucosa, mL/g)	12 653±3375	17 345±1224	6308±1819[bf]
Kidney (ng/g)	784.2±237.7	976.9±114.9	594.4±195.3[e]
K_p (kidney, mL/g)	17.7±4.7	32.7±5.3[c]	13.3±5.1[f]
8-week			
Plasma (ng/mL)	38.4±4.8	25.3±1.7[c]	40.7±0.7[f]
Cerebral cortex (ng/g)	4.04±0.34	3.19±0.26[c]	3.45±0.42
K_p (cerebral cortex, mL/g)	0.10±0.01	0.13±0.02	0.09±0.01[f]
Hippocampus (ng/g)	3.70±0.20	3.69±0.47	4.37±0.64
K_p (hippocampus, mL/g)	0.10±0.02	0.15±0.02[c]	0.11±0.02[f]
Liver (ng/g)	69.4±10.2	66.6± 6.2	120.9±34.1[be]
K_p (liver, ml/g)	1.77±0.11	2.70±0.27	2.98±0.85[b]
Intestinal mucosa (ng/g)	101 135±23 658	77 296±8577	210 123±55 354[bf]
K_p (intestinal mucosa, mL/g)	2777±366	3087±331	5170±1321
Kidney (ng/g)	422.5±103.2	149.3±34.1[c]	578.0±139.9[bf]
K_p (kidney, mL/g)	17.9±3.4	5.9±1.4[c]	14.2±3.2[f]

The insulin-treated rats (Diabetes+insulin) were subcutaneouly administered insulin at 10 U·kg^{-1}·d^{-1} twice a day for consecutive 5 and 8 weeks. The STZ-induced diabetic rats (Diabetes) and age-matched normal control rats (Control) only received vehicle. The concentrations of Rho123 in plasma and tissues were measured at 45 min followed administration of Rho123 (0.2 mg/kg, iv). Each data represents the mean±SD of five rats. Intestinal mucosa was represented by ng/g protein, while brain, liver and kidney were represented by ng/g tissue. K_p represents the tissue-to-plasma concentration ratio. [b]P<0.05, [c]P<0.01 *vs* control group; [e]P<0.05, [f]P<0.01 *vs* diabetic group.

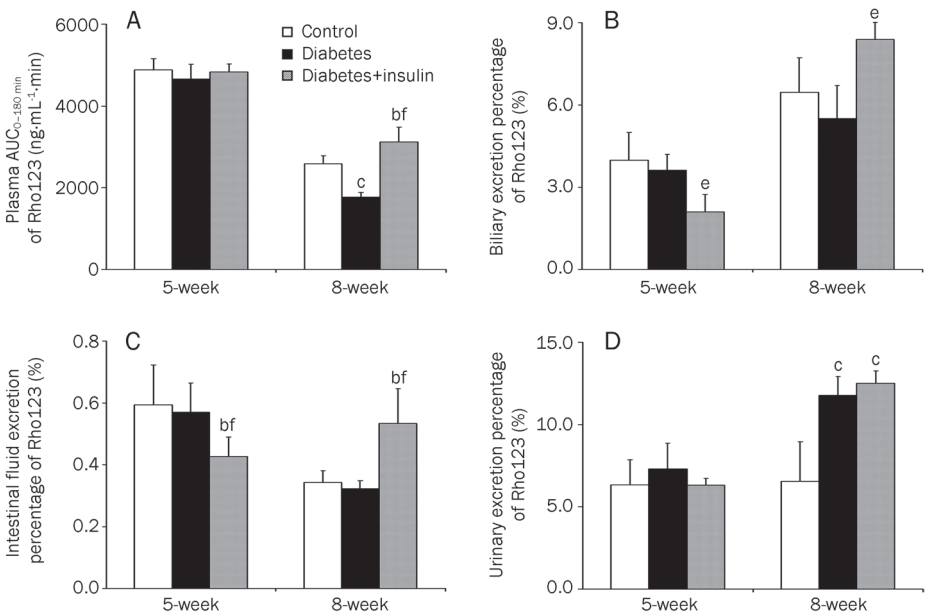

Figure 3. Effects of diabetes on plasma $AUC_{0-180\ min}$ (A) and accumulated excretion percentages of Rho123 in biliary fluid (B), intestinal fluid (C) and urine (D). Insulin-treated rats (■, Diabetes+insulin) were subcutaneously administered insulin at a concentration of 10 U·kg^{-1}·d^{-1} twice a day consecutively for 5 or 8 weeks. STZ-induced diabetic rats (■, Diabetes) and age-matched normal control rats (□, Control) only received vehicle. Each data point represents the mean±SD of five rats. [b]P<0.05, [c]P<0.01 *vs* control group; [e]P<0.05, [f]P<0.01 *vs* diabetic group.

rather than decreased in the cerebral cortex of diabetic rats. The reason and mechanism for the different alterations in the two *Abcb1* isoforms remain unknown, although it has been proposed that alterations in *Abcb1b* mRNA levels may compensate for the changes of *Abcb1a*[26]. In addition to their common function as a drug efflux transporter, the *Abcb1* isoforms appear to have their own specific function: *Abcb1a* was reported to regulate cell volume by influencing swelling activated chloride currents via a protein kinase C sensitive phosphorylation site on P-GP[27], while *Abcb1b* has been shown to be involved in apoptosis[28] and cellular stress[29, 30]. However, these views remain controversial[31, 32].

The expression levels of P-GP protein in the indicated tissues were measured by Western blot. The results show that P-GP levels were decreased in the cerebral cortex, liver and intestinal mucosa of diabetic rats, while they were increased in the hippocampus and kidney (Figure 2). These results are in good accordance with the alterations in *Abcb1* mRNA levels in most tissues. Although *Abcb1b* mRNA levels in the cerebral cortex of diabetic rats were increased, we found lowered P-GP expression. This result indicates that *Abcb1b* has a nominal contribution to P-GP expression in the cerebral cortex. We also observed that *Abcb1a* mRNA levels in the liver of 5-week diabetic rats were increased, but P-GP expression was still decreased, suggesting that the expression of P-GP in the liver is mainly attributed to translation of *Abcb1b*. This hypothesis is supported by a previous report[33].

Rho123, a typical substrate of P-GP, has been widely used as an index of P-GP mediated transport in *in vitro* and *in vivo* studies[34–40]. In the present study, Rho123 also served as a marker for evaluating P-GP function. The tissue-to-plasma concentration ratio and the biliary excretion, intestinal fluid excretion and urinary excretion of Rho123 were used for assaying P-GP activity in indicated tissues including cerebral cortex, hippocampus, liver, intestinal mucosa and kidney. The results demonstrate that clear increases in the tissue-to-plasma concentration ratios were found in most tissues of diabetic rats, while there was a decrease in the ratio in the kidney of 8-week diabetic rats. As the results show (Table 3), the higher tissue-to-plasma concentration ratios were due to lowered plasma concentrations and increased tissue concentrations. The decrease in Rho123 exposure in the plasma may result from increases of P450s or other metabolism-related enzymes induced by diabetes[41], and the increase in urinary excretion of Rho123 that we observed may also contribute to a decrease of exposure. The increased levels of Rho123 in various tissues may result from an impairment in tissue barrier integrity or P-GP function. In the brain, P-GP is mainly expressed on the luminal membrane of brain microvessel endothelia and extrudes its substrate from brain to plasma. The increases in tissue-to-plasma concentration ratios in the brain indicate that there is an impairment of P-GP function in the BBB. This finding in the cerebral cortex is in accordance with the alterations of P-GP expression and agrees with our previous reports[15, 16]. Amazingly, although P-GP protein expression was increased in the hippocampi of diabetic rats, the tissue-to-plasma concentration ratio was still increased. This indicates that there are some factors that cause a decrease in the binding affinity of P-GP to its substrate or to ATP, which contributes to lowered efflux activity of P-GP. The alteration in cell-cell contact[42] and disruption of tight junctions[43, 44] in the BBB of diabetic rats may be the causes of the increases in the tissue-to-plasma concentration ratios in the brain.

P-GP is also expressed on the apical membranes of the canalicular membranes of hepatocytes, intestinal mucosa and proximal tubules. P-GP acts as an excretion pump and excretes its substrates from cells to the bile, intestinal fluid and urine. Therefore, alterations in the tissue-to-plasma concentration ratios may reflect changes in Rho123 uptake via cells and alterations in tissue excretory functions. Lowered biliary excretion of Rho123 in diabetic rats (Figure 3) may partly explain the increases in the liver-to-plasma concentration ratio, indicating the impairment of P-GP function in the liver. The intestinal fluid excretion of Rho123 in diabetic rats only showed a small downward trend. The decreases in biliary excretion and intestinal fluid excretion were also in accordance with the P-GP expression levels in the liver and intestinal mucosa. Although the increased excretion of Rho123 in the urine and the enhanced expression of P-GP in the kidney may partly explain the decreased kidney-to-plasma concentration ratio of 8-week diabetic rats, the finding did not explain the fact that the kidney-to-plasma concentration ratio was increased in 5-week diabetic rats. The mechanism that gives rise to this phenomenon remains unclear, but it does not exclude the possibility of increased uptake via the kidney.

Reduced insulin levels in plasma are one of the significant features of diabetes. Therefore, we investigated the effects of insulin treatment on the expression and function of *Abcb1*/P-GP under diabetic conditions. We found that expression of *Abcb1*/P-GP in various tissues showed different sensitivity to insulin. The levels of *Abcb1a* mRNA in the cerebral cortex and intestinal mucosa were highly dependent on insulin levels; thus, insulin treatment nearly restored the levels of *Abcb1a* mRNA in the cerebral cortex and intestinal mucosa of diabetic rats to the values of age-matched normal control rats. In contrast, insulin inhibited the expression of *Abcb1* in the hippocampus. In addition to insulin deficiency, diabetes has been linked to increased levels of systemic inflammatory mediators, such as cytokines, which have been reported to regulate the function and expression of P-GP[45-47]. All of these results indicate that expression of *Abcb1*/P-GP in various tissues might be regulated by different factors, and this deduction has been supported by many reports. Nawa *et al* reported that decreases in P-GP expression in the intestines of diabetic mice are correlated with iNOS activity. Co-administration of the iNOS inhibitors L-N^G-nitroarginine ester and aminoguanidine has been shown to attenuate the decrease in P-GP expression induced by diabetes[17]. However, Liu *et al* found that the decrease in expression and function of BCRP in the cerebral cortex could not be reversed by co-administration of aminoguanidine[48]. Zhao *et al* proposed that endotoxin decreases P-GP levels in the brains of mice[49], but Heemskerk

et al showed that endotoxin increases the expression of *Abcb1*/P-GP in the rat kidney[50]. A further study showed that the up-regulation of *Abcb1*/P-GP may be mediated by iNOS activity and that co-administration of aminoguanidine may block expression of *Abcb1*/P-GP induced by endotoxin. With regard to *Abcb1*/P-GP expression in diabetic animals, the reports remain conflicting. Tramonti *et al* reported that both renal tubular *Abcb1a* and *Abcb1b* mRNA levels were significantly up-regulated in sham-operated diabetic rats (SD) compared with sham-operated control rats (SN) on the 14th day after administration of STZ, but more marked alterations in *Abcb1a* mRNA levels were found compared with *Abcb1b* levels[18]. On the contrary, Anger *et al* found that liver *Abcb1a* mRNA levels were significantly down regulated, but the levels of *Abcb1b* mRNA were unaffected in the rats on the 9th day after STZ administration. Renal *Abcb1a* showed a downward trend[51]. Liu *et al* proposed that *Abcb1a* levels were suppressed in the cerebral cortex of 3-week and 5-week diabetic rats, while *Abcb1b* levels were decreased in 3-week diabetic rats but increased in 5-week diabetic rats[31]. However, Reichel *et al* reported that P-GP and BCRP expression levels were increased in blood-brain barrier capillaries on the 14th day after STZ administration. In the choroid plexus, only BCRP showed elevated gene expression. Protein expression was not altered, and the functional capability of P-GP and BCRP also showed no change[52]. The discrepancy among these studies may be due to differences in the tissues and duration of diabetes, as well as the isoform of *Abcb1*. Our present study demonstrates that the effects caused by the onset of diabetes on *Abcb1*/P-GP expression are tissue specific, and they are also dependent on the *Abcb1* isoform and the duration of diabetes. Furthermore, the findings in the present study may partly explain the above discrepancy.

Considering that P-GP regulates the absorption, distribution and excretion of various medicines, the alterations in P-GP expression under diabetic conditions may lead to significant alterations in the distribution of drugs, bringing about changes in toxicological/pharmacological activity. For example, the pharmacological activities of phenobarbital in the CNS[15] and of second-generation histamine HI-receptor antagonists[20] were reported to be enhanced in diabetic mice.

Previous studies have shown that besides medical agents, P-GP also transports some physiological substrates, such as steroid hormones and β-amyloid[53, 54], and that P-GP may regulate ion channel activity via direct interaction, suggesting that functional alteration of P-GP has a significant impact on the physiological environment[55]. For instance, alterations in steroid hormones levels were reported to be involved in the development of depression, indicating that the changes in P-GP function under diabetic conditions may be related to depressive symptoms in diabetic patients[56, 57]. Liu *et al* also proposed that diabetes may increase β-amyloid in the cerebral cortices and hippocampi of rats and that this is a significant cause of memory impairment in diabetic animals[53]. Furthermore, alterations in P-GP expression have been shown to trigger the development of sugar cataracts, one of the many complications of diabetes[55]. All of these results indicate that alterations in P-GP expression and function are important to elucidate the mechanisms of the development of diabetic complications. However, the mechanisms and factors that result in tissue-specific alterations of P-GP need to be further investigated.

In summary, our present study demonstrates that alterations in the expression and function of *Abcb1*/P-GP under diabetic conditions are tissue specific, *Abcb1* isoform specific and diabetic duration dependent. These results provide useful information for the elucidation of drug interactions and pharmacokinetic variability associated with diabetes mellitus.

Acknowledgements

The work was supported by the National Natural Science Foundation of China (No 81072693 and 30672499) and the BASF Innovation Fund 2010.

Author contributions

Lu-lu ZHANG and Xiao-dong LIU designed the experiments and analyzed the data; Lu-lu ZHANG wrote the paper; Xiao-dong LIU and Li LIU revised the paper; Lu-lu ZHANG, Liang LU, Shi JIN, Xin-yue JING, Dan YAO, Nan HU, and Ru DUAN performed the research; and Guang-ji WANG and Lin XIE contributed new analytic tools.

References

1 Bae SK, Yang SH, Lee SJ, Kwon JW, Kim WB, Lee DC, *et al*. Pharmacokinetic changes of DA-7867, a new oxazolidinone, after intravenous and oral administration to rats with short-term and long-term diabetes mellitus induced by streptozotocin. Eur J Pharm Sci 2005; 25: 337–45.

2 Kim YC, Oh EY, Kim SH, Lee MG. Pharmacokinetics and pharmacodynamics of intravenous torasemide in diabetic rats induced by alloxan or streptozotocin. Biopharm Drug Dispos 2005; 26: 371–8.

3 Kim YC, Oh EY, Kim SH, Lee MG. Pharmacokintics of diclofenac in rat model of diabetes mellitus induced by alloxan or steptozotocin. Biopharm Drug Dispos 2006; 27: 85–92.

4 Brady JM, Cherrington NJ, Hartley DP, Buist SC, Li N, Klaassen CD. Tissue distribution and chemical induction of multiple drug resistance genes in rats. Drug Metab Dispos 2002; 30: 838–44.

5 Marchetti S, Mazzanti R, Beijnen JH, Schellens JH. Concise review: clinical relevance of drug drug and herb drug interactions mediated by the ABC transporter ABCB1 (MDR1, P-glycoprotein). Oncologist 2007; 12: 927–41.

6 Dey S, Patel J, Anand BS, Jain-Vakkalagadda B, Kaliki P, Pal D, *et al*. Molecular evidence and functional expression of P-glycoprotein (MDR1) in human and rabbit cornea and corneal epithelial cell lines. Invest Ophthalmol Vis Sci 2003; 44: 2909–18.

7 Fromm MF. Importance of P-glycoprotein at blood-tissue barriers. Trends Pharmacol Sci 2004; 25: 423–9.

8 Nishio N, Katsura T, Ashida K, Okuda M, Inui K. Modulation of P-glycoprotein expression in hyperthyroid rat tissues. Drug Metab Dispos 2005; 33: 1584–7.

9 Yu DK. The contribution of P-glycoprotein to pharmacokinetic drug-drug interactions. J Clin Pharmacol 1999; 39: 1203–11.

10 Liu XD, Pan GY, Xie L, Hou YY, Lan W, Su Q, *et al*. Cyclosporine A enhanced protection of nimodipine against brain damage induced by hypoxia-ischemia in mice and rats. Acta Pharmacol Sin 2002; 23:

225–9.
11 Lickteig AJ, Fisher CD, Augustine LM, Aleksunes LM, Besselsen DG, Slitt AL, *et al*. Efflux transporter expression and acetaminophen metabolite excretion are altered in rodent models of nonalcoholic fatty liver disease. Drug Metab Dispos 2007; 35: 1970–8.
12 Naud J, Michaud J, Boisvert C, Desbiens K, Leblond FA, Mitchell A, *et al*. Down-regulation of intestinal drug transporters in chronic renal failure in rats. J Pharmacol Exp Ther 2007; 320: 978–85.
13 Tada Y, Wada M, Kuroiwa K, Kinugawa N, Harada T, Nagayama J, *et al*. MDR1 gene overexpression and altered degree of methylation at the promoter region in bladder cancer during chemotherapeutic treatment. Clin Cancer Res 2000; 6: 4618–27.
14 Yu S, Yu Y, Liu L, Wang X, Lu S, Liang Y, *et al*. Increased plasma exposures of five protoberberine alkaloids from *Coptidis Rhizoma* in streptozotocin-induced diabetic rats: is P-GP involved? Planta Med 2010; 76: 876–81.
15 Liu H, Zhang D, Xu X, Liu X, Wang G, Xie L, *et al*. Attenuated function and expression of P-glycoprotein at blood-brain barrier and increased brain distribution of phenobarbital in streptozotocin-induced diabetic mice. Eur J Pharmacol 2007; 561: 226–32.
16 Liu H, Xu X, Yang Z, Deng Y, Liu X, Xie L. Impaired function and expression of P-glycoprotein in blood-brain barrier of streptozotocin–induced diabetic rats. Brain Res 2006; 1123: 245–52.
17 Nawa A, Fujita Hamabe W, Tokuyama S. Inducible nitric oxide synthase-mediated decrease of intestinal P-glycoprotein expression under streptozotocin-induced diabetic conditions. Life Sci 2010; 86: 402–9.
18 Tramonti G, Xie P, Wallner EI, Danesh FR, Kanwar YS. Expression and functional characteristic of tubular transporters: P-glycoprotein, PEPT1, and PEPT2 in renal mass reduction and diabetes. Am J Physiol Renal Physiol 2006; 291: 972–80.
19 van Waarde WM, Verkade HJ, Wolters H, Havinga R, Baller J, Bloks V, *et al*. Differential effects of streptozotocin-induced diabetes on expression of hepatic ABC-transporters in rats. Gastroenterology 2002; 122: 1842–52.
20 Kamei J, Hirano S, Miyata S, Saitoh A, Onodera K. Effects of first- and second-generation histamine-H1-receptor antagonists on the pentobarbital-induced loss of the righting reflex in streptozotocin-induced diabetic mice. J Pharmacol Sci 2005; 97: 266–72.
21 Ke LD, Chen Z, Yung WK. A reliability test of standard-based quantitative PCR: exogenous vs endogenous standards. Mol Cell Probes 2000; 14: 127–35.
22 Liu W, Saint DA. Validation of a quantitative method for real time PCR kinetics. Biochem Biophys Res Commun 2002; 294: 347–53.
23 Livak KJ, Schmittgen TD. Analysis of relative gene expression data using real-time quantitative PCR and the $2^{-\Delta\Delta ct}$ method. Methods 2001; 25: 402–8.
24 Applied–Biosystems. Relative quantitation of gene expression. User Bulletin #2. ABI PRISM 7700 Sequence Detection System. 1997.
25 Jing X, Liu X, Wen T, Xie S, Yao D, Liu X, *et al*. Combined effects of epileptic seizure and phenobarbital induced overexpression of P-glycoprotein in brain of chemically kindled rats. Br J Pharmacol 2010; 159: 1511–22.
26 Schinkel AH, Smit JJ, van Tellingen O, Beijnen JH, Wagenaar E, van Deemter L, *et al*. Disruption of the mouse mdr1a P-glycoprotein gene leads to a deficiency in the blood-brain barrier and to increased sensitivity to drugs. Cell 1994; 77: 491–502.
27 Bond TD, Valverde MA, Higgins CF. Protein kinase C phosphorylation disengages human and mouse-1a P-glycoproteins from influencing the rate of activation of swelling-activated chloride currents. J Physiol 1998; 508: 333–40.
28 Lecureur V, Thottassery JV, Sun D, Schuetz EG, Lahti J, Zambetti GP, *et al*. Mdr1b facilitates p53-mediated cell death and p53 is required for Mdr1b upregulation *in vivo*. Oncogene 2001; 20: 303–13.
29 Zhou G, Kuo MT. Wild-type p53-mediated induction of rat mdr1b expression by the anticancer drug daunorubicin. J Biol Chem 1998; 273: 15387–94.
30 Ziemann C, Bürkle A, Kahl GF, Hirsch-Ernst KI. Reactive oxygen species participate in mdr1b mRNA and P-glycoprotein overexpression in primary rat hepatocyte cultures. Carcinogenesis 1999; 20: 407–14.
31 Liu H, Liu X, Jia L, Liu Y, Yang H, Wang G, *et al*. Insulin therapy restores impaired function and expression of P-glycoprotein in blood-brain barrier of experimental diabetes. Biochem Pharmacol 2008; 75: 1649–58.
32 Liu H, Yang H, Wang D, Liu Y, Liu X, Li Y, *et al*. Insulin regulates P-glycoprotein in rat brain microvessel endothelial cells via an insulin receptor-mediated PKC/NF-κB pathway but not a PI3K/Akt pathway. Eur J Pharmacol 2009; 602: 277–82.
33 Kameyama N, Arisawa S, Ueyama J, Kagota S, Shinozuka K, Hattori A, *et al*. Increase in P-glycoprotein accompanied by activation of protein kinase C alpha and NF-kappaB p65 in the livers of rats with streptozotocin-induced diabetes. Biochim Biophys Acta 2008; 1782: 355–60.
34 Barta CA, Sachs-Barrable K, Feng F, Wasan KM. Effects of monoglycerides on P-glycoprotein: modulation of the activity and expression in Caco-2 cell monolayers. Mol Pharm 2008; 5: 863–75.
35 Nishimura A, Honda N, Sugioka N, Takada K, Shibata N. Evaluation of carbamazepine pharmacokinetic profiles in mice with kainic acid-induced acute seizures. Biol Pharm Bull 2008; 31: 2302–8.
36 Pires MM, Emmert D, Hrycyna CA, Chmielewski J. Inhibition of P-glycoprotein-mediated paclitaxel resistance by reversibly linked quinine homodimers. Mol Pharmacol 2009; 75: 92–100.
37 Tanaka S, Masuda M, Nakajima K, Ido N, Ohtsuka T, Nishida M, *et al*. P-glycoprotein function in peripheral T lymphocyte subsets of myasthenia gravis patients: clinical implications and influence of glucocorticoid administration. Int Immunopharmacol 2009; 9: 284–90.
38 Tomita M, Kishimoto H, Takizawa Y, Hayashi M. Effects of intestinal ischemia/reperfusion on P-glycoprotein mediated biliary and renal excretion of rhodamine123 in rat. Drug Metab Pharmacokinet 2009; 24: 428–37.
39 Kato R, Moriguchi J, Irie T, Nakagawa M, Kusukawa Y, Matsumura H, *et al*. Effects of lipopolysaccharide on P-glycoprotein expression and activity in the liver and kidneys. Eur J Pharmacol 2010; 636: 155–8.
40 Cermanova J, Fuksa L, Brcakova E, Hroch M, Kucera O, Kolouchova G, *et al*. Up-regulation of renal Mdr1 and Mrp2 transporters during amiodarone pretreatment in rats. Pharmacol Res 2010; 61: 129–35.
41 Borbás T, Benko B, Dalmadi B, Szabó I, Tihanyi K. Insulin in flavin-containing monooxygenase regulation. Flavin-containing monooxygenase and cytochrome P450 activities in experimental diabetes. Eur J Pharm Sci 2006; 28: 51–8.
42 Huber JD, VanGilder RL, Houser KA. Streptozotocin-induced diabetes progressively increases blood-brain barrier permeability in specific brain regions in rats. Am J Physiol Heart Circ Physiol 2006; 291: 2660–8.
43 Hawkins BT, Davis TP. The blood-brain barrier/neurovascular unit in health and disease. Pharmacol Rev 2005; 57: 173–85.
44 Hawkins BT, Ocheltree SM, Norwood KM, Egleton RD. Decreased blood-brain barrier permeability to fluorescein in streptozotocin-treated rats. Neurosci Lett 2007; 411: 1–5.
45 Goralski KB, Hartmann G, Piquette-Miller M, Renton KW. Down-

regulation of mdr1a expression in the brain and liver during CNS inflammation alters the *in vivo* disposition of digoxin. Br J Pharmacol 2003; 139: 35–48.

46 Kathryn T. Dyslipidaemia, inflammation and endothelial dysfunction in diabetes mellitus. Int Congr Ser 2004; 1262: 511–4.

47 Tambur AR, Markham PN, Gebel HM. IL-4 Inhibits P-Glycoprotein in normal and malignant NK cells. Hum Immunol 1998; 59: 483–7.

48 Liu YC, Liu HY, Yang HW, Wen T, Shang Y, Liu XD, *et al*. Impaired expression and function of breast cancer resistance protein (Bcrp) in brain cortex of streptozocin-induced diabetic rats. Biochem Pharmacol 2007; 74: 1766–72.

49 Zhao YL, Du J, Kanazawa H, Sugawara A, Takagi K, Kitaichi K, *et al*. Effect of endotoxin on doxorubicin transport across blood-brain barrier and P-glycoprotein function in mice. Eur J Pharmacol 2002; 445: 115–23.

50 Heemskerk S, van Koppen A, van den Broek L, Poelen GJ, Wouterse AC, Dijkman HB, *et al*. Nitric oxide differentially regulates renal ATP-binding cassette transporters during endotoxemia. Pflugers Arch 2007; 454: 321–34.

51 Anger GJ, Magomedova L, Piquette-Miller M. Impact of acute streptozotocin-induced diabetes on ABC transporter expression in rats. Chem Biodivers 2009; 6: 1943–59.

52 Reichel V, Burghard S, John I, Huber O. P-glycoprotein and breast cancer resistance protein expression and function at the blood-brain barrier and blood-cerebrospinal fluid barrier (choroid plexus) in streptozotocin-induced diabetes in rats. Brain Res 2011; 1370: 238–45.

53 Liu Y, Liu H, Yang J, Liu X, Lu S, Wen T, *et al*. Increased amyloid beta-peptide (1–40) level in brain of streptozotocin-induced diabetic rats. Neuroscience 2008; 153: 796–802.

54 Ueda K, Okamura N, Hirai M, Tanigawara Y, Saeki T, Kioka N, *et al*. Human P-glycoprotein transports cortisol, aldosterone, and dexamethasone, but not progesterone. J Biol Chem 1992; 267: 24248–52.

55 Miyazawa T, Kubo E, Takamura Y, Akagi Y. Up-regulation of P-glycoprotein expression by osmotic stress in rat sugar cataract. Exp Eye Res 2007; 84: 246–53.

56 Anderson RJ, Freedland KE, Clouse RE, Lustman PJ. The prevalence of comorbid depression in adults with diabetes: a meta-analysis. Diabetes Care 2001; 24: 1069–78.

57 Goodyer IM, Herbert J, Tamplin A, Altham PM. First-episode major depression in adolescents. Affective, cognitive and endocrine characteristics of risk status and predictors of onset. Br J Psychiatry 2000; 176: 142–9.

Acta Pharmacologica Sinica (2011) 32: 967–972
 1671-4083/11 $32.00
www.nature.com/aps

Original Article

Effects of ticlopidine on pharmacokinetics of losartan and its main metabolite EXP-3174 in rats

Si-hyung YANG[1], Young-ah CHO[2], Jun-shik CHOI[3, *]

[1]College of Medicine, Dankook University, Cheonan 330–714, Korea; [2]College of Medicine, Research Institute of Life Science, Gyeongsang National University, Jinju 660–701, Korea; [3]College of Pharmacy, Chosun University, Gwangju 501–759, Korea

Aim: Losartan and antiplatelet agent ticlopidine can be prescribed concomitantly for prevention or therapy of cardiovascular diseases. Hence, the effects of ticlopidine on the pharmacokinetics of losartan and its active metabolite EXP-3174 were evaluated in rats.
Methods: Ticlopidine (4 or 10 mg/kg *po*) was administered 30 min before administration of losartan (9 mg/kg *po* or 3 mg/kg iv). The activity of human CYP2C9 and 3A4 were measured using the CYP inhibition assay kit. The activity of P-gp was evaluated using rhodamine-123 retention assay in MCF-7/ADR cells.
Results: Ticlopidine (10 mg/kg) significantly increased the areas under the plasma concentration-time curves (AUCs) and peak plasma concentration (C_{max}) of oral losartan (9 mg/kg), as well as the AUCs of the active metabolite EXP-3174. Ticlopidine (10 mg/kg) did not significantly change the pharmacokinetics of intravenous losartan (3 mg/kg). Ticlopidine inhibited CYP2C9 and 3A4 with IC_{50} values of 26.0 and 32.3 μmol/L, respectively. The relative cellular uptake of rhodamine-123 was unchanged.
Conclusion: The significant increase in the AUC of losartan (9 mg/kg) by ticlopidine (10 mg/kg) could be attributed to the inhibition of CYP2C9- and 3A4-mediated losartan metabolism in small intestine and/or in liver. The inhibition of P-gp in small intestine and reduction of renal elimination of losartan by ticlopidine are unlikely to be causal factors.

Keywords: pharmacokinetics; losartan; EXP-3174; ticlopidine; CYP2C subfamily; CYP3A; P-glycoprotein

Acta Pharmacologica Sinica (2011) 32: 967–972; doi: 10.1038/aps.2011.32; published online 13 Jun 2011

Introduction

Losartan (DuP 753, MK-954), an angiotensin II receptor antagonist, has a low side-effect profile and is approved for the treatment of hypertension, alone or in combination with other agents[1]. After oral administration, losartan is almost completely absorbed and extensively metabolized to a carboxylic acid derivative, EXP-3174, mainly by cytochrome P450 (CYP) 2C9 and 3A4[2]. EXP-3174 is a major active metabolite in both rats and humans and is a more potent inhibitor of angiotensin II receptor than losartan, with high-affinity receptor specificity[3]. Losartan has also been reported to be a substrate of P-glycoprotein (P-gp)[4]. Considering that losartan is a substrate of both CYP enzymes and P-gp, the modulation of CYP and P-gp activities may cause significant changes in the pharmacokinetic profiles of losartan and its active metabolite, EXP-3174.

Ticlopidine, a potent antiplatelet agent induced by adenosine diphosphate, is used for the treatment of a variety of platelet-dependent disease states[5]. Several papers recommend ticlopidine as a valuable alternative when patients cannot tolerate aspirin[6, 7]. It has been reported that ticlopidine causes significant inhibition of several drugs metabolized by the hepatic CYP enzyme system[8, 9].

Clinically, losartan and ticlopidine can be prescribed concomitantly for the prevention or therapy of cardiovascular diseases. However, the pharmacokinetic interaction between ticlopidine and losartan *in vivo* has not yet been reported. Therefore, the present study aimed to evaluate the effect of ticlopidine on the pharmacokinetics of losartan and its active metabolite, EXP-3174, in rats. The effects of ticlopidine on P-gp, CYP2C9, and 3A4 activities were also evaluated.

Materials and methods

Chemicals

Losartan, EXP-3174, L-158.809 (internal standard), acetonitrile, methanol, and *tert*-butylmethylether were purchased from Merck Corporation (Darmstadt, Germany). Ticlopidine was purchased from Sigma-Aldrich Corporation (St Louis, MO, USA). All other chemicals were of reagent grade, and all solvents were of HPLC grade.

* To whom correspondence should be addressed.
E-mail jsachoi@chosun.ac.kr
Received 2011-01-04 Accepted 2011-03-23

Rats

The protocols for the animal studies were approved by the Animal Care Committee of Chosun University (Gwangju, Korea). Male Sprague-Dawley rats (7–8 weeks old, weighing 270–300 g) were purchased from Dae Han Laboratory Animal Research Company (Eumsung, Korea). The procedures used to maintain and handle the rats were similar to reported methods[10].

Oral and intravenous administrations of losartan and ticlopidine

Losartan was orally or intravenously administrated, whereas ticlopidine was administrated orally. Oral losartan and ticlopidine were dissolved in distilled water (5 and 4 mL, respectively). Intravenous losartan was dissolved in 0.9% NaCl solution (4 mL). The rats were randomly divided into six groups (n=6 each): oral losartan (9 mg/kg) without and with oral ticlopidine (4 or 10 mg/kg); intravenous losartan (3 mg/kg) without and with oral ticlopidine (4 or 10 mg/kg). The rats were fasted for at least 24 h prior to the beginning of the experiments. Each animal was anaesthetized with light ether and the right femoral artery (for blood sampling) or vein (for iv administration of losartan) was cannulated with a polyethylene tube (SP45, ID 0.58 mm, OD 0.96 mm; Natsume Seisakusho, Tokyo, Japan). Ticlopidine was orally administered 30 min before oral administration of losartan. Oral losartan and ticlopidine were administered using a gastric gavage tube. A blood sample (approximately 0.5 mL) was collected into a heparinized tube at 0 (control), 0.017 (end of the infusion), 0.1, 0.25, 0.5, 1, 2, 4, 8, and 12 h after iv administration, and 0, 0.1, 0.25, 0.5, 1, 2, 4, 6, 8, and 12 h after oral administration. Approximately 1 mL of whole blood collected from untreated rats was infused via the femoral artery at 0.25, 1, and 4 h to replace the blood loss due to blood sampling. Each blood sample was centrifuged at 16 810×g for 5 min, and 200 μL of each plasma sample was stored at -40 °C until HPLC analysis of losartan and EXP-3174 was performed[11].

HPLC assay

Plasma concentrations of losartan were determined using an HPLC assay, which was modified from the reported method[11]. Briefly, a 50 μL aliquot of L-158.809 (internal standard, 5 μg/mL dissolved in methanol) and a 0.5 mL aliquot of acetonitrile were added to a 0.2 mL aliquot of the plasma sample in a 2.0 mL polypropylene microtube. The solution was then mixed for 5 min using a vortex-mixer (Vortex-Genie 2, Scientific Industries, Bohemia, NY, USA) and centrifuged for 10 min (16 810×g). A 0.5 mL aliquot of the supernatant was transferred to a clean test tube and evaporated under a gentle stream of nitrogen gas at 35 °C. The residue was reconstituted in 150 μL of the mobile phase and 70 μL was injected directly onto a reversed-phase (C_{18}; Luna; 4.6 mm id×250 mm, particle size 5 μm, Phenomenex, Torrance, CA, USA) HPLC column. The HPLC system used in this study was comprised of a Waters 1515 isocratic HPLC Pump, a Waters 717 plus autosampler, a Waters 474 scanning fluorescence detector (Waters, Milford, MA, USA), and an HPLC column temperature controller (ThermaSphere TS-430, Phenomenex, Torrance, CA, USA). The mobile phase, acetonitrile-0.01 mol/L phosphate buffer (41:59, *v/v*, pH 2.5, adjusted with phosphoric acid), was run at a flow rate of 0.8 mL/min and the column eluent was monitored using an ultraviolet detector at 215 nm. The retention times of L-158.809 (internal standard), losartan, and EXP-3174 were 6.27, 11.4, and 17.8 min, respectively. The lower limit of quantification for both losartan and EXP-3174 in rat plasma was 5 ng/mL. The coefficients of variation for losartan and EXP-3174 were below 13.9% and 15.9%, respectively.

CYP inhibition assay

The inhibition assays for human CYP2C9 and 3A4 enzyme activities were performed in multiwell plates using the CYP inhibition assay kit (Gentest, Woburn, MA, USA) as previously described[12]. Briefly, human CYP enzymes were obtained from baculovirus-infected insect cells. CYP substrates [150 mmol/L 7-methoxy-4-trifluoromethyl coumarin (7-MFC) and 50 mmol/L 7-benzyloxy-4-(trifluoromethyl) coumarin (7-BFC) for CYP2C9 and 3A4, respectively] were incubated with or without test compounds in a reaction mix containing 1 pmol of P450 enzyme and the NADPH-generating system (1.3 mmol/L NADP, 3.54 mmol/L glucose 6-phosphate, 0.4 U/mL glucose 6-phosphate dehydrogenase and 3.3 mmol/L $MgCl_2$) in potassium phosphate buffer (pH 7.4). Reactions were terminated after 30 min by the addition of stop solution. Metabolite concentrations were measured with a spectrofluorometer (Molecular Device, Sunnyvale, CA, USA) set at an excitation wavelength of 409 nm and an emission wavelength of 530 nm. Positive controls (2 μmol/L sulfaphenazole and 1 μmol/L ketoconazole for CYP2C9 and 3A4, respectively) were run on the same plate and produced 99% inhibition. All experiments were performed in duplicate, and the results are expressed as percent inhibition.

Rhodamine-123 retention assay

MCF-7/ADR, a doxorubicin-resistant human breast cancer cell line, was used and seeded on 24-well plates at a density of 10^5 cells. At 80% confluence, the cells were incubated in FBS-free DMEM for 18 h. The culture medium was then changed to Hanks' balanced salt solution, and the cells were incubated at 37 °C for 30 min. After incubating the cells with 20 μmol/L rhodamine-123 in the presence of ticlopidine (1, 3, 10, and 30 μmol/L) for 90 min, the medium was completely removed. The cells were then washed three times with ice-cold phosphate buffer (pH 7.0) and lysed in lysis buffer. Rhodamine-123 fluorescence was measured in the cell lysates using excitation and emission wavelengths of 480 and 540 nm, respectively. Fluorescence values were normalized to the total protein content of each sample and presented as a ratio compared with control values. Verapamil (100 μmol/L) was used as a positive control.

Pharmacokinetic analysis

Standard methods[13] were used to calculate the following

pharmacokinetic parameters using non-compartmental analysis (WinNonlin software version 4.1; Pharsight Corporation, Mountain View, CA, USA): total area under the concentration–time curve (AUC)[14], time-averaged total body clearance (CL), terminal half-life, first moment of AUC (AUMC), mean residence time (MRT), and apparent volume of distribution at steady state (V_{ss}). The extent of absolute oral bioavailability (F) was estimated by $AUC_{oral}/AUC_{iv}\times Dose_{iv}/Dose_{oral}\times 100$. The peak concentration (C_{max}) and the time to reach peak concentration (t_{max}) of losartan and EXP-3174 were determined directly from the experimental data.

Statistical analysis

P-values <0.05 were deemed to be significant using the Social Package of Statistical Sciences (SPSS) *posteriori* analysis of variance (ANOVA) for the unpaired data and then individual differences among groups were determined using Duncan's multiple range test. All data are expressed as the mean±standard deviation (SD).

Results

Inhibition of CYP2C9 and 3A4

The inhibitory effects of ticlopidine on CYP2C9 and 3A4 activities are shown in Figure 1. Ticlopidine inhibited CYP2C9 and 3A4 with IC_{50} values of 26.0 and 32.3 μmol/L, respectively.

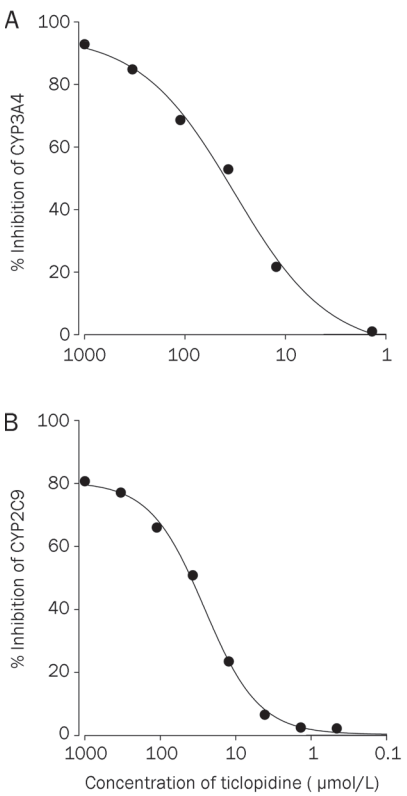

Figure 1. Inhibitory effects of ticlopidine on CYP3A4 (A) and 2C9 (B) activity. All experiments were performed in duplicate, and results were expressed as the percent inhibition.

Rhodamine-123 retention assay

The effects of ticlopidine on the cellular accumulation of rhodamine-123 in MCF-7 and MCF-7/ADR cells are shown in Figure 2. Accumulation of rhodamine-123 was reduced in MCF-7/ADR cells overexpressing P-gp compared to MCF-7 cells lacking P-gp. The relative cellular uptake of rhodamine-123 was comparable between the two conditions at the concentration range of 1–30 μmol/L ticlopidine.

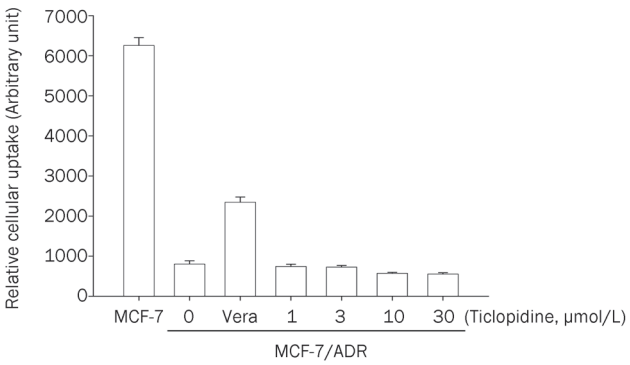

Figure 2. Effect of ticlopidine on the cellular accumulation of rhodamine-123 in MCF-7 and MCF-7/ADR cells. Mean±SD (n=6).

Effect of ticlopidine on the pharmacokinetics of oral losartan

Rats were given oral administration of losartan (9 mg/kg) with and without oral administration of ticlopidine at doses of 4 and 10 mg/kg. The mean arterial plasma concentration-time profiles of losartan are shown in Figure 3. The relevant pharmacokinetic parameters of losartan are listed in Table 1. Absorption of losartan was rapid; losartan was detected in plasma at the first blood sampling time point (5 min) with a rapid t_{max} (1–2 h) for all rats studied (Figure 3). The AUC and

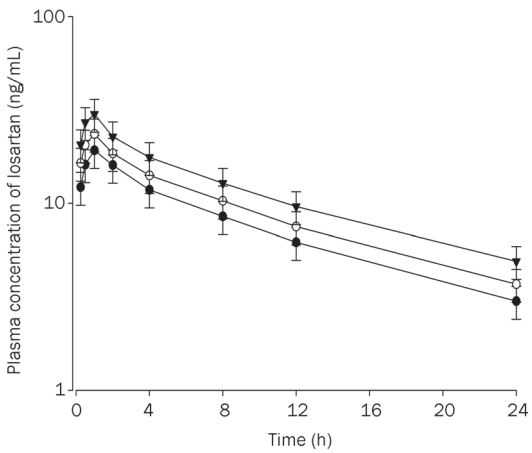

Figure 3. Mean plasma concentration-time profiles of losartan after oral (9 mg/kg) administration of losartan to rats without (control) and with ticlopidine at doses of 4 and 10 mg/kg. Mean±SD (n=6). –●–: Control (only losartan 9 mg/kg alone); –○–: Losartan 9 mg/kg+ticlodipine 4 mg/kg; –▼–: Losartan 9 mg/kg+ticlodipine 10 mg/kg.

Table 1. Pharmacokinetic parameters of losartan after oral (9 mg/kg) administration without (control) and with ticlopidine at doses of 4 and 10 mg/kg. n=6. [b]P<0.05 *vs* control group (only losartan alone).

Parameter	Control	Losartan+Ticlodipine	
		4 mg/kg	10 mg/kg
$AUC_{0-\infty}$ (ng·mL^{-1}·h)	143.1±33.2	178.9±34.9	236.0±39.6[b]
C_{max} (ng/mL)	15.6±2.2	17.6±3.0	23.3±3.7[b]
t_{max} (h)	1.00±0.55	1.00±0.55	0.84±0.26
$t_{1/2}$ (h)	9.40±1.51	9.60±1.54	9.61±1.64
F (%)	15.6±3.6	19.5±4.7	25.7±5.2[b]
RB (%)	100	125	165

$AUC_{0-\infty}$, total area under the plasma concentration-time curve from time zero to infinity; C_{max}, peak plasma concentration; t_{max}, time to reach the peak plasma concentration; $t_{1/2}$, terminal half-life; F, extent of absolute oral bioavailability; RB, relative bioavailability.

C_{max} of losartan after oral administration with losartan and 10 mg/kg ticlopidine were significantly greater (by 65.0% and 49.4%, respectively) than those of control rats. The F of losartan was 64.7%.

Effect of ticlopidine on the pharmacokinetics of active metabolite EXP-3174

Rats were given oral administration of losartan (9 mg/kg) with and without oral ticlopidine at doses of 4 and 10 mg/kg. The mean arterial plasma concentration-time profiles of EXP-3174 are shown in Figure 4. The relevant pharmacokinetic parameters of losartan are listed in Table 2. The AUC and C_{max} of EXP-3174 after oral administration of losartan with 10 mg/kg ticlopidine were significantly greater than those of control rats (by 41.8% and 36.8%, respectively). The AUC ratio ($AUC_{EXP-3174}/AUC_{losartan}$) was not significantly decreased (P>0.05) compared to control rats.

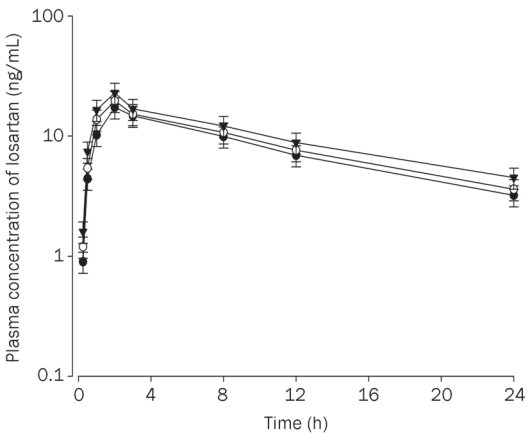

Figure 4. Mean plasma concentration-time profiles of EXP-3174 after oral (9 mg/kg) administration of losartan to rats without and with ticlopidine at doses of 4 and 10 mg/kg. Mean±SD (n=6). –●–: Control (only losartan 9 mg/kg alone); –○–: Losartan 9 mg/kg+ticlodipine 4 mg/kg; –▼–: Losartan 9 mg/kg+ticlodipine 10 mg/kg.

Table 2. Pharmacokinetic parameters of EXP-3174 after oral (9 mg/kg) administration without (control) and with ticlopidine at doses of 4 and 10 mg/kg. n=6. [b]P<0.05 *vs* control group (only losartan alone).

Parameter	Control	Losartan+ticlodipine	
		4 mg/kg	10 mg/kg
$AUC_{0-\infty}$ (ng·mL^{-1}·h)	206.1±33.1	211.0±41.5	292.3±44.8[b]
C_{max} (ng/mL)	17.4±2.40	19.8±3.18	23.8±4.72
t_{max} (h)	2.00±0.63	2.00±0.63	1.68±0.52
$t_{1/2}$ (h)	7.21±1.07	7.66±1.82	8.33±2.08
$AUC_{EXP-3174}/AUC_{losartan}$	1.44±0.23	1.19±0.19	1.23±0.29

$AUC_{0-\infty}$, total area under the plasma concentration-time curve from time zero to infinity; C_{max}, peak plasma concentration; t_{max}, time to reach the peak plasma concentration; $t_{1/2}$, terminal half-life.

Effect of ticlopidine on the pharmacokinetics of intravenous losartan

Mean arterial plasma concentration-time profiles of losartan following intravenous administration of losartan (3 mg/kg) to rats in the presence or absence of ticlopidine (4 and 10 mg/kg) are shown in Figure 5. The corresponding pharmacokinetic parameters are shown in Table 3.

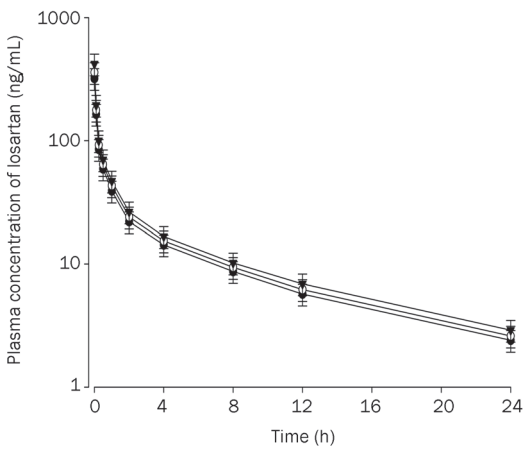

Figure 5. Mean plasma concentration-time profiles of losartan after iv (3 mg/kg) administration to rats without and with ticlopidine at doses of 4 and 10 mg/kg. Mean±SD (n=6). –●–: Control (only losartan 3 mg/kg alone); –○–: Losartan 9 mg/kg+ticlodipine 4 mg/kg; –▼–: Losartan 9 mg/kg+ticlodipine 10 mg/kg.

The AUC of losartan was increased by ticlopidine treatment, but was not statistically significant compared to the control. The $t_{1/2}$ of losartan was also prolonged, but this increase was not significant. The pharmacokinetics of intravenous losartan was not affected by the concurrent use of ticlopidine, in contrast to those of oral losartan. Accordingly, there was enhanced oral bioavailability in the presence of ticlopidine, while there was no significant change in the pharmacokinetics of intravenous losartan. This finding may be due to the inhibi-

Table 3. Pharmacokinetic parameters of losartan after intavenous (3 mg/kg) administration to rats without (control) and with ticlopidine at doses of 4 and 10 mg/kg. *n*=6.

Parameter	Control	Losartan+ticlodipine	
		4 mg/kg	10 mg/kg
$AUC_{0-\infty}$ (ng·mL^{-1}·h)	288.1±74.2	314.2±81.2	345.0±85.1
CLt (mL·h^{-1}·kg^{-1})	3.78±1.07	3.56±1.02	3.33±1.01
$t_{1/2}$ (h)	8.7±2.0	8.8±2.0	8.9±2.2
RB (%)	100	108	119

$AUC_{0-\infty}$, total area under the plasma concentration-time curve from time zero to infinity; CLt, total body clearance; $t_{1/2}$, terminal half-life; RB, relative bioavailability.

tion of CYP3A-mediated metabolism of losartan in the small intestine and/or in the liver rather than the reduction of renal elimination of losartan by ticlopidine.

Discussion

This study evaluated the effect of ticlopidine on the bioavailability and pharmacokinetics of losartan in rats to investigate a potential drug interaction between the two drugs. In previous pharmacokinetic studies, losartan was administered to rats orally at doses of 3–10 mg/kg[15–17]. Thus, a 9 mg/kg dose of losartan was used in the present study.

It has been reported that the pharmacokinetics of losartan are similar between rats and humans[18]. In both rats and humans, EXP-3174 has been found in plasma. The *F* of losartan was reported to be 31.5%–38.2% in rats and 33% in humans. The urinary excretion of losartan within 24 h after oral administration was shown to be approximately 0.3% and 5% of the dose in rats and humans, respectively, which suggests a small contribution of renal clearance to total body clearance[18]. These data support that the rat is a suitable animal model for pharmacokinetic studies of losartan.

Oral administration of losartan with 10 mg/kg ticlopidine significantly increased the AUC (by 65.0%), suggesting that ticlopidine can effectively inhibit the metabolism of losartan in the intestine and/or liver. However, the $AUC_{EXP-3174}$ was also significantly increased (by 41.8%) in the presence of 10 mg/kg ticlopidine. EXP-3174 is eliminated by both renal (accounting for 55% of its clearance) and non-renal routes[19]. One explanation could be that the renal elimination and/or further metabolism of EXP-3174 might be affected by ticlopidine, although further metabolism of EXP-3174 has not been reported. More experiments will be necessary to prove these hypotheses. Although the $AUC_{EXP-3174}$ was also significantly increased in the presence of 10 mg/kg ticlopidine, the AUC ratio ($AUC_{EXP-3174}$/$AUC_{losartan}$) was not significantly decreased (P>0.05) compared to control rats. After oral losartan administration, EXP-3174 showed a greater AUC than losartan because of its low clearance rate. Similar results have been reported previously, showing that EXP-3174 has a greater AUC and a longer terminal half-life than losartan in both rats and humans[20, 21].

Because losartan is a substrate of P-gp, the effect of ticlopidine on P-gp activity levels of losartan was evaluated using rhodamine-123 in a cell-based assay. The relative cellular uptake of rhodamine-123 was not affected (Figure 2), suggesting that ticlopidine does not inhibit P-gp activity. The inhibitory effects of ticlopidine against CYP2C9- and 3A4-mediated metabolism were confirmed by the employment of recombinant CYP enzymes. As shown in Figure 1, ticlopidine exhibited inhibitory effects against CYP2C9- and 3A4-mediated metabolism with IC_{50} values of 26.0 and 32.3 μmol/L, respectively. This finding shows that the AUC of losartan increased significantly after its oral administration with 10 mg/kg ticlopidine, although the *in vitro* CYP inhibition of losartan was not potent. Although *in vitro* studies are useful methods to study inhibitory mechanisms, they are limited because test conditions may not accurately correspond to *in vivo* conditions. Thus, there may be some discrepancies between *in vivo* and *in vitro* data. In a study using human liver microsomes and recombinant human CYP enzymes, it was reported that ticlopidine is a potent, competitive inhibitor of both CYP2C19 and 2D6, but is only a weak inhibitor of CYP2C9 and 3A[22]. It was also reported that ticlopidine has a high inhibitory potency for CYP2C19 *in vitro* and *in vivo*[23].

CYP1A and 3A isoforms were primarily expressed in rat intestine, whereas CYP2C was not detectable in rat intestine using RT-PCR and immunoblot analysis[24]. Thus, the significant increase in AUC of losartan after oral administration with losartan and ticlopidine (10 mg/kg) may be attributable to the inhibition of CYP2C and 3A subfamilies-mediated losartan metabolism in the liver and/or the intestine rather than the inhibition of P-gp activity by ticlopidine. Similar results were reported showing that concomitant intake of grapefruit juice significantly altered some of the pharmacokinetic parameters of losartan and its metabolite EXP-3174 in healthy volunteers via the inhibition of CYP3A4 metabolism[25]. It was also reported that neurological symptoms occurred in an epileptic patient in association with increased carbamazepine levels, due to a probable drug interaction between ticlopidine and carbamazepine (which is mainly metabolized via CYP3A4[26]).

There are likely to be some differences in the enzyme activities of the CYP2C and 3A subfamilies between rats and humans[27]. The protein homologies between CYP2C and 3A in rats and humans have been reported to be very similar, 73% and 77%, respectively[28]. For example, the $AUC_{losartan}$ and $AUC_{EXP-3174}$ were significantly increased and decreased, respectively, by administration of bucolome, a CYP2C9 inhibitor, in both rats and humans[16]. This result supports that rat isoforms with very similar enzymatic properties to CYP2C9 could be involved in the metabolic clearance of losartan in rats, although rats do not have the CYP isoforms orthologous to human CYP2C9.

The significant increase in the AUC of losartan after oral administration with losartan and ticlopidine (10 mg/kg) may be attributable to the inhibition of CYP2C and 3A subfamilies-mediated losartan metabolism in the small intestine and/or in the liver. The inhibition of P-gp in the small intestine and the

reduction of renal elimination of losartan by ticlopidine are unlikely to be causal factors.

Author contribution

Si-hyung YANG and Young-ah CHO designed the research; Young-ah CHO performed the research; Si-hyung YANG analyzed the data; Jun-shik CHOI wrote the paper.

References

1 Triggle DJ. Angiotensin II receptor antagonism: losartan — sites and mechanisms of action. Clin Ther 1995; 17: 1005–30.
2 Yasar U, Tybring G, Hidestrand M, Oscarson M, Ingelman-Sundberg M, Dahl ML, *et al*. Role of CYP2C9 polymorphism in losartan oxidation. Drug Metab Dispos 2001; 29: 1051–6.
3 Wong PC, Price WA Jr, Chiu AT, Duncia JV, Carini DJ, Wexler RR, *et al*. Nonpeptide angiotensin II receptor antagonists. XI. Pharmacology of EXP3174: an active metabolite of DuP 753, an orally active antihypertensive agent. J Pharmacol Exp Ther 1990; 255: 211–7.
4 Soldner A, Spahn-Langguth H, Mutschler E. HPLC assays to simultaneously determine the angiotensin-AT1 antagonist losartan as well as its main and active metabolite EXP-3174 in biological material of humans and rats. J Pharm Biomed Anal 1998; 16: 863–73.
5 Saltiel E, Ward A. Ticlopidine. A review of its pharmacodynamic and pharmacokinetic properties, and therapeutics efficacy in platelet-dependent disease states. Drugs 1987; 34: 222–62.
6 Ito MK, Smith AR, Lee ML. Ticlopidine: a new platelet aggregation inhibitors. Clin Pharm 1992; 11: 603–17.
7 Flores-Runk P, Raasch RH. Ticlopidine and antiplatelet therapy. Ann Pharmacother 1993; 27: 1090–8.
8 Birmelé B, Lebranchu Y, Bagros P, Nivet H, Furet Y, Pengloan J. Interaction of cyclosporin and ticlopidine. Nephrol Dial Transplant 1991; 6: 150–1.
9 Knudsen JB, Bastain W, Sefton CM, Allen JG, Dickinson JP. Pharmacokinetics of ticlopidine during chronic oral administration to healthy volunteers and its effects on antipyrine pharmacokinetics. Xenobiotica 1992; 22: 579–89.
10 Choi DH, Li C, Choi JS. Effects of myricetin, an antioxidant, on the pharmacokinetics of losartan and its active metabolite, EXP-3174, in rats: possible role of cytochrome P450 3A4, cytochrome P450 2C9 and P-glycoprotein inhibition by myricetin. J Pharm Pharmacol 2010; 62: 908–14.
11 Zarghi A, Foroutan SM, Shafaati A, Khoddam A. A rapid HPLC method for the determination of losartan in human plasma using a monolithic column. Arzneimittelforschung 2005; 55: 569–72.
12 Crespi CL, Miller VP, Penman BW. Microtiter plate assays for inhibition of human, drug-metabolizing cytochromes P450. Anal Biochem 1997; 248: 188–90.
13 Gibaldi M, Perrier D. Pharmacokinetics. 2nd ed. New York: Marcel-Dekker; 1982.
14 Chiou WL. Critical evaluation of potential error in pharmacokinetic studies using the linear trapezoidal rule method for the calculation of the area under the plasma level-time curve. J Pharmacokinet Biopharm 1978; 6: 539–46.
15 Shibasaki M, Fujimori A, Takanashi M, Kusayama T, Tokioka T, Satoh Y, *et al*. Pharmacological profile of YM358, a novel nonpeptide angiotensin AT1 receptor antagonist. Eur J Pharmacol 1997; 335: 167–73.
16 Kobayashi M, Takagi M, Fukumoto K, Kato R, Tanaka K, Ueno K. The effect of bucolome, a CYP2C9 inhibitor, on the pharmacokinetics of losartan. Drug Metab Pharmacokinet 2008; 23: 115–9.
17 Yan YD, Kim HK, Seo KH, Lee WS, Lee GS, Woo JS, *et al*. The physicochemical properties, *in vitro* metabolism and pharmacokinetics of a novel ester prodrug of EXP3174. Mol Pharm 2010; 7: 2132–40.
18 Yoshitani T, Yagi H, Inotsume N, Yasuhara M. Effect of experimental renal failure on the pharmacokinetics of losartan in rats. Biol Pharm Bull 2002; 25: 1077–83.
19 Tamaki T, Nishiyama A, Kimura S, Aki Y, Yoshizumi M, Houchi H, *et al*. EXP3174: the major active metabolite of losartan. Cardiovasc Drug Rev 1997; 15: 122–36.
20 Munafo A, Christen Y, Nussberger J, Shum LY, Borland RM, Lee RJ, *et al*. Drug concentration response relationships in normal volunteers after oral administration of losartan, an angiotensin I1 receptor antagonist. Clin Pharmacol Ther 1992; 51: 513–21.
21 Lo MW, Goldberg MR, McCrea JB, Lu H, Furtek CI, Bjornsson TD. Pharmacokinetics of losartan, an angiotensin II receptor antagonist, and its active metabolite EXP-3174 in humans. Clin Pharmacol Ther 1995; 58: 641–9.
22 Ko JW, Desta Z, Soukhova NV, Tracy T, Flockhart DA. *In vitro* inhibition of the cytochrome P450 (CYP450) system by the antiplatelet drug ticlopidine: potent effect on CYP2C19 and CYP2D6. Br J Clin Pharmacol 2000; 49: 343–51.
23 Foti RS, Wahlstrom JL. CYP2C19 inhibition: the impact of substrate probe selection on *in vitro* inhibition profiles. Drug Metab Dispos 2008; 36: 523–8.
24 Kaminsky LS, Zhang QY. The small intestine as a xenobiotic-metabolizing organ. Drug Metab Dispos 2003; 31: 1520–5.
25 Zaidenstein R, Soback S, Gips M, Avni B, Dishi V, Weissgarten Y, *et al*. Effect of grapefruit juice on the pharmacokinetics of losartan and its active metabolite E3174 in healthy volunteers. Ther Drug Monit 2001; 23: 369–73.
26 Brown RI, Cooper TG. Ticlopidine-carbamazepine interaction in a coronary stent patient. Can J Cardiol 1997; 13: 853–4.
27 Cao X, Gibbs ST, Fang L, Miller HA, Landowski CP, Shin HC. Why is it challenging to predict intestinal drug absorption and oral bioavailability in human using rat model. Pharm Res 2006; 23: 1675–86.
28 Lewis DFV. Cytochrome P450. Substrate specificity and metabolism. In: Cytochromes P450: structure, function, and mechanism. Bristol: Taylor & Francis; 1996; p 122–3.

Acta Pharmacologica Sinica (2011) 32: 973–980
 1671-4083/11 $32.00
www.nature.com/aps

Original Article

Proliposomes for oral delivery of dehydrosilymarin: preparation and evaluation *in vitro* and *in vivo*

Chang CHU, Shan-shan TONG, Ying XU, Li WANG, Min FU, Yan-ru GE, Jiang-nan YU*, Xi-ming XU*

Department of Pharmaceutics, School of Pharmacy, Jiangsu University, Zhenjiang 212013, China

Aim: To formulate proliposomes with a polyphase dispersed system composed of soybean phospholipids, cholesterol, isopropyl myristate and sodium cholate to improve the oral bioavailability of dehydrosilymarin, an oxidized form of herbal drug silymarin.
Methods: Dehydrosilymarin was synthesized from air oxidation of silymarin in the presence of pyridine, and proliposomes were prepared by a film dispersion-freeze drying method. Morphological characterization of proliposomes was observed using a transmission electron microscope. Particle size and encapsulation efficiency of proliposomes were measured. The *in vitro* release of dehydrosilymarin from suspension and proliposomes was evaluated. The oral bioavailability of dehydrosilymarin suspension and proliposomes was investigated in rabbits.
Results: The proliposomes prepared under the optimum conditions were spherical and smooth with a mean particle size in the range of 7 to 50 nm. Encapsulation efficiency was 81.59%±0.24%. The *in vitro* accumulative release percent of dehydrosilymarinloaded proliposomes was stable, which was slow in pH 1.2, and increased continuously in pH 6.8, and finally reached 86.41% at 12 h. After oral administration in rabbits, the relative bioavailability of proliposomes versus suspension in rabbits was 228.85%.
Conclusion: Proliposomes may be a useful vehicle for oral delivery of dehydrosilymarin, a drug poorly soluble in water.

Keywords: silymarin; dehydrosilymarin; proliposomes; oral bioavailability; pharmacokinetics

Acta Pharmacologica Sinica (2011) 32: 973–980; doi: 10.1038/aps.2011.25; published online 13 Jun 2011

Introduction

Milk thistle (*Silybum marianum*) is one of the few herbal drugs whose excellent pharmacological profile readily lends itself to proof of clinical efficacy[1]. Silymarin, the seed extract of milk thistle, has been widely used to maintain liver health and treat liver disorders[2]. Different dosage forms of silymarin have been reported[3, 4].

Dehydrosilymarin is a novel compound synthesized from silymarin, exhibited markedly greater pharmacological activity in comparison with silymarin. Nevertheless, the poor water-solubility of dehydrosilymarin hindered the effectiveness of dehydrosilymarin compared to silymarin[5].

Recently, great interest has been shown in the use of liposomes for improving oral absorption and bioavailability of hydrophobic drugs[6]. Liposomes are enclosed vesicles composed of phosphatidylcholine and cholesterol lipid bilayers, which have been extensively studied as drug carriers[7, 8]. The similarity between liposomal lipid bilayers and biomembranes and the relatively small size of liposomes significantly facilitate their oral absorption[9]. However, liposomes still lack a significant medical impact despite a relatively long history of investigation. Limited physical and biological stability are the major barriers in their development, such as with aggregation, sedimentation, fusion, phospholipid hydrolysis and/or oxidation[4]. Accordingly, the development of stable liposomes is a prerequisite for their exploitation in the delivery of therapeutic drugs[10, 11]. For many years, attempts have been made to improve the stability of liposomes by several methods, including preparing more stable bilayers[12], coating their surface with protecting polymers[13–16], and modifying charge[17–19].

Proliposomes are defined as dry, free-flowing particles with a dispersed system that can immediately form a liposomal suspension when in contact with water. Compared with conventional liposomes, proliposomes exhibit more advantages in promoting drug absorption. Because of their solid properties, the physical stability of liposomes can be improved upon without influencing their intrinsic characteristics. Therefore, proliposomes would be a potential vehicle to help improve the oral absorption of hydrophobic drugs. The underlying mechanism allowing proliposomes to improve oral absorption might be partially explained by the presence of bile salts, which can

* To whom correspondence should be addressed.
E-mail xuxm@ujs.edu.cn (Xi-ming XU);
yjn@ujs.edu.cn (Jiang-nan YU)
Received 2010-12-09 Accepted 2011-03-01

interact with phospholipids in the gastrointestinal tract to form mixed micelles for vehicles/mesophases to increase the solubility of hydrophobic drugs[20, 21].

Expanding on our previous work[5], novel proliposomes (a polyphase dispersed system containing trace micelles and emulsions) loaded with dehydrosilymarin were prepared. The physicochemical characteristics and *in vitro* release characteristics of dehydrosilymarin treatment were evaluated. Furthermore, the oral absorption of the dehydrosilymarin suspension and dehydrosilymarin-loaded proliposomes was investigated and compared in rabbits.

Materials and methods

Materials

Silymarin was kindly provided by Zhongxing Pharmaceutical Co Ltd (Jiangsu, China). Soybean phospholipid, which contained approximately 82% (*w/w*) phosphatidylcholine, was purchased from Taiwei Co Ltd (Shanghai, China). Cholesterol was supplied by Shanghai Chemical Reagent Co (Shanghai, China). Sodium cholate was obtained from Sigma Chemical Co (USA). Isopropyl myristate and all other reagents were from Sinopharm Chemical Reagent Co Ltd (Shanghai, China). Other chemical reagents were of analytical grade or better.

Synthesis of dehydrosilymarin

Dehydrosilymarin was prepared essentially according to a reported method[22], which was originally designed for the preparation of dehydrosilybin. In brief, silymarin was dissolved in pyridine and heated to 90 °C under reflux for 77 h with stirring. After the reaction, pyridine was removed using a rotary evaporator. To remove the residual pyridine, toluene was introduced and evaporated. The remaining pellet was dissolved in ethyl acetate, loaded onto a silica gel column, and then eluted with hot acetone. After those procedures, acetone was removed from the products with distillation. The remaining pellet was re-dissolved in hot ethanol and filtered through a Double-ring #102 filter paper (Xinhua Paper Industry Co Ltd, Hangzhou, China). The pass-through fraction was air dried until approximately 4 g of brown dehydrosilymarin pellet was obtained. Dehydrosilymarin's structure was verified by IR and NMR, which were consistent with the results reported in the literature[23] (spectra not shown).

Preparation of dehydrosilymarin-loaded proliposomes

Dehydrosilymarin-loaded proliposomes were prepared by the film dispersion-freeze drying method. Dehydrosilymarin (0.1 g) and phospholipids (0.3 g) were dissolved in acetone solution and heated to 40 °C under reflux in a water bath for at least 3 h with stirring. After the organic solvent was evaporated off using a rotary evaporator (Heidolph Co, Germany) under vacuum, a thin film was formed on the wall of the flask. The film was dissolved with ethanol after 0.075 g cholesterol, 0.2 g isopropyl myristate (IPM) and 0.2 g sodium cholate were added with ultrasound conditions. The solution was then completely evaporated, and the dried residues were gathered and transferred into a petri dish. Distilled water (10 mL) containing 5% mannitol was added to produce the liposomal suspension at room temperature. After freezing at -80 °C for 2 h and drying under vacuum for 24 h (Alpha 2–4, CHRIST, Germany), the yellow dehydrosilymarin-loaded proliposome powder was produced.

Characteristics of dehydrosilymarin-loaded proliposomes

Morphological characterization

The morphology of dehydrosilymarin-loaded proliposomes was observed by transmission electron microscope (TEM) (JEM-2100, JEOL, Japan). The formulation was diluted with distilled water and shaken thoroughly to obtain liposomal dispersion. A 2 μL drop of suspension was placed on a carbon-coated copper grid and dried in bright light until a thin liquid film formed on one side. This sheet of copper with stained film was set onto the end of a long iron bar and inserted into the TEM for sample viewing and photography.

Particle size measurement

A certain amount of dehydrosilymarin-loaded proliposomes was diluted with distilled water to form liposomes. The particle size of the so-formed liposomal suspension was measured using Zetasizer 3000 (Malvern, UK).

Determination of entrapment efficiency

Determination of the content of dehydrosilymarin in dehydrosilymarin-loaded proliposomes

The content of dehydrosilymarin in dehydrosilymarin-loaded proliposomes was determined as follows. A measured number of dehydrosilymarin-loaded proliposomes (0.2 g) were hydrated with 100 mL of distilled water. The obtained liposomal suspension (1 mL) was mixed with anhydrous alcohol (9 mL) and analyzed with a UV-spectrophotometer (UV-2401, Shimazu, Japan) at 255 nm, the maximum absorption wavelength of dehydrosilymarin. Blank liposome, with an absorption maximum about 208 nm, did not interfere with drug detection. The concentration of dehydrosilymarin can be mathematically calculated with the standard curve.

Determination of entrapment efficiency of dehydrosilymarin-loaded proliposomes

The percentage of drug entrapped within the proliposomes was measured according to the method described by Xiao[4]. A suitable quantity of proliposomes loaded with 0.1 g dehydrosilymarin was reconstituted with 100 mL of distilled water. The percentage of dehydrosilymarin encapsulated into proliposomes was measured after separating free drug from dehydrosilymarin-loaded proliposomes with 0.22 μm cellulose nitrate membrane. Because dehydrosilymarin is slightly soluble in water, after dispersing the proliposomes with water, non-trapped dehydrosilymarin was filtrated via cellulose nitrate membrane. The encapsulation efficiency (EE%) of dehydrosilymarin in the reconstituted liposomes was calculated with the following formula:

$$EE\% = C_a / C_b \times 100\%$$

where C_a and C_b denote the concentration of dehydrosilymarin

in the reconstituted liposomes after (a) and before filtration (b).

In vitro release studies

The *in vitro* release studies were conducted according to the release test method described by China Pharmacopoeia (2010 edition, paddle method) with minor modifications. Briefly, proliposomes entrapping 0.1 g dehydrosilymarin were instilled into a dialysis bag (MWCO 3500 D, 25 mm×5 m, Shanghai Green Bird Science and Technology Development, China) after exposure to distilled water. Dialysis bags were fixed on the paddles before immersion into the dissolution medium (pH 1.2 HCl, 900 mL; pH 6.8 phosphate buffered saline, 900 mL) containing 0.1% sodium dodecyl sulfate as a surfactant (sink condition). The entire set was placed on a dissolution tester (ZRS-8G, Tianjin University Radio Power Station, China) set to a constant speed of 100 revolutions per minute at 37 °C. At different time intervals, 10 mL samples were withdrawn and filtered using 0.22 μm cellulose nitrate membranes, and 10 mL of fresh medium was supplemented into the beaker. The samples were measured spectrophotometrically at 255 nm.

Determination of dehydrosilymarin in rabbit plasma by RP-HPLC

In our study, the plasma concentrations of dehydrosilymarin were determined by a HPLC-UV method. Dehydrosilymarin was separated at 25 °C by a C_{18} column (VP-ODS, 150 mm×4.6 mm, 5 μm, Shimazu, Japan) and analyzed at 255 nm. The mobile phase was composed of methanol/double distilled water/methanoic acid in a volume ratio of 57/43/0.2 (*v*/*v*/*v*) at a flow rate of 1.2 mL/min.

After plasma samples had been thawed, dehydrosilymarin in rabbit plasma was extracted by liquid-liquid extraction procedures as follows: 200 μL of rabbit plasma was added to a 10 mL polypropylene screw-capped conical tube, which was followed by the addition of 20 μL of internal standard solution (α-naphthol, 100 μg/mL in methanol), 20 μL of methanol, 50 μL of a 0.5 mol/L K_2HPO_4 solution and 5 mL of anhydrous diethyl ether, in order. After vortexing for 2 min, the mixture was centrifuged at 3000 revolutions per minute (Clements GS 200 centrifuge) for 10 min. The organic layer was transferred to another tube and evaporated under a light stream of nitrogen at 37 °C. The residues were re-suspended in 200 μL of mobile phase and vortexed for 30 s. Aliquots (20 μL) of the supernatant were injected for HPLC analysis. Quantitation was based on the peak area ratio (A_{DSLY}/A_{IS}). Linearity was observed over the concentration range of 0.22–55 μg/mL. Moreover, the limit of detection (S/N≥3), within-day and between-day precisions, and recovery method of dehydrosilybin in rabbit plasma were also determined by HPLC.

Bioavailability studies

The bioavailability of dehydrosilymarin-loaded proliposomes was compared with that of dehydrosilymarin suspension. Dehydrosilymarin-loaded proliposomes were diluted with distilled water to form liposomal suspension, while a dehydrosilymarin suspension was prepared by dispersing the milling drug in water by ultrasonic resuspension. Six rabbits weighing 2.5±0.5 kg (supplied by the Laboratory Animal Center of Jiangsu University) were randomly divided into two groups and fasted overnight prior to the experiment, while water was available *ad libitum* following the regulations for the administration of affairs concerning experimental animals (State Council of the China, 1988). All research protocols were approved by the Research Ethics Committee of Jiangsu University. The rabbits in each group were given the dehydrosilymarin liposomal suspension and dehydrosilymarin suspension through gavage administration for a dose of dehydrosilymarin of 80 mg/kg. Approximately 1.2 mL of blood was collected through the peripheral ear vein into heparinized tubes at 0.25, 0.5, 1, 2, 3, 4, 6, 8, 10, and 12 h. Blood samples were immediately separated by centrifugation (3000 revolutions per minute for 10 min), and subsequent plasma samples were stored at -20 °C until further analysis.

The peak concentration (C_{max}) and peak time (t_{max}) were derived directly from the experimental points as raw data. The other pharmacokinetic parameters were calculated by the software program BAPP 2.3 (Nanjing Baikang Pharmaceutical Co Ltd, China).

Results

Synthesis of dehydrosilymarin

The experimental results demonstrated that reaction time and reaction temperature could affect the synthetic product. Too long a reaction time or too high a reaction temperature would result in carbonation. Finally, dehydrosilymarin was prepared at 90 °C under reflux for 77 h with stirring. The yield of dehydrosilymarin was generally approximately 70%–80%.

Preparation of dehydrosilymarin-loaded proliposomes

The shape, outward appearance and entrapment efficiency of proliposomes were characterized. The results proved that the proliposomes was smooth and sphericeal in appearance with better dispersion and high entrapment efficiency. The proliposomes can be administered orally in the form of powders or filled into capsules.

Characteristics of dehydrosilymarin in dehydrosilymarin-loaded proliposomes

The dehydrosilymarin-loaded proliposomes turned into a liposomal suspension when diluted with distilled water. The morphological characterization of dried dehydrosilymarin-loaded liposomes is shown in Figure 1. The observed liposome droplets were spherical.

Because the particle size of the preparation made a large impact on its *in vitro* and *in vivo* performance, we measured the size distribution of dehydrosilymarin-loaded proliposomes after diluting them with distilled water. The result is displayed in Figure 2. It can be seen from the picture that the particle size of dehydrosilymarin-loaded liposomes was distributed in the range of 7 to 50 nm, and the average diameter was 15.5 nm, which was consistent with the results of the TEM

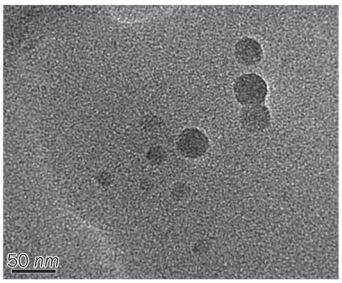

Figure 1. Transmission electron micrograph for liposomal dispersion at×4000 magnification.

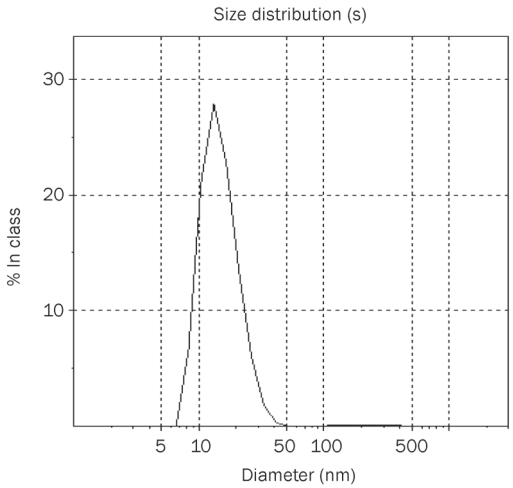

Figure 2. Size distribution of dehydrosilymarin-loaded proliposomes.

analysis. We were pleased to note that the relatively small size of liposomes may have the potential to facilitate the oral absorption of dehydrosilymarin.

The content of dehydrosilymarin in dehydrosilymarin-loaded proliposomes after hydration with water was 25.00±5.93 μg/mL (n=3), and the drug loading percentage was approximately 12.5%.

The entrapment efficiency of dehydrosilymarin in proliposomes was 81.59%±0.24% (n=3), which was predominately dependent on the dehydrosilymarin/phospholipid ratio and sodium cholate/phospholipid. Increasing the amount of phospholipid in addition to adding a moderate amount of surfactants in the prescription can increase drug encapsulation efficiency. However, excessive amounts of phospholipid not only increased the viscosity of the final preparation, but also yielded a sharp reduction in the drug loading efficiency, while the toxicity of surfactant also limited its dosage.

In vitro release studies

As shown in Figure 3, the release of dehydrosilymarin from suspension and proliposomes was poor in pH 1.2, with less than 20% of drug going into the medium after 12 h. Despite a slightly higher release of the drug from suspension than from

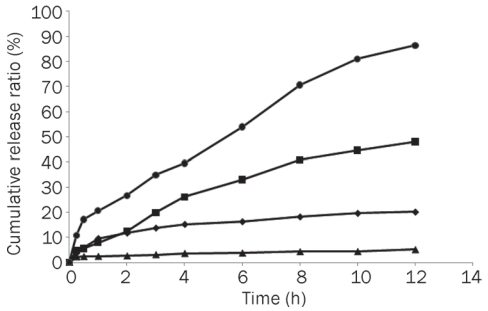

Figure 3. *In vitro* release profiles of dehydrosilymarin from suspension and proliposomes in different release mediums containing 0.1 % of sodium dodecyl sulfate as surfactant. (♦), suspension in 900 mL HCl (pH 1.2); (▲), proliposomes in 900 mL HCl (pH 1.2); (■), suspension in 900 mL phosphate buffered saline (pH 6.8); (●), proliposomes in 900 mL phosphate buffered saline (pH 6.8).

proliposomes in pH 1.2, the release of the drug from proliposomes was tremendously increased compared with that of the drug suspension in pH 6.8. Furthermore, dehydrosilymarin was continuously released from proliposomes in PBS, and the cumulative release ratio was up to 86.41% at 12 h.

Rabbit bioavailability experiments

Dehydrosilybin, the main active ingredient of dehydrosilymarin, was measured as the indicator of bioavailability. In accordance with previous pretreatment and chromatographic conditions, blank rabbit plasma, blank rabbit plasma spiked with dehydrosilybin and a sample after oral administration of dehydrosilymarin-loaded proliposomes were analyzed by HPLC (Figure 4). Good separation of the main peak and the hybridized peak was achieved in the present chromatographic conditions. The retention time of internal standard and dehydrosilybin was approximately 7.5 and 17.5 min, respectively.

Within the concentration range of 0.22–55 μg/mL, the peak area ratio (R) of dehydrosilybin as a whole compared to the internal standard correlated well to the spiked plasma concentration: R=0.5691C–0.0058, r=0.9991. The lowest limit of quantification for the determination of dehydrosilybin in rabbit plasma was found to be 50 ng/mL. The relative standard deviations of intra-day and inter-day assay and the spiked recoveries of dehydrosilybin from rabbit plasma are shown in Table 1.

The oral bioavailabilities of dehydrosilymarin-loaded proliposomes and drug powders were compared in rabbits. Figure 5 shows the drug plasma profiles after gavage administration of dehydrosilymarin-loaded liposomal suspension and dehydrosilymarin suspension (n=3). The liposomal suspension was obtained by dispersing proliposome powders in distilled water. The dehydrosilymarin suspension was prepared by mixing dehydrosilymarin powders with distilled water. As seen in the graph, the plasma concentration of dehydrosilymarin suspension was at a low and stable level at 12 h, although a slight peak was observed at 2 h. The drug concentration of dehydrosilymarin-loaded liposomal suspension

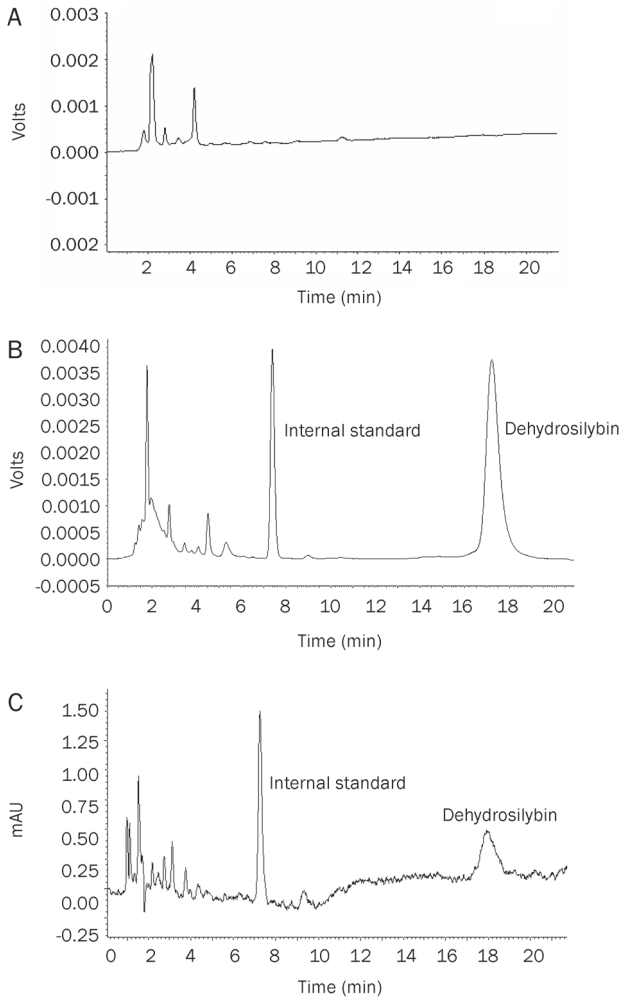

Figure 4. Typical chromatograms of dehydrosilybin: (A) blank rabbit plasma; (B) blank rabbit plasma spiked with dehydrosilybin; (C) a sample after oral administration of dehydrosilymarin-loaded proliposomes.

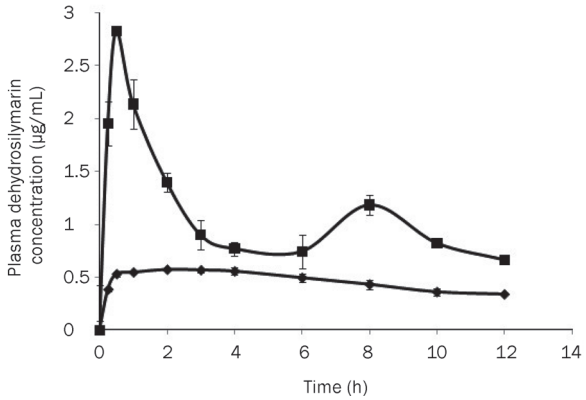

Figure 5. Mean plasma concentration-time curves of dehydrosilybin after oral administration of dehydrosilymarin suspension and dehydrosilymarin-loaded liposomal suspension (*n*=3, 80 mg/kg). (♦), dehydrosilymarin suspension; (■), dehydrosilymarin-loaded liposomal suspension. Data expressed as mean±SD.

was much higher than that of dehydrosilymarin suspension at every time point, and doubly sharp peaks at maximum concentrations were seen as a result, which is a characteristic of enterohepatic circulation[24]. Moreover, C_{max} was approximately 0.57 μg/mL after the dehydrosilymarin suspension was orally administered to rabbits with a t_{max} of 2.00 h. Meanwhile, after oral administration of the dehydrosilymarin-loaded liposomal suspension, the value of C_{max} was approximately 2.83 μg/mL with a t_{max} of 0.50 h. In conclusion, the dehydrosilymarin-loaded proliposomes took less time to reach the maximum plasma concentration in comparison with the dehydrosilymarin suspension, and the C_{max} was approximately 4.96-fold higher than that of the dehydrosilymarin suspension.

The pharmacokinetic parameters calculated by the software program BAPP 2.3 are shown in Table 2. It was found that the curves plotting the plasma concentration of dehydrosilybin over time after the oral administration of the dehydrosilymarin suspension and dehydrosilymarin-loaded liposomal suspension in rabbits were both in accordance with a non-compartment model. As shown in Table 2, dehydrosilymarin-loaded proliposomes exhibited higher absorption in 12 h. The AUC_t of the vesicle was approximately 2.29-fold higher than that of the dehydrosilymarin suspension, which meant that the relative bioavailability of dehydrosilymarin-loaded proliposomes was approximately 228.85%.

Table 2. Pharmacokinetic parameters of dehydrosilymarin suspension and dehydrosilymarin-loaded liposomal suspension (*n*=3, 80 mg/kg). Data expressed as mean±SD.

Parameters	Unit	Dehydrosilymarin	Dehydrosilymarin-loaded proliposomes
AUC_t	μg·mL^{-1}·h	5.58±0.21	12.77±1.39
$t_{1/2}$	h	20.63±5.03	7.48±0.30
t_{max}	h	2.00	0.50
MRT	h	21.33±0.24	6.98±0.71

Table 1. The precision and recovery tests of dehydrosilybin in rabbit plasma. Data expressed as mean±SD. *n*=5.

Added (μg/mL)	Within-day		Between-day		Recovery (%)
	Concentration (μg/mL)	RSD (%)	Concentration (μg/mL)	RSD (%)	
1.0	1.02±0.10	10.21	1.22±0.17	14.22	121.8
5.0	5.49±0.03	0.51	5.84±0.60	10.34	116.9
50.0	55.27±5.14	9.29	61.37±5.40	8.79	122.7

In vitro and *in vivo* correlation

The *in vitro* and *in vivo* correlation was analyzed using the software program BAPP 2.3. The Wegner-Nelson method was applied to compare the *in vitro* drug release curve with the *in vivo* absorption curve. The linear regression equations of drug powders and proliposomes *in vivo* versus release percentages *in vitro* after 1–12 h were calculated. As presented in Table 3, F_r was the *in vitro* release percentage, and F_a was the *in vivo* absorption percentage. Apparently, the *in vivo* absorption of dehydrosilymarin and proliposomes significantly correlated with the *in vitro* drug release at both pH 1.2 and pH 6.8; the *in vitro* release study could be used to help predict the drug absorption *in vivo*.

Discussion

Silymarin is a flavonoid complex extracted from seeds of the milk thistle (*Silybum marianum*)[25] that contains the main active compounds silybin, silychristine and silydianin[2]. Silybin, the major active moiety, has been widely used in the prevention and treatment of various liver diseases. Nevertheless, the bioavailability of silybin is rather limited due to its low solubility in water[26, 27]. The equilibrium solubility of silybin in water is approximately 51.06 μg/mL at 37 °C. Therefore, some preparations have been made in recent years to improve the solubility and bioavailability of silybin, including phospholipid complexes[28], sodium cholate/phospholipid complexes and povidone-sodium cholate-phospholipid mixed micelles[29, 30]. Recently, 2,3-dehydrosilybin, an oxidized form of silybin, has been reported to exhibit a significantly greater antioxidant and anticancer activity in comparison with silybin[22]. We synthesized dehydrosilymarin following the method originally designed for the preparation of dehydrosilybin and confirmed that dehydrosilymarin showed increased antiradical and antioxidative capacities than those of silybin, dehydrosilybin and silymarin[5]. The compositions of dehydrosilymarin were studied with HPLC-MS analysis (data not shown).

Prior to the preparation of proliposomes, we initially produced dehydrosilymarin-phospholipid complexes to improve the lipid solubility of dehydrosilymarin, which was convenient for the formation of liposomes. The results revealed that the mass ratio of dehydrosilymarin to phospholipid had the most significant effect on entrapment efficiency of proliposomes. With an increasing amount of phospholipid, the encapsulation efficiency of proliposomes was correspondingly increased. When the concentration of phospholipid reached a certain proportion, the encapsulation efficiency of proliposomes was mostly unchanged. Moreover, too high a concentration of phospholipid drastically decreased the drug loading percentage, and gradually increased the viscosity of the final preparation. As a result, optimal drug-lipid ratio was determined to be 1:3.

The cumulative release of dehydrosilymarin from proliposomes in pH 6.8 and pH 1.2 was compared to simulate the environment of the stomach and small intestine. Above all, it was important to disperse proliposomes with water to form a liposomal suspension; otherwise, the proliposomes powders would stick to the dialysis bag, thus affecting drug release from the liposomal suspension.

To simulate the *in vivo* release profiles of the vesicles, minute amounts of surfactant are typically incorporated into the release medium. In this study, 0.1% sodium dodecyl sulfate was employed as a surfactant, mimicking the presence of bile salts, which are the natural surfactants in the gastrointestinal tract.

The *in vitro* study showed that the release of dehydrosilymarin from proliposomes in pH 1.2 was relatively poor and that the drug was continuously released from proliposomes in pH 6.8. These results might be explained by the fact that the lipophilic drug was held by the small fragment of the liposomal membrane. Therefore, the drug that was loaded in the lipid membrane was released mainly through dissolution and diffusion from the lipid bilayer, which could decrease the release rate of dehydrosilymarin from proliposomes[31, 32]. However, the higher accumulative release ratio of proliposomes in pH 6.8 was attributed to the fact that the formulation afforded a greater solubilizing effect on the drug, thus enhancing the release rate.

A study on the pharmacokinetics of dehydrosilymarin-loaded proliposomes in rabbits after oral administration was also conducted. The results indicated that, in rabbits, the absorption profile of the proliposomes was much better than that from the suspension. We speculated that the underlying

Table 3. The correlative results of dehydrosilymarin powders and dehydrosilymarin-loaded proliposomes *in vitro* and *in vivo* (Checked the critical value table for *r*, when the degree of freedom *v* was 8, critical value $r_{8,\,0.05}$=0.632, which showed the correlation coefficients of regression equations of drugs $r>r_{8,\,0.05}$).

Formulation type	*t* (h)	0.25	0.5	1	2	3	4	6	8	10	12	*r*
Powders	F_r (%)	3.67	5.81	9.58	11.73	13.76	15.22	16.31	18.24	19.67	20.17	0.9886
in pH 1.2	F_a (%)	41.59	58.40	63.18	72.34	78.32	83.56	89.04	92.90	94.36	100.0	
Proliposomes	F_r (%)	2.30	2.40	2.51	2.67	3.19	3.71	3.85	4.38	4.46	5.22	0.9594
in pH 1.2	F_a (%)	25.33	40.12	40.76	44.57	46.84	51.29	61.89	81.08	91.19	100.0	
Powders	F_r (%)	4.81	5.61	7.99	12.46	19.96	26.15	33.00	40.83	44.66	48.04	0.9362
in pH 6.8	F_a (%)	41.59	58.40	63.18	72.34	78.32	83.56	89.04	92.90	94.36	100.0	
Proliposomes	F_r (%)	10.75	17.15	20.73	26.68	34.97	39.57	54.02	70.65	80.08	86.41	0.9887
in pH 6.8	F_a (%)	25.33	40.12	40.76	44.57	46.84	51.29	61.89	81.08	91.19	100.0	

mechanism for the improvement of oral absorption of proliposomes could be explained by the relatively small size of the proliposomes, the presence of bile salts and the similarity between liposomal lipid bilayers and biomembranes. Therefore, we deduced that proliposomes, as a new dosage form, provide a promising method to enhance the oral absorption of hydrophobic drugs. As noted in the results, the double peak phenomenon was observed for the plasma concentration versus time curve for dehydrosilymarin-loaded proliposomes. Enterohepatic cycling is known to be responsible for secondary peaks in relation with bile salts, the component of proliposomes.

Interestingly, although the plasma concentration of the dehydrosilymarin suspension was low, the MRT was relatively long (about 21.33 h after oral administration). However, we failed to detect the existence of the drug after oral administration of the same dosage of silymarin, which meant that the absorption of dehydrosilymarin *in vivo* was obviously better than silymarin. The reasons that dehydrosilymarin exhibited better bioavailability will be investigated in our further research.

In summary, the current study demonstrates that the oral bioavailability of the new drug dehydrosilymarin was significantly enhanced by proliposomes (a polyphase dispersed system composed of phospholipids, cholesterol, isopropyl myristate, and sodium cholate). The relatively small size of proliposomes, the presence of bile salts and the similarity between liposomal lipid bilayers and biomembranes might be responsible for the improved oral absorption. Moreover, the results *in vivo* significantly correspond with the *in vitro* release results, suggesting that the *in vitro* release study can be used to help predict drug absorption *in vivo*. However, the absorption mechanism of dehydrosilymarin will require further investigation.

Acknowledgements

This work was supported by the National Natural Science Foundation of China (No 30973677 and 30472098) and the Natural Science Fund from Jiangsu Municipal Government, Jiangsu, China (No 08KJB360001).

Author contribution

Xi-ming XU, Jiang-nan YU, and Yan-ru GE designed the research; Shan-shan TONG and Chang CHU performed the research; Xi-ming XU, Shan-shan TONG, Ying XU, Li WANG, Chang CHU, and Min FU analyzed the data; Chang CHU wrote the paper.

References

1 Weiss R, Fintelmann V. Herbal Medicine, 2nd ed. Thieme, Stuttgart, New York, 2000. p 109–11.
2 Schuppan D, Jia JD, Brinkhaus B, Hahn EG. Herbal products for liver diseases: a therapeutic challenge for the new millennium. Hepatology 1999; 30: 99–104.
3 Wu W, Wang Y, Que L. Enhanced bioavailability of silymarin by self-microemulsifying drug delivery system. Eur J Pharm Biopharm 2006; 63: 288–94.
4 Xiao YY, Song YM, Chen ZP, Ping QN. Preparation of silymarin proliposome: a new way to increase oral bioavailability of silymarin beagle dogs. Int J Pharm 2006; 319: 162–8.
5 Tong SS, Chu C, Wei Y, Wang L, Gao XZ, Xu XM, *et al*. Preparation and effects of 2,3-dehydrosilymarin, a promising and potent antioxidant and free radical scavenger. J Pharm Pharmacol 2011; 63: 238–44.
6 Chen YP, Lu Y, Chen JM, Lai J, Sun J, Hu FQ, *et al*. Enhanced bioavailability of the poorly water-soluble drug fenofibrate by using liposomes containing a bile salt. Int J Pharm 2009; 376: 153–60.
7 Ariën A, Goigoux C, Baquey C, Dupuy B. Study of *in vitro* and *in vivo* stability of liposomes loaded with calcitonin or indium in the gastrointestinal tract. Life Sci 1993; 53: 1279–90.
8 Ariën A, Henry-Toulmé N, Dupuy B. Calcitonin-loaded liposomes: stability under acidic conditions and bile salts-induced disruption resulting in calcitonin-phospholipid complex formation. Biochim Biophys Acta 1994; 1193: 93–100.
9 Aungust BJ. Novel formulation strategies for improving oral bioavailability of drugs with poor membrane permeation or presystemic metabolism. J Pharm Sci 1993; 82: 979–87.
10 Sivakumar PA, Panduranga Rao K. The use of cholesteryl pullulan for the preparation of stable vincristine liposomes. Carbohydr Polym 2003; 51: 327–32.
11 Lau KG, Hattori Y, Chopra S, O'Toole EA, Storey A, Nagai T, *et al*. Ultradeformable liposomes containing bleomycin: *in vitro* stability and toxicity on human cutaneous keratinocyte cell lines. Int J Pharm 2005; 300: 4–12.
12 Cocera M, Lopez O, Coderch L, Parra JL, de la Maza A. Permeability investigations of phospholipid liposomes by adding cholesterol. Colloids Surf A Physicochem Eng Asp 2003; 221: 9–17.
13 Dong C, Rogers JA. Polymer-coated liposomes: stability and release of ASA from carboxymethyl chitin coated liposomes. J Control Release 1991; 17: 217–24.
14 Henriksen I, Vhgen SR, Sande SA, Smistad G, Karlsen J. Interactions between liposomes and chitosan. II. Effect of selected parameters on aggregation and leakage. Int J Pharm 1997; 146: 193–204.
15 Takeuchi H, Kojima H, Yamamoto H, Kawashima Y. Evaluation of circulation profiles of liposomes coated with hydrophilic polymers having different molecular weights in rats. J Control Release 2001; 75: 83–91.
16 Guo J, Ping Q, Jiang G, Huang L, Tong Y. Chitosancoated liposomes: characterization and interaction with leuprolide. Int J Pharm 2003; 260: 167–73.
17 Winden E, Crommelin D. Short term stability of freeze-dried, lyoprotected liposomes. J Control Release 1999; 58: 69–86.
18 Glavas-Dodov M, Fredro-Kumbaradzi E, Goracinova K, Simonoska M, Calis S, Trajkovic-Jolevska S, *et al*. The effects of lyophilization on the stability of liposomes containing 5-FU. Int J Pharm 2005; 291: 79–86.
19 Sweeney LG, Wang Z, Loebenberg R, Wong JP, Lange CF, Finlay WH. Spray-freeze-dried liposomal ciprofloxacin powder for inhaled aerosold rug delivery. Int J Pharm 2005; 305: 180–5.
20 Hildebrand A, Beyer K, Neubert R, Garidel P, Blume A. Temperature dependence of the interaction of cholate and deoxycholate with fluid model membranes and their solubilization into mixed micelles. Colloids Surf B Biointerfaces 2003; 32: 335–51.
21 Porter CJ, Trevaskis NL, Charman WN. Lipid and lipid-based formulations: optimizing the oral delivery of lipophilic drugs. Nat Rev Drug Discov 2007; 6: 231–48.
22 Gazák R, Svobodová A, Psotová J, Sedmera P, Prikrylová V, Walterová D, *et al*. Oxidised derivatives of silybin and their antiradical and anti-

oxidant activity. Bioorg Med Chem 2004; 12: 5677–87.
23 Takemoto T, Ikegawa S, Nomoto K. Studies on constituents of *Silybum marianum* (L) Gaertn. I. New flavonolignans named 2,3-dehydrosilymarin and 2,3-dehydrosilychristin. Yakugaku Zasshi 1975; 95: 1017–21.
24 Morazzoni P, Montalbetti A, Malandrino S, Pifferi G. Comparative pharmacokinetics of silipide and silymarin in rats. Eur J Drug Metab Pharmacokinet 1993; 18: 289–97.
25 Luper S. A review of plants used in the treatment of liver disease: part 1. Altern Med Rev 1998; 3: 410–21.
26 Křen V, Walterova D. Silybin and silymarin-new effects and applications. Biomed Pap Med Fac Univ Palacky Olomouc Czech Repub 2005; 149: 29–41.
27 Gažák R, Walterová D, Křen V. Silybin and silymarin-new and emerging applications in medicine. Curr Med Chem 2007; 14: 315–38.
28 Xiao YY, Song YM, Chen ZP, Ping QN. The preparation of silybin-phospholipid complex and the study on its pharmacokinetics in rats. Int J Pharm 2006; 307: 77–82.
29 Yu JN, Zhu Y, Wang L, Peng M, Tong SS, Cao X, *et al*. Enhancement of oral bioavailability of the poorly water-soluble drug silybin by sodium cholate/phospholipid-mixed micelles. Acta Pharmacol Sin 2010; 31: 759–64.
30 Zhu Y, Yu JN, Tong SS, Wang L, Peng M, Cao X, *et al*. Preparation and *in vitro* evaluation of povidone-sodium cholate-phospholipid mixed micelles for the solubilization of poorly soluble drugs. Arch Pharm Res 2010; 33: 911–7.
31 Cocera M, Lopez O, Coderch L. Alterations in stratum corneum lipid liposomes due to the action of Triton X-100: influence of the level of ceramides on this process. J Control Release 2000; 68: 387–96.
32 Du B, Li Y, Li XT, A YM, Chen CQ, Zhang ZZ. Preparation, characterization and *in vivo* evaluation of 2-methoxyestradiol-loaded liposomes. Int J Pharm 2010; 384: 140–7.